

# **Thermoconvective Instability in Porous Media**

Emily Dodgson

A thesis submitted for the degree of Doctor of Philosophy

University of Bath

Department of Mechanical Engineering

October 2011

## **COPYRIGHT**

Attention is drawn to the fact that copyright of this thesis rests with the author. A copy of this thesis has been supplied on condition that anyone who consults it is understood to recognise that its copyright rests with the author and that they must not copy it or use material from it except as permitted by law or with the consent of the author.

This thesis may be made available for consultation within the University Library and may be photocopied or lent to other libraries for the purposes of consultation.

.....

# Contents

<b>1</b>	<b>Introduction</b>	<b>1</b>
1.1	Porous Media . . . . .	2
1.2	Darcy's Law . . . . .	4
1.3	Approximations and Assumptions . . . . .	6
1.3.1	Oberbeck-Boussinesq Approximation . . . . .	6
1.3.2	Local Thermal Equilibrium . . . . .	8
1.4	Convection . . . . .	9
1.5	Stability . . . . .	10
1.6	The Darcy-Bénard problem . . . . .	11
1.6.1	Stability of Darcy-Bénard Flow . . . . .	12
1.7	The Free Convection Boundary Layer . . . . .	13
1.8	Absolute vs. Convective Instability . . . . .	14
<b>2</b>	<b>The Inclined Boundary Layer Problem</b>	<b>15</b>
2.1	Introduction . . . . .	15
2.2	Stability of Thermal Boundary Layers . . . . .	18
2.2.1	Measuring Instability in Boundary Layer Flows . . . . .	19
2.2.2	The Vertical Boundary Layer in a Porous Medium . . . . .	19

2.2.3	Stability of the Near Vertical Boundary Layer in a Porous Medium . . . . .	21
2.2.4	The Horizontal Boundary Layer in a Porous Medium . . . . .	23
2.2.5	Stability of the Generally Inclined Boundary Layer in a Porous Medium . . . . .	24
2.2.6	Extensions to the Thermal Boundary Layer Problem . . . . .	25
2.2.7	Thermal Boundary Layers in a Clear Fluid . . . . .	26
2.3	Determining the Basic Flow in Inclined Boundary Layers . . . . .	27
2.4	Use of the Parallel Flow Approximation in Inclined Boundary Layer Flows . . . . .	29
2.5	Governing Equations . . . . .	30
2.5.1	Nondimensionalisation . . . . .	31
2.5.2	Velocity Potential . . . . .	31
2.5.3	Coordinate Transformation . . . . .	34
2.6	Boundary Conditions . . . . .	37
<b>3</b>	<b>Boundary Layer - Numerical Methods and Validation</b>	<b>39</b>
3.1	Numerical Methods . . . . .	39
3.1.1	Fourier Decomposition . . . . .	40
3.1.2	Spatial Discretisation . . . . .	42
3.1.3	Boundary Conditions . . . . .	44
3.1.4	Temporal Discretisation . . . . .	45
3.1.5	Structure of the Implicit Code . . . . .	47
3.1.6	Gauss-Seidel with Line Solving . . . . .	47
3.1.7	Arakawa Discretisation . . . . .	49
3.1.8	MultiGrid Schemes . . . . .	51

3.1.9	Methodology for Calculating Critical Distance . . . . .	52
3.1.10	Convergence . . . . .	53
3.2	Verification of the Implicit Code . . . . .	54
3.2.1	Run Times . . . . .	54
3.2.2	Mesh Density . . . . .	54
3.2.3	Number of Fourier Modes . . . . .	55
3.2.4	Length of Domain . . . . .	56
3.2.5	Thickness of the Layer . . . . .	56
3.2.6	Buffer Zone . . . . .	57
3.2.7	Timestep . . . . .	59
<b>4</b>	<b>Inclined Boundary Layer Results and Discussion</b>	<b>60</b>
4.1	Steady Basic State . . . . .	61
4.2	Case 1a. Unforced Global Disturbance . . . . .	64
4.2.1	Typical Time History . . . . .	67
4.2.2	Comparison of Elliptic and Parabolic Results for Case 1 . . . . .	73
4.3	Case 1b. Evolution of an Isolated Disturbance . . . . .	76
4.4	Verifying the Convective Nature of Case 1 . . . . .	84
4.4.1	Effect of Time Discretisations . . . . .	85
4.4.2	Coordinate stretching in the $\eta$ -direction . . . . .	88
4.5	Case 2 - Global Forced Vortices . . . . .	89
4.5.1	Typical Steady State Profile . . . . .	90
4.5.2	Methodology for calculating $\xi_k$ . . . . .	94
4.5.3	Neutral Curves for Case 2 . . . . .	99
4.5.4	Comparison of Elliptic and Parabolic Results for Case 2. . . . .	102
4.5.5	Sub Harmonic Forcing . . . . .	105

4.6	Case 3 - Leading Edge Forced Vortices . . . . .	111
4.7	Conclusions . . . . .	117
4.8	Further Work . . . . .	119
<b>5</b>	<b>Front Propagation in the Darcy-Bénard Problem</b>	<b>120</b>
5.1	Introduction to Front Propagation . . . . .	121
5.1.1	Front Propagation Theory . . . . .	122
5.1.2	The Unifying Theory for “Pulled” Fronts . . . . .	123
5.1.3	Front Propagation in the Rayleigh-Bénard Problem . . . . .	123
5.2	Equations of Motion . . . . .	125
5.3	Weakly Nonlinear Analysis: 2D Front Propagation . . . . .	128
5.3.1	Numerical Calculation of Speed of Propagation . . . . .	129
5.3.2	Effect of Varying the Initial Conditions . . . . .	133
5.4	Nonlinear Numerical Analysis: 2D Front Propagation . . . . .	140
5.4.1	Numerical Method . . . . .	140
5.4.2	The 2D, Nonlinear, Propagating Front . . . . .	142
5.4.3	Asymptotic Velocity . . . . .	144
5.4.4	Wavenumber Selection . . . . .	145
5.5	Weakly Nonlinear Analysis: 3D Front Propagation . . . . .	149
5.5.1	Numerical Calculation of $v_{as}$ for Longitudinal Rolls . . . . .	150
5.5.2	Effect of Varying the Initial Conditions . . . . .	152
5.5.3	Planform Selection . . . . .	156
5.6	Nonlinear Numerical Analysis: 3D Front Propagation . . . . .	159
5.6.1	Governing Equations . . . . .	159
5.6.2	Numerical Method . . . . .	160
5.6.3	Effect of Varying Initial Conditions . . . . .	161

5.6.4	Effect of Varying Fourier Wavenumber . . . . .	165
5.7	Conclusions . . . . .	169
5.8	Further Work . . . . .	170
<b>6</b>	<b>The Onset of Prandtl-Darcy Convection in a Horizontal Porous Layer subject to a Horizontal Pressure Gradient</b>	<b>171</b>
6.1	Background . . . . .	172
6.2	Governing Equations . . . . .	174
6.3	Linear Perturbation Analysis . . . . .	176
6.4	Numerical Method . . . . .	181
6.5	Numerical Results . . . . .	181
6.6	Asymptotic analysis for $Q \ll 1$ . . . . .	182
6.7	Asymptotic Analysis for $\gamma \ll 1$ . . . . .	189
6.8	Asymptotic Analysis for $Q \rightarrow \infty$ . . . . .	194
6.9	Conclusions . . . . .	197
<b>7</b>	<b>Final Conclusions and Further Work</b>	<b>198</b>
7.1	Overview . . . . .	199
7.2	Further Work . . . . .	200
<b>A</b>	<b>Multigrid Schemes</b>	<b>212</b>
A.1	MultiGrid Correction Scheme . . . . .	214
A.2	Multigrid Full Approximation Scheme . . . . .	215
<b>B</b>	<b>Weakly Nonlinear Analysis</b>	<b>218</b>
<b>C</b>	<b>Analytical Calculation of Speed of Propagation</b>	<b>223</b>

**D Variation of Nusselt Number with  $k$  in the 2D Darcy-Bénard Problem 224**

## **Acknowledgements**

I would like to thank Dr. D.A.S. Rees for all that he has taught me over the last three years, as well as the extra effort he has put in recently to help me finish the thesis. I could not have asked for a better supervisor. I am also grateful to Dr. R. Scheichl for acting as second supervisor.

Finally, my thanks to David and Prandtl the cat, it would not have been half as much fun without you.

## Summary

This thesis investigates three problems relating to thermoconvective stability in porous media. These are (i) the stability of an inclined boundary layer flow to vortex type instability, (ii) front propagation in the Darcy-Bénard problem and (iii) the onset of Prandtl-Darcy convection in a horizontal porous layer subject to a horizontal pressure gradient.

The nonlinear, elliptic governing equations for the inclined boundary layer flow are discretised using finite differences and solved using an implicit, MultiGrid Full Approximation Scheme. In addition to the basic steady state three configurations are examined: (i) unforced disturbances, (ii) global forced disturbances, and (iii) leading edge forced disturbances. The unforced inclined boundary layer is shown to be convectively unstable to vortex-type instabilities. The forced vortex system is found to produce critical distances in good agreement with parabolic simulations.

The speed of propagation and the pattern formed behind a propagating front in the Darcy-Bénard problem are examined using weakly nonlinear analysis and through numerical solution of the fully nonlinear governing equations for both two and three dimensional flows. The unifying theory of Ebert and van Saarloos (Ebert and van Saarloos (1998)) for pulled fronts is found to describe the behaviour well in two dimensions, but the situation in three dimensions is more complex with combinations of transverse and longitudinal rolls occurring.

A linear perturbation analysis of the onset of Prandtl-Darcy convection in a horizontal porous layer subject to a horizontal pressure gradient indicates that the flow becomes more stable as the underlying flow increases, and that the wavelength of the most dangerous disturbances also increases with the strength of the

underlying flow. Asymptotic analyses for small and large underlying flow and large Prandtl number are carried out and results compared to those of the linear perturbation analysis.

# Nomenclature

## Roman Symbols

$a$	constant describing streamwise decay for leading edge disturbance
$C$	arbitrary constant
$c$	specific heat of the solid, phase velocity of cells
$c_a$	acceleration coefficient
$c_F$	dimensionless form-drag constant
$c_P$	specific heat at constant pressure of the fluid
$E$	thermal energy
$F$	amplitude of propagating front
$\mathbf{g}$	gravity vector
$g$	gravitational constant
$H$	layer height
$h$	heat transfer coefficient
$J$	Jacobian
$K$	specific permeability
$k$	wavenumber, thermal conductivity
$\mathcal{L}$	elliptic operator
$L$	lengthscale

$l$	boundary layer thickness
$\mathbb{N}$	nonlinear terms
$N$	number of Fourier modes
$n$	iteration number
$N_\eta$	number of grid points in the $\eta$ direction
$N_\xi$	number of grid points in the $\xi$ direction
$Pr$	Prandtl-Darcy number
$P$	total pressure
$p$	static plus dynamic pressure
$Q$	nondimensional background velocity
$q$	surface heat flux
$q'''$	heat production per unit volume
$Ra$	Darcy-Rayleigh number
$Ra_l$	local Darcy-Rayleigh number based on local boundary layer thickness
$Ra_x$	local Darcy-Rayleigh number based on downstream distance
$Re$	Reynolds number
$T$	temperature
$t$	time
$\mathbf{U}$	velocity vector, $(U, V, W)$
$\mathbf{u}$	nondimensional velocity vector, $(u, v, w)$
$U, V, W$	Darcy velocity in $X, Y, Z$
$u, v, w$	nondimensional velocity in $x, y, z$
$X, Y, Z$	streamwise, spanwise and normal coordinates
$x, y, z$	nondimensional streamwise, spanwise and normal coordinates

## **Greek Symbols**

$\alpha$	angle of inclination to the horizontal
$\alpha_0$	angle of inclination from the vertical
$\beta$	coefficient of thermal expansion
$\chi$	dummy variable
$\gamma$	nondimensional acceleration coefficient
$\varepsilon$	small parameter in weakly nonlinear analysis
$\zeta$	dummy variable
$\eta$	scaled coordinate
$\theta$	nondimensional temperature
$\vartheta$	nonlinear saturation parameter
$\kappa$	thermal diffusivity
$\mu$	dynamic viscosity
$\xi$	scaled streamwise coordinate
$\rho$	density
$\sigma$	heat capacity ratio
$\tau$	scaled time
$\Phi$	porosity
$\phi^{(1)}, \phi^{(2)}, \phi^{(3)}$	velocity potential
$\psi$	stream function

## **Subscripts and Superscripts**

$a_s$	asymptotic value at large time
$b_1, b_2$	start and finish locations for buffer zone
$c$	minimal/minimising critical value
$f$	fluid phase

$i, j$	gridpoint indices
$k$	critical value for a given value of $k$
$m$	overall property
max	maximum value
$n$	iteration number
ref	reference quantity
$s$	solid phase
*	scaled value
0, 1, 2, ...	Fourier mode number
$\infty$	reference quantity
<b>0, 1, 2, ...</b>	term in asymptotic expansion

# Chapter 1

## Introduction

This thesis presents the results of an investigation into thermoconvective instabilities in porous media. Three topics have been investigated: (i) vortex instability in the inclined thermal boundary layer, (ii) front propagation in the Darcy-Bénard problem and (iii) the onset of Prandtl-Darcy convection in the presence of a horizontal pressure gradient. Each of these problems is addressed in turn in the subsequent chapters.

The aim of the present chapter is to introduce material which is common to all three problems while detailed literature surveys related to the three main topics are given later in the thesis. Subjects covered in the present chapter include porous media, Darcy's law, the approximations and assumptions employed in this thesis, the concept of stability, and a brief introduction to the Darcy-Bénard problem and the inclined boundary layer problem.

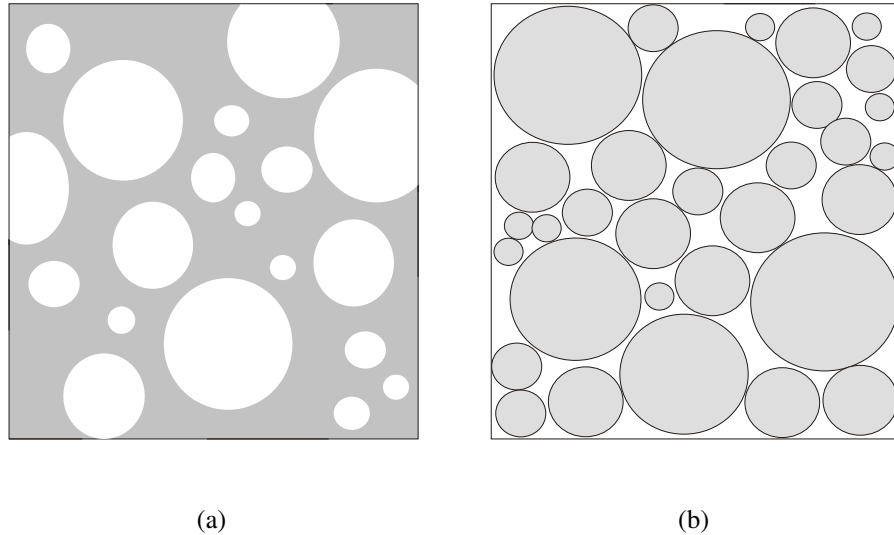


Figure 1.1: Microscopic structure of porous media with (a) solid matrix containing pores and (b) closely packed solids. Solid material is shown in grey, fluid is shown in white.

## 1.1 Porous Media

The term, porous medium, describes a material consisting of both solid and fluid phases, whereby the structure of the solid phase incorporates voids in which the fluid phase(s) are found. This can be formed either from a single solid with holes (e.g. a sponge), or a number of smaller solids packed closely together with small gaps between them (e.g. sand). A diagram showing the macroscopic structure of these two types of porous material is shown in Figure 1.1. The pores (shown in white) allow fluid to flow through the material. In the simplest configuration a single fluid fills the pore space (single phase flow), alternatively a liquid and a gas

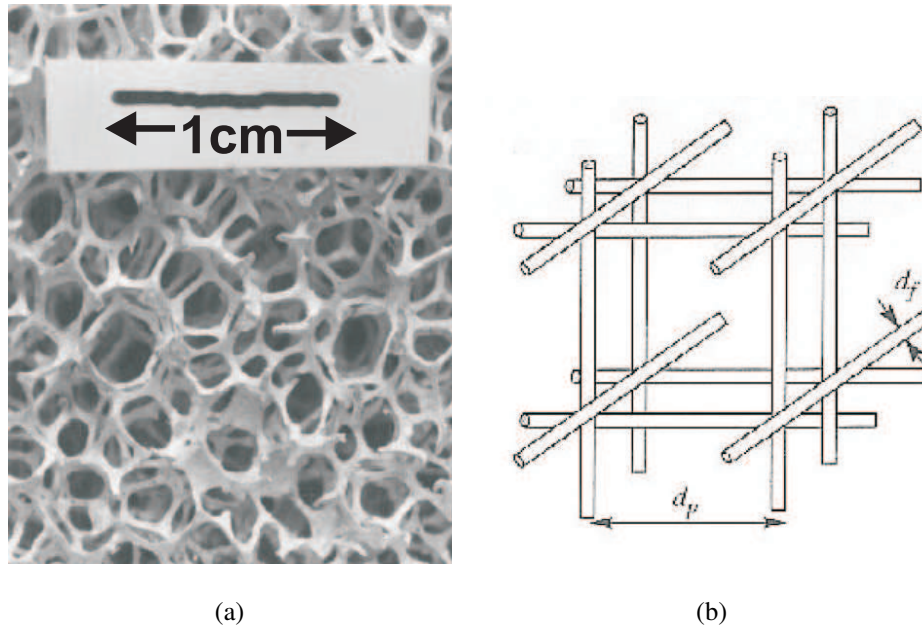


Figure 1.2: Structure of a metal foam: (a) sample microstructure and (b) schematic representation. This is Figure 1 from Bhattacharya et al (2002).

may share the pore space (two-phase flow). This work is concerned with single phase flow.

As the field of porous media has developed the area of metal foams has also become of interest. Metal foams are unique because of their open celled structure (Calmidi and Mahajan (2000)). Figure 1.2, from Bhattacharya et al (2002), shows an example of such a structure.

Porous media may be used to model natural and man-made phenomena as diverse as groundwater flows (soil saturated with water, McKibbin (2009)), reed beds in wetlands (Molle et al (2006)), the human body (tissue in fluid, Sigmund (2011)), industrial cooling processes (pellets being air-dried, Ljung et al (2011)), volcanoes (liquid magma in solid unmelted rock, Bonafede and Boschi (1992))

and methane convection in the regolith of Titan (Czechowski and Kossacki (2009)).

## 1.2 Darcy's Law

When seeking to model the behaviour of a flow through a porous material the investigator may choose between a microscopic or macroscopic approach. The microscopic approach consists of focusing on a small area or volume and modeling the pores as fluid-filled channels in the solid material using traditional fluid-mechanical techniques. This approach requires a detailed knowledge of the internal structure of the porous medium, and the computational resources required almost always well exceed reasonable limits when considering a sufficiently large domain.

The alternative is to take a macroscopic approach using global quantities such as permeability, to replace the detailed microstructure of the material. Equations are then required in which the superficial fluid velocity (i.e. the local average of the microscopic fluid velocities over the porous medium) appears rather than the detailed microscopic velocities. This work will take a macroscopic approach, based upon the equation known as Darcy's law.

In 1856 Darcy published his report on the public fountains of Dijon (quoted in Lage (1998)), which included an equation for relating the volumetric flow rate through a column of sand to the pressure difference along the column. This equation was further refined to include the effects of viscosity and permeability (see Lage (1998) for a full description) until it reached the form commonly known today as *Darcy's law*:

$$U = -\frac{K}{\mu} \frac{\partial P}{\partial X}, \quad (1.1)$$

where  $\partial P/\partial X$  is the pressure gradient in the flow direction,  $K$  is the specific permeability,  $\mu$  is the dynamic viscosity of the fluid, and  $U$  is the fluid speed, also known as the Darcy velocity, superficial velocity or flux velocity. This experimental law has subsequently been derived theoretically using volume averaging techniques by authors such as Whitaker (1986).

Darcy's law is valid for incompressible fluids and for low speed flows for which the microscopic Reynolds number (which is based on the typical pore or particle diameter) satisfies  $Re < 1$ . The law becomes increasingly inaccurate in the range  $1 < Re < 10$ . This is not a transition from laminar to turbulent flow, but is caused by form drag where wake effects and separation bubbles on the microscopic level signify the increasing importance of inertia in comparison with the surface drag due to friction. This deviation from the linearity of Darcy's law is well-described by what is usually termed Forchheimer's extension:

$$\nabla P = -\frac{\mu}{K} \mathbf{U} - c_F K^{-1/2} \rho_f |\mathbf{U}| \mathbf{U}, \quad (1.2)$$

where  $c_F$  is a dimensionless form-drag constant which varies with the nature of the porous medium,  $\mathbf{U}$  is the Darcy velocity vector and  $\rho_f$  is the fluid density. As the value of  $Re$  increases above 300 the microscopic flow does become turbulent, but this transition depends strongly on the microstructure of the medium (de Lemos (2006)).

## 1.3 Approximations and Assumptions

This section discusses approximations and assumptions which are employed in this thesis and which are common to all three problems examined.

### 1.3.1 Oberbeck-Boussinesq Approximation

When it is necessary to include the effects of buoyancy caused by thermal and/or solutal variations, the Oberbeck-Boussinesq approximation is commonly evoked. It is usually assumed that all properties of the porous medium are constant except for the density, and that changes in the density may be ignored except in the buoyancy term.

Darcy's law as given by Eqn. (1.1) is valid for a horizontal column. In the vertical ( $z$ ) direction the pressure will also vary with height according to the following:

$$P = p + \rho g z, \quad (1.3)$$

where  $p$  represents the static and dynamic pressure,  $\rho$  is the density and  $g$  is the gravitational constant. Substituting this identity into Darcy's Law gives

$$W = -\frac{K}{\mu} \left[ \frac{\partial p}{\partial z} + \rho g \right]. \quad (1.4)$$

For the problems investigated in this thesis density varies as a function of temperature as described by Eqn. (1.5), where  $\rho_\infty$  is the fluid density at some reference temperature  $T_\infty$  and  $\beta$  is the coefficient of thermal expansion.

$$\rho = \rho_\infty [1 - \beta (T - T_\infty)] \quad (1.5)$$

Substituting Eqn. (1.5) into Eqn. (1.4) gives

$$\mathbf{U} = -\frac{K}{\mu} [\nabla P - \rho_\infty \mathbf{g} \beta (T - T_\infty)] \quad (1.6)$$

where  $\mathbf{g}$  is the gravity vector and  $\nabla P = \nabla p + \rho_\infty \mathbf{g}$ . Physically this law now relates the velocity of the fluid to the pressure difference acting upon it and the buoyancy force generated by changes in fluid density.

The Boussinesq approximation also impacts on the continuity equation. The continuity equation equates the net mass flux into a representative elementary volume with the increase of mass of fluid within that volume as follows:

$$\Phi \frac{\partial \rho}{\partial t} + \nabla \cdot (\rho \mathbf{U}) = 0. \quad (1.7)$$

The porosity of the porous medium is denoted by  $\Phi$ , and is defined as the fraction of the total volume of the medium that is occupied by void space. Ignoring variations in density, except where they appear in the buoyancy term, reduces this expression to:

$$\nabla \cdot \mathbf{U} = 0. \quad (1.8)$$

Tritton (1988) reviews the limits of applicability of the Oberbeck-Boussinesq approximation. His key criteria for applicability may be summarised as follows;

- Imposed temperature differences should not produce excessive density differences.
- Viscous heating should be negligible.
- The variation of viscosity with temperature should be negligible.
- The vertical lengthscale of the system must be small compared with the vertical scale over which parameters such as pressure, density and temperature change.

Situations where the Boussinesq approximation breaks down include motions of the atmosphere which extend throughout its entire depth, motions occurring in the interior of planets and stars, and large scale subterranean flows.

### 1.3.2 Local Thermal Equilibrium

Assuming that the porous medium is isotropic and that radiation, viscous dissipation, and work done by pressure changes are negligible, then the first law of thermodynamics in a porous medium may (following Nield and Bejan (2006)), be expressed as :

$$(1 - \Phi)(\rho c)_s \frac{\partial T_s}{\partial t} = (1 - \Phi) \nabla \cdot (k_s \nabla T_s) + (1 - \Phi) q_s''' \quad (1.9)$$

for the solid phase, and

$$\Phi(\rho c_P)_f \frac{\partial T_f}{\partial t} + (\rho c_P)_f \mathbf{U} \cdot \nabla T_f = \Phi \nabla \cdot (k_f \nabla T_f) + \Phi q_f''' \quad (1.10)$$

for the fluid phase based upon averages over a representative elemental volume. The subscripts  $s$  and  $f$  refer to the solid and fluid phases respectively. The specific heat of the solid is denoted by  $c$ , whilst  $c_P$ ,  $k$ , and  $q'''$  represent the specific heat at constant pressure of the fluid, the thermal conductivity, and the heat production per unit volume respectively. In this thesis there is no heat generation involved in either the fluid or the solid phases and consequently the terms,  $q_s'''$  and  $q_f'''$  are neglected.

In this thesis it is assumed that the fluid and solid phases are in *Local Thermal Equilibrium* (LTE), that is the temperature and the rate of heat flux at the interface between the solid and fluid phases are in equilibrium. Therefore we set  $T_s = T_f = T$  and add Eqs. (1.9) and (1.10) to give the following:

$$(\rho c)_m \frac{\partial T}{\partial t} + (\rho c_P)_f \mathbf{U} \cdot \nabla T = \nabla \cdot (k_m \nabla T) \quad (1.11)$$

where

$$(\rho c)_m = (1 - \Phi)(\rho c)_s + \Phi(\rho c_P)_f, \quad (1.12)$$

$$k_m = (1 - \Phi)k_s + \Phi k_f, \quad (1.13)$$

are the overall heat capacity per unit volume and the overall thermal conductivity respectively.

In some cases the assumption breaks down, with the solid and fluid phases having significantly differing temperatures and the porous medium is said to be in *Local Thermal Non Equilibrium* (LTNE). It is then necessary to derive a relationship giving the relative temperatures of the two phases. Nield and Bejan (2006) give the simplest form of the heat transport equation in this case as

$$(1 - \Phi)(\rho c)_s \frac{\partial T_s}{\partial t} = (1 - \Phi) \nabla \cdot (k_s \nabla T_s) + h(T_f - T_s), \quad (1.14)$$

$$\Phi(\rho c_P)_f \frac{\partial T_f}{\partial t} + (\rho c_P)_f (U) \cdot \nabla T_f = \Phi \nabla \cdot (k_f \nabla T_f) + h(T_s - T_f), \quad (1.15)$$

where  $h$  is the heat transfer coefficient and  $\nabla T$  is the temperature gradient. Generally speaking the assumption of LTE is valid if one of the phases dominates (Rees (2010)) or if the characteristic lengthscale of the porous medium is small, which gives a large value of  $h$ . A review of developments in this area is given in Rees and Pop (2005). The work in this thesis has all been carried out assuming the porous medium to be in LTE.

## 1.4 Convection

Convection is a fluid movement which occurs as a result of density differences between different regions of a fluid. When acted upon by gravity the difference in density results in buoyancy forces. Lighter, less dense fluid seeks to rise relative to heavier fluid and heavier fluid sinks relative to its lighter surroundings. When the local temperature gradient has a horizontal component, such as when a uniform layer of fluid is enclosed between two plane surfaces which are held at different

but constant temperatures and where the layer is not horizontal, then the density differences drive the fluid motion directly. In the absence of a motive force such as an applied pressure gradient this is known as free convection. When the layer of fluid mentioned above is horizontal, then no buoyancy forces arise because the temperature gradient vector is aligned with the gravity vector, and therefore no flow occurs. However, if the layer is heated from below, then the fluid will be susceptible to instability and convective motion will arise if the buoyancy forces are strong enough to overcome the viscous, dissipative forces that act to maintain the fluid in place.

In a porous medium the ratio of buoyancy forces to viscous forces is summarised by the Darcy-Rayleigh number, defined as

$$\text{Ra} = \frac{\rho g \beta \Delta T K L}{\mu \kappa}, \quad (1.16)$$

where  $L$  is some lengthscale which is appropriate for the problem being considered. In many problems of interest, such as the porous-Bénard layer or free convection boundary layers, there will be a critical threshold  $\text{Ra}_c$  beneath which convective instability will not occur. The onset of convection will often result in a significant alteration in the flow pattern and consequently important characteristics such as heat transfer will be affected.

## 1.5 Stability

A physical system is stable if it returns to its original state after having been perturbed in some way. The original state may itself be steady or unsteady and the perturbations may be either infinitesimally small (for which the corresponding analysis is a linear stability analysis) or large. Two examples of systems which

are intrinsically unstable are the following: an inverted pendulum, and a vessel full of supercooled water. In these examples a small perturbation is sufficient to cause the basic state to evolve to a new state. Other examples include the Bénard and porous-Bénard layer where instability in the form of cellular convection will arise due to small-amplitude perturbations, but only when the appropriate Rayleigh number has been exceeded. There also exist examples for which a flow is linearly stable, but may only be destabilised by a sufficiently large disturbance, e.g. Poiseuille flow in a circular pipe (Smith and Bodonyi (1982)).

## 1.6 The Darcy-Bénard problem

The Darcy-Bénard problem, also known as Horton-Rogers-Lapwood convection, is the prototypical problem for thermoconvective stability in porous media and is the porous media analogue of Rayleigh-Bénard convection in a clear fluid. This problem has been the focus of much attention due to the relative ease with which analytical progress may be made in determining its stability properties in its classical form. A fully saturated layer of porous media is bounded above and below by impermeable, isothermal surfaces. The width of the layer is very much greater than the height, or else is taken to be infinite. The flow domain for such a problem is shown in Figure 1.3. When the lower boundary is hotter than the upper boundary (i.e  $T_0 > T_1$ ) this gives rise to a potentially unstable, stationary basic state where cooler denser fluid lies above that which is hotter and less dense.

When nondimensionalised the governing equations retain a single nondimensional group, the Darcy-Rayleigh number, as given by Eqn. (1.16), where  $L$  refers to the height of the layer. When we consider  $Ra$  to be the ratio of buoyancy forces

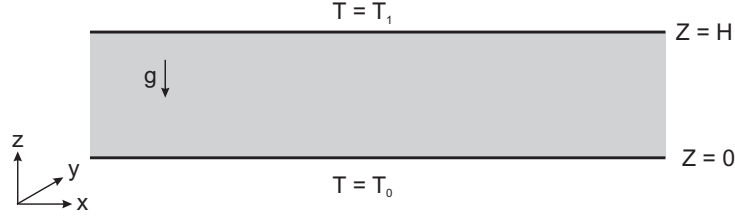


Figure 1.3: Diagram of the flow domain for the Darcy-Bénard problem.

to viscous forces it becomes clear that, for a medium with a given set of physical properties, the magnitude of the temperature difference between the upper and lower surfaces and the height of the layer will drive the increase in  $Ra$  necessary for instability.

This thesis will investigate two topics related to the classical Darcy-Bénard problem; front propagation in the Darcy-Bénard problem and the onset of Prandtl-Darcy convection in a horizontal layer subject to a horizontal pressure gradient.

### 1.6.1 Stability of Darcy-Bénard Flow

Horton and Rogers (1945) and Lapwood (1948) separately derived the linear neutral stability curve for the Darcy-Bénard problem which is given by Eqn. (1.17):

$$Ra = Ra_k = \frac{(k^2 + \pi^2)^2}{k^2}. \quad (1.17)$$

This describes the threshold in parameter space above which convection will occur in the flow domain. The minimum critical value derived is  $Ra_c = 4\pi^2$  and this occurs for the minimising wavenumber  $k_c = \pi$ . However, this Fourier mode analysis does not describe how a disturbance may spread, nor the preferred form

a disturbance may take. The stability of Darcy-Bénard flow is discussed in more detail in Chapters 5 and 6.

## 1.7 The Free Convection Boundary Layer

The free convection boundary layer is a thermal boundary layer which forms adjacent to an inclined heated surface embedded within, or bounding, a porous medium. For a constant temperature heated surface, increasing downstream distance from the leading edge leads to an increase in the thickness of the layer, however the thickness of the layer remains small in comparison to the distance from the leading edge. The local Darcy-Rayleigh number is given by Eqn. (1.16) where  $L$  in this case refers to the local thickness of the boundary layer and  $\Delta T$  is the difference between the temperature of the heated surface and the ambient temperature. Therefore as distance downstream increases it is reasonable to suppose that the local Darcy-Rayleigh number will eventually exceed the critical threshold for convection to occur. At this point perturbations to the flow may begin to be amplified and the layer would then be deemed unstable. The downstream distance at which this occurs will be a function of the angle of inclination of the layer and possibly the wavenumber. For a given wavenumber there will be a critical distance  $x_k$ , and for each angle of inclination there will be a wavenumber,  $k_c$  which minimises the critical distance giving  $x_c$ .

In this thesis the governing equations are nondimensionalised based upon a lengthscale which produces a Darcy-Rayleigh number of unity because there is not a physical value of  $L$  available. Hsu and Cheng (1979) use the parallel flow approximation and conduct a linear stability analysis to produce neutral stability

curves. However, aspects of this analysis, including the self-similar solution used to describe the basic boundary layer flow, and the parallel flow approximation, have been called into question. In order to progress without using these approximations this investigation solved the full, nonlinear, elliptic governing equations numerically. The results given in this thesis demonstrate that the linear stability analysis which uses the parallel flow approximation yields misleading information at arbitrary angles of inclination, implying as it does that an absolute instability exists.

## **1.8 Absolute vs. Convective Instability**

In this thesis stability is defined as either absolute or convective. Where there is an underlying flow, infinitesimal perturbations to the basic state may grow in magnitude but continue to be convected downstream by that flow. Thus, if at any chosen point in the domain, disturbances will always decay eventually, this is termed convective instability. An example of such a case is the vertical boundary layer in a clear fluid (Paul et al (2005)). However, if a disturbance is able to diffuse upstream faster than the background flow, then there will be at least a finite part of the domain in which disturbances continue to grow (in the linear sense); in such situations the instability is said to be absolute in that part of the domain. It is possible in the context of boundary layers to have situations where the instability is advective in one part of the domain (usually close to the leading edge) and absolute in the rest of the domain .

## Chapter 2

# The Inclined Boundary Layer

## Problem

This chapter introduces the inclined boundary layer problem. The current state of the art regarding the stability of boundary layer flows is reviewed. Issues related to the determination of the basic state and the use of the parallel flow approximation in this context are discussed. Finally the governing equations are developed to enable their numerical solution. Steps taken in this respect include nondimensionalisation, the introduction of a velocity potential and a coordinate transformation.

### 2.1 Introduction

We seek to investigate the vortex stability of the thermal boundary layer which is formed on an inclined heated surface embedded within or bounding a fully saturated porous medium. Figure 2.1 depicts the computational domain under consideration, where  $X$  and  $Z$  are the coordinate directions parallel to and perpendicular

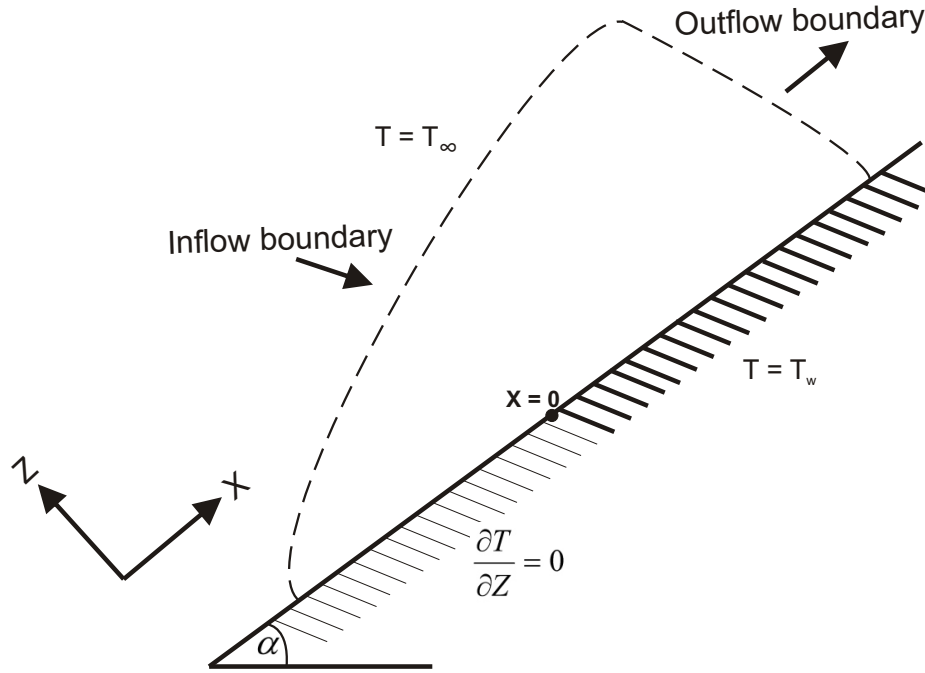


Figure 2.1: Diagram of the thermoconvective boundary layer problem showing the inflow and outflow boundaries which are required for the numerical simulations.

to the heated surface respectively.

The heated surface is inclined at an angle  $\alpha$  to the horizontal. The station,  $X = 0$ , is considered to be the nominal leading edge of the thermal boundary layer. Thus the surface is insulated when  $X < 0$ , while for  $X > 0$  the temperature of the surface is held at  $T_w$ , where  $T_w > T_\infty$ , the ambient temperature far from the heated surface. As a result of these boundary conditions a layer of heated fluid forms adjacent to the inclined surface. The heated fluid typically has a lower density than the fluid at the ambient temperature. The effect of gravity working on

these density differences leads to the generation of buoyancy forces. A component of this force lies along the heated surface resulting in the development of a convective flow along that surface. The flow acts to advect fluid out of the domain and entrain cold fluid towards the heated surface. As  $X$  increases, the thickness of the heated region of fluid increases due to the combined effect of surface heating and the accumulation of advected hot fluid from nearer the leading edge. However, the ratio of the thickness of the hot region and the distance from the leading edge decreases towards zero, thereby fulfilling all the mathematical requirements for the application of boundary layer theory. It may be shown that this ratio is proportional to  $X^{-1/2}$  (Cheng and Minkowycz (1977)).

We consider the manner in which vortices destabilise the thermal boundary layer formed adjacent to the solid surface, and how this is affected by both the angle at which the surface is inclined and the wavenumber of the disturbance. This type of inclined thermal boundary layer has a number of potential geothermal applications including the situation where a magmatic intrusion into an aquifer occurs (Cheng and Minkowycz (1977)).

The following assumptions are made:

- Darcy's law is valid (see Sect. 1.2).
- The Boussinesq approximation applies (see Sect. 1.3.1).
- The medium is homogeneous, rigid and isotropic.

The governing equations for this system are given by the continuity equation,

Darcy's law and the heat transport equation. They take the form:

$$\frac{\partial U}{\partial X} + \frac{\partial V}{\partial Y} + \frac{\partial W}{\partial Z} = 0, \quad (2.1)$$

$$U = -\frac{K}{\mu} \left[ \frac{\partial P}{\partial X} - \rho_{\infty} g \beta (T - T_{\infty}) \sin \alpha \right], \quad (2.2)$$

$$V = -\frac{K}{\mu} \frac{\partial P}{\partial Y}, \quad (2.3)$$

$$W = -\frac{K}{\mu} \left[ \frac{\partial P}{\partial Z} - \rho_{\infty} g \beta (T - T_{\infty}) \cos \alpha \right], \quad (2.4)$$

$$\sigma \frac{\partial T}{\partial t} + U \frac{\partial T}{\partial X} + V \frac{\partial T}{\partial Y} + W \frac{\partial T}{\partial Z} = \kappa \left[ \frac{\partial^2 T}{\partial X^2} + \frac{\partial^2 T}{\partial Y^2} + \frac{\partial^2 T}{\partial Z^2} \right]. \quad (2.5)$$

$U, V,$  and  $W$  are the Darcy velocities in the  $X, Y,$  and  $Z$  directions respectively.  $P$  is the pressure,  $\rho$  the density,  $\mu$  the dynamic viscosity,  $K$  the permeability, and  $\beta$  the volumetric thermal expansion coefficient. Following Nield and Bejan (2006) we define the thermal diffusivity by

$$\kappa = \frac{k_m}{(\rho c_P)_f}, \quad (2.6)$$

and the heat capacity ratio as

$$\sigma = \frac{(\rho c)_m}{(\rho c_P)_f}, \quad (2.7)$$

where  $c$  is the specific heat and  $k_m$  the overall thermal conductivity. These are the standard equations for convective flow in a porous medium and they may be found in Nield and Bejan (2006) as well as in numerous other publications.

## 2.2 Stability of Thermal Boundary Layers

This section briefly reviews the current knowledge regarding the stability of boundary layer flows.

### 2.2.1 Measuring Instability in Boundary Layer Flows

When considering the stability of boundary layer flows it is useful to think in terms of a local Darcy-Rayleigh Number,  $Ra_l$ , defined by Eqn. (2.8). This parameter is a function of  $l$ , the thickness of the boundary layer at a downstream location  $X$ :

$$Ra_l = \frac{\rho_\infty g \beta (T_w - T_\infty) K l}{\mu \kappa}. \quad (2.8)$$

For a generally inclined boundary layer which is induced by a constant temperature surface,  $l$  is proportional to  $X^{1/2}$  (Cheng and Minkowycz (1977)). When the surface is horizontal  $l$  is proportional to  $X^{2/3}$  (Cheng and Cheng (1976)). It follows in both these cases that as the distance from the leading edge of the boundary layer increases then so does  $Ra_l$ . It is reasonable to suppose that at a sufficient downstream distance  $Ra_l$  will pass the threshold value for instability to occur. At this point perturbations to the flow may begin to be amplified and the layer would then be deemed unstable. Consequently the question of interest for the boundary layer problem is: at what distance downstream does a disturbance start to grow? This differs from problems such as the Darcy-Bénard problem where stability is dependent upon a single well-defined value of  $Ra$ .

### 2.2.2 The Vertical Boundary Layer in a Porous Medium

Hsu and Cheng (1979) were the first to examine the instability of an inclined boundary layer to vortex disturbances. The basic flow used was that derived by Cheng and Minkowycz (1977), with the gravitational acceleration term replaced by the streamwise component of gravity. As the work of Cheng and Minkowycz (1977) was based upon the boundary layer approximation, the results of Hsu and Cheng (1979) are valid only in the case where the heated surface is vertical, and

they become increasingly inaccurate as the surface tends toward the horizontal. The reasons for this limitation are discussed in Sect. 2.3. The use of the parallel flow approximation renders their work qualitatively but not quantitatively correct (see Sect. 2.4). However, by using a linear stability analysis they found that the critical distance beyond which vortices start to grow is given by

$$x_c = 120.7 \left( \frac{\sin \alpha}{\cos^2 \alpha} \right). \quad (2.9)$$

A later analysis of the same stability problem by Storesletten and Rees (1998) found the coefficient to be equal to 110.7 (slightly different assumptions were used). The critical wavenumber of the disturbances was found to be proportional to  $\cos \alpha$  by both sets of authors. Given that  $\alpha$  is the angle of the surface from the horizontal, it may be seen that the critical distance recedes to infinity as  $\alpha \rightarrow \frac{\pi}{2}$ , i.e. the surface tends towards the vertical. This suggests strongly that the vertical boundary layer is stable to vortex disturbances.

The numerical study of Rees (1993) considered the fate of wave disturbances. In this paper the governing equations were solved by first transforming them into parabolic coordinates and by using an implicit finite difference discretisation. In this coordinate system the basic boundary layer has constant thickness in terms of the transformed  $z$ -variable (normal coordinate direction). Two-dimensional disturbances were introduced into the boundary layer and their evolution followed numerically. Both single cell and multiple cell disturbances were found to decay under all circumstances. Disturbances placed closer to the leading edge were found to decay more rapidly than an otherwise identical counterpart placed further downstream. Disturbances with a larger streamwise extent also decayed more slowly than those which are shorter. For the domain used, ( $\xi_{\max} = 64$  and  $\eta_{\max} = 15$  in terms of the transformed coordinate system) the basic boundary

layer flow was found to be nonlinearly stable, even when the starting problem (instantaneous temperature rise on the impermeable surface) was considered.

Given the above observation that disturbances decay increasingly slowly as the distance from the leading edge increases, Lewis et al (1995) extended the work of Rees (1993) to examine the asymptotic stability of the vertical boundary layer to two-dimensional waves at large distances from the leading edge. The key conclusion of the paper is that the disturbance does indeed continue to decay with increasing distance: the rate at which it decays was found to be proportional to  $x^{-2/3}$ , where  $x$  is the downstream distance. Disturbances were also found to be confined to a thin region adjacent to the heated surface and well within the boundary layer. Although the parallel flow approximation is used, this work remains of interest. Incorporation of non-parallelism would alter the values of the decay rate, but not the leading order term in the expansion (Lewis et al (1995)).

### **2.2.3 Stability of the Near Vertical Boundary Layer in a Porous Medium**

The evolution of vortex instability in the near-vertical limit has been examined in both the linear (Rees (2001b)) and nonlinear, (Rees (2002b), Rees (2003)) regimes. This work is reviewed by Rees (2002a). The near-vertical thermal boundary layer has been a subject of interest as the boundary layer approximation is sufficiently accurate in this limit so as to give reliable results (see Sect. 2.3). This means the fully nonlinear elliptic governing equations for the vortex disturbance reduce to a consistent set of nonlinear parabolic partial differential equations for the perturbation temperature and pressure which may then be solved to obtain neutral curves. A key difference between the near-vertical and generally

inclined case is that the streamwise diffusion is formally negligible in the former due to the boundary layer approximation being valid. The approach used by Rees (2002b) for the nonlinear regime consists of a spanwise Fourier decomposition and numerical solution using the Keller-Box method.

Neutral curves were derived in Rees (2001b) by monitoring the decay of disturbances with distance downstream. It was found that the quantitative dependence of the critical downstream distance  $x_k$  on the wavenumber depends on the location at which the disturbance is introduced, the profile of the initial disturbance and the manner in which the disturbance magnitude is defined. However, the shape taken by the neutral curve is the classical tear-drop, for which there is a maximum wavenumber beyond which all disturbances are stable.

Rees (2002b) extended the linear analysis into the nonlinear regime. While disturbances which are placed near to the leading edge first decay, then grow, and finally decay once more, it was shown that nonlinear saturation is responsible for premature decay, i.e. decay occurs before the disturbance reaches the location of the upper branch in the linear neutral curve. The maximum strength attained by the disturbance was found (Rees (2002b)) to be influenced by:

- The wavelength of the disturbance.
- The amplitude of the disturbance.
- The point of introduction of the disturbance into the boundary layer.

The decay of the nonlinear vortices suggests the presence of secondary instabilities as  $Ra_\tau$  continues to increase with distance downstream because the boundary layer thickness increases (Rees (2002a)). Rees (2003) examines the effect of sub-harmonic disturbances and as might be expected finds that the location at which

the onset of destabilisation occurs is related to the size of the subharmonic disturbance, and this behaviour is explained well by reference to the neutral curves. The inclusion of inertia terms serves to stabilise the flow, but has a significant impact on the critical wavenumber of the most dangerous vortex due to the resulting increase in the boundary layer thickness (Rees (2002a)).

#### **2.2.4 The Horizontal Boundary Layer in a Porous Medium**

The linear vortex stability of a horizontal thermal boundary layer was studied by Bassom and Rees (1995), based upon the analytical, leading order boundary layer solution to the basic state given by Rees and Bassom (1991). Storesletten and Rees (1998) show that this leading order solution does not represent the basic flow with sufficient accuracy for the results of stability analysis to be considered reliable.

The nonlinear wave stability of a horizontal thermal boundary layer with wedge angle  $\frac{3}{2}\pi$  has been studied by Rees and Bassom (1993). The non-parallel flow was studied using two dimensional numerical simulations of the full time-dependent equations of motion. A Schwarz-Christofel transform was again used to cause the basic boundary layer to have uniform thickness in the new variables. Small perturbations to the basic flow were found to increase in amplitude very rapidly and the flow quickly entered the non-linear regime after only a small movement downstream. Non-linear and non-parallel effects were apparent in the flow; these effects include cell-merging and the ejection of plumes from the boundary layer. The transition to strong convection was found to be smooth rather than abrupt as is implied by the concept of a neutral curve (Rees and Bassom (1993)). There remains a need to extend the modelling to three dimensions in order to determine

whether waves or vortices are the most dangerous form of disturbance (Rees and Bassom (1993)).

### **2.2.5 Stability of the Generally Inclined Boundary Layer in a Porous Medium**

There is a significant qualitative difference between the respective stability properties for horizontal and vertical boundary layers. The vertical boundary layer is nonlinearly stable to both wave (Rees (1993), Lewis et al (1995)) and vortex (Hsu and Cheng (1979)) disturbances. Vortex disturbances in the near vertical boundary layer grow, but then decay again as downstream distance increases (Rees (2002b)). A horizontal boundary layer with wedge angle  $\frac{3}{2}\pi$  was found to be nonlinearly unstable to wave disturbances by Rees and Bassom (1993), and quickly becomes chaotic. Due to the inadequacies of the parallel flow approximation (see Sect. 2.3) and the inability of the similarity boundary layer solution to model the basic flow (see Sect. 2.4), previously published work on layers at arbitrary inclinations (Hsu and Cheng (1979), Jang and Chang (1988c), Jang and Chang (1988a)) cannot be held to be accurate (Rees (1998)). Consequently there remains a need to examine the stability of generally inclined boundary layer flows so as to gain an increased understanding of how the differing stability characteristics of horizontal and vertical boundary layer flows may be reconciled.

Due to the analytical difficulties presented by the nonlinear, non-parallel flows involved it will be necessary to proceed numerically to solve the full elliptic governing equations, and it is this which will form the focus of Chapters 3 - 4 in this thesis. This work will focus on the stability of the generally inclined layer to vortex disturbances.

## 2.2.6 Extensions to the Thermal Boundary Layer Problem

A number of extensions to the horizontal and inclined problems discussed above have also been examined. For self similar flows these examined the effect of mixed convection on the horizontal (Hsu and Cheng (1980b)) and inclined (Hsu and Cheng (1980a)) configurations, mass transfer in the horizontal case (Jang and Chang (1988b)) and maximum density effects in the inclined situation (Jang and Chang (1987)). Viscosity variation with temperature is also considered (Jang and Leu (1993)) as well as variable porosity, permeability and thermal diffusivity effects on the stability of flow over a horizontal surface (Jang and Chen (1993b)). Jang and Chen (1993a) examined the combined effects of Forchheimer form drag (fluid inertia) and thermal dispersion on horizontal free convection. Inertia is found to destabilise the flow by serving to increase the thickness of the boundary layer, whilst thermal diffusion has a stabilising effect.

In terms of nonsimilar flows the effect of inertia on the stability of convection over a horizontal surface with power-law heating, both with (Chang and Jang (1989a)) and without (Chang and Jang (1989b)) the Brinkman (viscous) terms, have been studied. Jang and Chen (1994) included variable porosity, permeability and thermal diffusivity effects in the absence of the advective inertia terms. The viscous boundary effects and inertia effects for mixed convection flow over a horizontal surface with powerlaw heating are studied in Lie and Jang (1993). Viscous and inertia effects are both found to stabilise the flow in this case, in contrast to the results of Chang and Jang (1989a). When considered by Jang et al (1995) uniform suction at the heated surface was found to stabilise the flow, whilst uniform blowing at the heated surface had the opposite effect.

Without exception these papers employ a basic flow derived using the boundary

layer approximation. This was shown to be insufficiently accurate as a representation of the basic flow by Storesletten and Rees (1998), as discussed in Sect. 2.3. The parallel flow approximation is also used by all these papers and again there are a number of issues with this approximation which would bring the results into question; see Sect. 2.4.

### **2.2.7 Thermal Boundary Layers in a Clear Fluid**

Experimental work by Lloyd and Sparrow (1970) and Sparrow and Hussar (1969) found that the clear fluid thermal boundary layer on an inclined heated plate is destabilised by two-dimensional wave disturbances for  $\alpha > 76^\circ$ . This is in contrast to the situation in a porous medium where the flow is nonlinearly stable when the heated surface is vertical. Both waves and longitudinal vortices are observed for  $73^\circ < \alpha < 76^\circ$  and stationary longitudinal vortices appear in a perturbed flow when  $\alpha < 73^\circ$ . The parallel, linear stability analysis of Iyer and Kelly (1974) shows that the critical distance for vortices decreases with  $\alpha$ , and is below that of travelling waves for  $\alpha < 86^\circ$ . However, the growth rate of the travelling waves is much higher than that of the vortices, hence their appearance at much lower angles of inclination in the experimental results. Tumin (2003) demonstrates that nonparallel effects have a stabilising effect on the flow in a clear fluid, but that this does not affect the qualitative nature of the results.

## 2.3 Determining the Basic Flow in Inclined Boundary Layers

The determination of the basic steady state boundary layer in the semi-infinite inclined configuration is complicated by the lack of a natural lengthscale with which to nondimensionalise Eqs. (2.1 – 2.5). In previous work three different methods have been used to deal with this absence and thereby to enable the derivation of a solution to the basic flow. These are:

1. Using a local Rayleigh number,
2. Using a fictitious lengthscale,
3. Using a length scale suggested by the physical parameters.

Cheng and Cheng (1976) and Cheng and Minkowycz (1977) were the first to use a local Rayleigh number  $Ra_x$  to obtain a similarity solution for a two-dimensional horizontal and vertical heated surface respectively. Chang and Cheng (1983), and Cheng and Hsu (1984) then developed the approximation of the basic flow using higher order boundary layer theory. Following introduction of a stream function

$$U = \frac{\partial \psi}{\partial Z}, \quad V = 0, \quad W = -\frac{\partial \psi}{\partial X} \quad (2.10)$$

the two-dimensional governing equations are

$$\frac{\partial^2 \psi}{\partial X^2} + \frac{\partial^2 \psi}{\partial Z^2} = \frac{\rho_\infty g \beta K}{\mu} \left[ \frac{\partial T}{\partial Z} \sin \alpha - \frac{\partial T}{\partial X} \cos \alpha \right] \quad (2.11)$$

$$\kappa \left[ \frac{\partial^2 T}{\partial X^2} + \frac{\partial^2 T}{\partial Z^2} \right] = \frac{\partial \psi}{\partial Z} \frac{\partial T}{\partial X} - \frac{\partial \psi}{\partial X} \frac{\partial T}{\partial Z}. \quad (2.12)$$

The local Rayleigh number is defined in this context as

$$Ra_x = \frac{\rho g \beta K \Delta T \sin \alpha}{\mu \kappa} X, \quad (2.13)$$

and what is commonly referred to as the boundary layer approximation is invoked. The boundary layer approximation assumes that the boundary layer thickness is much smaller than the distance from the leading edge, i.e.  $X \gg Z$ . As a consequence the  $X$ -derivative terms in the left hand sides of Eqs. (2.11) and (2.12) are neglected, thus rendering these equations parabolic. Subsequent transformations, along with the definition of  $Ra_x$  are then used to develop a similarity solution that describes the shape of the basic flow. The assumption of  $X \gg Z$  means that  $Ra_x \gg 1$  is a necessary condition for this work to be valid. Consequently it is inconsistent to use this basic flow as a basis for a stability analysis that then returns finite values for critical distance. This is demonstrated by Rees (1998) with respect to the inclined heated surface, and by Rees and Pop (2010) for a mixed convection boundary layer flow adjacent to a nonisothermal horizontal surface in a porous medium with variable permeability. The severe impact of this inconsistency on the accuracy of such a stability analysis was also demonstrated by Storesletten and Rees (1998). The boundary layer assumption is therefore valid only for near-vertical, or vertical boundary layers where the critical distance retreats sufficiently far from the leading edge for all the conditions for the neglect of the streamwise diffusion terms to be met.

The second set of methods which involve the use of a fictitious lengthscale are useful for understanding the basic flow but present a number of difficulties in terms of formulating a rigorous stability analysis; these were discussed in detail in Rees (1998, 2002a) and therefore this method will not be discussed further here.

The final method listed above consists of defining a lengthscale,  $L$  in terms of the properties of the medium (Rees (1998)). Setting

$$L = \frac{\mu \kappa}{\rho g \beta K \Delta T} \quad (2.14)$$

results in a Rayleigh number of unity. An alternative point of view is that a unit value of  $Ra$  yields a natural lengthscale in terms of the properties of the fluid and the porous medium. This method of nondimensionalisation allows numerical simulations of the full nonlinear equations to be attempted, without having to invoke the boundary layer approximation (Rees (1998)). It was also used by Rees and Bassom (1991) to derive the exact solutions to the basic state for a vertical boundary layer on a flat plate and a horizontal upward facing heated surface, with a wedge angle of  $\frac{3}{2}\pi$ . It is this method that is employed in this thesis.

## 2.4 Use of the Parallel Flow Approximation in Inclined Boundary Layer Flows

Bassom and Rees (1995) examined the effect of the parallel flow approximation when used in the stability analysis of flow over a horizontal plate (Hsu et al (1978)). The use of this approximation means that disturbances are assumed to have a prescribed streamwise variation. Typically a disturbance is taken to be constant with respect to downstream distance, allowing derivatives with respect to this parameter to be neglected and easier calculation of neutral curves because the critical distance is computed as the eigenvalue of an ordinary differential eigenvalue problem (Bassom and Rees (1995)). However, this constitutes a constraint of the disturbance which is unlikely to occur in reality, especially in the context of a boundary layer flow which is itself nonsimilar, as discussed in Sect. 2.3.

The classical tear-drop neutral-stability curve predicted by parallel theory for the horizontal plate (Hsu et al (1978)) shows there are two wavenumbers corresponding to neutral stability, one at  $k = O(x^{-1})$  and one at  $k = O(x^{-1/3})$ , where

$x$  is downstream distance. The non-parallel asymptotic analysis for the shorter wavenumber at large distances downstream shows this mode to be dominated by non-parallel effects at leading order, whilst the other is adequately described by parallel theory (Bassom and Rees (1995)). Physically this might be expected as the long wavelength disturbances will spread across the whole of the boundary layer, the shape of which is non-parallel.

Zhao and Chen (2002) examined the effect of incorporating non-parallelism into the study of flow over a horizontal or inclined layer, albeit one in which the basic flow is derived based upon the boundary layer approximation. The non-parallel model produced a more stable flow than the parallel work. Linear stability analysis of the near-vertical layer (Rees (2001b)), based on the exact solution of Rees and Bassom (1991), shows that vortex disturbances grow at much smaller critical distances than those based upon the parallel flow approximation. In summary, in order to fully and accurately describe the stability of the flow over an inclined heated surface it is necessary to include nonparallel effects. Consequently this thesis will not employ the parallel flow approximation, but will solve the fully nonlinear equations including the streamwise diffusion terms.

## **2.5 Governing Equations**

The governing equations are first nondimensionalised. A velocity potential is introduced, along with a coordinate transformation which facilitates the application of the boundary conditions and results in an efficient distribution of the mesh density.

### 2.5.1 Nondimensionalisation

The governing equations as given by Eqs. (2.1 – 2.5) are nondimensionalised using the following scalings:

$$\begin{aligned} (X, Y, Z) &= L(x, y, z), & (U, V, W) &= \frac{\kappa}{L}(u, v, w), \\ \hat{P} &= \frac{\kappa\mu}{K}P, & \hat{t} &= \frac{\sigma L^2}{\kappa}t, & \hat{T} &= \theta\Delta T + T_\infty \end{aligned} \quad (2.15)$$

where  $\Delta T$  is the temperature difference between the temperature of the heated surface ( $T_w$ ) and the ambient temperature ( $T_\infty$ ).

Substitution of the identities given in (2.15) into Eqs. (2.1 – 2.5), and dropping the circumflexes gives

$$\frac{\partial u}{\partial x} + \frac{\partial v}{\partial y} + \frac{\partial w}{\partial z} = 0, \quad (2.16)$$

$$u = -\frac{\partial P}{\partial x} + \theta \sin \alpha, \quad v = -\frac{\partial P}{\partial y}, \quad w = -\frac{\partial P}{\partial z} + \theta \cos \alpha, \quad (2.17)$$

$$\nabla^2 \theta = u \frac{\partial \theta}{\partial x} + v \frac{\partial \theta}{\partial y} + w \frac{\partial \theta}{\partial z} + \frac{\partial \theta}{\partial t}. \quad (2.18)$$

As discussed in Sect. 2.3 there is no physical lengthscale upon which to base the nondimensionalisation, and therefore we have used the natural lengthscale,

$$L = \frac{\mu\kappa}{\rho g \beta K \Delta T}, \quad (2.19)$$

which yields a unit Darcy-Rayleigh number.

### 2.5.2 Velocity Potential

There are various ways in which Darcy's law and the heat transport equation may be solved for three-dimensional convection problems. These are

- using primitive variables,
- using a pressure/temperature formulation,
- using a velocity potential/temperature formulation.

Formulations using primitive variables are often used in engineering computations, but are relatively complicated to encode due to the need to have staggered grids. The use of the upwinding schemes required by these methods also means that great care has to be taken to ensure that a sufficiently accurate solution is obtained.

The pressure/temperature formulation for porous media flows may be encoded using non-staggered grids. However, for this problem all the boundary conditions for the pressure are of Neumann type which poses difficulties for multigrid Poisson solvers. The pressure only appears in the governing equations in derivative form and without a fixed value on at least one boundary the solution frequently tends to oscillate without converging or exhibits slow convergence.

The velocity potential/temperature formulation does not require staggered grids or upwinding, and has some Dirichlet boundary conditions on solid surfaces. The disadvantage of this method, however, is that it requires the solution of the three components of the velocity potential  $\phi^{(1)}$ ,  $\phi^{(2)}$ , and  $\phi^{(3)}$  rather than just the pressure  $P$ .

The velocity potential may be thought of as the three dimensional analogue of the streamfunction and it is applicable when the flow is irrotational and incompressible. The non-dimensionalised governing equations for Darcy flow in an inclined layer may be stated as

$$\mathbf{u} = -\nabla P + \mathbf{G}, \quad (2.20)$$

where

$$\mathbf{G} = \begin{pmatrix} \theta \sin \alpha \\ 0 \\ \theta \cos \alpha \end{pmatrix}. \quad (2.21)$$

To eliminate the pressure terms we take the curl of Eqn. (2.20):

$$\nabla \times \mathbf{u} = -\nabla \times \nabla \mathbf{P} + \nabla \times \mathbf{G}. \quad (2.22)$$

The term  $\nabla \times \nabla \mathbf{P}$  is zero by definition. The fluid is taken to be incompressible (solenoidal), therefore  $\nabla \cdot \mathbf{u} = 0$ . If a vector field has zero divergence it may be represented (Holst and Aziz (1972), Hirasaki and Hellums (1968)) by a vector potential  $\phi$  defined as

$$\mathbf{u} = \nabla \times \phi. \quad (2.23)$$

The divergence of such a potential will also be zero:  $\nabla \cdot \phi = 0$ . Substituting (2.23) into (2.22) gives

$$\nabla \times (\nabla \times \phi) = \nabla(\nabla \cdot \phi) - \nabla^2 \phi = \nabla \times \mathbf{G}, \quad (2.24)$$

$$\implies -\nabla^2 \phi = \nabla \times \mathbf{G}, \quad (2.25)$$

or, when split into its component parts,

$$\nabla^2 \phi^{(1)} = -\frac{\partial \theta}{\partial y} \cos \alpha, \quad (2.26)$$

$$\nabla^2 \phi^{(2)} = \left[ \frac{\partial \theta}{\partial x} \cos \alpha - \frac{\partial \theta}{\partial z} \sin \alpha \right], \quad (2.27)$$

$$\nabla^2 \phi^{(3)} = \frac{\partial \theta}{\partial y} \sin \alpha, \quad (2.28)$$

with the heat transport equation taking the following form

$$\frac{\partial \theta}{\partial t} = \nabla^2 \theta + \frac{\partial(\phi^{(1)}, \theta)}{\partial(y, z)} + \frac{\partial(\phi^{(2)}, \theta)}{\partial(z, x)} + \frac{\partial(\phi^{(3)}, \theta)}{\partial(x, y)}, \quad (2.29)$$

and where the Jacobian operator is defined as follows,

$$\frac{\partial(\chi_1, \chi_2)}{\partial(\zeta_1, \zeta_2)} = \frac{\partial\chi_1}{\partial\zeta_1} \frac{\partial\chi_2}{\partial\zeta_2} - \frac{\partial\chi_1}{\partial\zeta_2} \frac{\partial\chi_2}{\partial\zeta_1}. \quad (2.30)$$

### 2.5.3 Coordinate Transformation

Based upon the exact solution for the vertical boundary layer which was found by Rees and Bassom (1991), a parabolic coordinate transformation is introduced. We use

$$x = \frac{1}{4}(\xi^2 - \eta^2), \quad z = \frac{1}{2}\xi\eta, \quad (2.31)$$

which is also a Schwarz-Christoffel mapping, and therefore mesh lines are everywhere orthogonal. Figure 2.2 shows the grid resulting from this transformation with lines of constant  $\xi$  and  $\eta$  plotted in Cartesian coordinates.

The shape of the resulting mesh mimics the shape of the spatially developing boundary layer and it means that isotherms tend to follow lines of constant values of  $\eta$  (for the vertical case lines of constant  $\eta$  are isotherms). This facilitates the application of the boundary conditions because the heated surface is now at  $\eta = 0$  while the insulated part of the bounding surface is at  $\xi = 0$ . An additional advantage with this coordinate system is that the mesh is very dense close to the leading edge but becomes coarser at large distances downstream. This type of mesh is a very efficient means of resolving the boundary layer flow because changes at the leading edge occur very quickly, and the boundary layer is very thin here, so high resolution is required. Downstream the flow field changes more slowly and the layer is thicker.

This transformation gives rise to the following substitutions for the partial deriva-

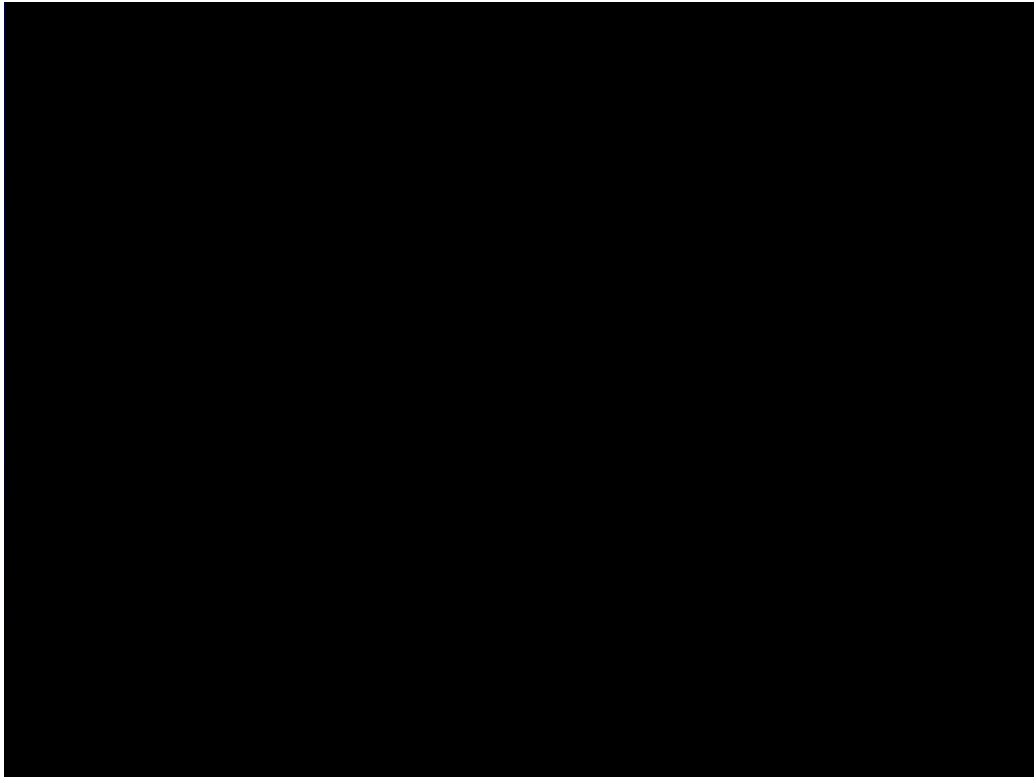


Figure 2.2: Lines of constant  $\xi$  (black) and  $\eta$  (blue) plotted in Cartesian coordinates.

tives

$$\frac{\partial}{\partial x} = \frac{2}{(\xi^2 + \eta^2)} \left( \xi \frac{\partial}{\partial \xi} - \eta \frac{\partial}{\partial \eta} \right), \quad (2.32)$$

$$\frac{\partial}{\partial z} = \frac{2}{(\xi^2 + \eta^2)} \left( \eta \frac{\partial}{\partial \xi} + \xi \frac{\partial}{\partial \eta} \right), \quad (2.33)$$

$$\frac{\partial^2}{\partial x^2} + \frac{\partial^2}{\partial z^2} = \frac{4}{(\xi^2 + \eta^2)} \left( \frac{\partial^2}{\partial \xi^2} + \frac{\partial^2}{\partial \eta^2} \right). \quad (2.34)$$

Substitution of the above into Eqs. (2.26 – 2.28) gives Eqs. (2.35 – 2.37):

$$\frac{\partial^2 \phi^{(1)}}{\partial \xi^2} + \frac{\partial^2 \phi^{(1)}}{\partial \eta^2} + \frac{(\xi^2 + \eta^2)}{4} \frac{\partial^2 \phi^{(1)}}{\partial y^2} = -\frac{(\xi^2 + \eta^2)}{4} \frac{\partial \theta}{\partial y} \cos \alpha, \quad (2.35)$$

$$\begin{aligned} \frac{\partial^2 \phi^{(2)}}{\partial \xi^2} + \frac{\partial^2 \phi^{(2)}}{\partial \eta^2} + \frac{(\xi^2 + \eta^2)}{4} \frac{\partial^2 \phi^{(2)}}{\partial y^2} &= \frac{1}{2} \left[ \left( \xi \frac{\partial \theta}{\partial \xi} - \eta \frac{\partial \theta}{\partial \eta} \right) \cos \alpha \right. \\ &\quad \left. - \left( \eta \frac{\partial \theta}{\partial \xi} + \xi \frac{\partial \theta}{\partial \eta} \right) \sin \alpha \right], \quad (2.36) \end{aligned}$$

$$\frac{\partial^2 \phi^{(3)}}{\partial \xi^2} + \frac{\partial^2 \phi^{(3)}}{\partial \eta^2} + \frac{(\xi^2 + \eta^2)}{4} \frac{\partial^2 \phi^{(3)}}{\partial y^2} = \frac{\partial \theta}{\partial y} \sin \alpha. \quad (2.37)$$

Substitution into Eqn. (2.29) and rearrangement yields Eqn. (2.38):

$$\begin{aligned} \frac{\partial \theta}{\partial t} &= \frac{4}{(\xi^2 + \eta^2)} \left[ \frac{\partial^2 \theta}{\partial \xi^2} + \frac{\partial^2 \theta}{\partial \eta^2} + \frac{(\xi^2 + \eta^2)}{4} \frac{\partial^2 \theta}{\partial y^2} + \frac{\partial(\phi^{(2)}, \theta)}{\partial(\eta, \xi)} \right. \\ &\quad \left. + \frac{1}{2} \frac{\partial \phi^{(1)}}{\partial y} \left( \eta \frac{\partial \theta}{\partial \xi} + \xi \frac{\partial \theta}{\partial \eta} \right) - \frac{1}{2} \frac{\partial \theta}{\partial y} \left( \eta \frac{\partial \phi^{(1)}}{\partial \xi} + \xi \frac{\partial \phi^{(1)}}{\partial \eta} \right) \right. \\ &\quad \left. + \frac{1}{2} \frac{\partial \theta}{\partial y} \left( \xi \frac{\partial \phi^{(3)}}{\partial \xi} - \eta \frac{\partial \phi^{(3)}}{\partial \eta} \right) - \frac{1}{2} \frac{\partial \phi^{(3)}}{\partial y} \left( \xi \frac{\partial \theta}{\partial \xi} - \eta \frac{\partial \theta}{\partial \eta} \right) \right]. \quad (2.38) \end{aligned}$$

These equations, together with the boundary conditions given in Sect. 2.6, form the complete nonlinear elliptic system of governing equations for the boundary layer flow.

## 2.6 Boundary Conditions

The following boundary conditions are applied to define the problem.

$$\theta = 1, \phi^{(1)} = \phi^{(2)} = \frac{\partial \phi^{(3)}}{\partial \eta} = 0 \quad \text{on} \quad \eta = 0 \quad (2.39)$$

$$\theta = \phi^{(1)} = \phi^{(3)} = \frac{\partial \phi^{(2)}}{\partial \eta} = 0 \quad \text{on} \quad \eta = \eta_{\max} \quad (2.40)$$

$$\frac{\partial \theta}{\partial \xi} = \phi^{(2)} = \phi^{(3)} = \frac{\partial \phi^{(1)}}{\partial \xi} = 0 \quad \text{on} \quad \xi = 0 \quad (2.41)$$

$$\frac{\partial^2 \theta}{\partial \xi^2} = \frac{\partial^2 \phi^{(1)}}{\partial \xi^2} = \frac{\partial^2 \phi^{(2)}}{\partial \xi^2} = \frac{\partial^2 \phi^{(3)}}{\partial \xi^2} = 0 \quad \text{on} \quad \xi = \xi_{\max}. \quad (2.42)$$

The boundary conditions on the solid surface at  $\eta = 0$  and  $\xi = 0$ , have been proved rigorously by Hirasaki and Hellums (1968). At the solid surface at  $\eta = 0$ ,  $w$ , the velocity in the  $z$  coordinate direction, is equal to zero. From the derivation of the velocity potential we know that,

$$w = \frac{\partial \phi^{(2)}}{\partial x} - \frac{\partial \phi^{(1)}}{\partial y}, \quad (2.43)$$

which implies that

$$\frac{\partial \phi^{(2)}}{\partial x} = \frac{\partial \phi^{(1)}}{\partial y}, \quad (2.44)$$

and it is shown by Hirasaki and Hellums (1968) that  $\phi^{(2)} = \phi^{(1)} = C$ , where  $C$  is some constant. As

$$\frac{\partial \phi^{(1)}}{\partial x} + \frac{\partial \phi^{(2)}}{\partial y} + \frac{\partial \phi^{(3)}}{\partial z} = 0, \quad (2.45)$$

this gives

$$\frac{\partial \phi^{(3)}}{\partial z} = 0, \quad (2.46)$$

which implies

$$\frac{\partial \phi^{(3)}}{\partial \eta} = 0. \quad (2.47)$$

The work of Hirasaki and Hellums (1968), which is summarised more clearly in Aziz and Hellums (1967), shows that  $C$  may be taken to be zero. At the inflow boundary at  $\eta = \eta_{\max}$ , fluid is assumed to enter the domain perpendicularly to the boundary. This implies that

$$\frac{\partial \phi^{(2)}}{\partial \eta} = 0. \quad (2.48)$$

For the outflow at  $\xi = \xi_{\max}$  it was decided to set all second derivatives to zero. This was felt to provide the most ‘freedom’ to the solution and although it is an imperfect choice it was felt to be the least worst option. This approach was also taken by Rees and Bassom (1993) and was found to provide good results in the presence of outflow through the boundary. The effect of these boundary conditions, and of the alternative of using a buffer zone at outflow are discussed in Sect. 3.2.6.

## **Chapter 3**

# **Boundary Layer - Numerical Methods and Validation**

This chapter describes the numerical methods used to solve the governing equations derived in Sect. 2.5 for the inclined boundary layer problem. The verification work undertaken to ensure the accuracy of the results produced by these numerical methods is also discussed.

### **3.1 Numerical Methods**

This section outlines the numerical methods used to solve the governing equations for the inclined boundary layer problem as given by Eqs. (2.35 – 2.38). The methods are coded in Fortran 95, compiled using the GNU Fortran compiler, on a Linux CentOS5.5 operating system consisting of  $8 \times 2.4\text{GHz}$  CPUs.

### 3.1.1 Fourier Decomposition

A spanwise Fourier decomposition is introduced to reduce the computational effort required to solve the nonlinear equations for the 3D domain. The Fourier decomposition means it is only necessary to solve numerically in the  $\xi, \eta$  plane.

The following Fourier series are introduced;

$$\phi^{(1)} = \sum_{n=1}^N \phi_n^{(1)} \sin(nky), \quad (3.1)$$

$$\phi^{(2)} = \frac{1}{2}\phi_0^{(2)} + \sum_{n=1}^N \phi_n^{(2)} \cos(nky), \quad (3.2)$$

$$\phi^{(3)} = \sum_{n=1}^N \phi_n^{(3)} \sin(nky), \quad (3.3)$$

$$\theta = \frac{1}{2}\theta_0 + \sum_{n=1}^N \theta_n \cos(nky), \quad (3.4)$$

where  $\theta, \phi^{(1)}, \phi^{(2)}$  and  $\phi^{(3)}$  are functions of  $\xi, \eta$  and  $t$ . The momentum equations now take the following form:

$$\mathcal{L}_n \phi_n^{(1)} = \frac{(\xi^2 + \eta^2)}{4} nk \theta_n \cos \alpha, \quad (3.5)$$

$$\mathcal{L}_n \phi_n^{(2)} = \frac{1}{2} \left[ \left( \xi \frac{\partial \theta_n}{\partial \xi} - \eta \frac{\partial \theta_n}{\partial \eta} \right) \cos \alpha - \left( \eta \frac{\partial \theta_n}{\partial \xi} + \xi \frac{\partial \theta_n}{\partial \eta} \right) \sin \alpha \right], \quad (3.6)$$

$$\mathcal{L}_n \phi_n^{(3)} = -\frac{(\xi^2 + \eta^2)}{4} nk \theta_n \sin \alpha. \quad (3.7)$$

The elliptic operator,  $\mathcal{L}_n$ , is defined according to,

$$\mathcal{L}_n \phi = \frac{\partial^2 \phi}{\partial \xi^2} + \frac{\partial^2 \phi}{\partial \eta^2} - \frac{(\xi^2 + \eta^2)}{4} n^2 k^2 \phi. \quad (3.8)$$

In the above Fourier series we have  $1 \leq n \leq N$  for Eqs. (3.5) and (3.7) and  $0 \leq n \leq N$  for Eqn. (3.6). Substitution into Eqn. (2.38) gives

$$\frac{\partial \theta_0}{\partial t} = \frac{4}{(\xi^2 + \eta^2)} \left[ \mathcal{L}_0 \theta_0 + \frac{1}{2} \frac{\partial (\phi_0^{(2)}, \theta_0)}{\partial (\eta, \xi)} + 2\mathbb{N}_0 \right]. \quad (3.9)$$

where  $\mathbb{N}_0$  are the nonlinear terms contributing to the zero mode. For all other modes

$$\begin{aligned} \frac{\partial \theta_n}{\partial t} = & \frac{4}{(\xi^2 + \eta^2)} \left[ \mathcal{L}_n \theta_n + \mathbb{N}_n + \frac{1}{4} n k \phi_n^{(1)} \left( \eta \frac{\partial \theta_0}{\partial \xi} + \xi \frac{\partial \theta_0}{\partial \eta} \right) \right. \\ & + \frac{1}{4} n k \phi_n^{(3)} \left( -\xi \frac{\partial \theta_0}{\partial \xi} + \eta \frac{\partial \theta_0}{\partial \eta} \right) \\ & \left. + \frac{1}{2} \left( \frac{\partial(\phi_0^{(2)}, \theta_n)}{\partial(\eta, \xi)} + \frac{\partial(\phi_n^{(2)}, \theta_0)}{\partial(\eta, \xi)} \right) \right], \end{aligned} \quad (3.10)$$

where  $\mathbb{N}_n$  represents the nonlinear terms contributing to mode  $n$ . The nonlinear terms arise from the interactions of the vortex modes with one another. Thus modes  $l$  and  $m$  give rise to the following terms in mode  $(l+m)$  and mode  $(l-m)$ :

$$\begin{aligned} \mathbb{N}_{l \pm m} = & \frac{1}{2} \frac{\partial(\phi_l^{(2)}, \theta_m)}{\partial(\eta, \xi)} + \frac{l k \phi_l^{(1)}}{4} \left( \eta \frac{\partial \theta_m}{\partial \xi} + \xi \frac{\partial \theta_m}{\partial \eta} \right) \\ & \mp \frac{m k \theta_m}{4} \left( \eta \frac{\partial \phi_l^{(1)}}{\partial \xi} + \xi \frac{\partial \phi_l^{(1)}}{\partial \eta} \right) \pm \frac{m k \theta_m}{4} \left( \xi \frac{\partial \phi_l^{(3)}}{\partial \xi} - \eta \frac{\partial \phi_l^{(3)}}{\partial \eta} \right) \\ & - \frac{l k \phi_l^{(3)}}{4} \left( \xi \frac{\partial \theta_m}{\partial \xi} - \eta \frac{\partial \theta_m}{\partial \eta} \right). \end{aligned} \quad (3.11)$$

These governing equations are a set of nonlinear, partial differential equations, which are parabolic in time. The following boundary conditions are used:

$$\begin{aligned} \eta = 0 : & \theta_0 = 2, \theta_{n \geq 2} = 0, \phi_n^{(1)} = \phi_0^{(2)} = \phi_n^{(2)} = \frac{\partial \phi_n^{(3)}}{\partial \eta} = 0, \\ \eta = \eta_{\max} : & \theta_0 = \theta_n = \phi_n^{(1)} = \phi_n^{(3)} = \frac{\partial \phi_0^{(2)}}{\partial \eta} = \phi_n^{(2)} = 0, \\ \xi = 0 : & \frac{\partial \theta_0}{\partial \xi} = \frac{\partial \theta_n}{\partial \xi} = \phi_n^{(1)} = \phi_0^{(2)} = \phi_n^{(2)} = \frac{\partial \phi_n^{(3)}}{\partial \xi} = 0, \\ \xi = \xi_{\max} : & \frac{\partial^2 \theta_0}{\partial \xi^2} = \frac{\partial^2 \theta_n}{\partial \xi^2} = \frac{\partial^2 \phi_n^{(1)}}{\partial \xi^2} = \frac{\partial^2 \phi_0^{(2)}}{\partial \xi^2} = \frac{\partial^2 \phi_n^{(2)}}{\partial \xi^2} = \frac{\partial^2 \phi_n^{(3)}}{\partial \xi^2} = 0. \end{aligned} \quad (3.12)$$

Case	Description of Case	Initial Condition ( $t = 0$ ), for $\theta_1$
1a.	Uniform disturbance in $\theta_1$ , with a zero boundary condition at $\eta = 0$ .	$\theta_1 = A\eta e^{-\eta^2}$
1b.	Isolated disturbance in $\theta_1$ , with a zero boundary condition at $\eta = 0$ .	$\theta_1 = A \sin\left(\frac{(\xi - \xi_1)\pi}{10}\right) e^{-\eta^2}$ for $\xi_1 \leq \xi \leq \xi_1 + 10$ and $\eta > 0$
2.	Uniform disturbance in $\theta_1$ with a nonzero boundary condition (forcing term) at $\eta = 0$	$\theta_1 = Ae^{-\eta^2}$
3.	Leading edge disturbance in $\theta_1$ with a nonzero boundary condition (forcing term) at $\eta = 0$	$\theta_1 = Ae^{-\eta^2} e^{-a\xi^2}$

Table 3.1: Summary of cases based upon variation of  $\eta = 0$  boundary condition.

The imposition of  $\theta_0 = 2$  at  $\eta = 0$  represents a unit temperature at the hot surface.

Results for three different cases are presented in Chapter 4. These cases are differentiated by the boundary condition imposed on  $\theta_1$  at  $\eta = 0$  and are summarised in Table 3.1

### 3.1.2 Spatial Discretisation

The governing equations, Eqs. (3.5 – 3.10) are discretised using second order accurate central differences in  $\xi$  and  $\eta$ . A uniform grid is used where the coordinates of a point are given by  $\xi_i$  and  $\eta_j$ . The temperature at the point where  $\xi = \xi_i$  and  $\eta = \eta_i$  is denoted by  $\theta_{i,j}$ . The temperature at the next point in the positive  $\xi$ -direction is denoted by  $\theta_{i+1,j}$ . This means that the following approximations may

be made for the first and second derivatives of a variable  $\zeta$  in the  $\xi$ -direction:

$$\frac{\partial \zeta}{\partial \xi} \approx \frac{\zeta_{i+1,j} - \zeta_{i-1,j}}{2\delta\xi}, \quad (3.13)$$

$$\frac{\partial^2 \zeta}{\partial \xi^2} \approx \frac{\zeta_{i+1,j} - 2\zeta_{i,j} + \zeta_{i-1,j}}{\delta\xi^2}. \quad (3.14)$$

Eqn. (3.5) can therefore be approximated by

$$\begin{aligned} \frac{(\xi_i^2 + \eta_j^2)}{4} nk\theta_{i,j} \cos \alpha &= \frac{\phi_{i+1,j}^{(1)} - 2\phi_{i,j}^{(1)} + \phi_{i-1,j}^{(1)}}{\delta\xi^2} + \frac{\phi_{i,j+1}^{(1)} - 2\phi_{i,j}^{(1)} + \phi_{i,j-1}^{(1)}}{\delta\eta^2} \\ &\quad - \frac{(\xi_i^2 + \eta_j^2)}{4} n^2 k^2 \phi_{i,j}^{(1)}. \end{aligned} \quad (3.15)$$

The coefficients, such as values of  $(\xi_i^2 + \eta_j^2)/4$  at each location, are calculated and stored at each point of the grid at the beginning of the code. This increases computational speed as they do not have to be recalculated each time they are used. The finite difference stencil for  $\phi^{(1)}$  as given by Eqn. (3.5) is

$$\begin{pmatrix} 0 & & \frac{1}{\delta\eta^2} & & 0 \\ \frac{1}{\delta\xi^2} & -\frac{2}{\delta\xi^2} & -\frac{2}{\delta\eta^2} & -\frac{(\xi_i^2 + \eta_j^2)}{4} n^2 k^2 & \frac{1}{\delta\xi^2} \\ 0 & & \frac{1}{\delta\eta^2} & & 0 \end{pmatrix} \phi_{i,j}^{(1)}. \quad (3.16)$$

The spatial discretisation does not change the nature of the governing equations which remain elliptic in space and parabolic in time.

### 3.1.3 Boundary Conditions

The following boundary conditions are applied at some point in the domain, for the representative independent variable  $\zeta$  and coordinate direction  $\xi$ :

$$\zeta = C \quad (\text{Dirichlet}), \quad (3.17)$$

$$\frac{\partial \zeta}{\partial \xi} = C \quad (\text{Neumann}), \quad (3.18)$$

$$\frac{\partial^2 \zeta}{\partial \xi^2} = C \quad (\text{Second Order Neumann}), \quad (3.19)$$

where  $C$  is a constant.

The Dirichlet boundary condition is implemented easily. The value of the function at the point at which this boundary condition is to be applied is defined as part of the initial profile. The smoother does not solve at this point, and instead only uses the value at that location in the computation of other points. The finite difference stencil remains unchanged but is only implemented on internal points.

The application of the first derivative Neumann boundary condition is slightly more complicated because it requires knowledge of a point outside the domain should a second order accurate approximation be required and the ghost point technique be used. The value of the independent variable at that ghost point is calculated using the central difference approximation based at the boundary. Consider applying the boundary condition given by Eqn. (3.18), for  $\zeta$  at  $\xi = 0$ . The central difference approximation, Eqn. (3.13) implies that

$$\zeta_{i-1,j} = \zeta_{i+1,j}, \quad (3.20)$$

at the boundary, i.e. when  $i = 0$ . The finite difference stencil (3.16) for  $\nabla^2 \phi^{(1)}$

may be rewritten as;

$$\begin{pmatrix} 0 & \frac{1}{\delta\eta^2} & 0 \\ 0 & -\frac{2}{\delta\xi^2} - \frac{2}{\delta\eta^2} - \frac{(\xi_0^2 + \eta_j^2)}{4} n^2 k^2 & \frac{2}{\delta\xi^2} \\ 0 & \frac{1}{\delta\eta^2} & 0 \end{pmatrix} \phi_{0,j}^{(1)}. \quad (3.21)$$

If the second derivative of  $\phi^{(1)}$  is zero at  $i = 0$  then the rearrangement of Eqn. (3.19) gives;

$$\zeta_{-1,j} = 2\zeta_{0,j} - \zeta_{1,j}, \quad (3.22)$$

and the finite difference stencil (3.16) becomes

$$\begin{pmatrix} 0 & \frac{1}{\delta\eta^2} & 0 \\ 0 & -\frac{2}{\delta\eta^2} - \frac{(\xi_0^2 + \eta_j^2)}{4} n^2 k^2 & 0 \\ 0 & \frac{1}{\delta\eta^2} & 0 \end{pmatrix} \phi_{0,j}^{(1)}. \quad (3.23)$$

### 3.1.4 Temporal Discretisation

To discretise the time derivatives in Eqs. (3.9 – 3.10) the backward Euler method is used. This is a first order accurate method, and is defined as follows

$$\left. \frac{\partial \theta_{i,j}^{n+1}}{\partial t} \right|_{t=t_{n+1},i,j} \simeq \frac{\theta_{i,j}^{n+1} - \theta_{i,j}^n}{\delta t}, \quad (3.24)$$

where  $n$  denotes the timestep. This identity is substituted into Eqs. (3.9) and (3.10), where all other terms are evaluated at  $t_{n+1}$ , and then the resulting set of difference equations are solved implicitly for  $\theta_{i,j}^{n+1}$ . To demonstrate the ideas discussed above, Eqn. (3.9) is discretised in full on the following page. The term on the left hand side of (3.25) is evaluated at  $t_n$ , the terms on the right hand side are solved implicitly for  $\theta$  at  $t_{n+1}$ . Here  $\mathbb{N}_0$  represents all nonlinear terms contributing to the zero mode and this occurs when  $l = m$  in Eqn. (3.11) for the mode  $(l - m)$ . Discretisation of Eqn. (3.11) then gives (3.26).

$$\begin{aligned}
-\frac{\theta_{0,i,j}^n}{\delta t} &= -\frac{\theta_{0,i,j}^{n+1}}{\delta t} + \frac{4}{(\xi_i^2 + \eta_j^2)} \left[ \frac{\theta_{0_{i+1,j}} - 2\theta_{0_{i,j}} + \theta_{0_{i-1,j}}}{\delta\xi^2} + \frac{\theta_{0_{i,j+1}} - 2\theta_{0_{i,j}} + \theta_{0_{i,j-1}}}{\delta\eta^2} + \frac{(\xi_i^2 + \eta_j^2)}{4} n^2 k^2 \theta_{0_{i,j}} \right] \\
&\quad + \frac{1}{2} \left[ \left( \frac{\phi_{0_{i,j+1}}^{(2)} - \phi_{0_{i,j-1}}^{(2)}}{2\delta\eta} \right) \left( \frac{\theta_{0_{i+1,j}} - \theta_{0_{i-1,j}}}{2\delta\xi} \right) - \left( \frac{\phi_{0_{i+1,j}}^{(2)} - \phi_{0_{i-1,j}}^{(2)}}{2\delta\xi} \right) \left( \frac{\theta_{0_{i,j+1}} - \theta_{0_{i,j-1}}}{2\delta\eta} \right) \right]^{n+1} \\
&\quad + 2\mathbb{N}_0. \tag{3.25}
\end{aligned}$$

$$\begin{aligned}
\mathbb{N}_0 &= \frac{1}{2} \left[ \left( \frac{\phi_{i,j+1}^{(2)} - \phi_{i,j-1}^{(2)}}{2\delta\eta} \right) \left( \frac{\theta_{m_{i+1,j}} - \theta_{m_{i-1,j}}}{\delta\xi} \right) - \left( \frac{\phi_{i+1,j}^{(2)} - \phi_{i-1,j}^{(2)}}{2\delta\xi} \right) \left( \frac{\theta_{m_{i,j+1}} - \theta_{m_{i,j-1}}}{2\delta\eta} \right) \right]^{n+1} \\
&\quad + \frac{lk\phi_{i,j}^{(1)}}{4} \left[ \eta \left( \frac{\theta_{m_{i+1,j}} - \theta_{m_{i-1,j}}}{2\delta\xi} \right) + \xi \left( \frac{\theta_{m_{i,j+1}} - \theta_{m_{i,j-1}}}{2\delta\eta} \right) \right]^{n+1} \\
&\quad + \frac{mk\theta_{m_{i,j}}}{4} \left[ \eta \left( \frac{\phi_{i+1,j}^{(1)} - \phi_{i-1,j}^{(1)}}{2\delta\xi} \right) + \xi \left( \frac{\phi_{i,j+1}^{(1)} - \phi_{i,j-1}^{(1)}}{2\delta\eta} \right) \right]^{n+1} \\
&\quad - \frac{mk\theta_{m_{i,j}}}{4} \left[ \xi \left( \frac{\phi_{i+1,j}^{(3)} - \phi_{i-1,j}^{(3)}}{2\delta\xi} \right) - \eta \left( \frac{\phi_{i,j+1}^{(3)} - \phi_{i,j-1}^{(3)}}{2\delta\eta} \right) \right]^{n+1} \\
&\quad - \frac{lk\phi_{i,j}^{(3)}}{4} \left[ \xi \left( \frac{\theta_{m_{i+1,j}} - \theta_{m_{i-1,j}}}{2\delta\xi} \right) - \eta \left( \frac{\theta_{m_{i,j+1}} - \theta_{m_{i,j-1}}}{2\delta\eta} \right) \right]^{n+1}. \tag{3.26}
\end{aligned}$$

This discretisation of the time derivatives renders the heat transport equation elliptic in nature, and therefore amenable to solution using a Gauss-Seidel approach (see Sect. 3.1.6). The implicit approach consists of solving Eqs. (3.9) and (3.10) for a value of  $\theta^{n+1}$ , and Eqs. (3.5 – 3.7) for updated values of  $\phi^{(1)}$ ,  $\phi^{(2)}$ , and  $\phi^{(3)}$  which satisfy the equations to an appropriate degree of accuracy,

### 3.1.5 Structure of the Implicit Code

The structure of the implicit code is as follows:

1. Input of the runtime parameters.
2. Read in the basic state solution (i.e.  $\theta_0$  and  $\phi_0^{(2)}$ ).
3. Define the disturbance profile by specifying a  $\theta_1$  profile.
4. Implicitly solve Eqs. (3.5 – 3.7) and Eqs. (3.9) and (3.10) for new values of  $\phi^{(1)}$ ,  $\phi^{(2)}$ ,  $\phi^{(3)}$  and  $\theta$  using Gauss-Seidel (see Sect. 3.1.6) and a MultiGrid Full Approximation Scheme (see Sect. 3.1.8).
5. Apply convergence test.
6. Repeat steps 4-5 until the convergence criterion is reached.

There is no need to calculate the profiles of  $\phi^{(1)}$ ,  $\phi^{(2)}$  and  $\phi^{(3)}$  the first time step number 4 is carried out because the backward Euler method in  $t$  is being employed.

### 3.1.6 Gauss-Seidel with Line Solving

The algorithm used to solve the governing equations given by Eqs. (3.5 – 3.10) is a Gauss-Seidel (GS) smoother. This means the code solves the discretised governing equations at each grid point in turn. For a GS scheme the most up to date value

of each variable at an individual grid point is used. If a neighbouring point has already been updated then that new value will be used to calculate the up-to-date value at the current point.

Point solvers perform satisfactorily when  $\delta\xi \approx \delta\eta$  and in these cases outperform line solvers in terms of operation count. However the speed of iterative convergence of a point solver degrades rapidly as the ratio  $\delta\xi/\delta\eta$  increases or decreases from 1, whereas line solvers retain their convergence speed in terms of the number of iterations. The line-solve also helps to propagate the effect of boundary conditions across the line of data points by solving for that line simultaneously. Use of the line-solve gives rise to a tridiagonal matrix which can be solved very efficiently. Eqn. (3.5), which is discretised in (3.15) and which may be rearranged for a  $\xi$ -direction line relaxation, yields

$$\begin{aligned} \frac{\phi_{i+1,j}^{(1)} - 2\phi_{i,j}^{(1)} + \phi_{i-1,j}^{(1)}}{\delta\xi^2} - \frac{2\phi_{i,j}^{(1)}}{\delta\eta^2} \\ - \frac{(\xi_i^2 + \eta_j^2)}{4} n^2 k^2 \phi_{i,j}^{(1)} = - \frac{\phi_{i,j+1}^{(1)} + \phi_{i,j-1}^{(1)}}{\delta\eta^2} \\ + \frac{(\xi_i^2 + \eta_j^2)}{4} nk\theta_{i,j} \cos \alpha, \end{aligned} \quad (3.27)$$

for  $i = 0$  to  $i = i_{\max}$ . In matrix form this can be written, for the beginning of a row as:

$$\begin{bmatrix} \mathbb{B}_1 & \frac{1}{\delta\xi^2} & 0 & 0 \\ \frac{1}{\delta\xi^2} & \mathbb{B}_2 & \frac{1}{\delta\xi^2} & 0 \\ 0 & \frac{1}{\delta\xi^2} & \mathbb{B}_3 & \frac{1}{\delta\xi^2} \\ 0 & 0 & \ddots & \ddots \end{bmatrix} \begin{bmatrix} \phi_{1,j}^{(1)} \\ \phi_{2,j}^{(1)} \\ \phi_{3,j}^{(1)} \\ \vdots \end{bmatrix} = \begin{bmatrix} \frac{(\xi_i^2 + \eta_j^2)}{4} nk\theta_{1,j} \cos \alpha - \frac{\phi_{1,j+1}^{(1)} + \phi_{1,j-1}^{(1)}}{\delta\eta^2} \\ \frac{(\xi_i^2 + \eta_j^2)}{4} nk\theta_{2,j} \cos \alpha - \frac{\phi_{2,j+1}^{(1)} + \phi_{2,j-1}^{(1)}}{\delta\eta^2} \\ \frac{(\xi_i^2 + \eta_j^2)}{4} nk\theta_{3,j} \cos \alpha - \frac{\phi_{3,j+1}^{(1)} + \phi_{3,j-1}^{(1)}}{\delta\eta^2} \\ \vdots \end{bmatrix} \quad (3.28)$$

where

$$\mathbb{B}_i = -\frac{2}{\delta\xi^2} - \frac{2}{\delta\eta^2} - \frac{(\xi_i^2 + \eta_j^2)}{4} n^2 k^2. \quad (3.29)$$

The subscript relating to the mode number has been omitted above for clarity. The boundary condition  $\phi^{(1)} = 0$  at  $i = 0$  has also been implemented in the above. Typically, if  $\delta\xi > \delta\eta$  ( $\delta\eta > \delta\xi$ ) then a  $\xi$ -direction ( $\eta$ -direction) line solve should be used. However, in this case to further speed up convergence a line-solve is carried out in each direction:  $\xi$  followed by  $\eta$ .

### 3.1.7 Arakawa Discretisation

In clear fluids the use of standard discretisation for the Jacobian results in the solution exhibiting a structure termed ‘noodling’, that is ‘eddies a few grid intervals in size and of elongated, filament shape’, which then intensify causing computational instability (Arakawa (1966)). It has been shown that this is the result of aliasing errors, that is the misrepresentation of shorter waves because of the inability of the grid to resolve them (Phillips (1959) in Arakawa (1966)). Arakawa (1966) derived a discretisation scheme which conserves the kinetic energy and square of the vorticity, thus preventing computational instability and reducing the error due to aliasing. For two representative variables,  $\chi$  and  $\zeta$ , in the coordinate

directions,  $x, y$ , this discretisation is:

$$\begin{aligned}
\mathbb{J}_{i,j}(\chi, \psi) &= \frac{1}{12\delta x \delta y} \\
& [ (\zeta_{i,j-1} + \zeta_{i+1,j-1} - \zeta_{i,j+1} - \zeta_{i+1,j+1}) (\chi_{i+1,j} - \chi_{i,j}) \\
& + (\zeta_{i-1,j-1} + \zeta_{i,j-1} - \zeta_{i-1,j+1} - \zeta_{i,j+1}) (\chi_{i,j} - \chi_{i-1,j}) \\
& + (\zeta_{i+1,j} + \zeta_{i+1,j+1} - \zeta_{i-1,j} - \zeta_{i-1,j+1}) (\chi_{i,j+1} - \chi_{i,j}) \\
& + (\zeta_{i+1,j-1} + \zeta_{i+1,j} - \zeta_{i-1,j-1} - \zeta_{i-1,j}) (\chi_{i,j} - \chi_{i,j-1}) \\
& + (\zeta_{i+1,j} - \zeta_{i,j+1}) (\chi_{i+1,j+1} - \chi_{i,j}) \\
& + (\zeta_{i,j-1} - \zeta_{i-1,j}) (\chi_{i,j} - \chi_{i-1,j-1}) \\
& + (\zeta_{i,j+1} - \zeta_{i-1,j}) (\chi_{i-1,j+1} - \chi_{i,j}) \\
& + (\zeta_{i+1,j} - \zeta_{i,j-1}) (\chi_{i,j} - \chi_{i+1,j-1}) ]. \tag{3.30}
\end{aligned}$$

Simulations were run using both the Arakawa discretisation and the second order accurate central difference approximations for the first derivative as given by Eqn. (3.13). For forced vortices with  $\alpha = 55^\circ$ ,  $k = 0.04$ , the critical distance for the given wavenumber  $\xi_k = 37.4832$  when the traditional finite difference approximation to  $\mathbb{J}$  is used, and  $\xi_k = 37.4640$  when the Arakawa discretisation is employed. This amounts to a difference of  $5 \times 10^{-4}\%$  in  $\xi_k$ . It was found that the use of the Arakawa discretisation has no impact on the convective or absolute nature of the unforced disturbances.

Arakawa's discretisation is known to be important in cavity flows where velocities are large, and timesteps appreciable. It is possible that the coefficient

$$\frac{4}{(\xi^2 + \eta^2)} \tag{3.31}$$

which appears in Eqs. (3.9) and (3.10) renders the effective timestep very small, and therefore the use of the Arakawa discretisation becomes very much less im-

portant. Given that the difference between the results using the two different discretisations is so small and given that the Arakawa discretisation is much more computationally intensive the code used to generate the results shown in Chapter 4 did not use Arakawa's approximation to  $\mathbb{J}$ .

### 3.1.8 MultiGrid Schemes

By far the greatest performance gain is achieved by using MultiGrid (MG) schemes. These rely on the following key ideas.

- The GS scheme quickly eliminates oscillatory errors, but is much slower at reducing smooth errors.
- Transferring a profile from a fine grid to a coarse grid makes it appear more oscillatory.
- A good initial guess reduces the number of GS iterations necessary to reach the solution.

All MG schemes therefore rely on the idea of solving the equations on a sequence of coarser grids, on which the GS will quickly converge because the error appears more oscillatory, and using the results to correct the initial guess on the original grid. Depending on the nature of the governing equations different schemes must be used. For the implicit code discussed here the nonlinearity of the equations being solved means that a Full Approximation Scheme (FAS) methodology is required. If the governing equations were linear then the simpler Multi-Grid Correction Scheme (MGCS) could be employed. Both of these schemes are described in more detail in Appendix A.

Without a MG scheme the GS smoother requires in excess of 900 relaxation sweeps in order to achieve the chosen convergence criterion. Implementation

of the FAS means convergence is achieved in 10 – 15 V-cycles (depending on timestep), with 2 relaxation sweeps per level and typically 7 levels, giving the equivalent workload of 20 – 30 sweeps on the finest grid. The results shown in Chapter 4 were generated using the FAS algorithm.

### **3.1.9 Methodology for Calculating Critical Distance**

When investigating the Darcy-Bénard problem, instability is defined in terms of whether disturbances grow or decay in time and there is no ambiguity involved because the use of (i) the maximum disturbance temperature, (ii) the surface rate of heat transfer, or (iii) the disturbance energy are entirely equivalent in terms of defining growth (Rees (2001b)). In boundary layer flows instability involves spatial growth or decay of a disturbance and these different measures give different results.

In the case of the thermal boundary layer it was decided to judge instability based upon criteria applied to the primary disturbance mode, that is the mode for which  $n = 1$ . Changes in the basic state ( $n = 0$ ) are a result of the interaction of higher modes and thus it is reasonable to assume that the disturbance must have undergone significant growth before its magnitude is large enough to affect the basic state. This would not, therefore, be an appropriate means of detecting initial growth.

The concept of maximum disturbance temperature is self-explanatory. As outlined in Rees (2001b), one measure of the thermal energy of the disturbance may be taken to be proportional to the cross-stream temperature profile of the primary

vortex integrated in the  $z$ -direction:

$$E = \int_0^\infty \theta_1 dz = \frac{\xi}{2} \int_0^\infty \theta_1 d\eta \quad (3.32)$$

Neutral stability may be deemed to occur at a maximum or minimum defined as when

$$\frac{dE}{dx} = \frac{2}{\xi} \frac{dE}{d\xi} = 0 \quad (3.33)$$

is satisfied. Linear interpolation is therefore used to determine where

$$\frac{dE_1}{d\xi} = \int_0^\infty \left( \xi \frac{\partial \theta_1}{\partial \xi} + \theta_1 \right) d\eta = 0. \quad (3.34)$$

The surface heat flux  $q_1$  is calculated from the temperature gradient at the heated surface. It is necessary to understand the effect that the choice of criterion has on the value of critical distance, and this is examined in Sect. 4.5.2.

### 3.1.10 Convergence

There are two types of convergence to be considered in the code: (i) convergence of the MultiGrid Scheme at each timestep and (ii) convergence of the flow to a steady state profile. The MultiGrid FAS scheme is judged to have converged when the maximum value of residual across all grid points is less than  $1 \times 10^{-8}$ .

Steady state convergence is judged to have been reached when the maximum change in  $\theta$  over one timestep for all modes and all locations is also less than  $1 \times 10^{-8}$ . In some cases where the initial disturbance is very small, or decays severely, it is necessary to ensure that the steady state convergence test is not applied until after a certain threshold time in order to get a genuinely steady state profile. For all cases detailed in Table 3.1 the code has been run to a steady state convergence criterion of  $1 \times 10^{-10}$  for a selection of cases to verify that no further changes occur beyond the  $1 \times 10^{-8}$  threshold.

$\xi_{\max}$	$\eta_{\max}$	$N_{\xi}$	$N_{\eta}$	$\xi_k$
50	8	64	64	37.4872
50	8	96	64	37.4832
50	8	144	64	37.4815
50	8	192	64	37.4810

Table 3.2: Effect of the mesh density in the  $\xi$ -direction on critical distance.

## 3.2 Verification of the Implicit Code

This section addresses the detailed verification undertaken to ensure that the results of the implicit code are quantitatively correct. Verification included studies on the effects of mesh density, domain length, domain height, number of Fourier modes, buffer zones and the timestep.

### 3.2.1 Run Times

For a domain with  $\xi_{\max} = 50$ ,  $\eta_{\max} = 8$ ,  $N_{\xi} = 96$ ,  $N_{\eta} = 64$ ,  $N = 2$  and  $\alpha = 55^\circ$  the steady state for a Case 2 (forced) vortex is reached at  $t \approx 5400$ . A typical clock time for such a model is approximately 20 minutes.

### 3.2.2 Mesh Density

The effect of altering the mesh density in both the  $\xi$ - and  $\eta$ -directions has been examined. Table 3.2 shows the variation in  $\xi_k$  with respect to changes in  $\delta\xi$  when  $\alpha = 55^\circ$ ,  $k = 0.04$  and  $N = 2$ .

The results shown in Chapter 4 are computed using a mesh density of  $\delta\xi =$

$\xi_{\max}$	$\eta_{\max}$	$N_{\xi}$	$N_{\eta}$	$\xi_k$
50	8	256	32	37.1134
50	8	256	64	37.4771
50	8	256	128	37.7192

Table 3.3: Effect of the mesh density in the  $\eta$ -direction on critical distance.

$\frac{50}{96} = 0.5208$ . As shown in Table 3.2 doubling this mesh density to  $\delta\xi = \frac{50}{192} = 0.2604$  results in a 0.005% change in the value of  $\xi_k$ . This was deemed to be sufficiently mesh-independent for the purposes of this investigation.

Table 3.3 summarises the effect of changing  $\delta\eta$  on  $\xi_k$ . For the present purpose the value of  $\xi_k$  is calculated based upon the evolution of  $q_1$  (see Sect. 3.1.9). The results in Table 3.3 are for  $\alpha = 50^\circ$ , and  $k = 0.04$  with  $\eta_{\max} = 8$ ,  $\xi_{\max} = 50$  and  $N = 2$ . For the results shown in Chapter 4 a mesh density of  $\delta\eta = \frac{8}{64} = 0.125$  was used. Halving this to  $\delta\eta = \frac{8}{128}$  results in a 0.6% change in the value of  $\xi_k$ .

### 3.2.3 Number of Fourier Modes

The greater the number of Fourier modes ( $N$ ) used the more accurate the solution will be. However each additional mode represents a substantial computational effort, and therefore a balance must be struck between accuracy and efficiency.

Table 3.4 summarises the effect of including extra modes, when  $\alpha = 55^\circ$ ,  $k = 0.04$ ,  $\xi_{\max} = 50$ ,  $\eta_{\max} = 8$ ,  $N_{\xi} = 96$ ,  $N_{\eta} = 64$ . It shows that the incorporation of additional modes above  $N = 2$  has no effect on  $\xi_k$  to 4 decimal places. Consequently the results in Chapter 4 are based upon  $N = 2$ .

Number of Modes	$\xi_k$	Execution Time (s) for 100 timesteps
1	37.4796	109.71
2	37.4832	203.57
4	37.4832	444.22
8	37.4832	1177.43

Table 3.4: Values of  $\xi_k$  and execution time by number of Fourier modes.

Value of $\xi_{max}$	$\xi_k$
50	37.4832
100	37.4832

Table 3.5: Values of  $\xi_k$  by domain length.

### 3.2.4 Length of Domain

Altering the length of domain was found to have no effect on  $\xi_k$ , as would be expected. Table 3.5 summarizes the results for  $\alpha = 55^\circ$ ,  $k = 0.04$ ,  $N = 2$ ,  $\delta\xi = 0.5208$  and  $\delta\eta = 0.125$ .

### 3.2.5 Thickness of the Layer

Increasing the thickness of the layer from  $\eta_{max} = 8$  to  $\eta_{max} = 16$  results in a change in  $\xi_k$  from  $\xi_k = 37.4832$  to  $\xi_k = 37.1427$ , a difference of 0.9%. It appears, therefore, that the choice of  $\eta_{max}$  is slightly restrictive, and does influence  $\xi_k$ . However it is felt that the choice of  $\eta_{max}$  represents a reasonable compromise between accuracy and computational expense.

### 3.2.6 Buffer Zone

In the case of a clear fluid (i.e. Navier-Stokes flow) Kloker and Konzelmann (1993) note that the presence of the outflow boundary can result in the reflection of an outgoing disturbance back into the computational domain. To avoid this a buffer zone (also termed “relaminarization zone” or “sponge region”), is introduced which gradually damps out the disturbance before it reaches the outflow boundary. Rees and Bassom (1993) found that a buffer zone was not necessary when computing two-dimensional flow over a horizontal heated surface in a porous medium, whereas Paul et al (2008) found it to be essential when examining clear fluid flow along a vertical surface. It was necessary therefore to verify whether such a buffer zone was required in this work.

A buffer zone is implemented by replacing the calculated value of some variable ( $\Xi^{\text{old}}$ ), with a new value ( $\Xi^{\text{new}}$ ) after each timestep according to the following relationship:

$$\Xi^{\text{new}} = F(\xi)\Xi^{\text{old}} + [1 - F(\xi)]\Xi^{\text{basic}}, \quad (3.35)$$

where  $\Xi^{\text{basic}}$  is the basic boundary layer and the buffer function is defined by

$$F(\xi) = \begin{cases} 1 & \xi < \xi_{b1} \\ 1 - 10\gamma^3 + 15\gamma^4 - 6\gamma^5, & \xi \geq \xi_{b1}, \end{cases}, \quad (3.36)$$

where

$$\gamma = \frac{\xi - \xi_{b1}}{\xi_{b2} - \xi_{b1}}. \quad (3.37)$$

Figure 3.1 shows the variation of  $F$  over the domain, where the dashed line represents the start of the buffer zone,  $\xi_{b1} = 60$ , and the end of the bufferzone,  $\xi_{b2} = 100$ . This function is the same as was used by Paul et al (2008), and is a good choice for the buffer zone because the function is very smooth at both

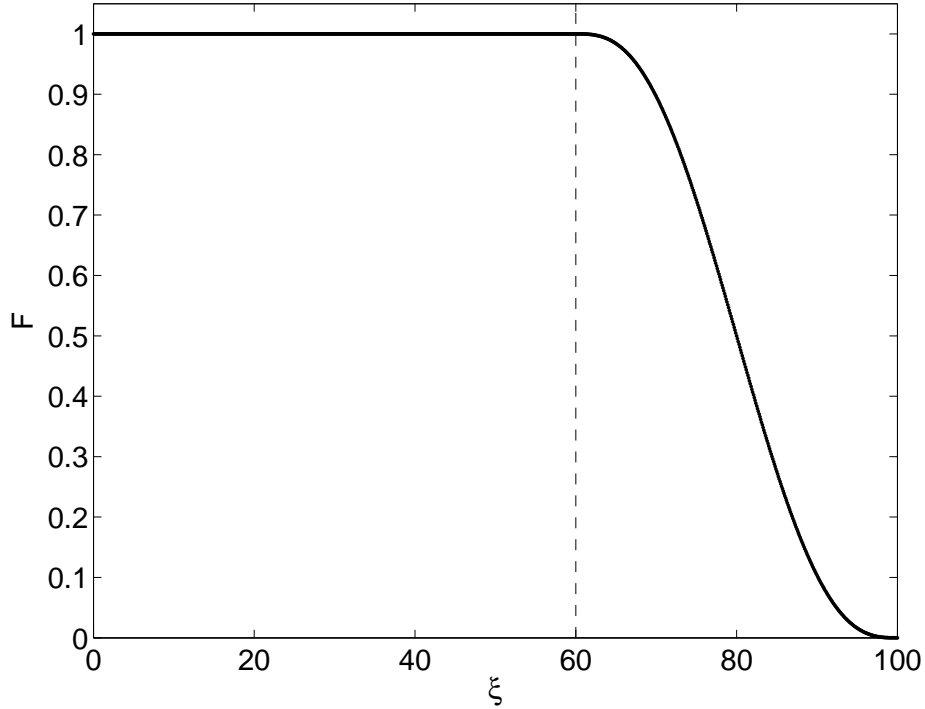


Figure 3.1: The value of the buffer function,  $F(\xi)$  over the flow domain.

extremes: both the first and second derivatives are zero when  $\gamma = 0$  and  $\gamma = 1$ . Additionally  $F = 0$  at  $\gamma = 1$ .

In the case of the inclined boundary layer the basic flow is zero apart from  $\theta_0$  and  $\phi_0^{(2)}$ . The code was run both with and without the buffer zone and with no difference between the results, either in terms of the absolute/convective nature of a disturbance, or in terms of critical distances. With no reflection apparent when the buffer zone is absent, the results shown in Chapter 4 are produced without a bufferzone.

### 3.2.7 Timestep

A variable timestep is used as the presence of the coefficient

$$\frac{4}{(\xi^2 + \eta^2)} \quad (3.38)$$

in Eqs. (3.9) and (3.10) results in temperature changes occurring on a much shorter timescale close to the leading edge (where  $\xi$  and  $\eta$  are small), and increasingly slowly as  $\xi$  and  $\eta$  increase. In terms of the code this means that a small timestep is required initially, as leading edge adjustments occur quickly. The pace of change then slows, and consequently the timestep may be increased. For the results given in Chapter 4 the maximum timestep varies between  $2.5 \leq \delta t_{\max} \leq 7.5$  with higher inclinations being able to sustain larger  $\delta t$ . The timestep is varied based upon the maximum change in  $\theta$  at any given location over one timestep using

$$\delta t^{\text{new}} = A \frac{\delta t^{\text{old}}}{\max \delta \theta}, \quad (3.39)$$

where  $A$  is some constant. The range of  $\delta t$  was investigated to ensure it did not affect either the qualitative or quantitative nature of the results.

## Chapter 4

# Inclined Boundary Layer Results and Discussion

This chapter presents the results of an investigation into the stability of inclined thermal boundary layers with respect to disturbances in the form of streamwise vortices. We begin by determining the steady basic state, and present heat transfer profiles showing how this varies with angle of inclination, as well as demonstrating the distance from the leading edge beyond which the basic state becomes essentially self-similar. Three different perturbation cases are then examined.

Case 1 consists of global (Case 1a.) or isolated (Case 1b.) disturbances with  $\theta_1 = 0$  at the  $\eta = 0$  boundary; such disturbances are termed ‘unforced’. In this case the disturbance is found to be convective in nature, with the disturbance growing in magnitude but being advected out of the domain. We investigate how this growth varies with angle of inclination and wavenumber. The evolution of the isolated disturbance is observed by tracking its leading and trailing edge to determine whether the instability is likely to ever become absolute in nature. Results

are discussed with reference to the parabolic results of Rees (2001b).

In Case 2 a global disturbance is introduced with a nonzero forcing term on the  $\eta = 0$  boundary. This forced-vortex system generates a steady state vortex and neutral curves are produced relating  $\alpha, k$  and the downstream distance beyond which disturbances start to grow,  $\xi_c$ . These neutral curves are compared to those produced using a parabolic solver similar to that used by Rees (2001b), altered to take account of the forcing boundary condition. Comparison of these results allows us to see the influence of steamwise diffusion on the critical distance. Preliminary results as to the effect of subharmonic forcing on both the temperature profile and critical distances for forced vortices are also discussed.

In Case 3 the effect on the steady basic flow of a localised leading edge disturbance which includes a forcing term at  $\eta = 0$  is examined. The impact of the shape of the leading edge disturbance on the downstream evolution of the flow is investigated and neutral curves are produced relating  $\alpha, k$  and the downstream distance beyond which disturbances start to grow,  $\xi_c$ . These results are briefly compared to those for Case 2.

## 4.1 Steady Basic State

The basic state used for this analysis is calculated numerically using the implicit, FAS method described in Chapter 3. Figure 4.1 shows profiles for (a)  $\theta_0$  and (b)  $\phi_0^{(2)}$  when  $\alpha = 55^\circ$ . As the basic flow is two dimensional  $\phi^{(1)}$  and  $\phi^{(3)}$  are everywhere zero, and  $\phi^{(2)}$  is analogous to the stream function. The initial condition that was used is

$$\theta_0 = 2e^{-\eta/3}, \quad (4.1)$$

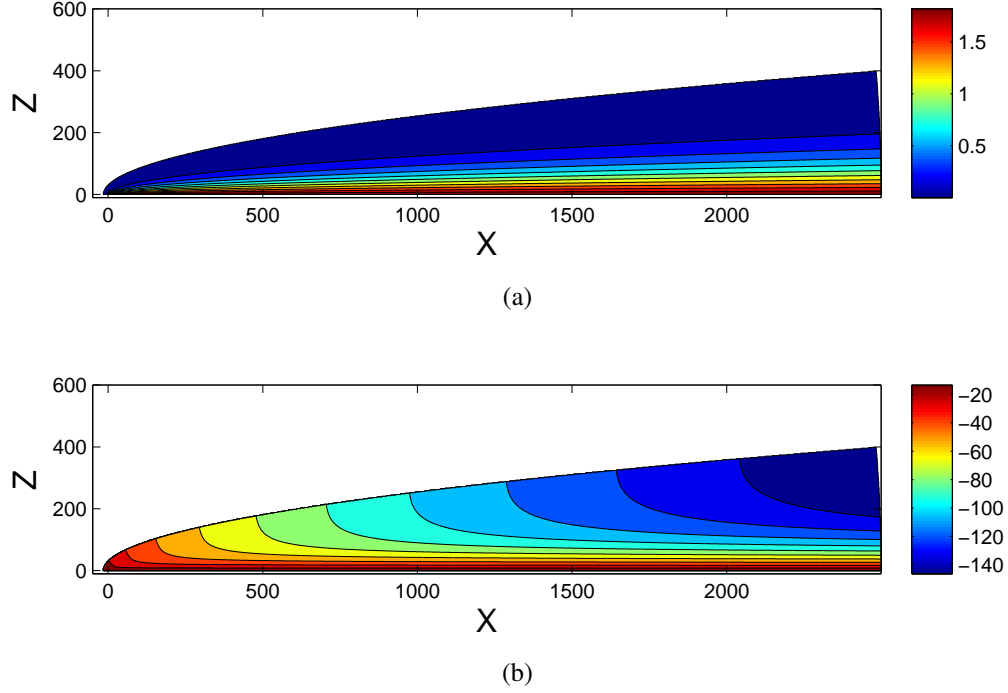


Figure 4.1: Steady basic state solutions,  $\alpha = 55^\circ$ , for contours of (a)  $\theta_0$  and (b)  $\phi_0^{(2)}$ .

with a grid density of  $\delta\xi = 50/96$ ,  $\delta\eta = 8/64$ , with  $\eta_{\max} = 8$ . The value of  $\xi_{\max}$  changes depending on the angle of inclination. For  $\alpha = 55^\circ$ , as shown in Figure 4.1,  $\xi_{\max} = 100$ . At lower angles of inclination the steady state is prone to travelling waves, which although they reduce in amplitude with time can significantly increase the time required to reach the steady state. Consequently shorter domains have been used at lower angles of inclination, e.g.  $\xi_{\max} = 50$  when  $\alpha = 35^\circ$ .

Figure 4.2 shows the rate of heat transfer,  $q_0$ , at the heated surface with respect to  $\xi$ . Heat transfer is calculated as

$$\left. \frac{\partial \theta_0}{\partial \eta} \right|_{\eta=0}. \quad (4.2)$$

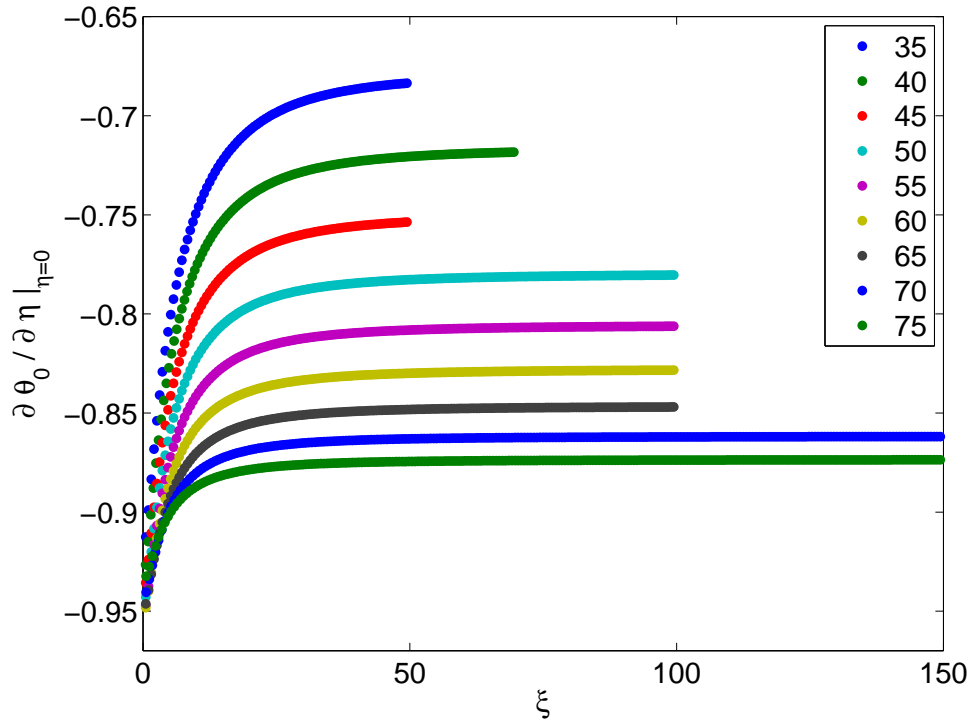


Figure 4.2: Profiles of  $q_0$  (heat transfer rate) against  $\xi$  for the steady basic state,  $35^\circ \leq \alpha \leq 75^\circ$ .

At lower angles of inclination the heat transfer rate is smaller in magnitude. The buoyancy force acting along the heated surface is proportional to  $\sin \alpha$ , consequently the underlying flow is stronger at higher angles of inclination. This results in the heat being advected away from the leading edge more rapidly and therefore higher temperature gradients and larger rates of heat transfer arise with increasing angles of inclination.

Previously (for example, Hsu and Cheng (1979)) the steady basic state for thermal boundary layers in a porous medium at arbitrary angles of inclination has

been described as being self-similar based upon the similarity variable  $\eta$  :

$$\eta = \frac{z}{x^{1/2}}. \quad (4.3)$$

This similarity solution has been shown to be a poor approximation to the shape of the boundary layer near the leading edge (Storesletten and Rees (1998)) but becomes more accurate as downstream distance increases. The coordinate transformation used in this work to produce a mesh that mimics the shape of the spatially developing boundary layer is given by (2.31) and is based upon the same definition of  $\eta$ . Consequently results showing that the heat transfer is constant in  $\xi$  signify that the flow has become self-similar.

We define the basic steady state as being self similar when

$$\left| \frac{q_\xi - q_\infty}{q_\infty} \right| < 10^{-4} \quad (4.4)$$

where  $q_\xi$  is the surface rate of heat transfer at a given downstream location, and  $q_\infty$  is the rate of heat transfer at the furthest distance downstream available. This gives the distance at which the solution become self similar as  $\xi = 64.89$  for  $\alpha = 75^\circ$  and  $\xi = 69.35$  for  $\alpha = 70^\circ$ .

## 4.2 Case 1a. Unforced Global Disturbance

This section describes computations of the evolution of unforced vortices, that is those induced by an initial disturbance profile given by

$$\theta_1 = 0.01\eta e^{-\eta^2} \quad (4.5)$$

which is applied to the whole domain  $0 \leq \eta \leq \eta_{\max}$  and  $0 \leq \xi \leq \xi_{\max}$ . This profile corresponds to a vortex pattern with wavenumber  $k$ . The boundary condition  $\theta_1 = 0$  at  $\eta = 0$  is maintained for all time.

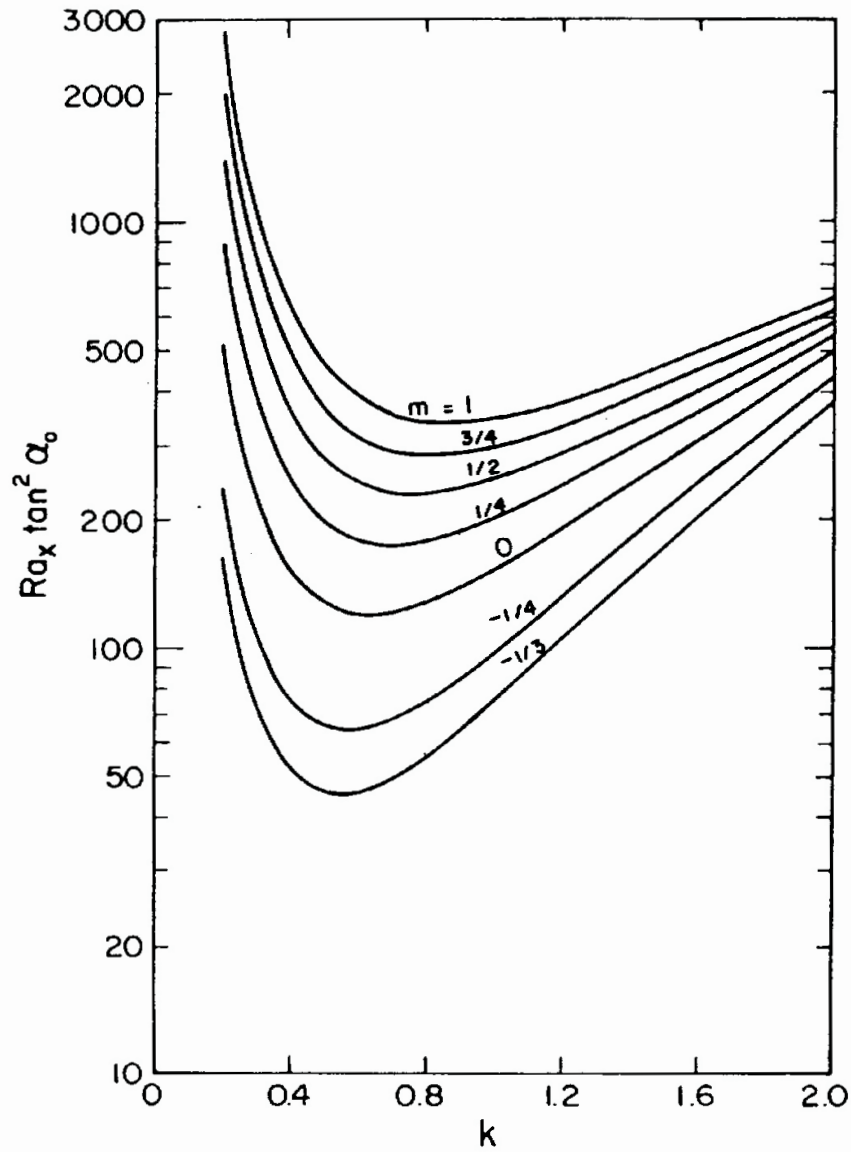


Figure 4.3:  $Ra_x \tan^2 \alpha_0$  as a function of spanwise wavenumber  $k$ . This is Figure 2 from Hsu and Cheng (1979). A constant temperature surface corresponds to  $m = 0$ .  $k$  here is a scaled nondimensional wavenumber and is not equivalent to  $k$  as used elsewhere in this thesis.

Figure 4.3 from Hsu and Cheng (1979) shows the critical local Darcy-Rayleigh Number,  $Ra_x$  scaled by  $\alpha_0$  which denotes the angle of inclination from the *vertical*. The line  $m = 0$  corresponds to the Case 1 configuration: a uniformly heated surface at  $\eta = 0$ .  $Ra_x$  is defined as

$$Ra_x = \frac{\rho g \beta K \Delta T \cos \alpha_0}{\mu \kappa} X. \quad (4.6)$$

This is equivalent to  $x \sin \alpha$ , the nondimensionalised downstream distance scaled by the angle of inclination from the horizontal, where nondimensionalisation is based upon the lengthscale  $L$  given by Eqn. (2.14). Consequently

$$Ra_x \tan^2 \alpha_0 \equiv x \sin \alpha \cot^2 \alpha \equiv x \left( \frac{\cos^2 \alpha}{\sin \alpha} \right). \quad (4.7)$$

For consistency the streamwise wavenumber shown in Figure 4.3 also needs to be rescaled to make it equivalent to  $k$  as used in this chapter. When translated into the present notation the work of Hsu and Cheng (1979) gives the following value of  $x_c$  and  $k_c$ :

$$x_c = 120.7 \left( \frac{\sin \alpha}{\cos^2 \alpha} \right), \text{ and } k_c = 0.0578 \cos \alpha. \quad (4.8)$$

As an example, for  $\alpha = 55^\circ$  a minimal critical distance of  $x_c = 300.53$  ( $\xi_c = 34.67$ ), occurring at the critical wavenumber  $k_c = 0.033$  is produced. These neutral curves have been derived using the parallel flow approximation and boundary layer theory. Consequently, as discussed in Sect. 2.3 and Sect. 2.4, they are not correct at general angles of inclination but provide useful context for the results to follow.

### 4.2.1 Typical Time History

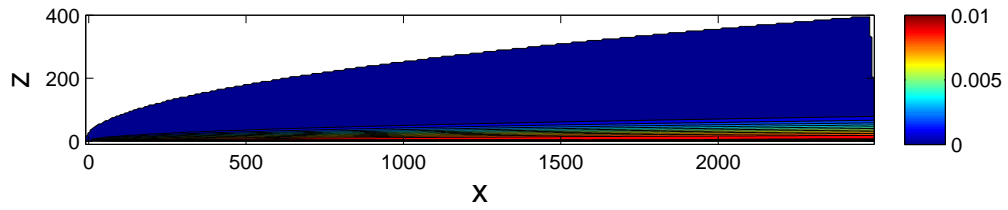
Figure 4.4 shows snapshots of the strength of the primary vortex profile as it evolves. In this case  $\theta_1$  is shown for  $\alpha = 55^\circ$  and  $k = 0.04$  with time increasing from (a) to (h). It is clear that the vortex is increasing in strength, but simultaneously moving downstream. This behaviour was found to be true for other inclinations and wavenumbers in the range  $35^\circ \leq \alpha \leq 60^\circ$  and  $k < 0.1$ . Therefore it was deemed necessary to take a closer look at the evolution of this disturbance with time.

Figures 4.5 and 4.6 show the evolution of  $q_1$  with respect to  $t$  for  $k = 0.02, 0.04$  and  $0.06$  for  $\alpha = 35^\circ$  and  $\alpha = 55^\circ$  respectively, where  $q_1$  is defined as

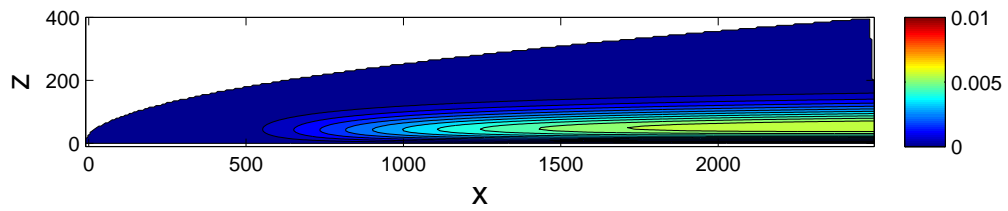
$$q_1 = \left. \frac{\partial \theta_1}{\partial \eta} \right|_{\eta=0}. \quad (4.9)$$

The seven series shown in each figure represent the evolution of  $q_1$  with respect to  $t$  at given downstream locations. The locations are equally spaced in  $\xi$  with  $\xi_{7/8}$  denoting the point where  $\xi = 7/8 \xi_{\max}$  for example. It should be noted that the results for  $\alpha = 35^\circ$  were generated on a domain with  $\xi_{\max} = 50$ , whilst for  $\alpha = 55^\circ$ ,  $\xi_{\max} = 100$  therefore  $\xi_{7/8}$  (and the other locations) are not the same for the two cases. The shorter domain in the  $\alpha = 35^\circ$  case means that the disturbance had not grown as large by the time it left the domain as for the case when  $\alpha = 55^\circ$ , however the size of the domain is limited by the appearance of travelling waves in the basic state which appear as the length of the domain increases. The lower angles of inclination are more susceptible to these and consequently the domain is restricted in this case.

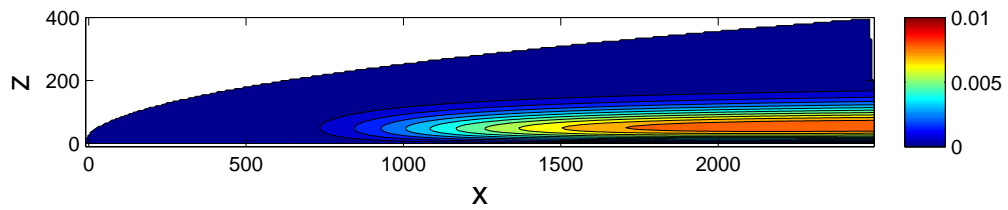
The work of Hsu and Cheng (1979) as summarised in (4.8) predicts growth at  $\xi = 20.3$  for  $k = 0.0473$  when  $\alpha = 35^\circ$ . Figure 4.5a, for which  $\alpha = 35^\circ$ , shows



(a)

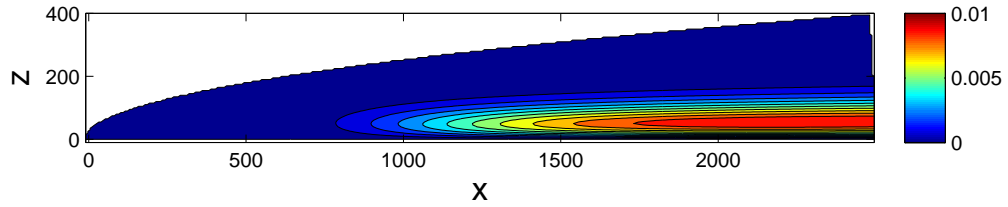


(b)

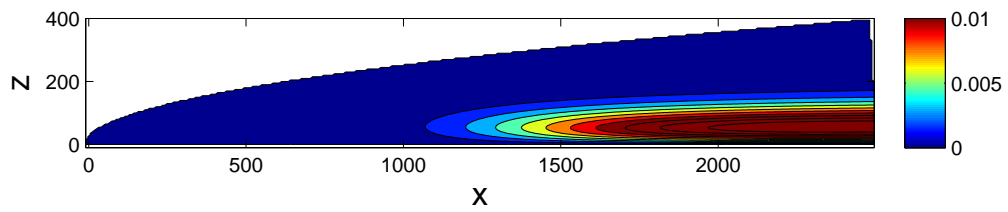


(c)

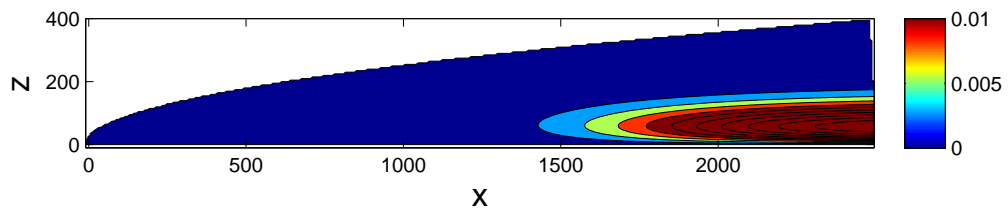
Figure 4.4: Contours of  $\theta_1$  when  $\alpha = 55^\circ$ ,  $k = 0.04$  at (a)  $t = 0.7$ , (b)  $t = 1275$ , (c)  $t = 1913$ , (d)  $t = 2088$ , (e)  $t = 3063$ , (f)  $t = 4293$ , (g)  $t = 5981$  and (h)  $t = 7293$ .



(d)

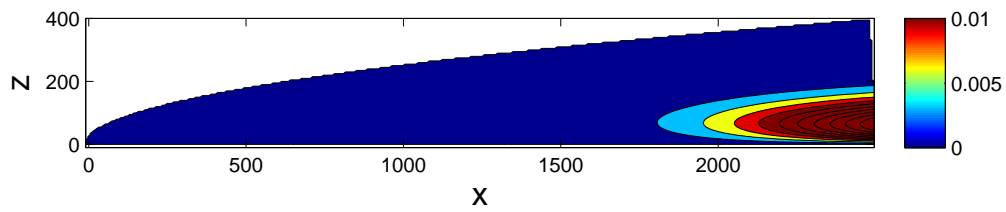


(e)

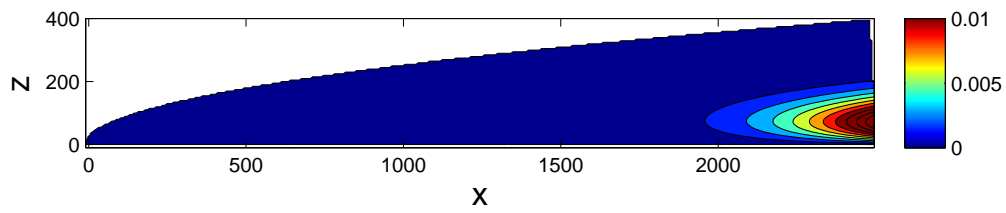


(f)

Figure 4.4: (*Cont.*) Contours of  $\theta_1$  when  $\alpha = 55^\circ$ ,  $k = 0.04$  at (a)  $t = 0.7$ , (b)  $t = 1275$ , (c)  $t = 1913$ , (d)  $t = 2088$ , (e)  $t = 3063$ , (f)  $t = 4293$ , (g)  $t = 5981$  and (h)  $t = 7293$ .

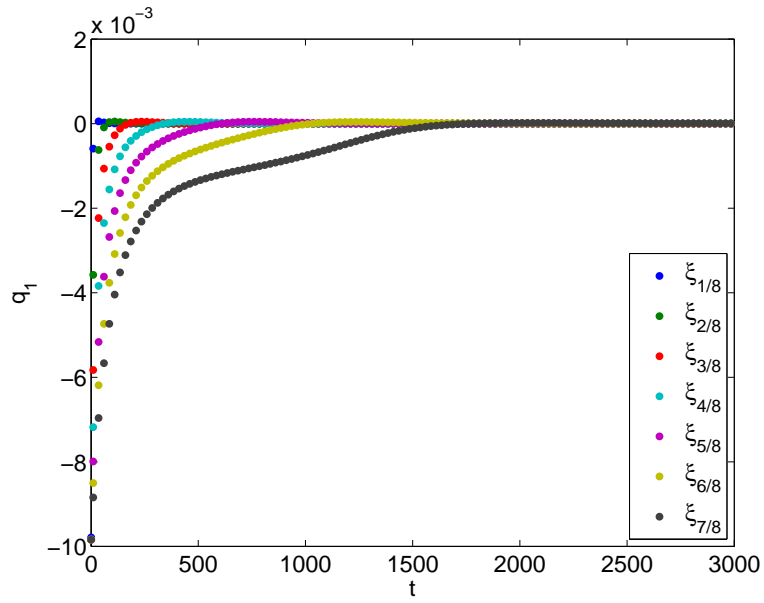


(g)

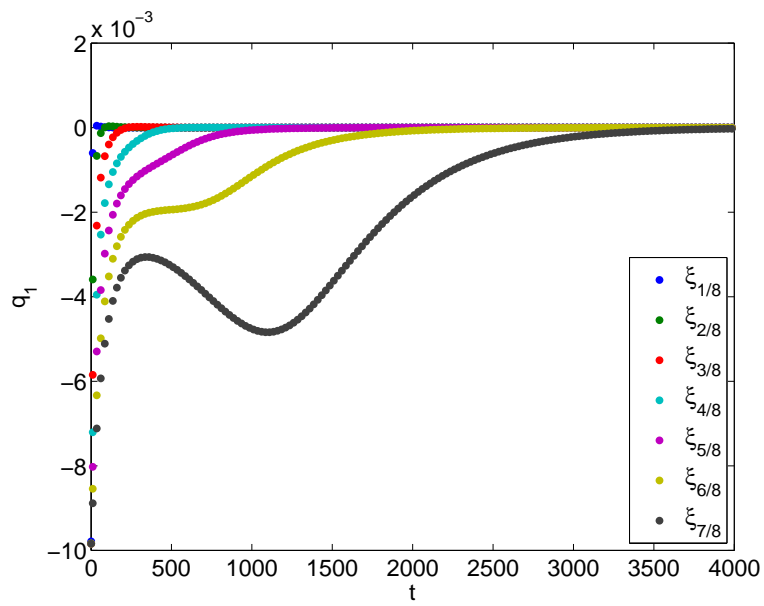


(h)

Figure 4.4: (*Cont.*) Contours of  $\theta_1$  when  $\alpha = 55^\circ$ ,  $k = 0.04$  at (a)  $t = 0.7$ , (b)  $t = 1275$ , (c)  $t = 1913$ , (d)  $t = 2088$ , (e)  $t = 3063$ , (f)  $t = 4293$ , (g)  $t = 5981$  and (h)  $t = 7293$ .

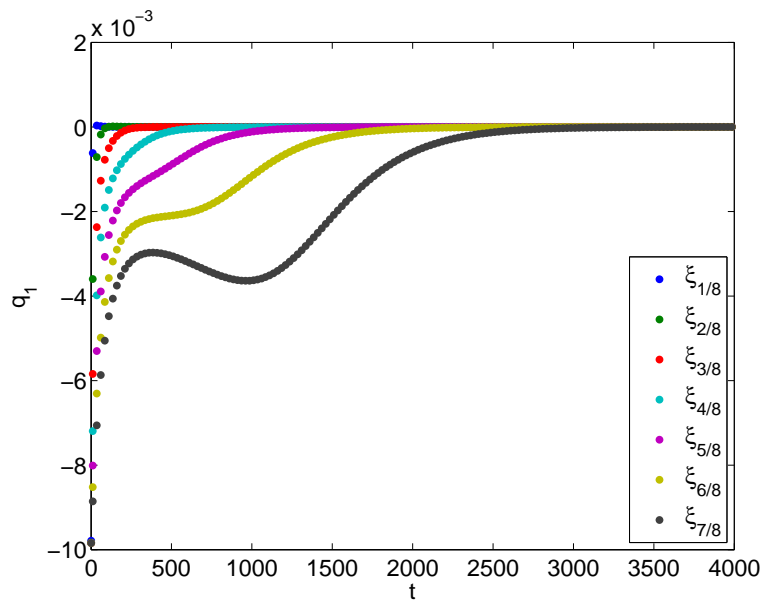


(a)



(b)

Figure 4.5:  $q_1$  against  $t$ ,  $\alpha = 35^\circ$ , (a)  $k = 0.02$ , (b)  $k = 0.04$  and (c)  $k = 0.06$ .



(c)

Figure 4.5: (Cont.)  $q_1$  against  $t$ ,  $\alpha = 35^\circ$ , (a)  $k = 0.02$ , (b)  $k = 0.04$  and (c)  $k = 0.06$ .

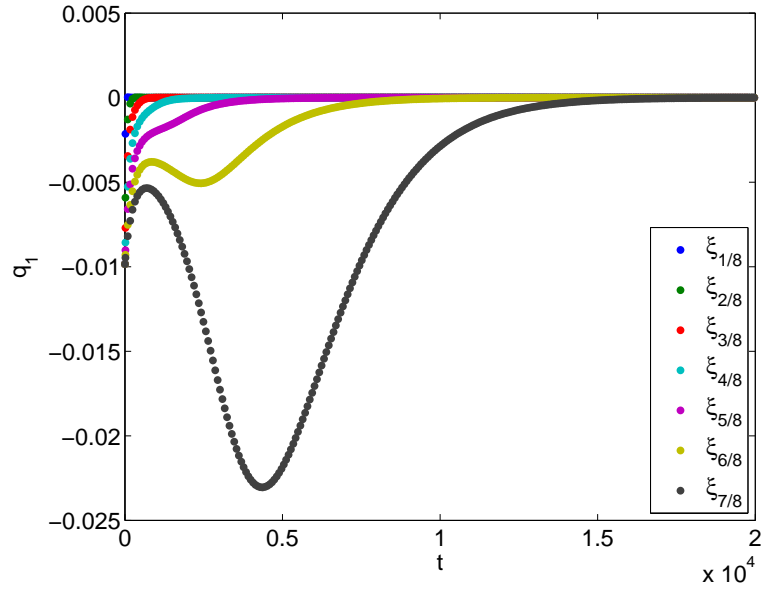
the disturbance decaying at all locations within the domain. This indicates that for  $k = 0.02$ , the critical distance for disturbances to grow is greater than  $\xi = 50$ . The situation changes for Figure 4.5b where at  $\xi = \xi_{7/8}$  the disturbance has begun to grow in strength at  $t \approx 320$ . The decay of the disturbance at  $\xi = \xi_{6/8}$  is also slower than when  $k = 0.02$ . When  $k = 0.06$ , as shown in Figure 4.5c, growth occurs at  $\xi = \xi_{7/8}$  when  $t \approx 400$ , although its magnitude is less than when  $k = 0.04$ . As for  $k = 0.04$ ,  $q_1$  always decays at  $\xi = \xi_{6/8}$ .

Figure 4.6 corresponds to  $\alpha = 55^\circ$ . Figure 4.6a shows significant growth occurring when  $k = 0.02$  as the disturbance travels downstream, with growth at two locations:  $\xi = \xi_{6/8}$  and  $\xi = \xi_{7/8}$ . Growth begins at  $\xi = \xi_{7/8}$  at  $t \simeq 680$  whilst at  $\xi = \xi_{6/8}$  growth begins at  $t \simeq 875$ . The disturbance also spreads out as it travels downstream, shown by the longer time required for the disturbance as a whole to travel past the fixed point at  $\xi = \xi_{7/8}$  when compared with  $\xi = \xi_{6/8}$ . In Figure 4.6b the magnitude of the disturbance at both  $\xi = \xi_{7/8}$  and  $\xi = \xi_{6/8}$  begins to increase at  $t \approx 650$ . However the growth of the disturbance at  $\xi = \xi_{6/8}$  is much stronger when  $k = 0.04$  than when  $k = 0.02$ , and there is also an interval of time when the magnitude of the disturbance at  $\xi = \xi_{5/8}$  increases very slightly. For  $k = 0.06$  the disturbance decays at all locations. It is interesting to note that this is in contrast to the results at  $\alpha = 35^\circ$ , where  $k = 0.02$  showed decay, with growth occurring when  $k = 0.06$ .

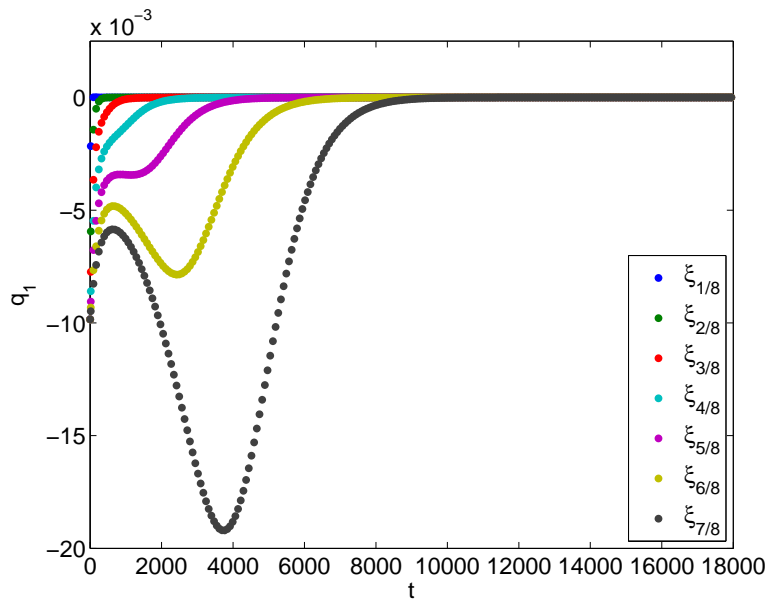
## 4.2.2 Comparison of Elliptic and Parabolic Results for Case 1

The parabolic solutions obtained by Rees (2001b) for the near-vertical configuration, give

$$\xi_c = 17.940 \frac{\sqrt{\sin \alpha}}{\cos \alpha}, \quad k_c = 0.05723 \cos \alpha, \quad (4.10)$$

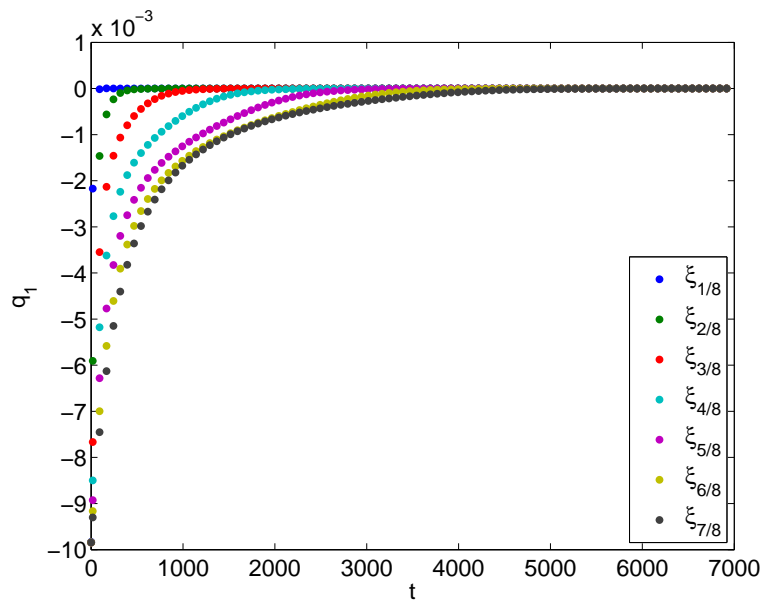


(a)



(b)

Figure 4.6:  $q_1$  against  $t$ ,  $\alpha = 55^\circ$ , (a)  $k = 0.02$ , (b)  $k = 0.04$  and (c)  $k = 0.06$ .



(c)

Figure 4.6: (Cont.)  $q_1$  against  $t$ ,  $\alpha = 55^\circ$ , (a)  $k = 0.02$ , (b)  $k = 0.04$  and (c)  $k = 0.06$ .

based upon critical values extrapolated to  $O(1)$  inclinations from the vertical. Therefore, for an inclination of say,  $55^\circ$ , one ought to have  $\xi_c = 28.31$  and  $k_c = 0.0328$ . We have modelled the flow behaviour in domains up to  $\xi_{\max} = 200$  and as yet have not been able to locate an absolute instability. It is clear that the parabolic equations do not portray well the behaviour of the elliptic simulations given so far for an arbitrarily inclined layer.

### 4.3 Case 1b. Evolution of an Isolated Disturbance

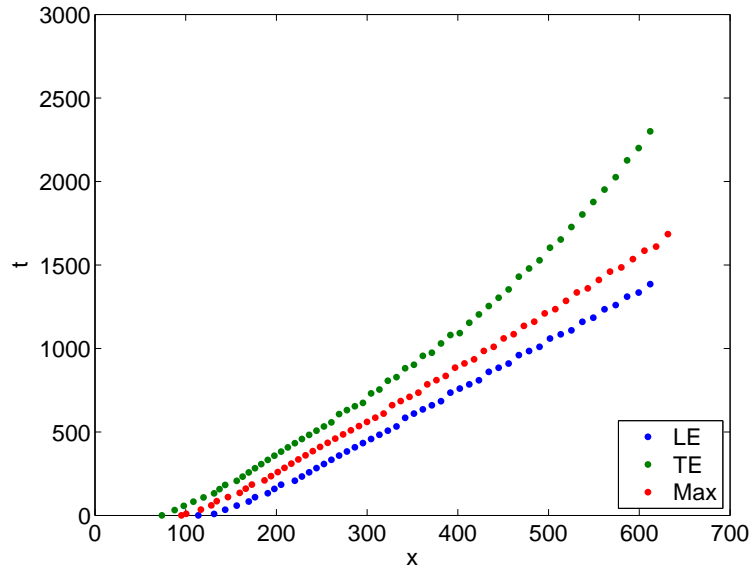
The evolution of a localised disturbance is examined now. The initial disturbance is defined as

$$\theta_1 = 0.01 \sin \left( \frac{(\xi - \xi_a)\pi}{10} \right) e^{-\eta^2}, \text{ for } \xi_1 \leq \xi \leq \xi_1 + 10, \text{ and } 0 < \eta \leq \eta_{\max}. \quad (4.11)$$

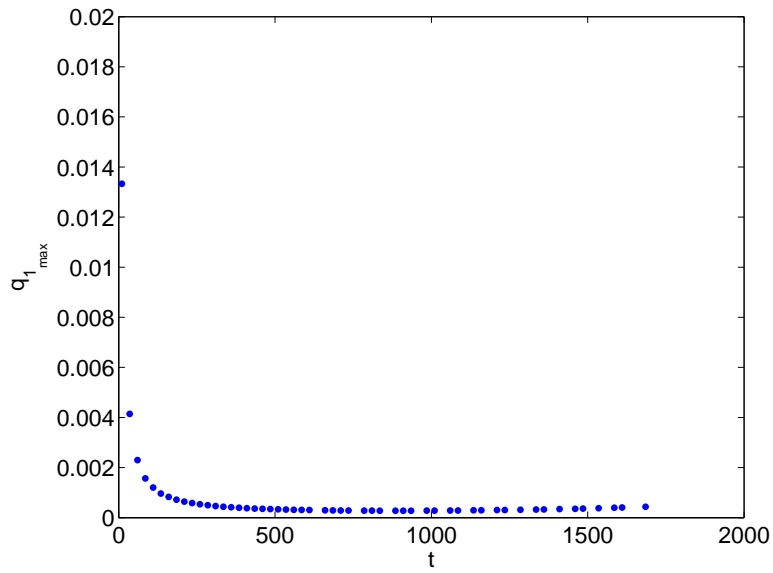
In general this disturbance evolves while travelling downstream and it is possible to define a leading and a trailing edge. The trailing (leading) edge is defined as the location closest to (farthest from) the origin at which the rate of heat transfer at the surface exceeds  $1 \times 10^{-4}$ . Other values of this threshold have been used, but the results remain qualitatively the same.

Figures 4.7 and 4.8 show the variation with time of the location of both the leading and trailing edges of the disturbance, and the maximum value of  $q_1$  with respect to  $\xi$  for  $\alpha = 35^\circ$  and  $\alpha = 55^\circ$  respectively. Presented alongside is a figure showing the value of the absolute maximum of  $q_1$  against  $t$  for each case.

Figure 4.7a shows the speed at which the trailing edge of the disturbance travels downstream reducing with downstream distance when  $\alpha = 35^\circ$  and  $k = 0.02$  whilst the speeds of the leading edge and the maximum remain roughly constant.

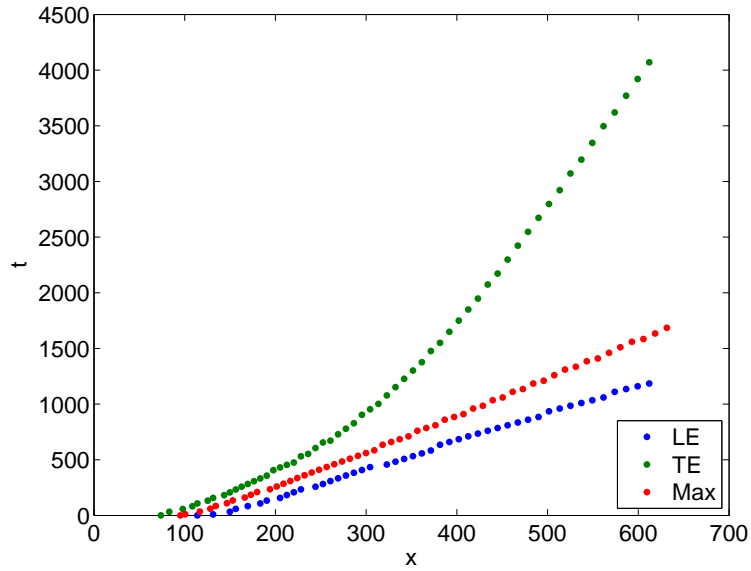


(a)

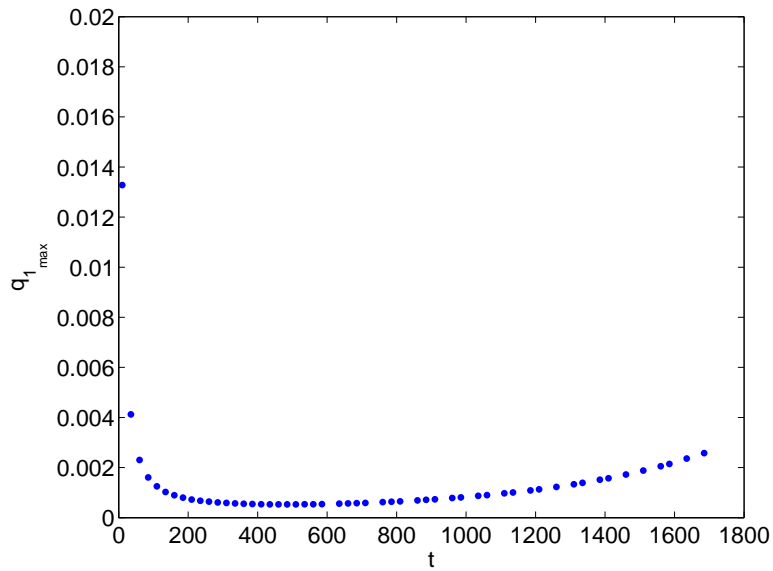


(b)

Figure 4.7: Disturbance location, and  $q_{1_{\max}}$  against  $t$  for  $\alpha = 35^\circ$ , (a) - (b)  $k = 0.02$   
(c) - (d),  $k = 0.04$ , and (e) - (f)  $k = 0.06$ .

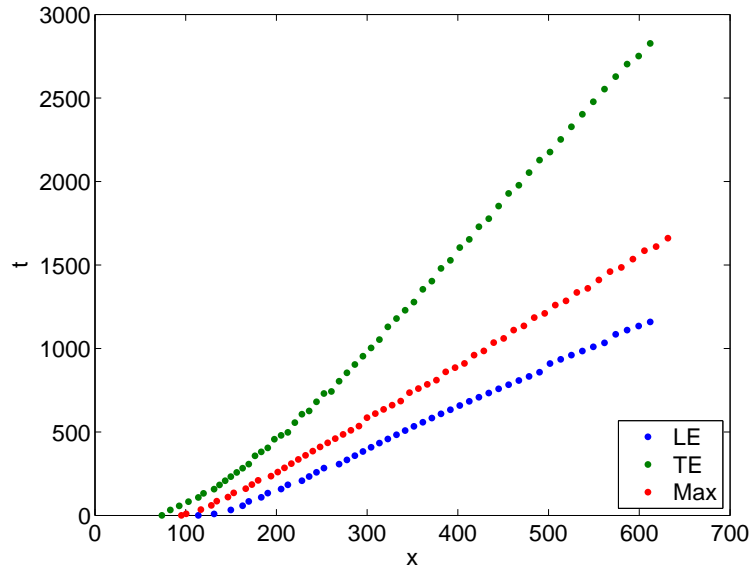


(c)

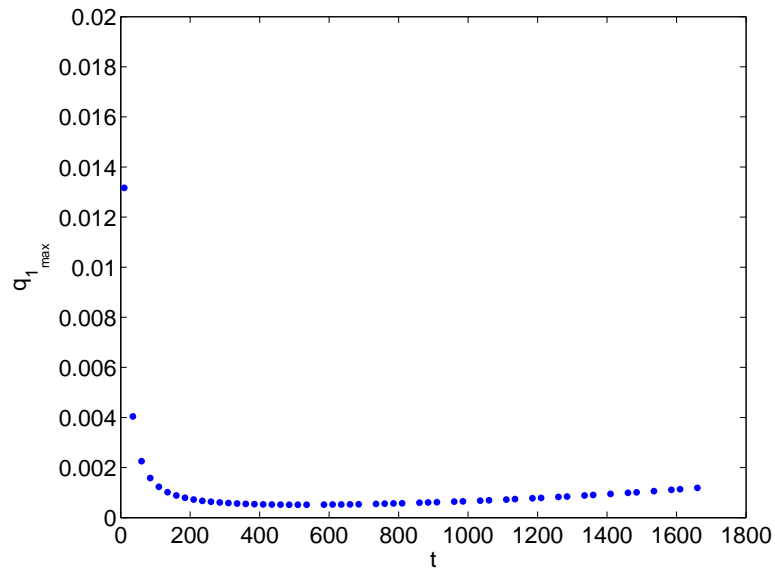


(d)

Figure 4.7: (Cont.) Disturbance location, and  $q_{1_{\max}}$  against  $t$  for  $\alpha = 35^\circ$ , (a) - (b)  $k = 0.02$  (c) - (d),  $k = 0.04$ , and (e) - (f)  $k = 0.06$ .



(e)



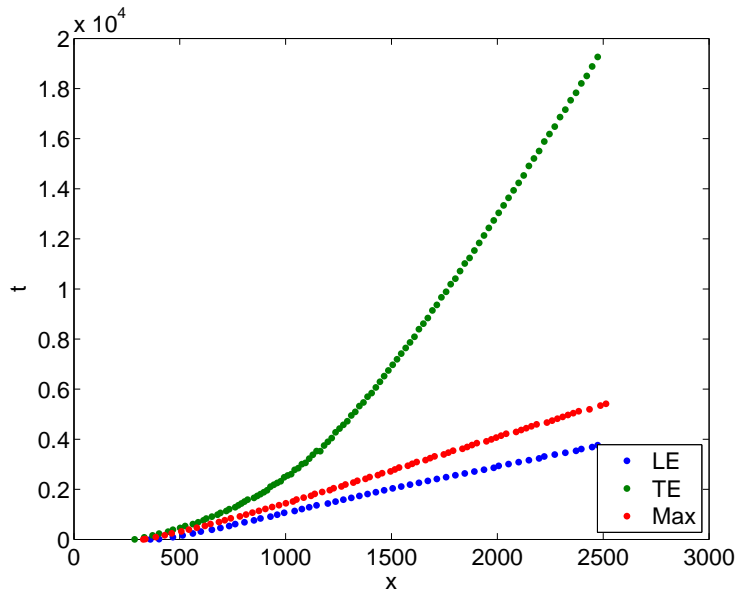
(f)

Figure 4.7: (Cont.) Disturbance location, and  $q_{1_{\max}}$  against  $t$  for  $\alpha = 35^\circ$ , (a) - (b)  $k = 0.02$  (c) - (d),  $k = 0.04$ , and (e) - (f)  $k = 0.06$ .

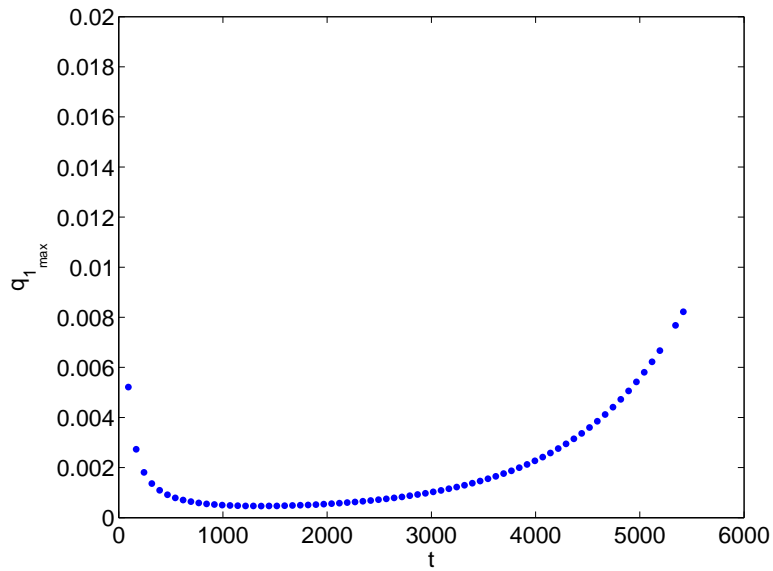
This indicates that upstream diffusion is partially offsetting some of the effects of the underlying flow which seeks to advect the disturbance downstream.

When  $k = 0.02$  we see very little growth in  $q_{1_{\max}}$ , however  $q_{1_{\max}}$  reaches a minimum at  $t \approx 800$ , at which time  $q_{1_{\max}}$  is located at  $x \approx 410$ . When  $k = 0.04$  Figure 4.7d shows stronger growth in  $q_{1_{\max}}$ , with growth beginning around  $t \approx 500$ ,  $x \approx 290$ , and this is reflected in a more pronounced slowing of the trailing edge in Figure 4.7c. We also see the beginning of some divergence between the location of the leading edge and the location of the maximum value of  $q_1$ . Increasing  $k$  to 0.06 gives less growth in  $q_{1_{\max}}$  and faster downstream travel for the trailing edge. In this case the minimum value of  $q_{1_{\max}}$  occurs at around  $t \approx 600$ ,  $x \approx 310$ .

Figure 4.8a, in which  $\alpha = 55^\circ$ , shows a significant slowing of the trailing edge with the disturbance taking until  $t \simeq 19000$  to exit the domain compared with  $t \simeq 9500$  when  $k = 0.04$ . This is explained by the much stronger growth experienced by the  $k = 0.02$  disturbance, as evidenced in Figure 4.8b. When  $k = 0.02$ , growth in  $q_{1_{\max}}$  occurs from  $t \approx 1400$ ,  $x \approx 750$ . For  $k = 0.04$ ,  $q_{1_{\max}}$  reaches a minimum when  $t \approx 1100$ , which corresponds to  $x \approx 750$ . For the  $k = 0.06$  case the disturbance seems to disappear; Figure 4.8e shows the leading and trailing edges of the disturbance coming together and the maximum, which as illustrated by Figure 4.8f is itself decaying, exits the domain at  $t \simeq 5100$ . The apparent disappearance of the leading and trailing edges is caused by the above mentioned absolute threshold ( $q_1 = 1 \times 10^{-4}$ ). If the threshold value had been defined as a function of the maximum value of  $q_1$  then the leading edge and trailing edge would not have disappeared as the magnitude of the disturbance reduces. However the aim of this section of work was to monitor whether the trailing edge of a disturbance became fixed in space (i.e. to determine if the instability is absolute),

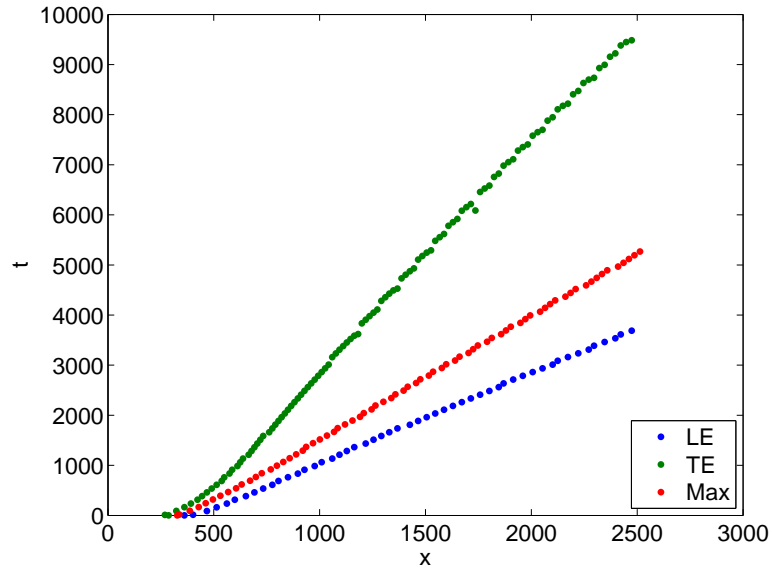


(a)

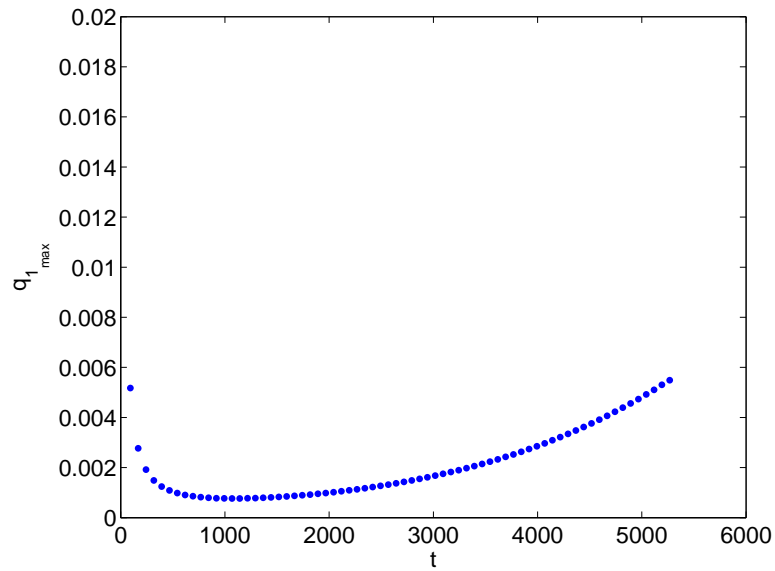


(b)

Figure 4.8: Disturbance location, and  $q_{1,max}$  against  $t$  for  $\alpha = 55^\circ$ , (a) - (b)  $k = 0.02$ , (c) - (d)  $k = 0.04$ , and (e) - (f)  $k = 0.06$ .

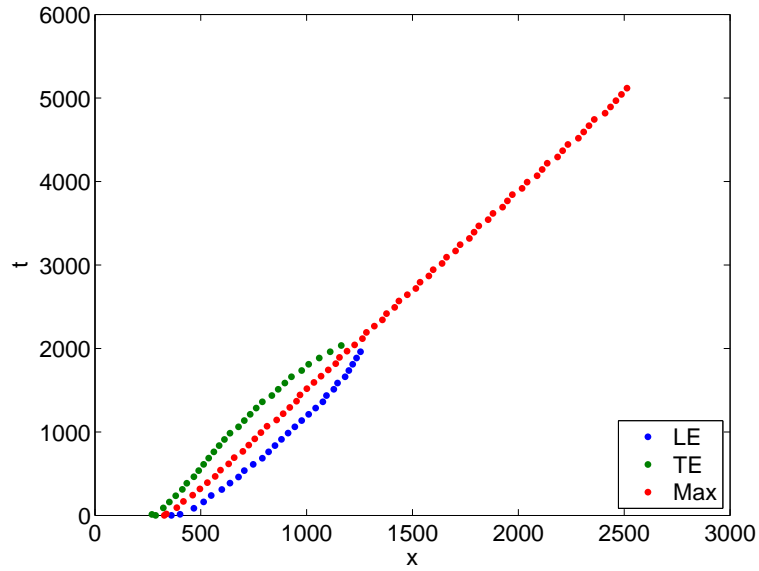


(c)

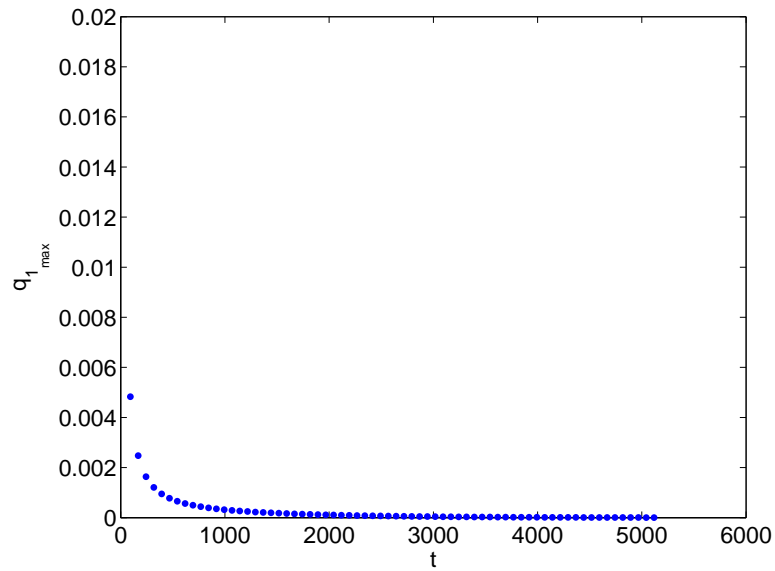


(d)

Figure 4.8: (Cont.) Disturbance location, and  $q_{1_{\max}}$  against  $t$  for  $\alpha = 55^\circ$ , (a) - (b)  $k = 0.02$ , (c) - (d)  $k = 0.04$ , and (e) - (f)  $k = 0.06$ .



(e)



(f)

Figure 4.8: (*Cont.*) Disturbance location, and  $q_{1_{\max}}$  against  $t$  for  $\alpha = 55^\circ$ , (a) - (b)  $k = 0.02$ , (c) - (d)  $k = 0.04$ , and (e) - (f)  $k = 0.06$ .

and consequently the fixed threshold method is the most appropriate technique to use.

Comparing the two angles of inclination shown in Figures 4.7 and 4.8 we see that the disturbance is moving much faster when  $\alpha = 55^\circ$  than when  $\alpha = 35^\circ$ . For example, Figure 4.7c shows the maximum value of the disturbance at  $x = 600$  and at  $t \simeq 1750$ , whereas in Figure 4.8c the maximum is located at  $x = 600$  at  $t \simeq 1000$ . This is to be expected with the stronger underlying flow at higher angles of inclination.

Although Figures 4.7 and 4.8 show that the downstream velocity of the trailing edge decreases, the curve remains far from vertical which would indicate the presence of an absolute instability, nor does it appear to be approaching a stationary state. It is clear, however, that for both Case 1a. (global) and Case 1b. (isolated) the disturbance can grow for a range of values of  $k$ . It is impossible to state definitively that the inclined boundary layer is always convectively unstable to unforced vortex type disturbances, because only finite domains may be modelled using the numerical methods employed here. However the computational results appear to support this conclusion.

## 4.4 Verifying the Convective Nature of Case 1

The expectation at the beginning of this project was that the Case 1 disturbance would prove to be absolutely unstable. However the results of the implicit code indicate this may not be the case. Additional work was undertaken to verify that the convective nature of the instability was not a result of numerical effects. This examined (i) the effect of the time discretisation (time stepping method) used and

(ii) whether the thickness of the boundary layer was constraining vortex development.

#### 4.4.1 Effect of Time Discretisations

Cossu and Loiseleux (1998) show through analysis of a dispersion relation that the absolute or convective nature of an instability can be modified by numerical effects relating to the discretisation of the governing equations. The mathematics involved in deriving and analysing the dispersion relation for the inclined thermal boundary layer is beyond the scope of this thesis. However, it was postulated that the first order accurate implicit scheme could have inadvertently changed the stability properties of the flow resulting in an absence of absolute instability. To examine this possibility two alternative discretisation schemes were employed, namely a first order accurate forward Euler method for the time derivatives which results in an explicit scheme, and a second order accurate backward difference method (the well-known BDF2).

The explicit code uses a forward Euler method, as opposed to the backward Euler described in Sect. 3.1.4. The forward Euler is based upon the relationship

$$\frac{\partial \theta_{i,j}^n}{\partial t} = \frac{\theta_{i,j}^{n+1} - \theta_{i,j}^n}{\delta t}, \quad (4.12)$$

giving

$$\theta_{i,j}^{n+1} = \theta_{i,j}^n + \frac{\partial \theta_{i,j}^n}{\partial t} \delta t, \quad (4.13)$$

where  $n$  denotes the timestep. The time derivative of temperature is determined for each point in the grid using either Eqn. (3.9) or Eqn. (3.10), according to the mode, and discretised using second order accurate central differences in space as described previously. The structure of the explicit code is as follows.

1. Input of runtime parameters.
2. Read in the basic state solution (i.e.  $\theta_0$  and  $\phi_0^{(2)}$ ).
3. Define the disturbance by specifying a  $\theta_1$  profile.
4. Use current  $\theta$  profiles to calculate right hand side of Eqs. (3.5 – 3.7).
5. Use a Line Solve GS scheme (see Sect. 3.1.6), with the MGCS (see Sect. 3.1.8) to solve Eqs. (3.5 – 3.7).
6. Use the current values of  $\theta$  and  $\phi^{(1)}$ ,  $\phi^{(2)}$  and  $\phi^{(3)}$  to calculate the change in  $\theta$  with respect to time using either Eqn. (3.9) or Eqn. (3.10).
7. Update  $\theta$  to new values using Eqn. (4.13).
8. Calculate convergence test.
9. Repeat steps 4-7 until convergence criterion reached.

This code is more straightforward computationally, but is much more constrained in terms of timestep than the implicit code. For the standard forward Euler the timestep for stability is limited to  $O(\delta\eta^2)$ , however the presence of the coefficient,

$$\frac{4}{(\xi^2 + \eta^2)}, \quad (4.14)$$

which is an effective diffusivity, acts to increase the severity of this restriction so that a stable timestep in the case of this problem will typically be of  $O(\delta\eta^4)$ . This is a severe restriction when solving on a domain which includes the origin because of the fine grid near the leading edge. This constraint was overcome by computing in a portion of the domain, as shown in Figure 4.9, where the computational domain is given by the area formed by the lines joining ABCD. The basic state was used to provide the boundary condition on the line AB and all other boundary conditions remain unchanged.

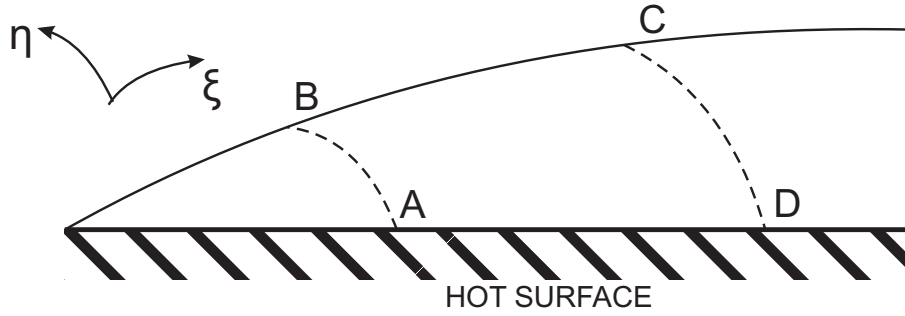


Figure 4.9: Domain for Explicit Computations.

The second order accurate backward difference scheme (BDF2) is based upon the discretisation,

$$3\theta_{i,j}^{n+1} = 4\theta_{i,j}^n - \theta_{i,j}^{n-1} + 2\delta t \frac{\partial \theta_{i,j}^{n+1}}{\partial t}, \quad (4.15)$$

where the derivative of  $\theta$  with respect to time is given by Eqn. (3.9) or Eqn. (3.10) depending on the mode. This scheme is implicit in nature, and has the same structure as described in Sect. 3.1.4, the only differences being the retention of the data for  $\theta^{n-1}$  and a straightforward alteration to the time discretisation.

Figure 4.10 shows the variation of  $q_1$  with  $t$  at five equally-spaced locations in  $\xi$  calculated using the forward Euler (Explicit), first order accurate backward Euler (BDF1) and second order accurate backward Euler (BDF2) when  $\alpha = 55^\circ$  and  $k = 0.04$ . The timestep differs between the different codes resulting in data points for the simulations appearing at different times, but it can be seen that the three sets of data lie on the same line. The Explicit and BDF2 codes were run for a variety of inclinations and wavenumbers, and, as in Figure 4.10, the results were found to be graphically indistinguishable from those of the implicit, first order

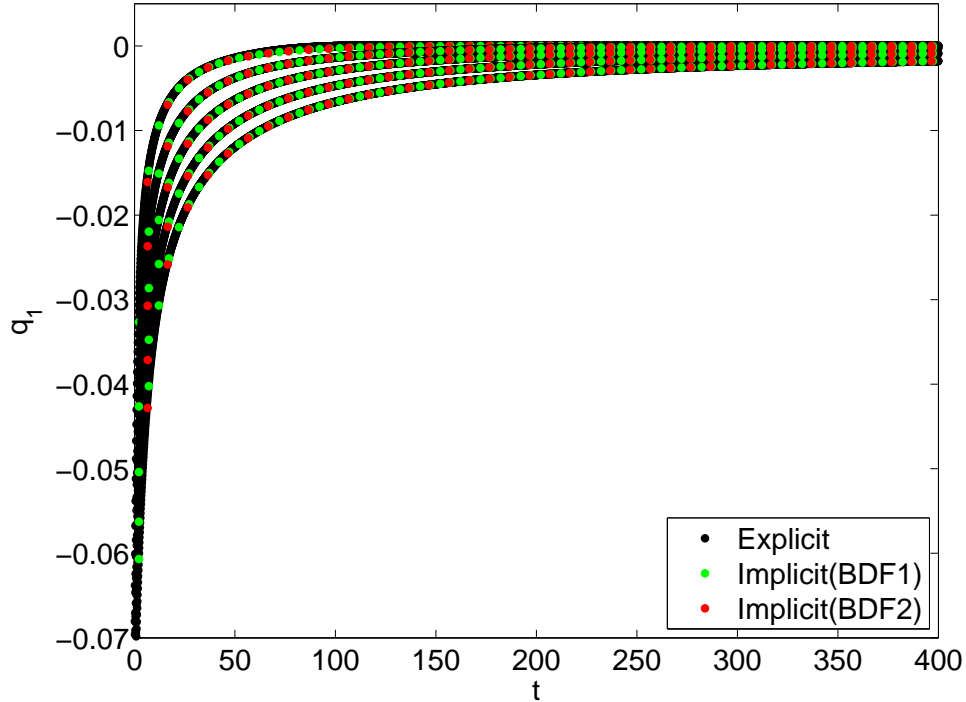


Figure 4.10: Comparisons of  $q_1$  vs.  $t$  at 5 streamwise locations for Explicit, BDF1 and BDF2 time discretisations when  $\alpha = 55^\circ$ ,  $k = 0.04$ .

accurate (BDF1) code in all cases.

#### 4.4.2 Coordinate stretching in the $\eta$ -direction

Returning to the implicit code we investigated the possibility that the  $\eta_{\max}$  boundary is too close to the heated surface and that this might inhibit the growth of an absolutely unstable vortex. A simple increase in the value of  $\eta_{\max}$  will increase the computational effort required significantly, which is undesirable. In order to avoid such an increase in work a coordinate-stretching transformation in the  $\eta$ -direction

is introduced:

$$\eta_{\text{old}} = e^{\eta_{\text{new}}} - 1. \quad (4.16)$$

The governing equations are now rewritten in terms of this new coordinate system with the following replacements for the  $\eta$  derivatives of

$$\frac{\partial}{\partial \eta_{\text{old}}} = e^{-\eta_{\text{new}}} \frac{\partial}{\partial \eta_{\text{new}}}, \quad \text{and} \quad \frac{\partial^2}{\partial \eta_{\text{old}}^2} = e^{-2\eta_{\text{new}}} \left[ \frac{\partial^2}{\partial \eta_{\text{new}}^2} - \frac{\partial}{\partial \eta_{\text{new}}} \right]. \quad (4.17)$$

In terms of coding this is quite a straightforward change, with values of  $e^{-\eta_{\text{new}}}$  and  $e^{-2\eta_{\text{new}}}$  calculated for each location on the grid at the start of the programme and called wherever an  $\eta$ -derivative is calculated.

The much thicker layers that could be calculated with the new  $\eta$ -coordinate allowed the simulation to run for longer, because plumes or breakouts from the layer did not approach closely to the inflow boundary. Despite this the qualitative nature of the results did not change; disturbances continue to be advected out of the domain.

## 4.5 Case 2 - Global Forced Vortices

It is quite possible that the numerical code contains errors, given that the hoped-for absolute instability has not been found. Therefore it was deemed necessary to introduce a forced vortex system because (i) this type of disturbance may be compared very easily with parabolic simulations which are almost identical to those of Rees (2001b) and (ii) the alteration to the elliptic code has the form of a single change in one line. Thus good comparisons here would form a further validation of the code and strengthen the assertion that the vortex instability is advective in nature.

Forced vortices were induced by the initial condition

$$\theta_1 = Ae^{-\eta^2}, \text{ on } 0 \leq \xi \leq \xi_{\max}, \text{ and } 0 \leq \eta \leq \eta_{\max}, \quad (4.18)$$

giving  $\theta_1 = A$  on the  $\eta = 0$  boundary. Physically this represents a continuous forcing in the disturbance mode (mode 1). Results presented in this chapter were produced using  $A = 0.01$ . The basic steady state (i.e. the profiles for  $\theta_0$  and  $\phi_0^{(2)}$ ) remains unchanged from that shown in Figure 4.1. The consequence of having a forced vortex situation is that the simulation generally tends towards a steady flow.

### 4.5.1 Typical Steady State Profile

Figures 4.11a - 4.11f show typical steady state profiles for the disturbed flows  $\theta_0$  and  $\theta_1$  when  $k = 0.06, 0.04$  and  $0.02$ .

When  $k = 0.06$ , Figure 4.11b shows that the vortex has remained weak and consequently the basic flow as shown in Figure 4.11a is only very slightly altered from that of the steady state shown in Figure 4.1a. At this value of  $k$  there is only a small range of values of  $x$  within which growth may occur, and the maximum value of  $\theta_1$  arises at  $x \simeq 850$ .

The corresponding situation for  $k = 0.04$  is shown in Figure 4.11d. Here the vortex pattern has benefitted from having a longer region of growth, and it reaches a maximum at  $x \simeq 2100$ . By comparing Figures 4.11a and 4.11c we see that there is a slight change in the isotherm pattern for  $\theta_0$ ; clearly convection has become moderately nonlinear as evidenced by the change in mode 0 as a result of interaction with modes 1 and 2. However the change in mode 0 is slight despite the much stronger growth in  $\theta_1$  at  $k = 0.04$ .

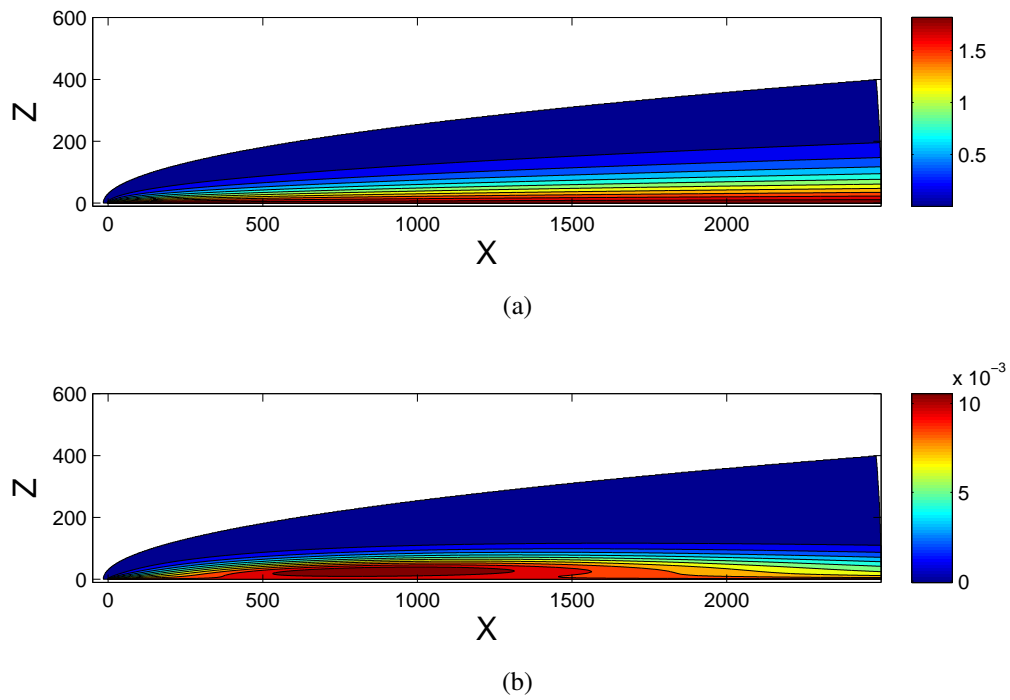
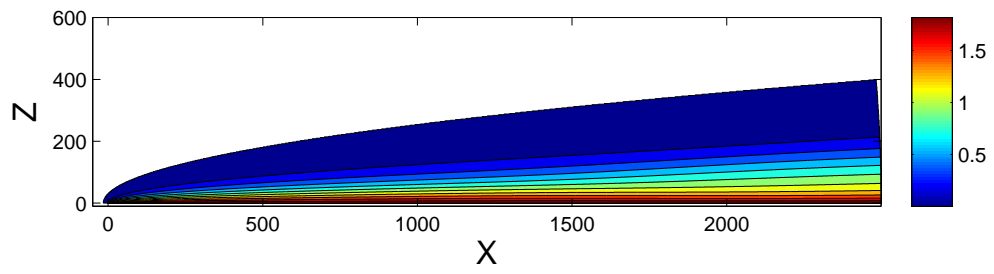
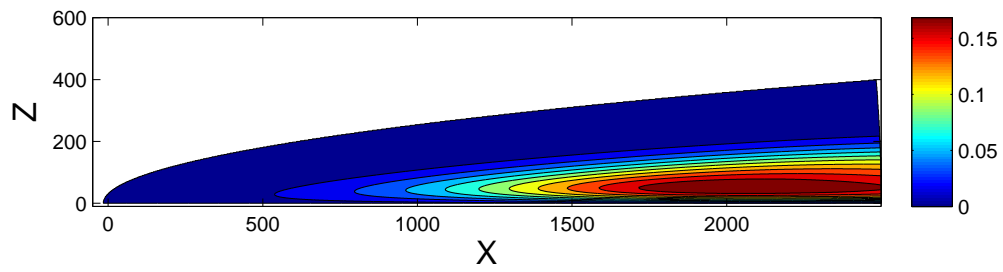


Figure 4.11:  $\theta_0$  and  $\theta_1$  for  $\alpha = 55^\circ$ , (a)-(b)  $k = 0.06$ , (c)-(d)  $k = 0.04$ , and (e)-(f)  $k = 0.02$ . Note different scales for  $\theta$  have been used.

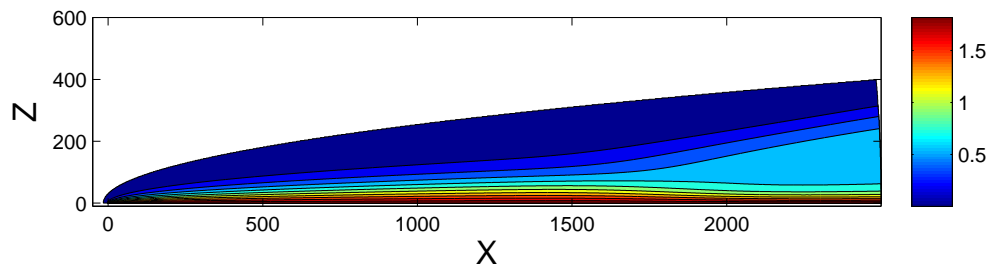


(c)

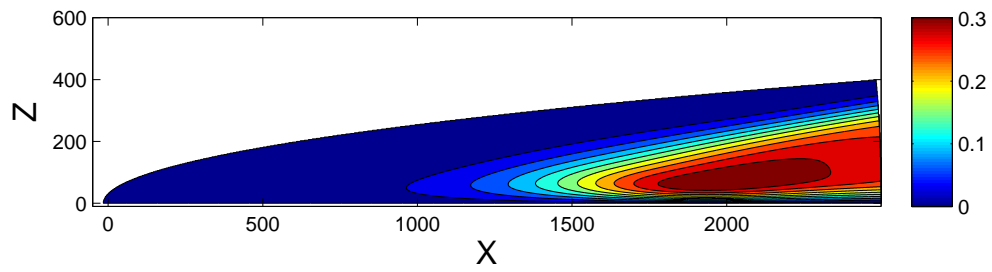


(d)

Figure 4.11: (*Cont.*)  $\theta_0$  and  $\theta_1$  for  $\alpha = 55^\circ$ , (a)-(b)  $k = 0.06$ , (c)-(d)  $k = 0.04$ , and (e)-(f)  $k = 0.02$ . Note different scales for  $\theta$  have been used.



(e)



(f)

Figure 4.11: (*Cont.*)  $\theta_0$  and  $\theta_1$  for  $\alpha = 55^\circ$ , (a)-(b)  $k = 0.06$ , (c)-(d)  $k = 0.04$ , and (e)-(f)  $k = 0.02$ . Note different scales for  $\theta$  have been used.

When  $k = 0.02$ , Figure 4.11f shows a vortex profile which is much stronger than those for the larger wavenumbers, although it begins its growth at a larger value of  $x$  than when  $k = 0.04$ . The strength of the vortex has modified the mean temperature profile,  $\theta_0$ , as shown in Figure 4.11e, quite substantially, and we see a marked increase in the temperature gradient of  $\theta_0$  after  $X = 2000$ .

Having reviewed the steady pattern obtained for the three different wavenumbers, it is also interesting to note how the thickness of the vortex system (in terms of the parabolic coordinate  $\eta$ ) varies with wavenumber. It is clear that the vortex becomes increasingly confined towards the heated surface as  $k$  increases.

#### 4.5.2 Methodology for calculating $\xi_k$

Given the steady state produced by the forced vortex system it is essential to attempt to calculate the distance downstream at which the disturbance begins to grow. As discussed in Sect. 3.1.9 there are three different methods that could be used to calculate the critical distance  $\xi_k$ . These are (i) the maximum disturbance temperature, (ii) the surface rate of heat transfer, or (iii) the disturbance energy. In the Darcy-Bénard problem instability is unambiguously defined as disturbances growing or decaying in time and the three methods are equivalent. In the boundary layer problem disturbances will be growing in space and time, and consequently these three measures of critical distance will produce differing results. An aim of this section is to examine the impact of the method used to calculate  $\xi_k$  and determine the most appropriate method to use for this work.

The work is primarily interested in the onset of instability. Consequently the maximum value of the disturbance, which will occur downstream of where the disturbance first begins to grow, will not be used.

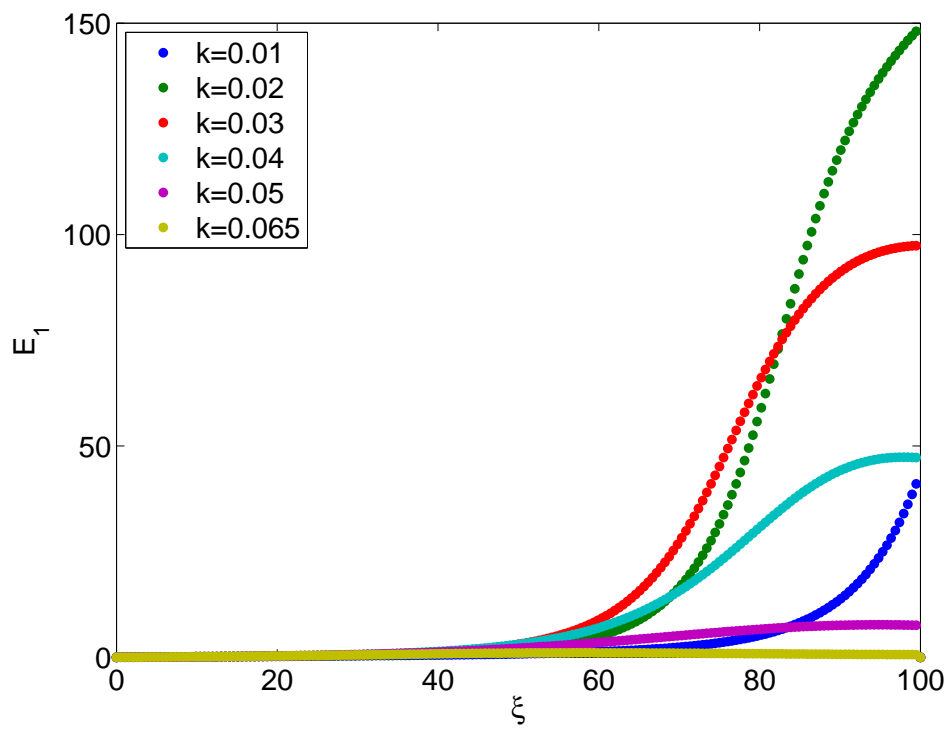


Figure 4.12: Profile of  $E_1$  versus  $\xi$ , when  $\alpha = 55^\circ$ .

Figure 4.12 shows profiles for  $E_1$ , a measure of thermal energy defined by Eqn. (3.34), when  $\alpha = 55^\circ$  for a range of wavenumbers. When  $k = 0.065$ ,  $E_1$  has a maximum at  $\xi \approx 47$ , therefore this would be the critical distance based upon the disturbance energy method, as discussed in Sect. 3.1.9. However examination of the steady state temperature profile shows that the disturbance has decayed in this case at all locations within the domain, that is to say this method has produced a spurious critical distance. Use of  $E_1$  as the criterion for determining critical distance results in decreasing values of  $\xi_k$  as  $k$  increases above  $k = 0.065$ , consequently the shape of the neutral curve is incorrect as we would expect to see a maximum wavenumber beyond which the boundary layer is stable to vortex disturbances. As a result  $E_1$  is not deemed an appropriate measure for determining critical distance.

Figure 4.13 shows the evolution of  $q_1$  (surface rate of heat transfer in mode 1) with  $\xi$ . When  $\xi$  is small the forcing boundary condition,  $\theta_1 = A$ , causes heat to pass into the fluid, and  $q_1$  is less than zero. Further downstream, where the vortex is growing,  $q_1$  is greater than zero and energy is being drawn from the basic state and is leaving the domain via the surface. Consequently  $q_1$  is used to calculate the critical distance based upon

$$q_1 = \frac{\partial \theta_1}{\partial \eta} = 1 \times 10^{-8} \quad (4.19)$$

with linear interpolation used to identify the value of  $\xi$  at which this occurs. No spurious critical distances are produced using this method, and the shape of the neutral curve is reasonable. Consequently this criterion will be used to produce the neutral curves shown in this chapter.

A further aspect of determining critical distance is to consider whether the surface heat flux is calculated in terms of the derivative of  $\theta$  with respect to  $z$  or  $\eta$ . It

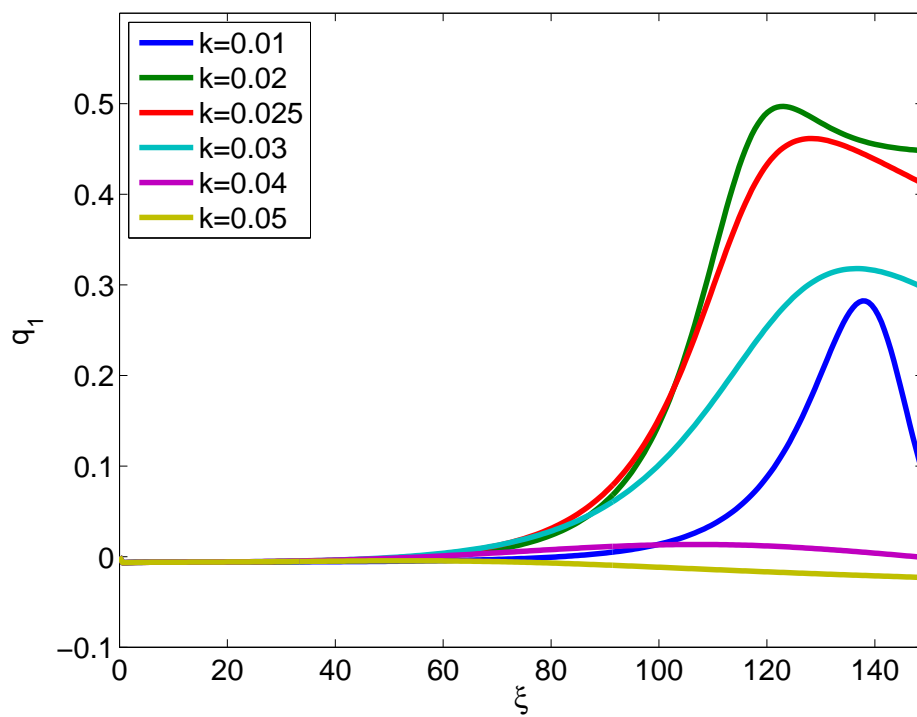


Figure 4.13: Evolution of the surface heat flux ( $q_1$ ) with  $\xi$  for  $\alpha = 65^\circ$ .

$k$	$q_{z1}$	$q_{\eta 1}$
0.0080	92.5614	92.5626
0.0100	81.7817	81.7818
0.0150	66.4595	66.4590
0.0200	58.6849	58.6847
0.0250	54.5450	54.5451
0.0300	52.7759	52.7760
0.0350	53.1825	53.1820
0.0400	56.9075	56.9087
0.0400	147.5570	147.5552
0.0425	61.9686	61.9691
0.0425	114.3936	114.3911
0.0430	63.7189	63.7196
0.0430	107.7066	107.7039

Table 4.1: Comparison of  $\xi_k$  calculated using derivative with respect to  $z$  or  $\eta$ ,  $\alpha = 65^\circ$ .

can be seen in Table 4.1 that the difference between the two criteria is slight and there is no absolute trend in terms of one criterion being more restrictive than the other. The results shown in this chapter are based upon  $q_1$  where the differentiation of  $\theta$  is with respect to  $\eta$ .

### 4.5.3 Neutral Curves for Case 2

Simulations for a wide range of values of  $k$  and  $\alpha$  were undertaken, and the value of  $\xi_k$  recorded for each of these cases. Figure 4.14 summarises these results in the form of neutral curves. The very clear conclusion is that onset takes place increasingly closer to the leading edge as the inclination tends towards the horizontal. The critical wavenumber also increases, showing that the wavelength of the most dangerous vortex decreases.

Table 4.2 gives the values of  $\xi_c$  and  $k_c$  for each angle of inclination. These are based upon the neutral curves shown in Figure 4.14 and are the minimum value of critical distance ( $\xi_c$ ), and the corresponding wavenumber ( $k_c$ ) for each angle of inclination. The values of  $\xi_c$  and  $k_c$  are calculated by fitting a parabolic curve between the three lowest values of  $\xi_k$  for each value of  $\alpha$  shown in Figure 4.14. Alongside these in Table 4.2 are presented scaled values of  $\xi_c$  and  $k_c$ :  $\xi_c^*$  and  $k_c^*$ , produced using the following scalings:

$$\xi_c^* = \left( \frac{\cos^2 \alpha}{\sin \alpha} \right)^{1/2} \xi_c, \text{ and } k_c^* = \left( \frac{1}{\cos \alpha} \right) k_c, \quad (4.20)$$

from Rees (2001b).

The length of domain used is varied depending on the angle of inclination. As previously discussed, for lower values of  $\alpha$  the boundary layer becomes increasingly susceptible to wave like disturbances, which while being only a transient feature increase the time taken to reach a steady state. Consequently the domain length was altered depending on the values of  $\alpha$  and  $k$  to reduce computational effort. Obviously in cases at either end of the range of wave number tested the critical distance quickly retreats far from the leading edge and judgement had to be exercised to ascertain how far it was worthwhile extending the domain in order

to capture  $\xi_c$ . It should also be noted that changing the magnitude of the constant  $A$  in Eqn. (4.18) in the range  $1 \times 10^{-7} \leq A \leq 0.01$  does not affect the value of critical distance that was calculated.

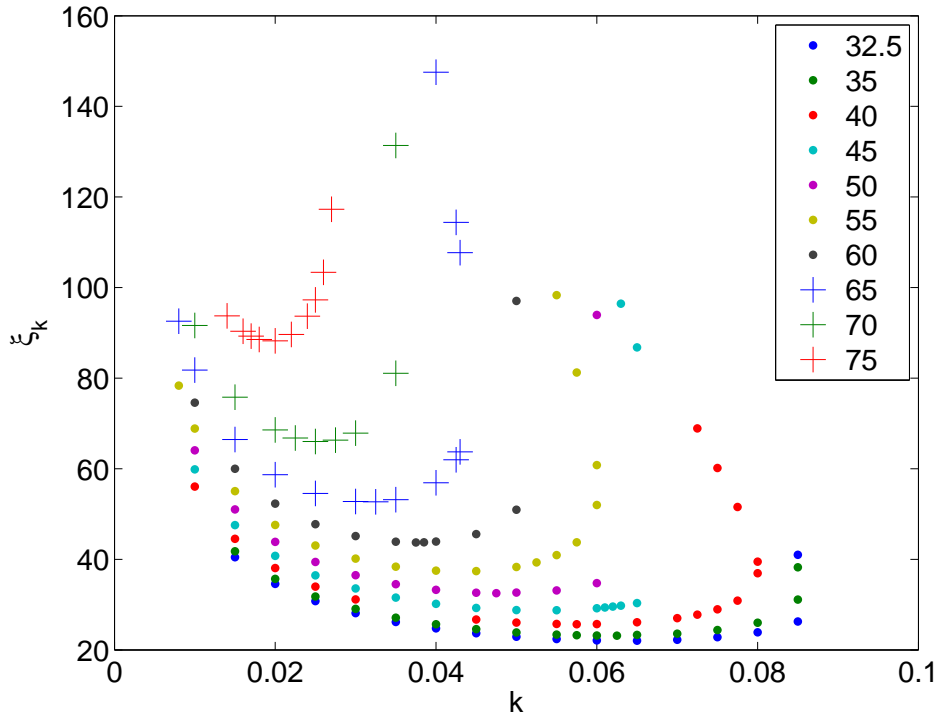


Figure 4.14: Neutral Curves, Case 2,  $32.5^\circ \leq \alpha \leq 75^\circ$ .

Figure 4.14 and Table 4.2 show that critical distances decrease with  $\alpha$ . For small values of  $\alpha$  the boundary layer is thicker for a given value of  $\xi$  because the component of the buoyancy force is proportional to  $\sin \alpha$ . Therefore heat is able to conduct further into the porous medium before being advected downstream and the boundary layer thickens. The local Rayleigh number,  $Ra_x$ , is a function of boundary layer thickness. The thickness of the boundary layer increases with

$\alpha$	$\xi_c$	$k_c$	$\xi_c^*$	$k_c^*$
32.5	22.0337	0.0635	25.35	0.075
35.0	23.1332	0.0614	25.02	0.075
40.0	25.6729	0.0575	24.53	0.075
45.0	28.7189	0.0530	24.15	0.075
50.0	32.5102	0.0474	23.88	0.074
55.0	37.3164	0.0429	23.65	0.075
60.0	43.7320	0.0375	23.50	0.075
65.0	52.6483	0.0316	23.37	0.075
70.0	65.9963	0.0256	23.29	0.075
75.0	88.1537	0.0194	23.21	0.075

Table 4.2: Comparison of the variation of  $\xi_c$ ,  $k_c$ ,  $\xi_c^*$  and  $k_c^*$  with  $\alpha$  for Case 2.

distance downstream and the relatively thicker boundary layer at low angles of inclination means threshold values of  $Ra_x$  are reached at smaller downstream distances.

The relationship between  $k_c$  and  $\alpha$  is also of interest. We recall that in the Darcy-Bénard problem the most dangerous disturbance is that which produces cells with a unit aspect ratio (Nield and Bejan (2006)). If the most unstable vortex were to have a unit (or at least a constant) aspect ratio, then its wavelength would be proportional to the boundary layer thickness. As discussed above the thickness of the layer increases with  $\alpha$  and hence the value of  $k_c$  would reduce with  $\alpha$ . However this is not supported by the results shown in Table 4.2.

At higher values of  $\alpha$  the boundary layer is thinner because of the stronger underlying flow and therefore the critical distance is increased. Consequently

the boundary layer will be much thicker in the region where disturbances start to grow. This scenario dictates that  $k_c$  should decrease with increasing  $\alpha$ , and this is supported by the results shown in Figure 4.14 and Table 4.2.

#### 4.5.4 Comparison of Elliptic and Parabolic Results for Case 2.

Figure 4.15 shows a comparison of the fully elliptic results calculated above with those produced by the linear parabolic code used in Rees (2001b) adapted slightly to take into account the vortex-forcing boundary condition. When translated into the present notation the parabolic simulations yield the following values of  $\xi_c$  and  $k_c$  which minimise  $\xi_c$ :

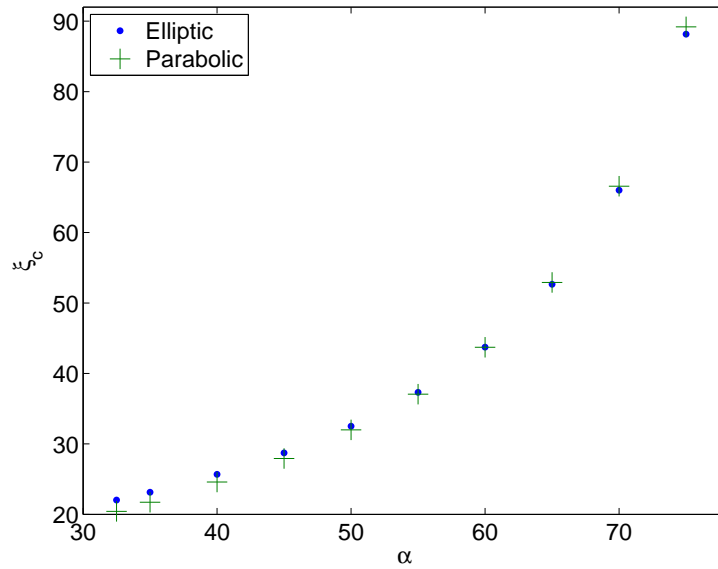
$$\xi_c = 23.49 \frac{\sqrt{\sin \alpha}}{\cos \alpha}, \quad k_c = 0.0703 \cos \alpha. \quad (4.21)$$

The agreement between the two sets of results is excellent in both  $\xi_c$  and  $k_c$ . The model used by Rees is applicable to the near-vertical boundary layer and therefore we would expect the agreement between the elliptic and parabolic model to improve as  $\alpha$  increases, which appears to be the case in Figure 4.15 and the final two columns of Table 4.2.

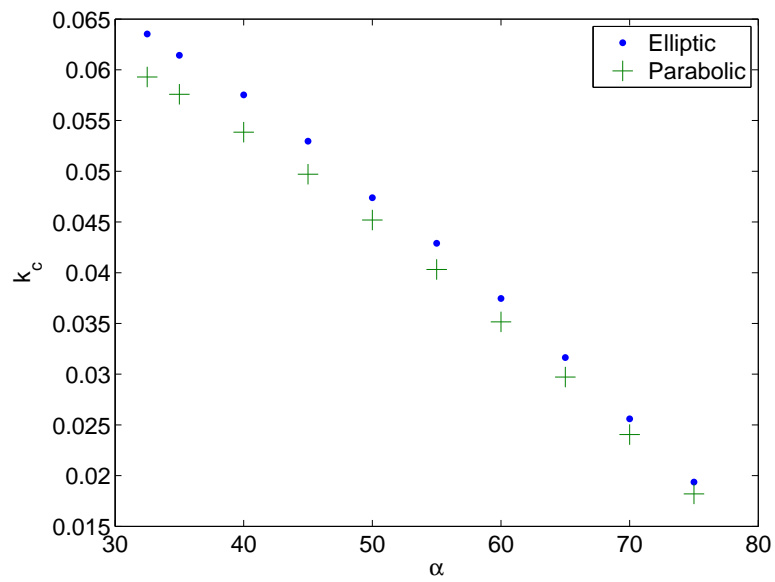
We also compare the elliptic and parabolic models by using the same scalings introduced by Rees (2001b) to collapse the neutral curves for different values of  $\alpha$  onto a single curve:

$$\xi^* = \left( \frac{\sin \alpha}{\cos^2 \alpha} \right)^{1/2} \xi, \quad \text{and, } k^* = \left( \frac{1}{\cos \alpha} \right) k, \quad (4.22)$$

and these are shown in Figure 4.16, where Figure 4.16b is a close up of Figure 4.16a in the region  $0.05 \leq k^* \leq 0.1$ . It is apparent from Figure 4.16 that for the elliptic simulation the results do not collapse onto a perfect single line.

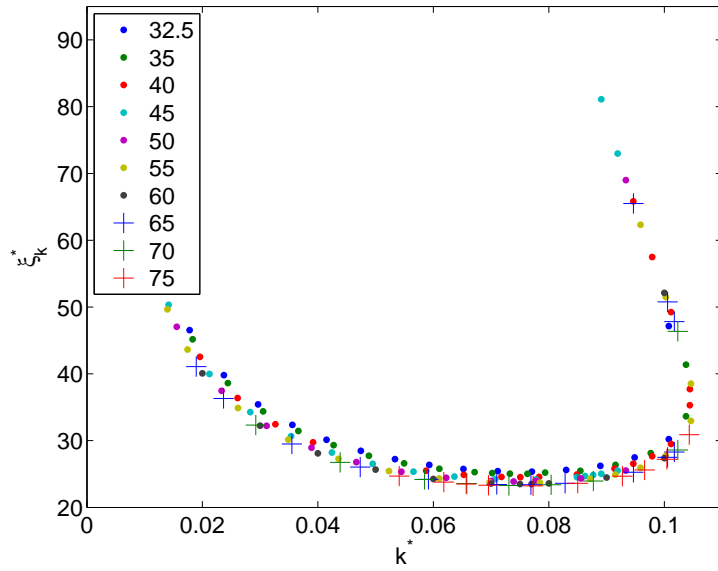


(a)

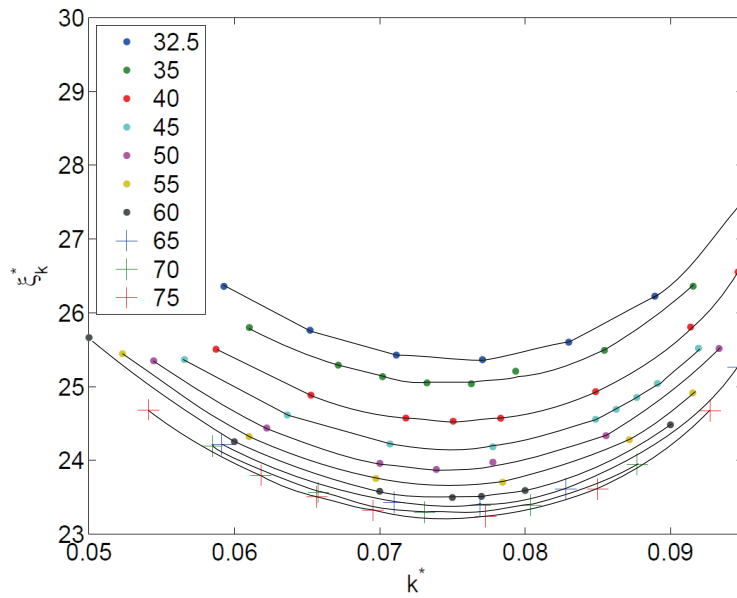


(b)

Figure 4.15: Comparison of (a)  $\xi_c$  and (b)  $k_c$  from elliptic and parabolic simulations, Case 2.



(a)



(b)

Figure 4.16: (a) Collapsed Neutral Curves for  $32.5^\circ \leq \alpha \leq 75^\circ$  showing  $\xi_k^*$  versus  $k^*$  (Case 2). (b) Close up of (a).

The elliptic simulations differ from the parabolic simulations due to the retention of the streamwise diffusion terms. We see in Figure 4.16 that for values of  $k^* \leq 0.1$  critical distances lie between a lower band formed by the  $\alpha = 75^\circ$  results and an upper band formed by the  $\alpha = 32.5^\circ$  results. Furthermore the results at each angle of inclination lie in a distinct well-defined curve, and as the angle of inclination increases, the distance between each curve decreases as a minimal curve is approached. Again given the applicability of the scalings to the near-vertical case, this is to be expected.

The results of Case 2 show very good agreement between our results and those predicted by the parabolic code, this close agreement confirms our code is working correctly and therefore increases confidence in the results from Case 1.

#### 4.5.5 Sub Harmonic Forcing

A preliminary investigation into the effect of subharmonic forcing on the temperature profile of the inclined boundary layer was carried out. Subharmonic forcing can be achieved without significant alteration to the code used so far in which the basic state has been denoted as mode 0, with the primary disturbance vortex occurring in mode 1. The primary disturbance vortex is redesignated as being that which occurs in mode 2, and four modes ( $N = 4$ ) are used in total. The subharmonic then occurs in mode 1, with a wavenumber half that of the primary vortex.

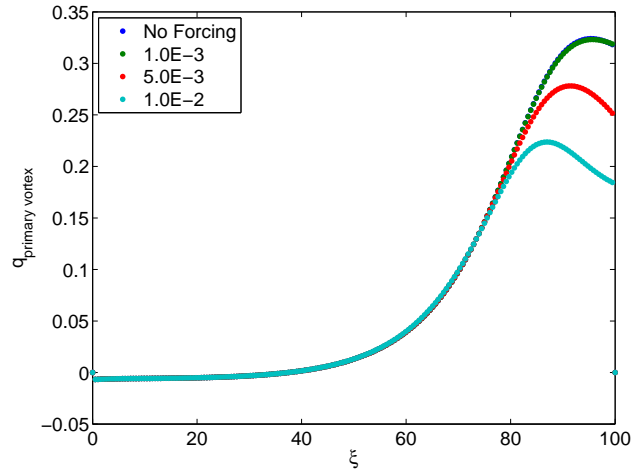
Computations have been carried out for both subharmonic destabilisation of the already established Case 2 steady state and for destabilisation of the basic state with a forced vortex in mode 2 and were found to be identical. The results presented in this section are for the latter case and the initial conditions are then

$$\theta_1 = Ae^{-\eta^2} \text{ and } \theta_2 = 0.01e^{-\eta^2} \quad (4.23)$$

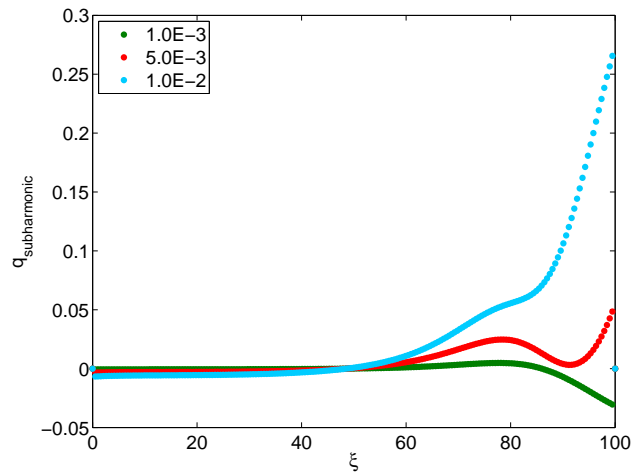
for  $0 \leq \eta < \eta_{\max}$ , giving rise to the boundary conditions  $\theta_1 = A$  and  $\theta_2 = 0.01$  at  $\eta = 0$ , where  $A$  is the amplitude of the subharmonic forcing.

Figures 4.17 and 4.18 show the surface rate of heat transfer when  $\alpha = 55^\circ$  for the primary vortex mode and subharmonic mode as a function of  $\xi$ . For a primary vortex with  $k = 0.04$  we see in Figure 4.17 the effect of subharmonic forcing is to destabilise the vortex pattern resulting in the decline in heat transfer occurring earlier with respect to  $\xi$ . Therefore the maximum value of  $q$  attained is reduced, although the difference between  $A = 0$  and  $A = 1 \times 10^{-3}$  is so small as to render the two lines indistinguishable in (a). For  $k = 0.0575$ , shown in Figure 4.18, the effect is opposite, with subharmonic forcing causing an increase in heat transfer and much larger values of  $q$ ; these maxima occur at lower  $\xi$  as the size of the subharmonic forcing is increased. In both cases  $\xi_k$  is unaffected by the subharmonic forcing as would be expected; the wavelength of the subharmonic disturbance is  $k = 0.02$  when  $k = 0.04$ , and the neutral curve in Figure 4.14 shows that the critical distance for disturbances with  $k = 0.02$  is greater than that for  $k = 0.04$ . A similar argument applies to the  $k = 0.0575$  case.

It would be of interest to examine a further range of  $\alpha$  and  $k$  to better understand the effects of subharmonic forcing. However the presence of the subharmonic forcing term amplifies the travelling waves which occur immediately after the initial perturbation and therefore results in a much longer time to reach the steady state. Consequently further investigation into this aspect of the flow behaviour has not been possible within the current timeframe.

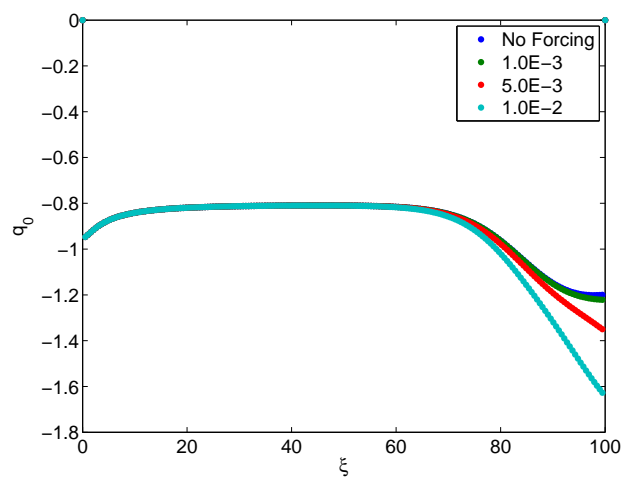


(a)



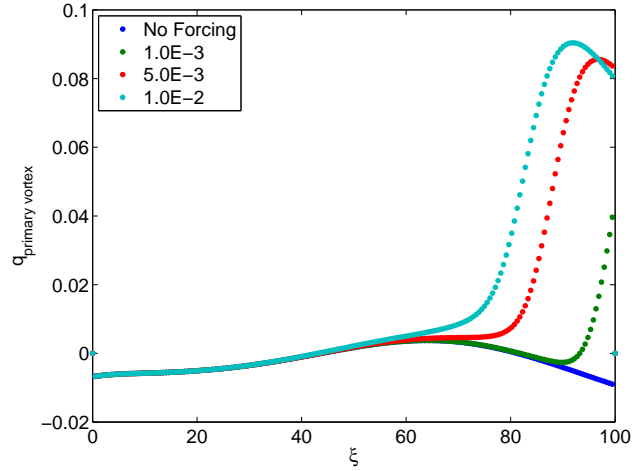
(b)

Figure 4.17: Surface heat transfer profiles for  $\alpha = 55^\circ$ ,  $k_2 = 0.04$  for  $A = 0$ , (no forcing),  $0.001$ ,  $0.005$ ,  $0.01$  in Eqn. (4.23) (a) primary vortex mode (mode 2), (b) subharmonic mode (mode 1) and (c) basic state (mode 0).  $k_2$  is the wavenumber of the primary vortex.

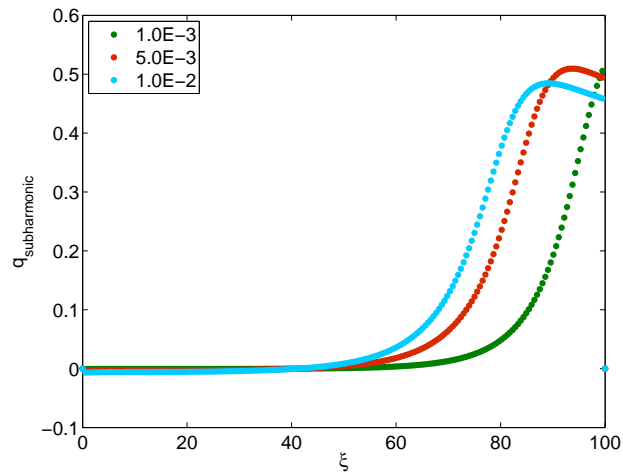


(c)

Figure 4.17: (*Cont.*) Surface heat transfer profiles for  $\alpha = 55^\circ$ ,  $k_2 = 0.04$  for  $A = 0$ , (no forcing), 0.001, 0.005, 0.01 in Eqn. (4.23) (a) primary vortex mode (mode 2), (b) subharmonic mode (mode 1) and (c) basic state (mode 0).  $k_2$  is the wavenumber of the primary vortex.

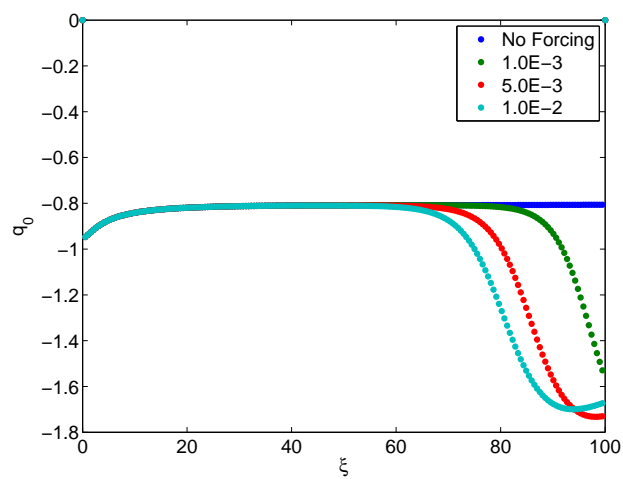


(a)



(b)

Figure 4.18: Surface heat transfer profiles for  $\alpha = 55^\circ$ ,  $k_2 = 0.0575$  for  $A = 0$ , (no forcing), 0.001, 0.005, 0.01 in Eqn. (4.23) (a) primary vortex mode (mode 2), (b) subharmonic mode (mode 1) and (c) basic state (mode 0).  $k_2$  is the wavenumber of the primary vortex.



(c)

Figure 4.18: (*Cont.*) Surface heat transfer profiles for  $\alpha = 55^\circ$ ,  $k_2 = 0.0575$  for  $A = 0$ , (no forcing), 0.001, 0.005, 0.01 in Eqn. (4.23) (a) primary vortex mode (mode 2), (b) subharmonic mode (mode 1) and (c) basic state (mode 0).  $k_2$  is the wavenumber of the primary vortex.

## 4.6 Case 3 - Leading Edge Forced Vortices

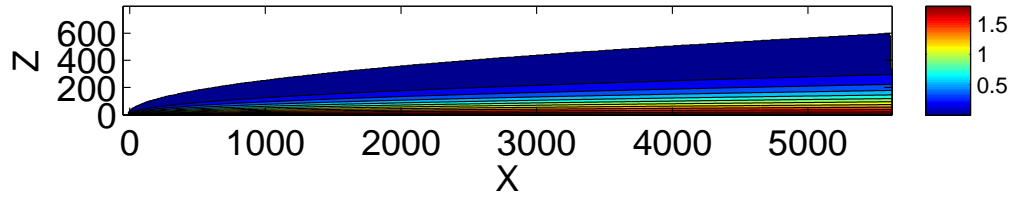
A localised disturbance near the leading edge is generated using the following profile for  $\theta_1$ :

$$\theta_1 = 0.01e^{-\eta^2} e^{-a\xi^2}, \text{ for } 0 \leq \xi \leq \xi_{\max}, \text{ and } 0 \leq \eta \leq \eta_{\max}. \quad (4.24)$$

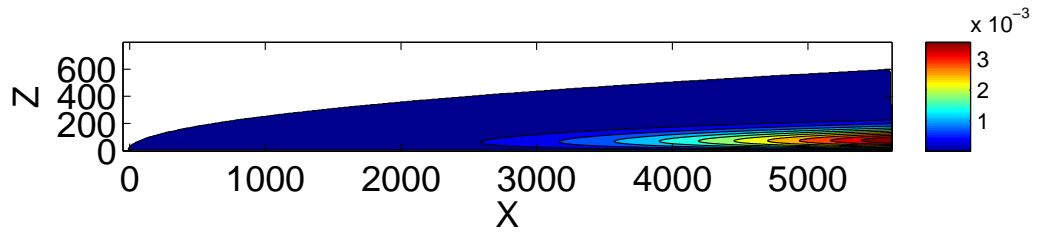
As in Case 2, the presence of the forcing boundary condition at  $\eta = 0$  leads to steady flow, which differs from that of the basic steady state. Figure 4.19 shows an example of this flow when  $\alpha = 55^\circ$ ,  $k = 0.04$  and  $a = 0.1$ . When compared with Figures 4.11c and 4.11d, which show contours of  $\theta_0$  and  $\theta_1$  for Case 2 at the same angle of inclination and wavenumber, we see that growth is much weaker in the case of the isolated disturbance.

Figure 4.20 shows the surface rate of heat transfer profile,  $q_1$  for a range of values of  $a$  used in the initial condition given by (4.24). The profiles all show the same behaviour: the initial disturbance dies away, but then begins to grow again at a location further downstream. The initial decay is due to the fact the disturbance is imposed upstream of the critical distance and once the critical distance is passed, the disturbance which has been propagating downstream then begins to be amplified. The rate of growth following the region of decay is inversely proportional to  $a$ , with smaller values of this parameter leading to a higher rate of growth. At the point where  $\partial q_1 / \partial \xi = 0$  the disturbance is neither growing nor decaying, i.e. it is marginally stable, and this is taken as the critical distance,  $\xi_k$ . Table 4.3 shows the value of  $\xi_k$  against  $a$  when  $\alpha = 55^\circ$  and  $k = 0.04$ . This shows that  $\xi_k$  is independent of  $a$ , as would be expected provided the disturbance has been imposed sufficiently far upstream of  $\xi_k$ .

Given the independence of  $\xi_k$  with respect to the parameter  $a$ , further simula-



(a)



(b)

Figure 4.19: Contours of (a)  $\theta_0$  and (b)  $\theta_1$ ,  $k = 0.04$ ,  $a = 0.1$ , and  $\alpha = 55^\circ$ , Case 3.

$a$	$\xi_k$
0.1	33.5403
0.5	33.5392
1.0	33.5391
5.0	33.5390
10.0	33.5390

Table 4.3:  $\xi_k$  for differing values of  $a$  when  $\alpha = 55^\circ$  and  $k = 0.04$ .

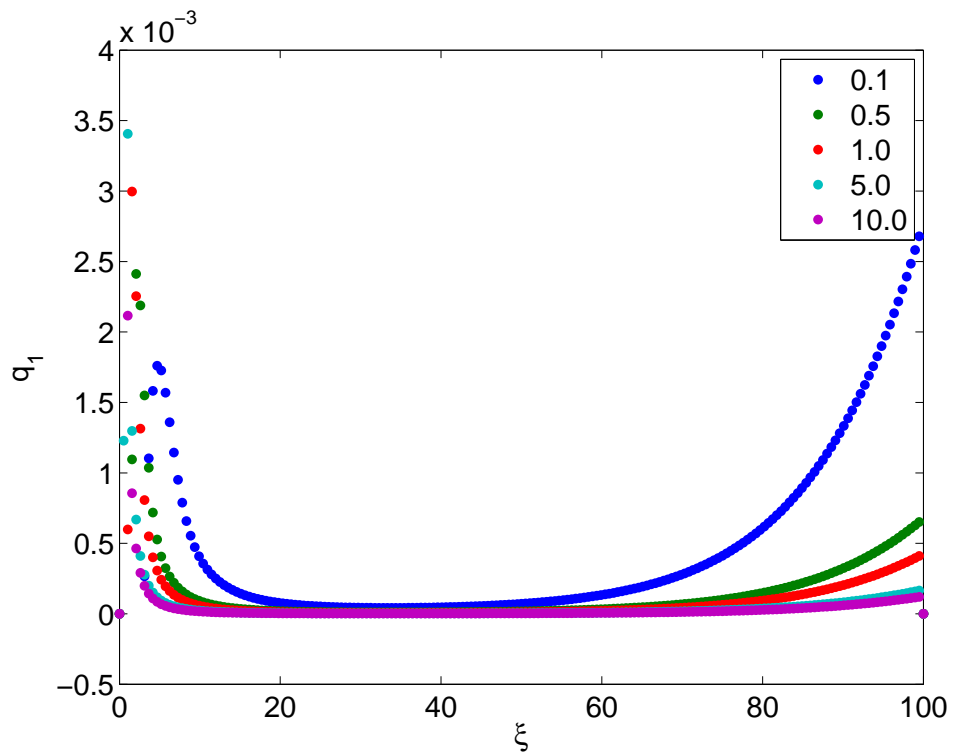


Figure 4.20: Surface Rate of Heat Transfer,  $q_1$  profile, for different values of  $a$ .

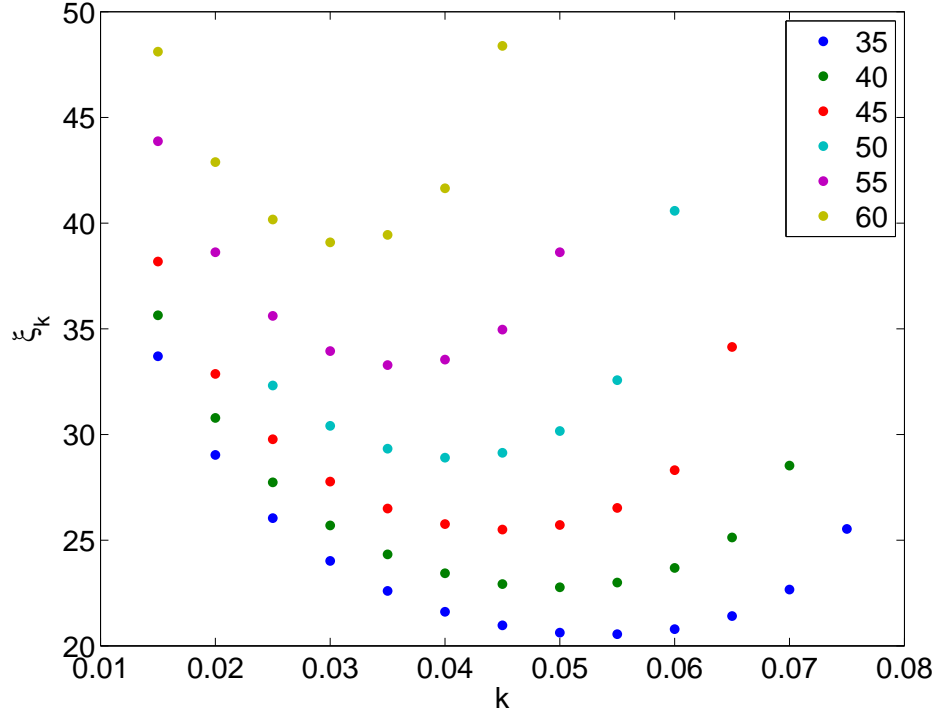


Figure 4.21: Neutral Curves, Case 3,  $35^\circ \leq \alpha \leq 60^\circ$ .

tions were undertaken for a wide range of values of  $\alpha$  and  $k$  and a fixed value of  $a = 1.0$ . The values of  $\xi_k$  were recorded in each case and the results are summarised in the form of neutral curves in Figure 4.21. As in Case 2, the trend is for  $\xi_c$  to increase and  $k_c$  to decrease with  $\alpha$ .

Again the elliptic and parabolic cases may be compared using the scalings from Rees (2001b), as given by Eqn. (4.22). The results of this rescaling are shown in Figure 4.22. As for Case 2 the results do not collapse onto a single perfect line, but do lie in a distinct well-defined curve for each angle of inclination. Again as the angle of inclination increases, the distance between each curve decreases as a

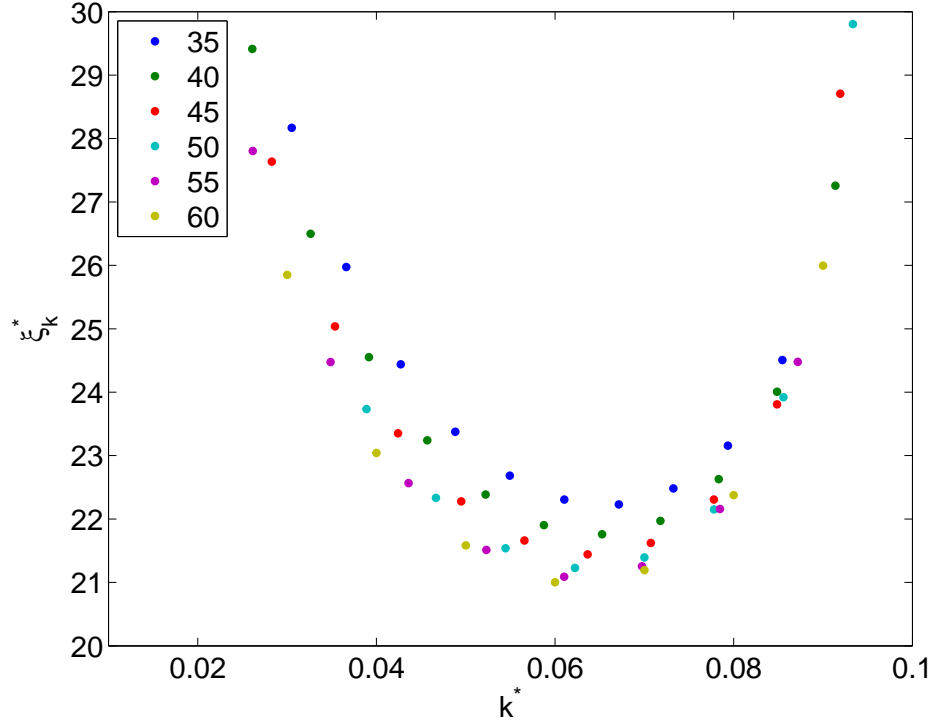


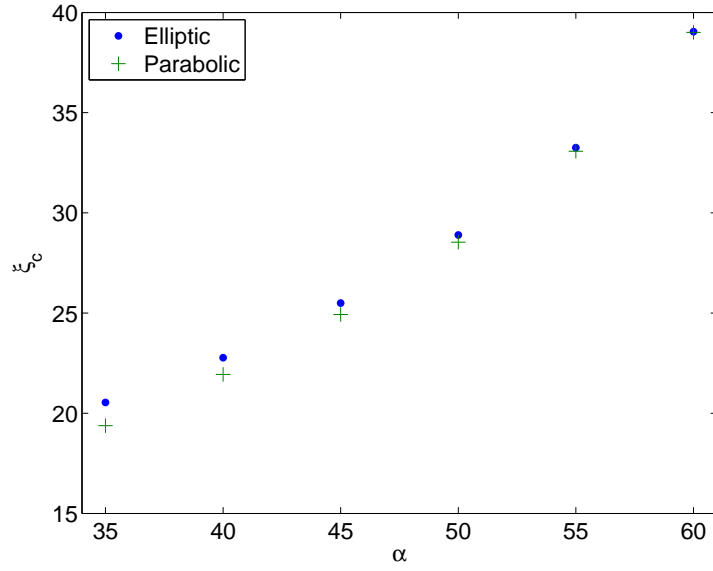
Figure 4.22: Collapsed Neutral Curves, Case 3,  $35^\circ \leq \alpha \leq 60^\circ$ .

minimal curve is approached.

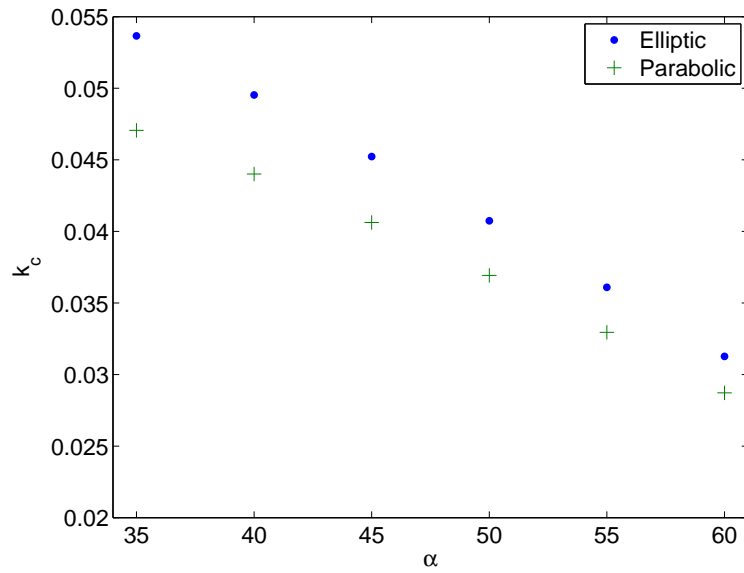
Figure 4.23 shows the minimum critical distance,  $\xi_c$ , and the corresponding wavenumber,  $k_c$ , for each angle of inclination examined, also included are values of  $\xi_c$  and  $k_c$  calculated using the results of Rees (2001b), which in the present notation give:

$$\xi_c = 20.95 \frac{\sqrt{\sin \alpha}}{\cos \alpha}, \quad k_c = 0.0574 \cos \alpha. \quad (4.25)$$

Table 4.4 gives the values of  $\xi_c$  and  $k_c$  as depicted in Figure 4.23, along with the scaled values of  $\xi_c^*$  and  $k^*$ . Again agreement between the parabolic and elliptic results improves with increasing angle of inclination, which is to be expected



(a)



(b)

Figure 4.23: Values of (a)  $\xi_c$  and (b)  $k_c$  against  $\alpha$ , Case 3.

$\alpha$	$\xi_c$	$k_c$	$\xi_c^*$	$k_c^*$
35	20.54	0.054	22.22	0.065
40	22.77	0.050	21.76	0.065
45	25.50	0.045	21.44	0.064
50	28.90	0.041	21.22	0.064
55	33.26	0.036	21.08	0.063
60	39.04	0.031	20.98	0.062

Table 4.4: Comparison of the variation of  $\xi_c$ ,  $k_c$ ,  $\xi_c^*$  and  $k_c^*$  with respect to  $\alpha$  for Case 3.

given the applicability of the parabolic results to the near vertical case.

Critical distances are reduced for Case 2 when compared to Case 3. This is a result of the slightly different methods used to calculate the critical distance: Case 3 critical distances are based on the turning point of  $q_1$  whereas Case 2 critical distances indicate where  $q_1$  exceeds a threshold value.

## 4.7 Conclusions

The stability of an inclined thermal boundary layer to vortex disturbances has been investigated for three cases, which differ in respect of the boundary and/or initial conditions which have been imposed. The basic steady state for a range of  $\alpha$  has been calculated and heat transfer profiles produced. These profiles demonstrate that the flow does not become self similar until a significant downstream distance has been reached, when  $\alpha = 75^\circ$  this distance is  $\xi = 64.89$ ,  $x = 1052.68$ .

In Case 1a it was found that a global disturbance grows in strength but is even-

tually advected out of the domain. This would indicate that streamwise diffusion in the upstream direction failed to overcome the underlying flow.

Case 1b examined the evolution of an isolated disturbance, and upstream diffusion effects were identified with the speed of the trailing edge of the disturbance being reduced in comparison with that of the leading edge. However these results did indicate that the flow was unlikely to become absolutely unstable at increased distances downstream. For Case 1 the boundary layer was found to be convectively unstable to vortex disturbances in the range  $35^\circ \leq \alpha \leq 60^\circ$ ,  $k \leq 0.01$  and  $50 \leq \xi_{\max} \leq 100$ .

In Case 2 a forced vortex system is generated based upon a periodic variation in the boundary condition. This forced vortex system leads to a steady state flow which differs from the basic steady state. Neutral curves showing  $\xi_k$  against  $k$  have been generated for values of  $k$  and  $\alpha$  in the range  $0.01 \leq k \leq 0.09$ ,  $32.5^\circ \leq \alpha \leq 75^\circ$ . Values of minimum critical distance,  $\xi_c$ , and its corresponding wavenumber,  $k_c$ , were identified for each angle of inclination. It was found that  $\xi_c$  increases and  $k_c$  decreases as  $\alpha$  increases. Comparison with the parabolic model of Rees (2001b) was excellent although the effect of upstream diffusion which is only present in the elliptic model can be seen and is more pronounced at lower  $\alpha$ . An initial investigation into the effects of subharmonic forcing demonstrates its destabilising effect on the vortex disturbances but further investigation is required to understand better this aspect of boundary layer behaviour.

Case 3 investigates the evolution of a forced vortex system based upon a localised disturbance near the trailing edge. Again this forced vortex system leads to a steady state flow which differs from the basic steady state flow. Heat transfer profiles show a region of decay in the strength of the vortex disturbance im-

mediately downstream of the location to which it is applied. However this region of decay is followed by growth further downstream. The critical distance is identified, and shown to be independent of the profile of the leading edge disturbance provided the disturbance is located upstream of the critical distance. Neutral curves are produced, and as in Case 2, show  $\xi_c$  increasing and  $k_c$  decreasing with  $\alpha$ . Comparison of the elliptic results with those of the parabolic model of Rees (2001b) is again excellent.

## 4.8 Further Work

This work has found the boundary layer to be convectively unstable to vortex disturbances in the range  $35^\circ \leq \alpha \leq 60^\circ$ ,  $k \leq 0.01$  and  $50 \leq \xi_{\max} \leq 100$ . However, much work remains to be done before a truly definitive statement on the nature of the flow may be made. The size of the computational domain, and the length of time for which simulations run could all be increased should computational resources allow, and this would permit an examination of a wider range of angles of inclination. Ultimately, whilst much effort has been expended to validate the numerical model, experimental data with which to compare its results would also be required before it can be considered completely reliable.

In terms of expanding the scope of the work a preliminary investigation into subharmonic forcing has also been undertaken, and produced some interesting results, but there remains much more to be done on this topic. Also, given the interest in topics such as Carbon Capture and Storage (CCS), it may prove useful to expand the model in the future to include aspects of flow behaviour such as chemical reactions and double diffusion.

## Chapter 5

# Front Propagation in the Darcy-Bénard Problem

This chapter describes an exploratory study into the way in which a disturbance in the form of a propagating convective front spreads in a Darcy-Bénard layer. Ahead of the front lies a quiescent region with no flow, while behind the front is a steady weakly nonlinear or strongly nonlinear convection pattern. Bringing front propagation theory to bear on this problem for the first time, the aim of this work is to outline some of the key features of this phenomenon in porous media. We start by presenting some key elements of front propagation theory, followed by the equations of motion for the Darcy-Bénard problem. Weakly nonlinear theory is then used to analyse the speed of propagation and pattern selection in the two-dimensional Darcy-Bénard problem. The effect of initial conditions on these criteria is also analysed. These results are compared with those of a nonlinear two dimensional finite difference scheme.

The investigation is then expanded to three-dimensions and weakly nonlinear

theory is used to determine the relative speeds at which fronts composed of transverse and longitudinal rolls propagate. A three-dimensional nonlinear finite difference model is used to investigate the form of the front as the Darcy-Rayleigh number  $Ra$  increases from its critical value  $Ra_c = 4\pi^2$ . Finally a brief summary of the key conclusions reached by this study is given.

## 5.1 Introduction to Front Propagation

Front propagation in the context of the Darcy-Bénard problem describes the situation where a thermal disturbance spreads horizontally across a porous layer into the unstable, quiescent state consisting of a temperature field which decreases linearly with height. The speed at which the disturbance propagates and the profile of the flow which is established in the wake of the propagating front has ramifications for the heat transfer properties of the porous layer. Moreover, as there is no underlying flow in the Darcy-Bénard problem, an indication of the speed at which a disturbance can propagate in a porous medium through the mechanisms of conduction and convection alone may be obtained.

One-dimensional front propagation in the clear-fluid analogue of the Darcy-Bénard problem, the Rayleigh-Bénard problem, has been examined numerically by Getling (1992). Fineberg and Steinberg (1987) and Lucke et al (1987) conducted experimental and numerical investigations respectively of the same problem in two dimensions. Kockelkoren et al (2003) examined front propagation in the Rayleigh-Bénard problem in the context of the universal front propagation theory developed by authors such as Ebert and van Saarloos (1998) and van Saarloos (2003). To the author's knowledge no study of front propagation, neither

experimental nor numerical, has been carried out for the Darcy-Bénard problem. Experimental work in this case presents a number of difficulties, not the least of which the need to maintain the unstable state in advance of the front for long periods of time in the presence of destabilising effects such as noise or small amplitude heterogeneities in the porous structures.

### **5.1.1 Front Propagation Theory**

Much effort has been expended in the field of front propagation in order to understand whether the speed and shape of a front, as well as the pattern it leaves in its wake, are intrinsic properties of the system and if so, how they may be predicted and understood. Fronts are classified into either “pulled” or “pushed” based upon the way in which they spread. In the former, the propagation speed is completely described by the behaviour of the leading edge where the amplitudes are small and consequently the properties of such a front may be determined by a linear spreading analysis. In this case the small-amplitude leading edge is pulling the whole nonlinear front forward. For a “pushed” front the full nonlinear equations are required to describe the behaviour and the name of this regime arises from the idea that the front is being pushed by the large amplitude region close to and behind the front (Cross and Greenside (2009), van Saarloos (2003)) .

The flow pattern left in the wake of a front may be termed as uniformly translating, coherent pattern forming or incoherent pattern forming, depending on whether the amplitude of the disturbance behind the front is uniform, periodically varying, or chaotic respectively (van Saarloos (2003)).

### 5.1.2 The Unifying Theory for “Pulled” Fronts

The unifying theory of Ebert and van Saarloos (Ebert and van Saarloos, 1998) shows that for “pulled” fronts the relaxation of both the front velocity,  $v$ , and the wavenumber of any pattern behind the front,  $k$ , towards their asymptotic values at large time ( $v_{as}$ ,  $k_{as}$ ) may be described algebraically. This is a slow relaxation to  $v_{as}$  with leading order terms  $1/t$  and  $1/t^{2/3}$ . The third term in the series is of  $O(1/t^2)$  and is dependent upon the initial conditions. Provided that the initial profile of a front is “sufficiently steep”, it will converge to a unique shape and velocity at large time (van Saarloos (2003)).

### 5.1.3 Front Propagation in the Rayleigh-Bénard Problem

Front propagation in the two-dimensional Rayleigh-Bénard problem has been studied using the Newell-Whitehead-Segel (NWS) amplitude equation (Getling (1992), Kockelkoren et al (2003), van Saarloos (2003)):

$$\tau_{\text{ref}} A_T = \varepsilon A + \xi_{\text{ref}}^2 A_{XX} - \vartheta |A|^2 A. \quad (5.1)$$

The coefficients  $\tau_{\text{ref}}$ ,  $\xi_{\text{ref}}$  and  $\vartheta$  are a problem-specific timescale, lengthscale and nonlinear saturation parameter respectively, while  $\varepsilon$  is the relative supercriticality. Eqn. (5.1) may be rescaled using the following parameters:

$$x = \frac{\varepsilon^{1/2}}{\xi_{\text{ref}}} X, \text{ and } t = \frac{\varepsilon}{\tau_{\text{ref}}} T. \quad (5.2)$$

After substitution of  $A = \sqrt{\varepsilon \vartheta} F$ , Eqn. (5.1) takes the form:

$$F_t = F + F_{xx} - |F|^2 F. \quad (5.3)$$

Getling (1992) identified an exact solution of Eqn. (5.3) in the form:

$$F = \frac{1}{2} [1 - \tanh[c_1(x - c_2t)]] \quad (5.4)$$

where  $c_1 = 1/2\sqrt{2}$  and the propagation speed is  $c_2 = 3/\sqrt{2}$ . However, numerical calculation of the front speed found that  $v_{as} = 2$  regardless of the initial conditions. This is because the front profile given by the exact solution is not maintained with increasing time. As the profile of the front evolves its velocity tends towards 2; the solution given by Eqn. (5.4) is exact but unstable. The initial velocity for a front governed by the NWS equation is strongly dependent on the width of the front given by the initial conditions, with wider initial fronts propagating faster at first. However these different profiles converge at large time to a definite speed,  $v_{as} = 2$  (Getling (1992)).

When observed experimentally, the advancing front in Rayleigh-Bénard convection is not uniformly translating, but coherent pattern forming, with convection cells formed in its wake (Fineberg and Steinberg (1987)). In such cases front propagation acts as a natural method for pattern selection (Montange et al, 1994). The wavenumber of the pattern behind the front relaxes towards an asymptotic value  $k_{as}$ . The rate of relaxation decreases with increasing length of the region covered by the pattern (Getling (1992)). An increase in the length of pattern behind the front implies the existence of more rolls and therefore increased inertia must be overcome before a wavenumber adjustment can occur. Adjustment occurs faster at lower values of Ra because the front propagation speed is reduced, therefore the front is narrower and there is less inertia to overcome. The NWS equation cannot be used to model pattern selection behind the front, instead higher order equations such as the Swift-Hohenberg equation are required (Kockelkoren et al (2003)).

The two-dimensional Rayleigh-Bénard problem, which has a critical Rayleigh

number of  $Ra_c = 1708$  (Tritton (1988)), has been examined experimentally by Fineberg and Steinberg (1987) in the range  $1708.68 \leq Ra \leq 2135$ . The experiment was designed to avoid inducing longitudinal rolls, and therefore the propagating front in this case consisted of two-dimensional transverse rolls. A re-examination of this experimental work by Kockelkoren et al (2003) found evidence of the slow relaxation towards  $v_{as} = 2$  as predicted by the unifying theory. Lucke et al (1987) used the 2D Oberbeck-Boussinesq equations to examine numerically the range  $1725 \leq Ra \leq 2049$ , for a box with an aspect ratio of 25 : 1. The speed of the front was found to be within 10% of that predicted by marginal stability theory. The wavenumber,  $k$ , of the pattern behind the front was also found to increase with increasing Rayleigh number. The drawback of both these investigations (experimental and numerical) is the necessarily small domain size they investigated, especially in terms of modelling wavenumber relaxation accurately. The wavenumber increase found by Lucke et al (1987) is possibly a symptom of the slower relaxation experienced by the higher Ra fronts as a consequence of their increased width (Getling (1992)).

## 5.2 Equations of Motion

We consider a horizontal, fully saturated porous layer, the height of which is very much less than the width and length. The flow domain for such a layer is shown in Figure 5.1. The boundary condition  $T_1 > T_2$  gives an unstable, stationary basic state where cooler denser fluid lies above that which is hotter and less dense. Assuming that Darcy's Law and the Boussinesq approximation both apply, that inertia effects are negligible and that the fluid and solid phases are in local thermal

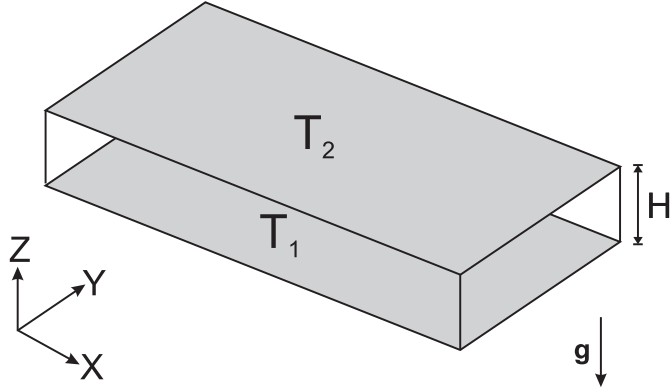


Figure 5.1: Diagram of the flow domain for the Darcy-Bénard problem.

equilibrium, the governing equations are;

$$\frac{\partial U}{\partial X} + \frac{\partial V}{\partial Y} + \frac{\partial W}{\partial Z} = 0, \quad (5.5)$$

$$U = -\frac{K}{\mu} \frac{\partial P}{\partial X}, \quad (5.6)$$

$$V = -\frac{K}{\mu} \frac{\partial P}{\partial Y}, \quad (5.7)$$

$$W = -\frac{K}{\mu} \left[ \frac{\partial P}{\partial Z} - \rho_{\infty} g \beta (T - T_{\infty}) \right], \quad (5.8)$$

$$\sigma \frac{\partial T}{\partial t} + U \frac{\partial T}{\partial X} + V \frac{\partial T}{\partial Y} + W \frac{\partial T}{\partial Z} = \kappa \left[ \frac{\partial^2 T}{\partial X^2} + \frac{\partial^2 T}{\partial Y^2} + \frac{\partial^2 T}{\partial Z^2} \right]. \quad (5.9)$$

These equations are nondimensionalised using the same scalings as in Sect. 2.5, where the lengthscale  $L$  is now given by the height of the layer. This gives

$$\frac{\partial u}{\partial x} + \frac{\partial v}{\partial y} + \frac{\partial w}{\partial z} = 0 \quad (5.10)$$

$$u = -\frac{\partial p}{\partial x}, \quad (5.11)$$

$$v = -\frac{\partial p}{\partial y}, \quad (5.12)$$

$$w = -\frac{\partial p}{\partial z} + \text{Ra} \theta, \quad (5.13)$$

$$\frac{\partial \theta}{\partial t} + u \frac{\partial \theta}{\partial x} + v \frac{\partial \theta}{\partial y} + w \frac{\partial \theta}{\partial z} = \nabla^2 \theta, \quad (5.14)$$

where

$$\text{Ra} = \frac{\rho_\infty g \beta \Delta T L K}{\mu \kappa}. \quad (5.15)$$

The system is subject to the boundary conditions

$$z = 0: \quad \theta = 1, w = 0, \frac{\partial p}{\partial z} = \text{Ra}, \quad (5.16)$$

$$z = 1: \quad \theta = 0, w = 0, \frac{\partial p}{\partial z} = 0. \quad (5.17)$$

This pressure-temperature formulation is employed in the weakly nonlinear analysis as described in Sect. 5.3 for two dimensions and Sect. 5.5 for three dimensions. The pressure boundary conditions are all Neumann conditions which can lead to numerical difficulties, so for the numerical studies described in Sect. 5.4 and Sect. 5.6 the velocity potential formulation is employed. The velocity poten-

tial is explained in Sect. 2.5.2, and gives rise to the following governing equations:

$$\nabla^2 \phi^{(1)} = -\text{Ra} \frac{\partial \theta}{\partial y}, \quad (5.18)$$

$$\nabla^2 \phi^{(2)} = \text{Ra} \frac{\partial \theta}{\partial x}, \quad (5.19)$$

$$\nabla^2 \phi^{(3)} = 0, \quad (5.20)$$

$$\frac{\partial \theta}{\partial t} = \nabla^2 \theta + \frac{\partial(\phi^{(1)}, \theta)}{\partial(y, z)} + \frac{\partial(\phi^{(2)}, \theta)}{\partial(z, x)} + \frac{\partial(\phi^{(3)}, \theta)}{\partial(x, y)}. \quad (5.21)$$

The system is subject to the boundary conditions

$$z = 0: \quad \theta = 1, \phi^{(1)} = \phi^{(2)} = \frac{\partial \phi^{(3)}}{\partial z} = 0 \quad (5.22)$$

$$z = 1: \quad \theta = 0, \phi^{(1)} = \phi^{(2)} = \frac{\partial \phi^{(3)}}{\partial z} = 0 \quad (5.23)$$

The boundary conditions on the extremes of  $x$  and  $y$  vary depending on whether the evolution of two dimensional cells or longitudinal vortices is being modelled, and are specified in the respective sections below. Two-dimensional flows (in  $x, z$ ) correspond to  $\phi^{(1)} = \phi^{(3)} = 0$ , and  $\phi^{(2)}$  is then the usual 2D streamfunction.

### 5.3 Weakly Nonlinear Analysis: 2D Front Propagation

Weakly nonlinear analysis is conducted to analyse the speed at which a 2D cell pattern propagates into the unstable basic state at values of  $\text{Ra}$  slightly above the critical value. The analysis which is outlined in Appendix B gives rise to the amplitude equation - Eqn. (5.24), which is a differently scaled version of the NWS equation, Eqn. (5.1).  $A(X, \tau)$  is the amplitude of the disturbance, where  $X$  is the

slow length scale and  $\tau$  is a scaled time based upon the disturbance growth.

$$\frac{\partial A}{\partial \tau} = \text{Ra}_2 A + 4 \frac{\partial^2 A}{\partial X^2} - A^3. \quad (5.24)$$

Rescaling using

$$\xi = \left( \frac{\text{Ra}_2}{4} \right)^{1/2} X \quad (5.25)$$

and substituting into Eqn. (5.24) gives

$$\frac{\partial A}{\partial \tau} = \text{Ra}_2 A + \text{Ra}_2 \frac{\partial^2 A}{\partial \xi^2} - A^3. \quad (5.26)$$

We let  $A = \sqrt{\text{Ra}_2} F$ , and substitute into Eqn. (5.26). Division by the common factor  $\text{Ra}_2 \sqrt{\text{Ra}_2}$  and rescaling with respect to time using

$$\hat{\tau} = \text{Ra}_2 \tau, \quad (5.27)$$

gives the Stuart-Landau equation in canonical form,

$$\frac{\partial F}{\partial \tau} = F + \frac{\partial^2 F}{\partial \xi^2} - F^3, \quad (5.28)$$

where the circumflex has been dropped for simplicity. Given that the two dimensional weakly nonlinear analysis reduces to this form, which is the same as that which describes front propagation in the Rayleigh-Bénard problem, the remaining work in this section is simply a confirmation of the work of others such as Getling (1992) but is included here for completeness.

### 5.3.1 Numerical Calculation of Speed of Propagation

Eqn. (5.28) will be solved numerically to determine the evolution of  $F$  across the domain, and from this the speed of propagation of the front is determined. The

equation is discretised spatially using second order accurate central differences; see Sect. 3.1.2. The boundary condition

$$\frac{\partial F}{\partial \xi} = 0 \text{ at } \xi = 0, \quad (5.29)$$

is imposed and may also be regarded as a symmetry condition. A second order accurate Runge-Kutta scheme is used to advance the solution in time. This scheme is used to discretise the time derivative of a variable  $\zeta$  with respect to time based upon;

$$\frac{\partial \zeta}{\partial \tau} = f(\tau, \zeta) \quad (5.30)$$

$$\zeta_{n+1} = \zeta_n + \frac{1}{2}(\chi_1 + \chi_2), \quad (5.31)$$

where the subscript  $n$  denotes the timestep and

$$\chi_1 = \delta \tau f(\tau_n, \zeta_n), \quad (5.32)$$

$$\chi_2 = \delta \tau f(\tau_{n+1}, \zeta_n + \chi_1). \quad (5.33)$$

Given that  $F$  will vary from zero ahead of the front to 1 behind the front, the leading edge is defined at each timestep as being the location where  $F = 0.5$ . This may lie between two computational points so it is necessary to interpolate either in  $\xi$  or  $\tau$  to locate the front precisely. Following experimentation it was found that it was preferable to calculate the value of  $\tau$  at which the value of  $F$  at the node closest to the advancing front reaches 0.5, rather than the value of  $\xi$  at which  $F = 0.5$  for a given time. The former method yields a much smoother curve than the latter.

The simulation is run and it produces a history of the front location,  $(\xi^f)$ , against time,  $(\tau)$ . The velocity is then calculated using central differences:

$$v_\tau = \frac{\xi_{\tau+\delta\tau}^f - \xi_{\tau-\delta\tau}^f}{2\delta\tau}. \quad (5.34)$$

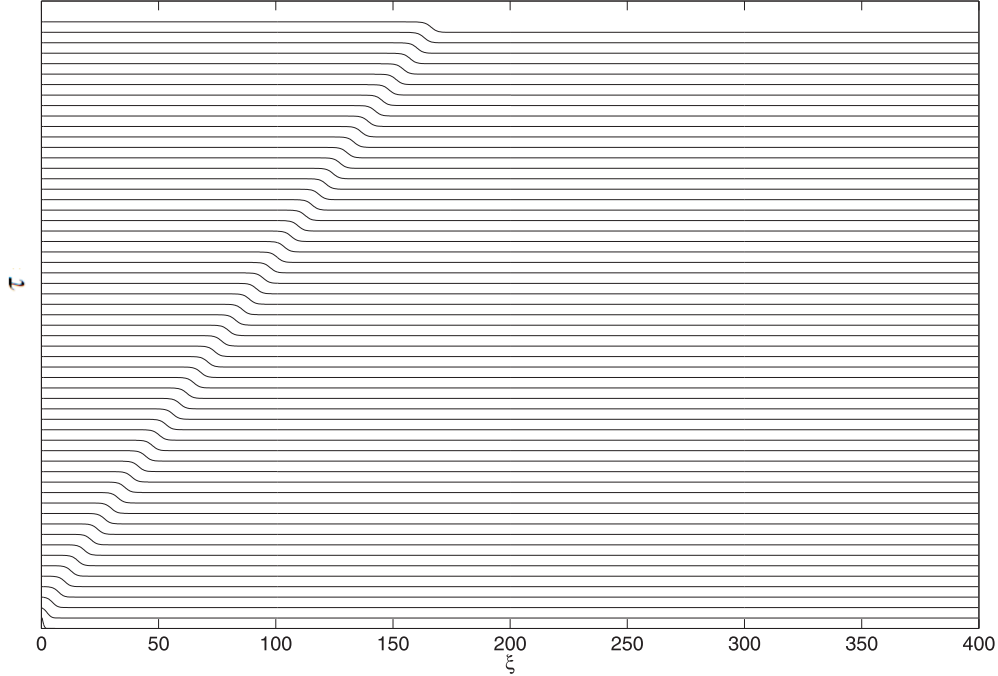


Figure 5.2: Space-time plot of the evolution of the profile of  $F$  across the domain. The initial condition is  $F = e^{-\xi^2}$ . The velocity profile for this propagating front is shown in Figure 5.3.

The accuracy of the simulation with respect to mesh density ( $\delta\xi$ ) and timestep ( $\delta\tau$ ) has also been examined. Varying  $\delta\xi$  in the range  $0.125 \geq \delta\xi \geq 0.03125$  results in a change in velocity of less than one percent. Varying  $\delta\tau$  in the range  $0.0005 \leq \delta\tau \leq 0.0015$  also produces a change in velocity of less than one percent.

Figure 5.2 shows a space-time plot of the evolution of  $F$  across the domain, with time increasing in the vertical direction. It is clear that  $F$  is uniformly translating, however, this does not mean that the corresponding front in the two dimensional Darcy-Bénard problem is uniformly translating as this equation describes an en-

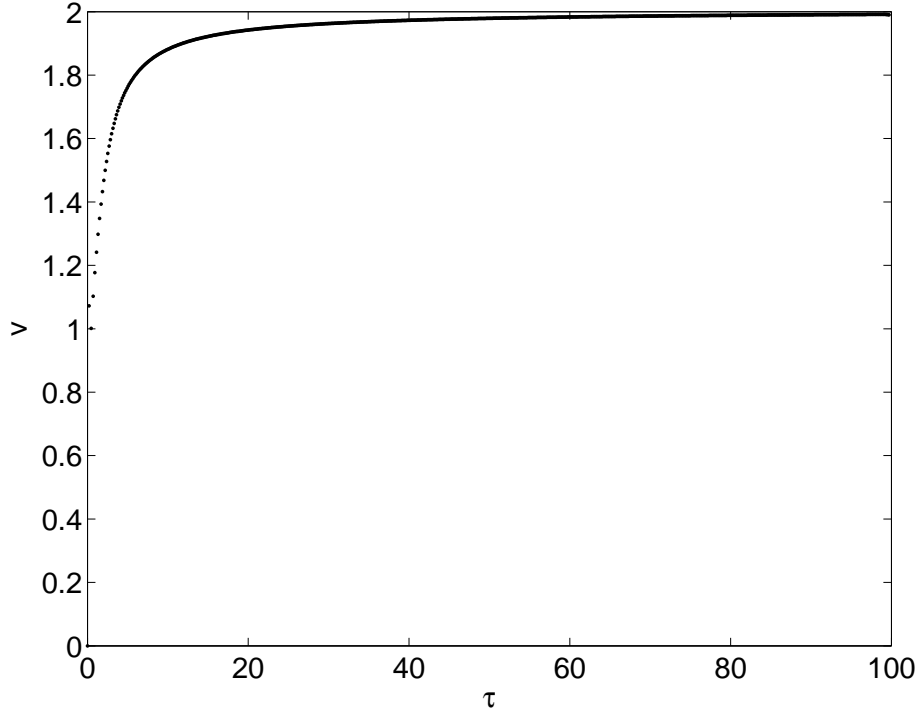


Figure 5.3: Profile of  $v$  versus  $\tau$ , with the initial condition  $F = e^{-\xi^2}$ .

velope within which the amplitude of the front lies.

Figure 5.3 shows a profile of the front velocity against time for the propagating front with the profile shown in Figure 5.2. Given the shape of this curve it is reasonable to apply Eqn. (5.35), as used by Kockelkoren et al (2003) based upon the unifying theory proposed by Ebert and van Saarloos (1998), in order to calculate the asymptotic velocity,  $v_{as}$ .

$$v(\tau) = v_{as} - \frac{A}{\tau} + \frac{B}{\tau^{3/2}} + \frac{C}{\tau^2} \quad (5.35)$$

This equation is solved simultaneously at four different points in time separated by equal intervals. This allows the coefficients  $A$ ,  $B$  and  $C$  to be calculated, and from

Eqn. (5.35) evaluated at $\tau =$	$A$	$B$	$C$	$v_{as}$
100, 110, 120	1.4163	1.0571	$-2.57 \times 10^{-7}$	2.0012
100, 200, 300	1.4567	1.4113	$-1.46 \times 10^{-6}$	2.0012
100, 300, 500	1.4722	1.6041	$-1.97 \times 10^{-6}$	2.0012
100, 600, 1100	1.4886	1.8914	$-2.50 \times 10^{-6}$	2.0011
100, 700, 1300	1.49007	1.9373	$-2.58 \times 10^{-6}$	2.0011

Table 5.1: Coefficients and  $v_{as}$  calculated for 2D Amplitude Equation.

these values  $v_{as}$  may be determined. It should be noted that Eqn. (5.35) describes the front relaxation at asymptotically large times but it may prove a reasonable approximation at shorter time. The coefficients and values of  $v_{as}$  calculated using this method are summarised in Table 5.1. These results are based upon  $\xi_{\max} = 4000$ ,  $\delta\xi = 0.125$  and  $\delta\tau = 0.0015$ .

We find that the first two terms of Eqn. (5.35) provide a reasonable approximation to the relaxation of the velocity, but that it appears our simulations do not run to sufficiently large time for the  $B$  and  $C$  coefficients to be calculated accurately. We see that calculating  $A$ ,  $B$ , and  $C$  over a larger time span gives more accurate results, this is because the universal theory is valid for large time.

### 5.3.2 Effect of Varying the Initial Conditions

To investigate the effect of different initial conditions on the propagating front we use a disturbance in the form

$$F = \frac{1 - \tanh(p(\xi - q))}{2}, \quad (5.36)$$

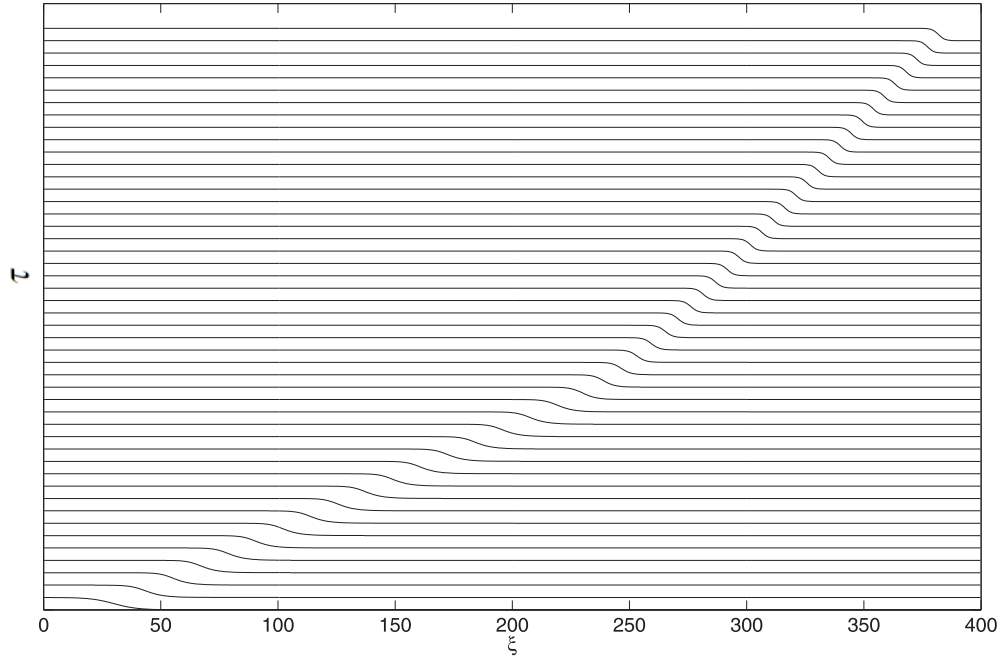


Figure 5.4: Space-time plot of the evolution of  $F$  across the domain for 2D cells, time increases in the vertical direction. The initial condition is given by Eqn. (5.36) where  $p = 0.1$  and  $q = 30.0$ . The velocity profile for a this propagating front is shown in Figure 5.5.

where  $p$  and  $q$  are constants. Figure 5.4 shows a space-time plot of the evolution of  $F$  across the domain with time increasing in the vertical direction, for an initial condition in the form of Eqn. (5.36) with  $p = 0.1, q = 30.0$ . Again the amplitude of  $F$  is uniform behind the front, however there is a significant change in the front velocity when the disturbance reaches  $\xi \approx 250$ . Beyond this point, the velocity of the front appears to be much closer to that shown in Figure 5.2, and the width of the front has decreased.

Figure 5.5 shows a comparison of the velocity profiles of a propagating front with respect to time for different initial conditions. Small values of  $p$  correspond to a shallower initial front profile. As the “steepness” of the front increases, the direction from which the velocity converges to  $v_{as}$  changes to an approach from below. This approach from below is well described by universal theory as given by Eqn. (5.35). Another interesting feature is that for all the initial profiles that lead to the velocity approaching its asymptotic value from above, the sudden change in velocity gradient as seen in Figure 5.4 occurs at almost exactly the same time.

Appendix C shows that Eqn. (5.37) is an exact solution of Eqn. (5.28) at  $\tau = 0$  which, with  $\beta = \pm\sqrt{1/8}$ , leads to a front propagation speed  $c = 3/\sqrt{2}$ . This speed is at odds with that found numerically ( $v_{as} = 2$ ) when the exact solution is used as an initial condition in Figure 5.5.

$$F = \frac{1}{2}(1 - \tanh \beta \xi) \quad (5.37)$$

This is a duplication of the result found by Getling (1992) for the NWS equation, and is discussed in Sect. 5.1.3.

It appears therefore that the front velocity may be linked to the shape of the propagating front, and this is examined in Figure 5.6, where all curves shown are translated in  $\xi$  so that  $F = 0.5$  occurs at  $\xi - \xi^f = 0$  on the horizontal axis.

Figure 5.6a shows the front profile at uniform intervals in time as it evolves from an initial condition in the form of Eqn. (5.36), with  $p = 0.07, q = 1.0$ . The earliest profile is the shallowest, appearing lowest on the left hand side and highest on the right. The vertical lines shown are from front profiles at early times where the front is still close enough to  $\xi = 0$  that the complete profile has not yet formed. There is an initial interval of time within which the shape changes, before settling towards a steeper profile, with successive profiles having such a similar form that

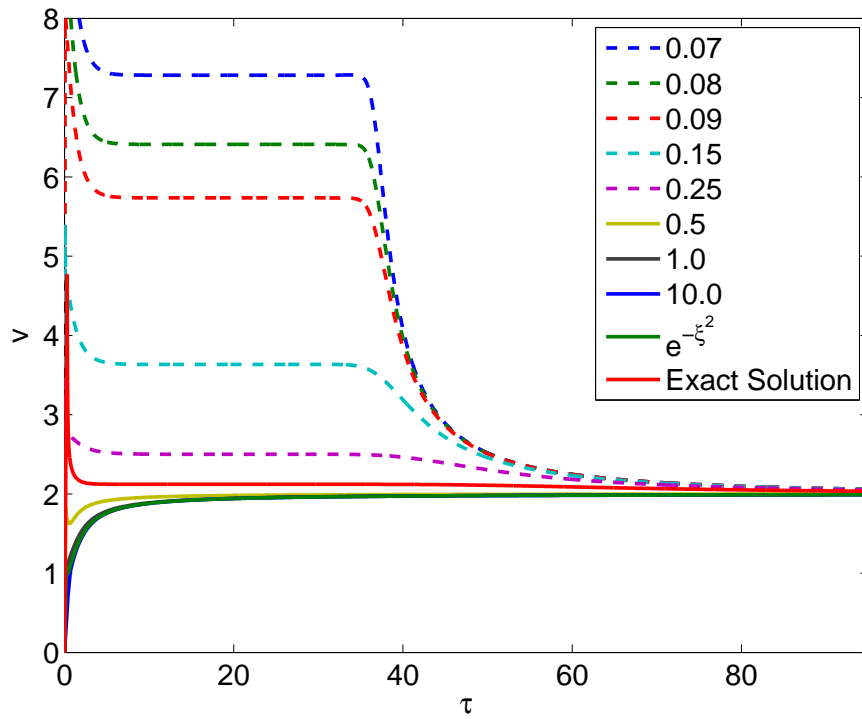
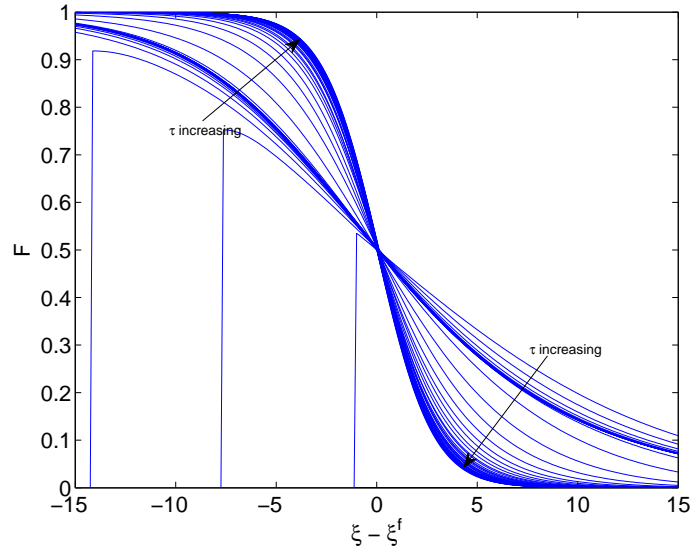
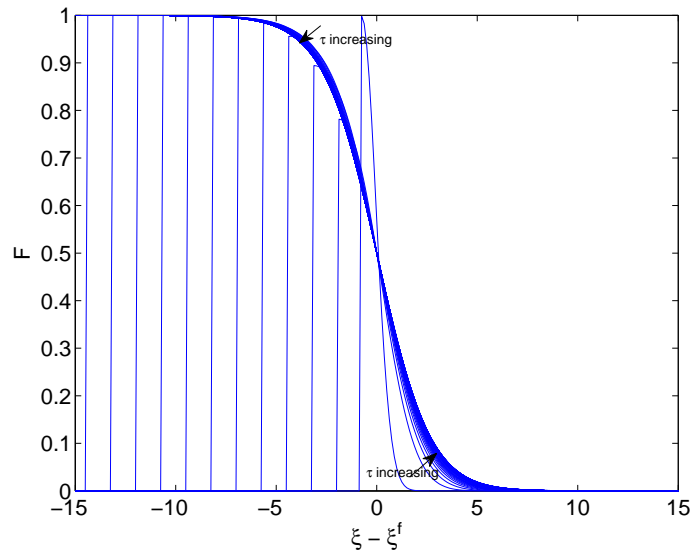


Figure 5.5:  $v$  versus  $\tau$  for differing initial conditions including Eqn. (5.36) with  $0.07 < p < 10$ ,  $q = 1.0$ ,  $F(\xi, 0) = e^{-\xi^2}$ , and the exact solution as given by Eqn. (5.37) included for reference.



(a)



(b)

Figure 5.6: Front profile at uniformly spaced time intervals for initial conditions (a) Eqn. (5.36) with  $p = 0.07$ ,  $q = 1.0$ , (b)  $e^{-\xi^2}$ , (c) the exact solution given by Eqn. (5.37).

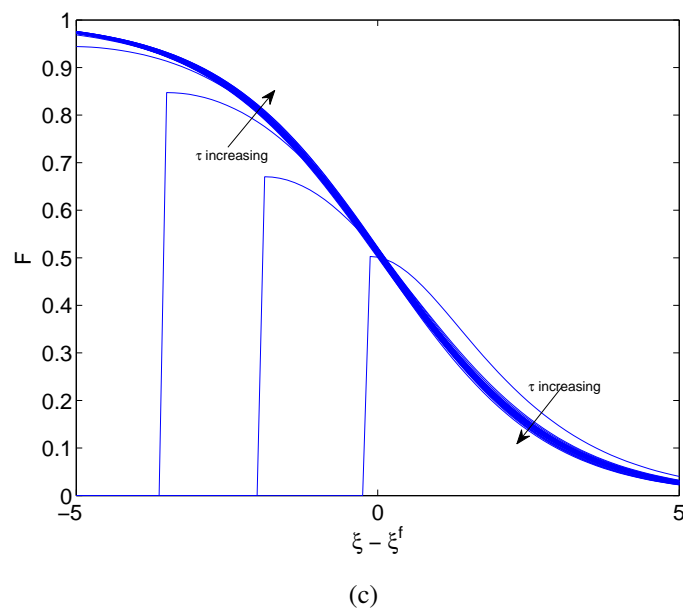


Figure 5.6: (Cont.) Front profile at uniformly spaced time intervals for initial conditions (a) Eqn. (5.36) with  $p = 0.07$ ,  $q = 1.0$ , (b)  $e^{-\xi^2}$ , (c) the exact solution given by Eqn. (5.37).

they group together and appear as a thicker line. Above  $\tau \approx 36$  the profile begins to change again and subsequent profiles are shown to relax towards a yet steeper form. In other words the sharp change in propagation speed shown in Figure 5.4, corresponds to a change in the shape of the leading edge of the front. Between the initial condition, and the shape of the front at large time there appears to be another “semi-attractive” profile towards which the front tends for a time, before undergoing another significant evolution.

When the initial condition has the decaying superexponential form,  $e^{-\xi^2}$ , the front profile evolves as shown in Figure 5.6b. In this case the initial condition is steeper than that at asymptotically large time, so the approach to this final profile is from the opposite direction to that seen in Figure 5.6a. This approach is rapid and there are no other “attractive” profiles in between. The fact the front is becoming shallower with increasing time, as compared with becoming steeper, as is the case in Figure 5.6a, may explain why the velocity profiles of these two cases relax to their asymptotic value from different directions.

Using the exact solution given by Eqn. (5.37) as an initial condition leads to the evolution of front profile as shown in Figure 5.6c. We see that there is a slight, but perceptible change, with the profile becoming steeper. This change in shape away from that of the exact solution explains why the predicted velocity of  $c = 3/\sqrt{2}$  is not realised numerically, this confirms the results of Getling (1992). It appears that in all three cases shown in Figure 5.6 the profile of the propagating front is tending to the same shape.

## 5.4 Nonlinear Numerical Analysis: 2D Front Propagation

We now conduct a fully nonlinear analysis of Darcy-Bénard front propagation in two dimensions to compare with the weakly nonlinear analysis above, as well as permitting the examination of a wider range of values of Ra. This is done by solving the full governing equations as given by Eqs. (5.18 – 5.21), with  $\phi^{(1)} = \phi^{(3)} = 0$ , for all time.

### 5.4.1 Numerical Method

Eqs. (5.19) and (5.21) are discretised spatially using second order accurate central differences and temporally using explicit first order accurate Euler (see Sect. 4.4.1). The multigrid correction scheme with a Gauss-Seidel pointwise solver is used to calculate  $\phi^{(2)}$ , which is equivalent to the stream function when in two dimensions. The following boundary conditions were imposed:

$$z = 0 : \quad \theta = 1 \quad \phi^{(2)} = 0, \quad (5.38)$$

$$z = z_{\max} : \quad \theta = 0 \quad \phi^{(2)} = 0, \quad (5.39)$$

$$x = 0 : \quad \frac{\partial^2 \theta}{\partial x^2} = 0 \quad \frac{\partial \phi^{(2)}}{\partial x} = 0, \quad (5.40)$$

$$x = x_{\max} : \quad \frac{\partial^2 \theta}{\partial x^2} = 0 \quad \frac{\partial^2 \phi^{(2)}}{\partial x^2} = 0. \quad (5.41)$$

The disturbance in the basic profile is initiated through the application of

$$\theta(x, z) = \theta_{basic}(z) + 0.01 \frac{1.0 - \tanh(\xi - 1.0)}{2.0} \sin(\pi z). \quad (5.42)$$

The location of the leading edge of the smooth front is determined by monitoring the value of the increase in heat transfer as a result of the disturbance, which

is given by Eqn. (5.43).

$$Q = \left. \frac{\partial \theta}{\partial z} \right|_{z=0} + \left. \frac{\partial \theta}{\partial z} \right|_{z=z_{\max}} + 2 \quad (5.43)$$

At  $O(\varepsilon)$  the thermal disturbance,  $\Theta_1$  profile is given in Appendix B by Eqn. (B.18), which is repeated below, where the complex exponential terms have been replaced by the equivalent trigonometric function:

$$\Theta_1 = \frac{1}{\pi^2} A \cos(\pi x) \sin(\pi z).$$

It follows therefore that

$$\left. \frac{\partial \Theta_1}{\partial z} \right|_{z=0} + \left. \frac{\partial \Theta_1}{\partial z} \right|_{z=1} = 0. \quad (5.44)$$

Importantly, this summation removes the  $x$ -dependent component of the solution. At  $O(\varepsilon^2)$  Appendix B shows that  $\Theta_2$  is proportional to  $\sin 2\pi z$  but with no  $x$ -dependence where

$$\left. \frac{\partial \Theta_2}{\partial z} \right|_{z=0} \text{ and } \left. \frac{\partial \Theta_2}{\partial z} \right|_{z=1} \quad (5.45)$$

have the same sign. Therefore the expression given in Eqn. (5.43) will be almost independent of  $x$  when  $Q$  is small because the flow is very weak and higher harmonics are negligible.

The front is defined as the location furthest downstream where  $Q = -1 \times 10^{-8}$ . Increasing this threshold value of  $Q$  did not affect the value of  $v_{as}$ , but it did increase the presence of spurious oscillations in the velocity profile. Oscillation occurs as the location of the front ‘‘jumps’’ forward once a newly formed cell has gained sufficient strength to exceed this threshold value for the first time.

Speed was again calculated based upon central differences. Results given below are based upon a mesh density  $\delta x = 0.0625$  and timestep  $\delta t = 0.00025$ . The

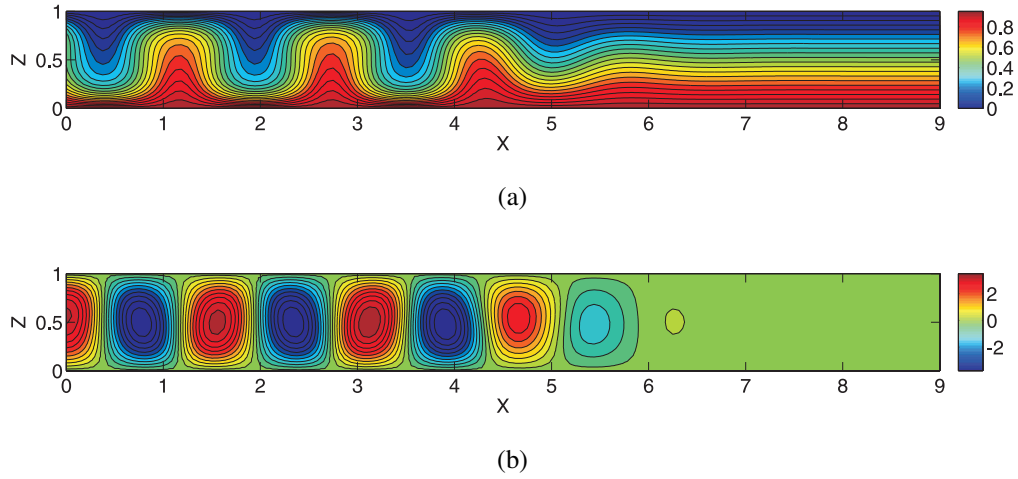


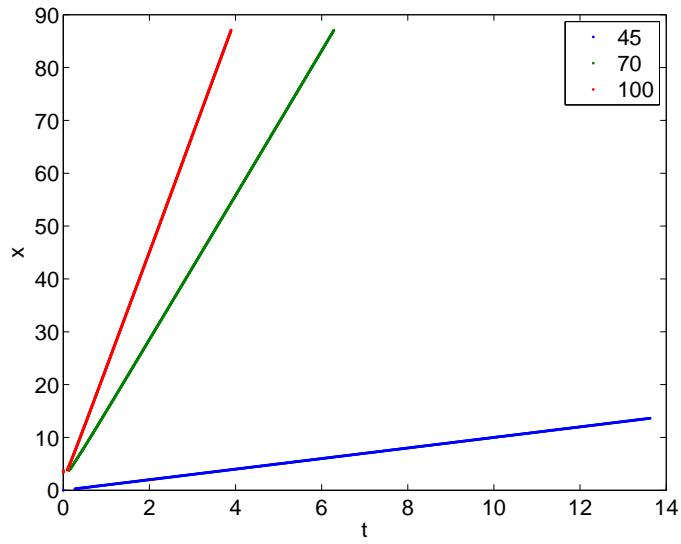
Figure 5.7: Contour plots of (a)  $\theta$  and (b)  $\phi^{(2)}$  for a propagating front when  $Ra = 80$ .

length of the domain was varied depending on the Rayleigh number in order to give sufficient time to enable the calculation of  $v_{as}$ . For  $Ra = 100$ ,  $x_{\max} = 180$ , while for  $Ra = 55$  a value of  $x_{\max} = 70$  was used.

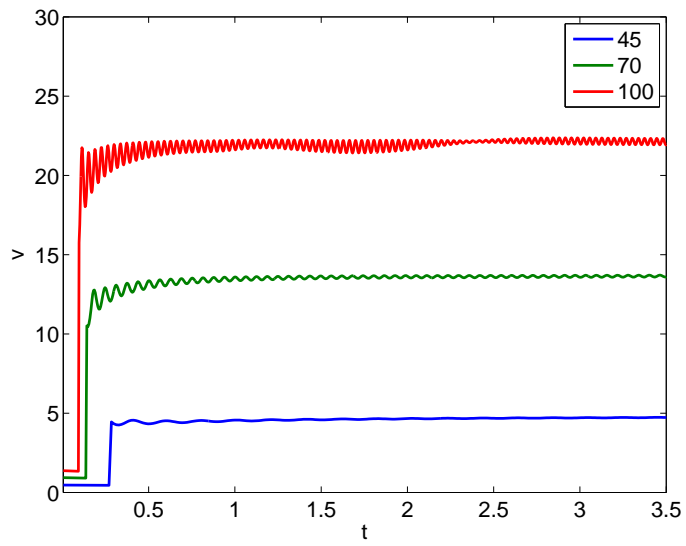
## 5.4.2 The 2D, Nonlinear, Propagating Front

Figures 5.7a and 5.7b show instantaneous profiles of  $\theta$  and  $\phi^{(2)}$  respectively for  $Ra = 80$ . Roughly square cells may be seen forming in Figure 5.7b and they increase in strength as they grow behind the front (see  $5 \leq x \leq 7$ ). The cells are a result of the changes in the temperature profile which can be seen in Figure 5.7a. These waves remain stationary after they form, as was found by Lucke et al (1987) for the Rayleigh-Bénard problem.

Figure 5.8 shows the location of the front and the associated velocity profiles for a range of values of  $Ra$ . As expected, fronts propagate faster when  $Ra$  in-



(a)



(b)

Figure 5.8: Comparison of (a)  $x$  vs.  $t$  and (b)  $v$  vs.  $t$  for  $Ra = 45, 70, 100$ .

creases. The oscillating shape of the front profile means that, as oscillations grow in magnitude enough for  $Q$  to exceed the threshold, the front location advances unevenly resulting in a varying velocity profile.

Figures 5.9 and 5.10 show how the effective wavelength,  $\lambda$ , of each cell varies with  $t$  for  $Ra = 41$  and  $Ra = 100$  respectively. The lines appearing from the direction of  $+\infty$  indicate the creation of new cells as the disturbance spreads across the layer. Both figures show that the cells which exist at any one point in time have different wavelengths. The largest wavelength always corresponds to the last cell to form, but as time progresses its wavelength adjusts towards an asymptotic value. The rate at which new cells are created increases with  $Ra$ . Higher values of  $Ra$  produce lower values of  $\lambda$  or higher values of  $k$ , which is consistent with the analysis of Straus (1974) with regard to the range of stable wavenumbers. Figure 5.10b shows a close up of the transient phase for  $Ra = 100$ , here we see that at such a high Rayleigh number the approach of  $\lambda$  towards its asymptotic value is oscillatory in nature. After this initial transient period, for both cases, the rate at which new cells are created, and the profile of  $\lambda$  with respect to  $t$  for an individual cell become regular. The length of this transient period is smaller at lower  $Ra$ .

### 5.4.3 Asymptotic Velocity

The asymptotic velocity of the front is calculated using Eqn. (5.35), this is the equation produced by unifying theory for a pulled front. The fact that Eqn. (5.35) describes the evolution of the velocity with respect to time accurately indicates that the 2D propagating front is a pulled front (i.e. its behaviour is described by linear spreading analysis of the leading edge). Figure 5.11 shows the variation of  $v_{as}$  with  $Ra$ , as being roughly  $2.0\sqrt{(Ra - Ra_c)}$  for moderately supercritical values

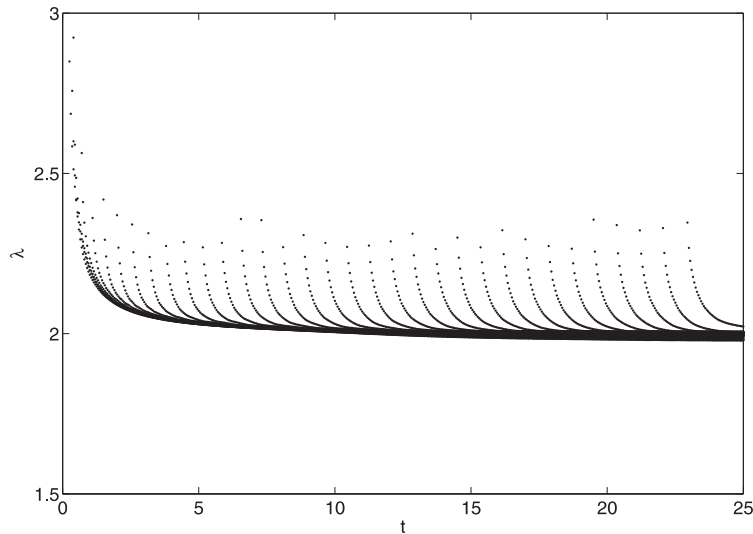


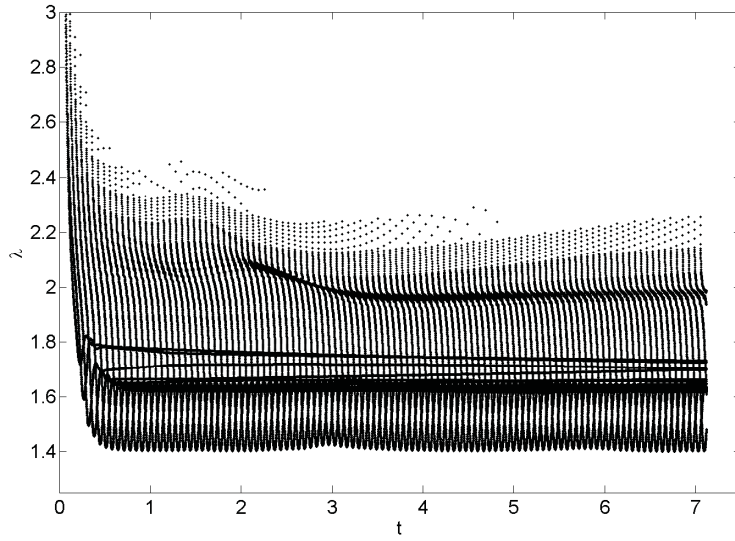
Figure 5.9: Variation of  $\lambda$  with Ra for Ra = 41.

of Ra and tending towards a more, although not completely, linear relationship at higher Ra. Comparison between the results of the weakly nonlinear and strongly nonlinear results is good at low values of Ra. At values of Ra  $> 80$  a least squares approximation to the data gives the relationship  $v_{as} = 0.2646Ra - 4.4071$ .

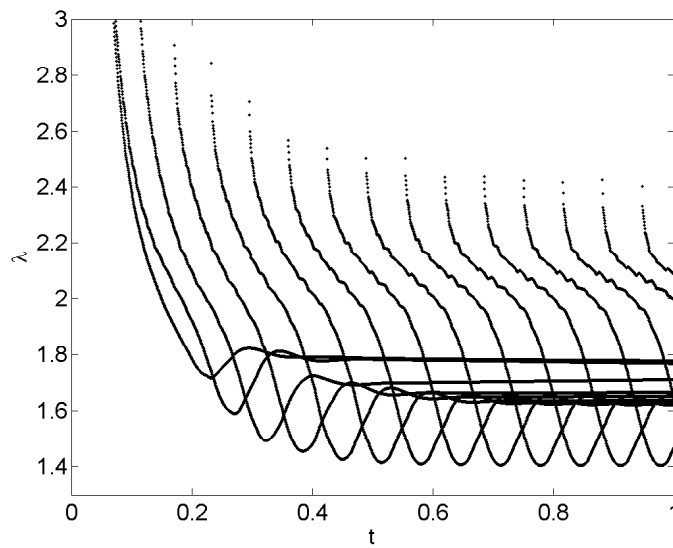
#### 5.4.4 Wavenumber Selection

Figure 5.12 shows the variation of wavenumber,  $k$  with Ra as given by the 2D nonlinear finite difference analysis .

We compare the value of  $k$  generated by the two-dimensional nonlinear code with that produced by a linear stability analysis. The linear stability analysis of Darcy-Bénard convection (Horton and Rogers (1945); Lapwood (1948)) gives the



(a)



(b)

Figure 5.10: Variation of  $\lambda$  with Ra for Ra = 100 for (a)  $0 \leq t \leq 7.5$ , and (b)  $0 \leq t \leq 1$  (transient phase).

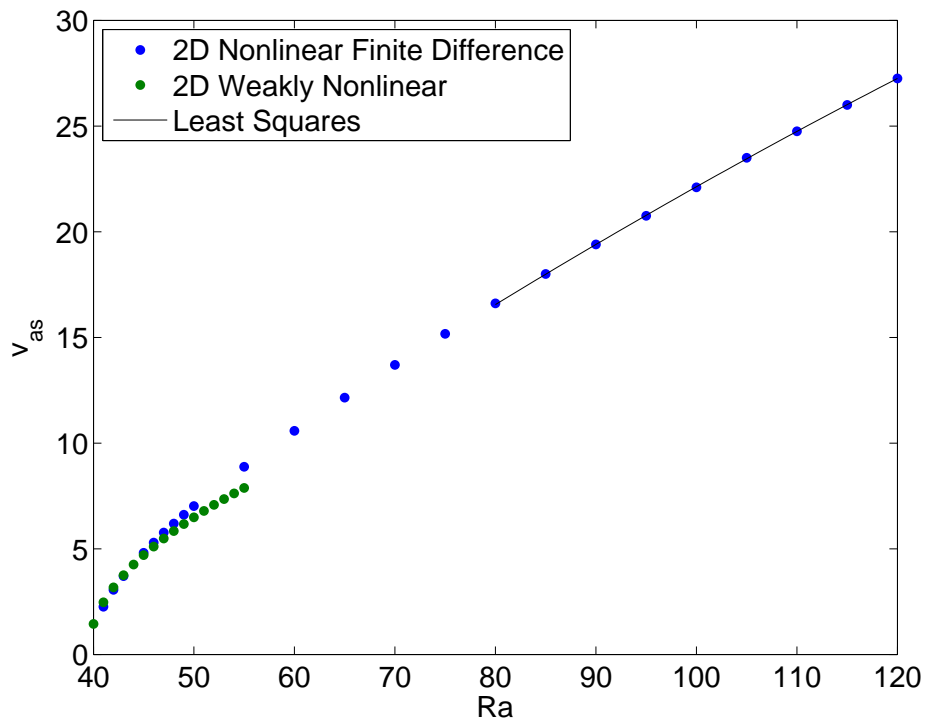


Figure 5.11: Comparison of variation of  $v_{as}$  with Ra for the 2D Nonlinear Finite Difference analysis and 2D Weakly Nonlinear analysis. Least squares approximation included for reference at  $Ra > 80$ .

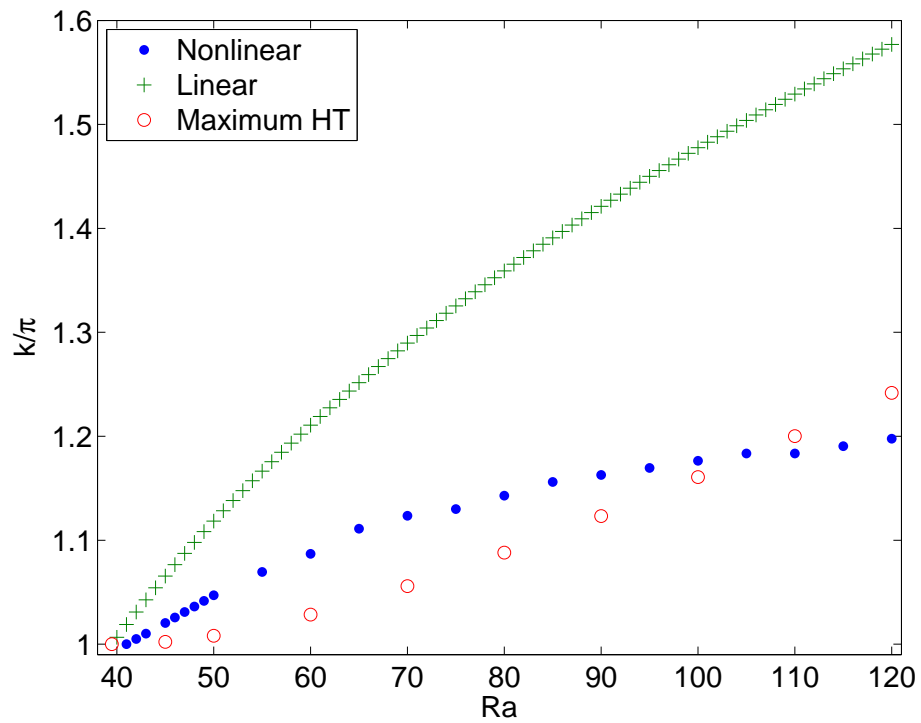


Figure 5.12: Preferred wavenumber  $k$ , for a given value of  $Ra$  as given by the nonlinear front computations. Also shown is the value of  $k$  predicted by linear stability theory, and that which maximises heat transfer (Nusselt number), as given in Appendix D by Rees (2011).

equation for the exponential growth rate  $\lambda$  as a function of Ra and  $k$ ;

$$\lambda = \frac{\text{Ra}k^2}{(k^2 + \pi^2)} - k^2 - \pi^2. \quad (5.46)$$

Setting  $\lambda = 0$  yields the neutral stability curve (disturbances neither growing or decaying). However the flow pattern generated behind the propagating front could conceivably be that for which the growth rate  $\lambda$  is a maximum, that is to say when  $\partial\lambda/\partial k = 0$ . Differentiation of Eqn. (5.46) gives Eqn. (5.47) the real roots of which are  $k = \pm\sqrt{\text{Ra}^{1/2}\pi - \pi^2}$ .

$$\text{Ra}\pi^2 = k^4 + 2\pi^2k^2 + \pi^4. \quad (5.47)$$

Figure 5.12 shows a wide discrepancy between the nonlinear and linear results, which becomes more pronounced with increasing values of Ra . It appears that the nonlinear effects cannot be predicted by this aspect of linear theory.

Also shown in Figure 5.12 is the wavenumber which maximises heat transfer (Nusselt Number) through the porous layer (Rees (2011)) . There are also significant differences between these, and the values of  $k_{as}$  returned by our finite difference model. It appears, therefore, that maximising the heat transfer rate does not drive wavenumber selection in this case.

## 5.5 Weakly Nonlinear Analysis: 3D Front Propagation

Weakly nonlinear analysis may be used to investigate the propagation speed of the front which is formed when the axes of the rolls formed behind the front either lie parallel ( $y$  direction) or perpendicular ( $x$  direction) to the direction ( $y$ ) in which the

front advances. The former may be referred to as longitudinal rolls, and the latter, transverse. The weakly nonlinear analysis again concentrates on Darcy-Rayleigh numbers slightly above the critical value, and more detail is given in Appendix B. For transverse rolls we recover Eqn. (5.24) and the results of Sect. 5.3 apply. For the longitudinal rolls, for which the front advances in the  $y$  direction, the amplitude equation takes the following form,

$$\frac{\partial A}{\partial \tau} = \text{Ra}_2 A - \frac{1}{\pi^2} \frac{\partial^4 A}{\partial Y^4} - A^3. \quad (5.48)$$

The following scalings are introduced:

$$\xi = (\text{Ra}_2 \pi^2)^{1/4} Y, \quad A = \sqrt{\text{Ra}_2} F, \quad \hat{\tau} = \frac{1}{\text{Ra}_2} \tau, \quad (5.49)$$

giving (after dropping the circumflex) the canonical form,

$$\frac{\partial F}{\partial \tau} = F - \frac{\partial^4 F}{\partial \xi^4} - F^3. \quad (5.50)$$

### 5.5.1 Numerical Calculation of $v_{as}$ for Longitudinal Rolls

Eqn. (5.50) is solved numerically in order to calculate the propagation speed of a front composed of longitudinal rolls. Second order accurate central differences in space are used. For the fourth derivative of  $F$  with respect to  $\xi$  the following five point stencil is required,

$$\frac{\partial^4 F_i}{\partial \xi^4} = \frac{F_{i+2} - 4F_{i+1} + 6F_i - 4F_{i-1} + F_{i-2}}{(\delta \xi)^4}. \quad (5.51)$$

The evolution of  $F$  in  $\tau$  is calculated using a second order accurate Runge-Kutta scheme, as described in Sect. 5.3 for the two-dimensional weakly nonlinear analysis. The method used for calculating the location of the front is also the same as

that described in Sect. 5.3. The boundary conditions

$$\frac{\partial F}{\partial \xi} = \frac{\partial^3 F}{\partial \xi^3} = 0, \text{ at } \xi = 0 \quad (5.52)$$

are applied and again are equivalent to symmetry conditions about  $\xi = 0$ . The second order accurate central difference stencil for the third derivative is as follows:

$$\frac{\partial^3 F_i}{\partial \xi^3} = \frac{F_{i+2} - 2F_{i+1} + 2F_{i-1} - F_{i-2}}{2(\delta\xi)^3} \quad (5.53)$$

which implies that

$$F_{i+2} = F_{i-2}, \quad (5.54)$$

as the first derivative boundary condition implies  $F_{i+1} = F_{i-1}$ , and the resulting stencil for the fourth derivative at  $\xi = 0$  is

$$\frac{\partial^4 F_0}{\partial \xi^4} = \frac{2F_2 - 8F_1 + 6F_0}{(\delta\xi)^4}. \quad (5.55)$$

Use of the first derivative boundary condition gives:

$$\frac{\partial^4 F_1}{\partial \xi^4} = \frac{F_3 - 4F_2 + 7F_1 - 4F_0}{(\delta\xi)^4}. \quad (5.56)$$

The accuracy of the simulation with respect to mesh density ( $\delta\xi$ ) and timestep ( $\delta\tau$ ) has been examined. The following results in this section use  $\delta\xi = 0.25$  and  $\delta\tau = 0.0003$ . Reducing the timestep to  $\delta\tau = 7.5 \times 10^{-5}$  results in a change in  $v_{as}$  of less than one percent. Employing mesh densities in the range  $0.166 \leq \delta\xi \leq 0.25$  also results in a change in  $v_{as}$  of less than one percent. Results in this section are based upon  $\delta\tau = 0.0003$  and  $\delta\xi = 0.25$ .

Figures 5.13a - 5.13d show the space-time evolution of the profile of  $F$  with time increasing in the vertical direction. In contrast to the case of transverse rolls,

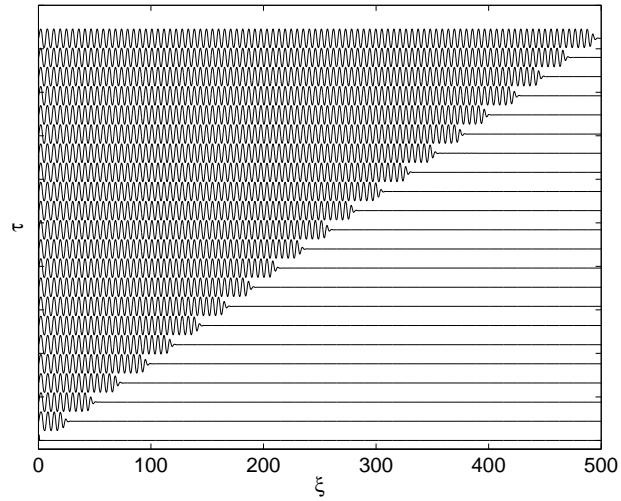
the profile of  $F$  is oscillatory behind the front, with the spatial oscillations remaining fixed in space following their creation. Depending on the initial condition the oscillation may be preceded by a period during which  $F$  is uniformly translating before becoming a coherent pattern forming front. The velocity-time profiles associated with these fronts are shown in Figure 5.15.

Figures 5.14a and 5.14b show the location of the front against time and the front velocity against time respectively. The oscillatory nature of the propagating front leads to the jumps in front location as shown in Figure 5.14a, these occur when a new oscillation becomes strong enough to exceed the threshold for the first time. When calculating the velocity using central differences these discontinuities can lead to very high instantaneous velocities as the location of the front has suddenly advanced. To overcome this the first point after each jump is located (using the large gap preceding it) and only these points are used to calculate the velocity, based upon Eqn. (5.34). This method obviously reduces the number of points at which the velocity can be calculated as shown by the reduced number of data points in Figure 5.14b. Given the shape of the velocity profile shown in Figure 5.14b the asymptotic velocity was calculated by simultaneously solving Eqn. (5.57) at two different times. This gives  $v_{as} = 2.94$  independent of the interval between the two points used in the calculation, however the value of  $A$  remains sensitive to this.

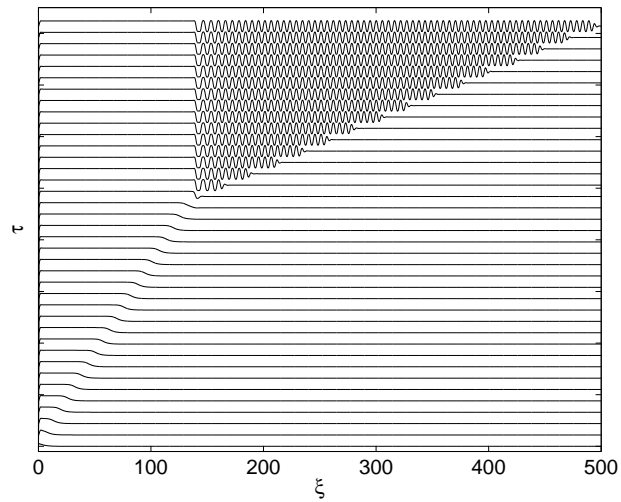
$$v(\tau) = v_{as} - \frac{A}{\tau} \quad (5.57)$$

## 5.5.2 Effect of Varying the Initial Conditions

Figure 5.15 summarises the effect of having different initial conditions on the velocity of the propagating front composed of longitudinal rolls. The initial con-

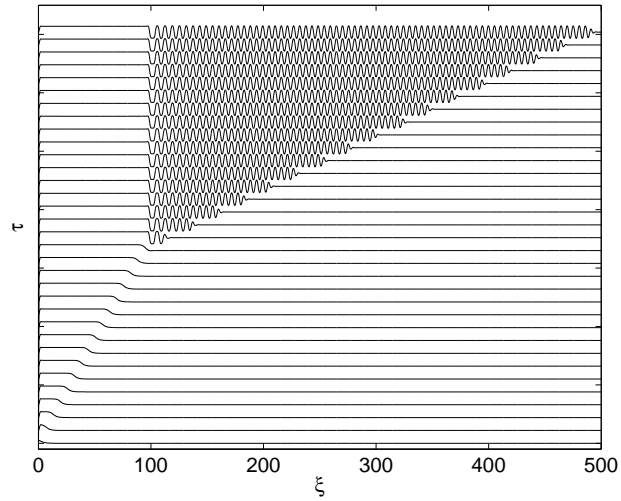


(a)

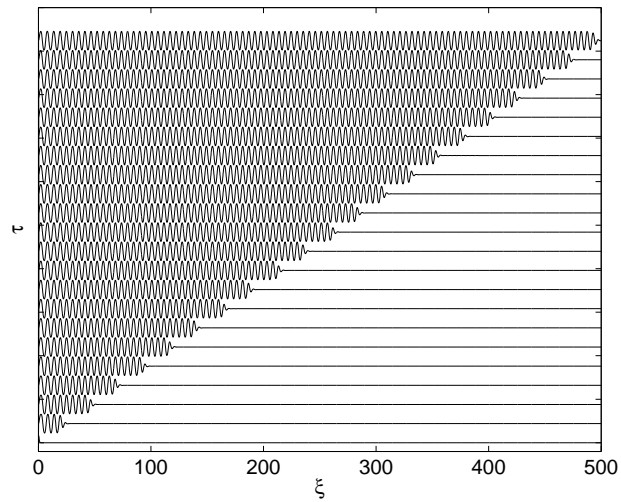


(b)

Figure 5.13: Space-time evolution of the profile of  $F$  across the domain for the transverse disturbance, time increases in the vertical direction, initial condition give by (a)  $e^{-\xi^2}$  and Eqn. (5.36) with (b)  $p = 0.07, q = 1.0$ , (c)  $p = 0.1, q = 1.0$  and (d)  $p = 1.0, q = 1.0$ . Velocity profiles associated with these fronts are shown in Figure 5.15.

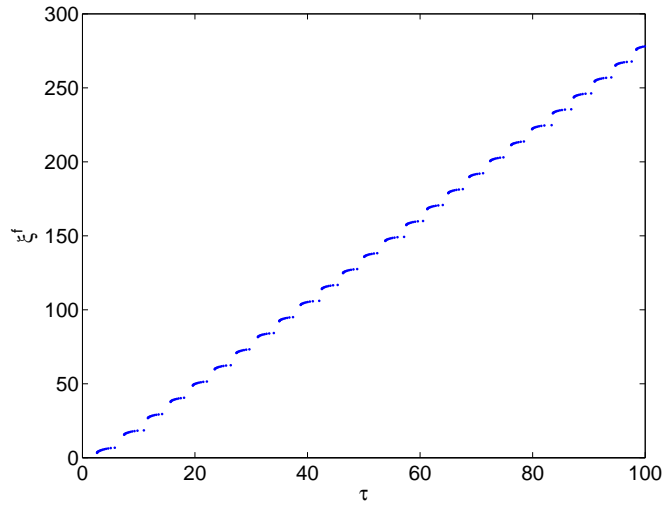


(c)

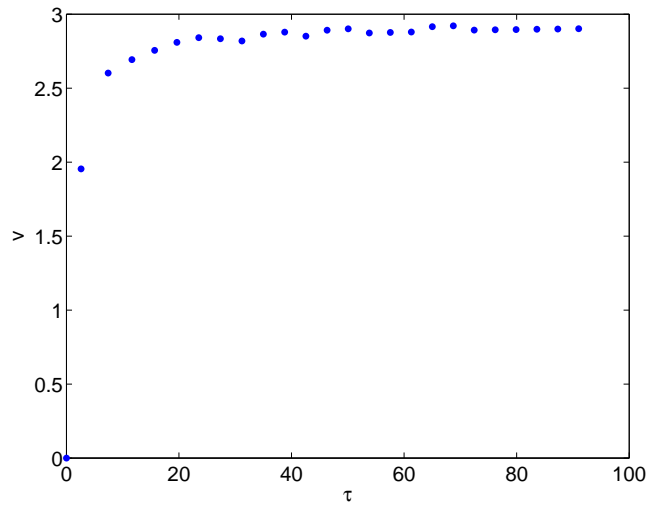


(d)

Figure 5.13: (*Cont.*) Space-time evolution of the profile of  $F$  across the domain for the transverse disturbance, time increases in the vertical direction, initial condition give by (a)  $e^{-\xi^2}$  and Eqn. (5.36) with (b)  $p = 0.07, q = 1.0$ , (c)  $p = 0.1, q = 1.0$  and (d)  $p = 1.0, q = 1.0$ . Velocity profiles associated with these fronts are shown in Figure 5.15.



(a)



(b)

Figure 5.14: (a) Location of front against time and (b) Velocity profiles as given by weakly nonlinear analysis for a propagating front composed of longitudinal vortices.  $p = 1.0, q = 1.0$ .

dition takes the form of Eqn. (5.36) with  $q = 1$  and  $p$  taking values in the range  $0.07 \leq p \leq 5.0$ . Depending on the steepness of the front profile the velocity may converge to its asymptotic velocity from above (shallower initial conditions) or below (steeper initial conditions). Again the value of  $\tau$  at which a significant change in the front profile takes place in Figure 5.13b appears to be independent of initial conditions. In the case of lower values of  $p$  the propagation of the front is initially uniformly translating before becoming coherent pattern forming, and the discontinuity in the velocity profile occurs at the transition between these two regimes.

### 5.5.3 Planform Selection

Having established the front propagation velocities for both transverse and longitudinal rolls within the weakly nonlinear regime, it is worth asking which type of pattern will propagate faster. The asymptotic velocity,  $v_{as}$ , for each planform has to be rescaled to allow a direct comparison. The equivalent asymptotic velocities of the longitudinal rolls,  $v_L$ , and transverse rolls,  $v_T$ , may be expressed as

$$v_T = v_{as(trans.)} \sqrt{Ra_2} \quad \text{and} \quad v_L = v_{as(long.)} \frac{Ra_2^{3/4}}{2\sqrt{\pi}}, \quad (5.58)$$

where  $v_{as(trans.)}$  is the asymptotic velocity calculated numerically using the weakly nonlinear analysis for transverse rolls, and  $v_{as(long.)}$  is the equivalent for longitudinal rolls. Using the above equations we may plot Figure 5.16 which shows the asymptotic velocity versus  $Ra_2$  for the two planforms. For values of  $Ra_2 < 33.8$  transverse rolls spread faster and so we would expect them to dominate any flow pattern. Above this value of  $Ra_2$  we would expect longitudinal rolls to become dominant.

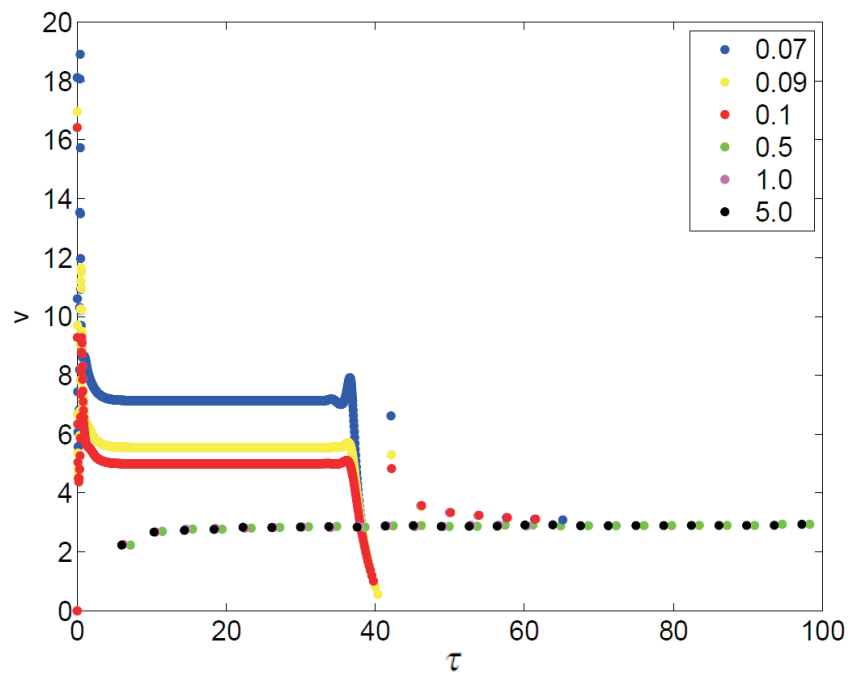


Figure 5.15: Velocity profiles as a function of initial conditions of the form given by Eqn. (5.36) with  $q = 1$  for different values of  $p$ , as calculated by the weakly nonlinear analysis of longitudinal rolls.

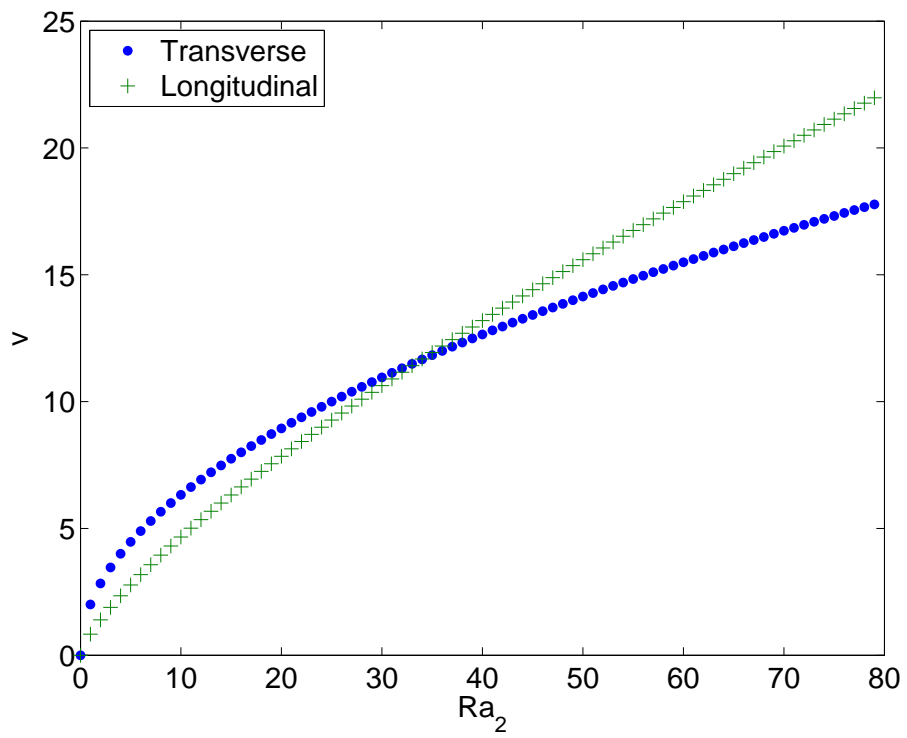


Figure 5.16:  $v_{as}$  versus  $Ra_2$  for transverse and longitudinal rolls.

## 5.6 Nonlinear Numerical Analysis: 3D Front Propagation

We now undertake a fully nonlinear, 3D, numerical study of longitudinal rolls based upon a spanwise Fourier decomposition of Eqs. (5.18 – 5.21).

### 5.6.1 Governing Equations

The following Fourier Series are introduced:

$$\theta = \frac{\theta_0}{2} + \sum_{n=1}^N \theta_n \cos(nkx), \quad (5.59)$$

$$\phi^{(1)} = \frac{\phi_0^{(1)}}{2} + \sum_{n=1}^N \phi_n^{(1)} \cos(nkx), \quad (5.60)$$

$$\phi^{(2)} = \sum_{n=1}^N \phi_n^{(2)} \sin(nkx), \quad (5.61)$$

$$\phi^{(3)} = \sum_{n=1}^N \phi_n^{(3)} \sin(nkx), \quad (5.62)$$

where  $k$  is the wavenumber and  $\theta_n$ ,  $\phi_n^{(1)}$ ,  $\phi_n^{(2)}$  and  $\phi_n^{(3)}$  are functions of  $(y, z, t)$ .

Substitution into Eqs. (5.18 – 5.21) gives;

$$\mathcal{L}_n \phi_n^{(1)} = -\text{Ra} \frac{\partial \theta_n}{\partial y}, \quad (0 \leq n \leq N) \quad (5.63)$$

$$\mathcal{L}_n \phi_n^{(2)} = -\text{Rank} \theta_n, \quad (1 \leq n \leq N) \quad (5.64)$$

$$\mathcal{L}_n \phi_n^{(3)} = 0, \quad (1 \leq n \leq N) \quad (5.65)$$

where the elliptic operator,  $\mathcal{L}_n$ , is defined according to,

$$\mathcal{L}_n \phi = \frac{\partial^2 \phi}{\partial y^2} + \frac{\partial^2 \phi}{\partial z^2} - n^2 k^2 \phi. \quad (5.66)$$

Substitution into Eqn. (5.59) gives ;

$$\frac{\partial \theta_0}{\partial t} = \mathcal{L}_0 \theta_0 + \frac{1}{2} \frac{\partial(\phi_0^{(1)}, \theta_0)}{\partial(y, z)} + 2\mathbb{N}_0 \quad (5.67)$$

where  $\mathbb{N}_0$  are the nonlinear terms contributing to the zero mode. For all other modes

$$\frac{\partial \theta_n}{\partial t} = \mathcal{L}_n \theta_n + \frac{1}{2} \left( \frac{\partial(\phi_0^{(1)}, \theta_n)}{\partial(y, z)} + \frac{\partial(\phi_n^{(1)}, \theta_0)}{\partial(y, z)} \right) - \frac{nk}{2} \phi_n^{(2)} \frac{\partial \theta_0}{\partial z} + \frac{nk}{2} \phi_n^{(3)} \frac{\partial \theta_0}{\partial y} + \mathbb{N}_n, \quad (5.68)$$

where  $\mathbb{N}_n$  represents the nonlinear terms contributing to mode  $n$ . The nonlinear terms arise from the interactions of the modes with each other, modes  $l$  and  $m$  giving rise to the following terms in modes  $(l+m)$  and  $(l-m)$  :

$$\mathbb{N}_{l \pm m} = \frac{1}{2} \frac{\partial(\phi_l^{(1)}, \theta_m)}{\partial(y, z)} \pm \frac{mk\theta_m}{2} \left( \frac{\partial \phi_l^{(2)}}{\partial z} - \frac{\partial \phi_l^{(3)}}{\partial y} \right) - \frac{lk}{2} \left( \phi_n^{(2)} \frac{\partial \theta_m}{\partial z} - \phi_n^{(3)} \frac{\partial \theta_m}{\partial y} \right). \quad (5.69)$$

The following boundary conditions are used:

$$z = 0 : \theta_0 = 2, \theta_n = \phi_n^{(1)} = \phi_n^{(2)} = \frac{\partial \phi_n^{(3)}}{\partial z} = 0, \quad (5.70)$$

$$z = z_{\max} : \theta_0 = \theta_n = \phi_n^{(1)} = \phi_n^{(2)} = \frac{\partial \phi_n^{(3)}}{\partial z} = 0, \quad (5.71)$$

$$y = 0 : \frac{\partial \theta_0}{\partial y} = \frac{\partial \theta_n}{\partial y} = \frac{\partial \phi_n^{(1)}}{\partial y} = \frac{\partial \phi_n^{(2)}}{\partial y} = \frac{\partial \phi_n^{(3)}}{\partial y} = 0, \quad (5.72)$$

$$y = y_{\max} : \frac{\partial^2 \theta_0}{\partial y^2} = \frac{\partial^2 \theta_n}{\partial y^2} = \frac{\partial^2 \phi_n^{(1)}}{\partial y^2} = \frac{\partial^2 \phi_n^{(2)}}{\partial y^2} = \frac{\partial^2 \phi_n^{(3)}}{\partial y^2} = 0. \quad (5.73)$$

## 5.6.2 Numerical Method

The governing equations are discretised using second order accurate finite differences and an explicit Euler timestepping scheme. A multigrid correction scheme

in conjunction with a line solver is used to calculate the values of  $\phi$ . The following results are calculated based upon a mesh density of  $\delta x = \delta y = \delta z = 1/8$ . Increasing the density to  $1/16$  results in a difference in  $v_{as}$  of less than 0.55% at  $Ra = 80$ . Three Fourier modes ( $n = 0, 1, 2$ ) were found to give a reasonable representation of the propagating front when compared with the results of a three-dimensional finite difference model, for values of  $Ra$  up to  $Ra = 120$ . A timestep of  $\delta t = 0.0005$  was used. Initial conditions take the following form,

$$\theta_0 = 2(1 - z), \text{ and } \theta_1 = C \frac{1 - \tanh(p(y - q))}{2} \sin \pi z, \quad (5.74)$$

with all other variables taken to be zero. For the results shown below,  $C = 0.001$  is taken.

### 5.6.3 Effect of Varying Initial Conditions

Figures 5.17 - 5.20 show the effect on the propagating front of altering the value of  $p$  in Eqn. (5.74). The undisturbed region ahead of the front corresponds to the light green region in the upper ( $X - Y$ ) contour plot in each of these Figures. For shallower (small  $p$ ) initial conditions the front propagates in the form of longitudinal rolls for a much longer distance into the domain. As  $p$  increases the longitudinal rolls do not persist for as long, and are instead replaced by square cells which are formed by a combination of longitudinal and transverse rolls. The square cells appear rectangular here due to the difference between the horizontal and vertical scales used. At the highest value of  $p$  shown here,  $p = 1.0$  in Figure 5.20, the square cells are in turn replaced by purely transverse rolls.

Figure 5.21 shows the variation of instantaneous velocity  $v$  of the propagating front with  $t$  for values of  $p$  in the range  $0.25 \leq p \leq 1$  when  $Ra = 80$ . The os-

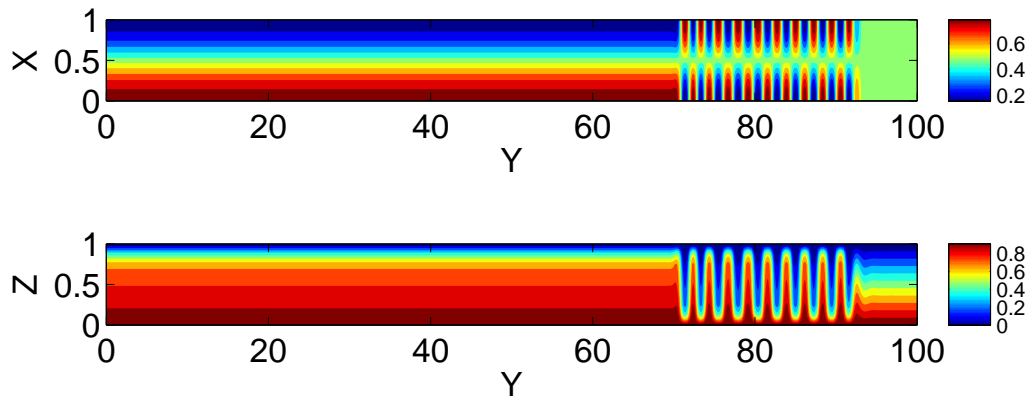


Figure 5.17: Contour plots of  $\theta$  when  $k = \pi$ ,  $Ra = 80$ ,  $p = 0.25$ ,  $q = 1.0$ , from above at  $z = 0.5$  (top), from the side on at  $x = 0$  (bottom).

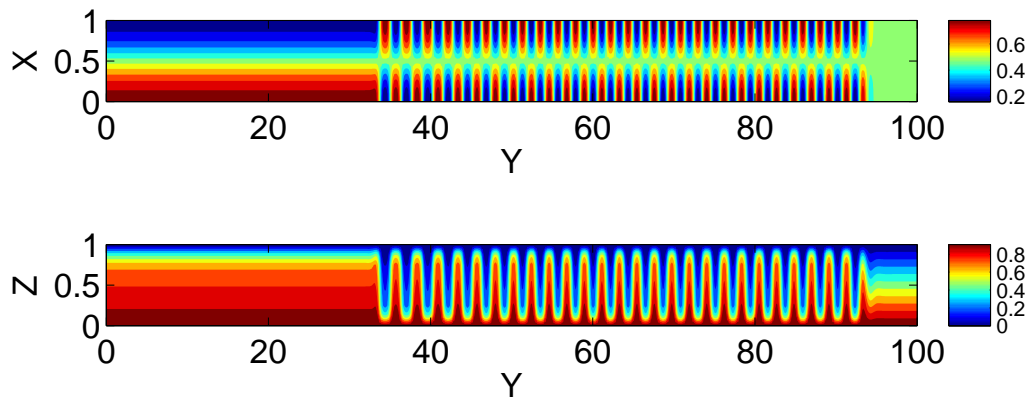


Figure 5.18: Contour plot of  $\theta$  when  $k = \pi$ ,  $Ra = 80$ ,  $p = 0.5$ ,  $q = 1.0$ , from above at  $z = 0.5$  (top), from the side at  $x = 0$  (bottom).

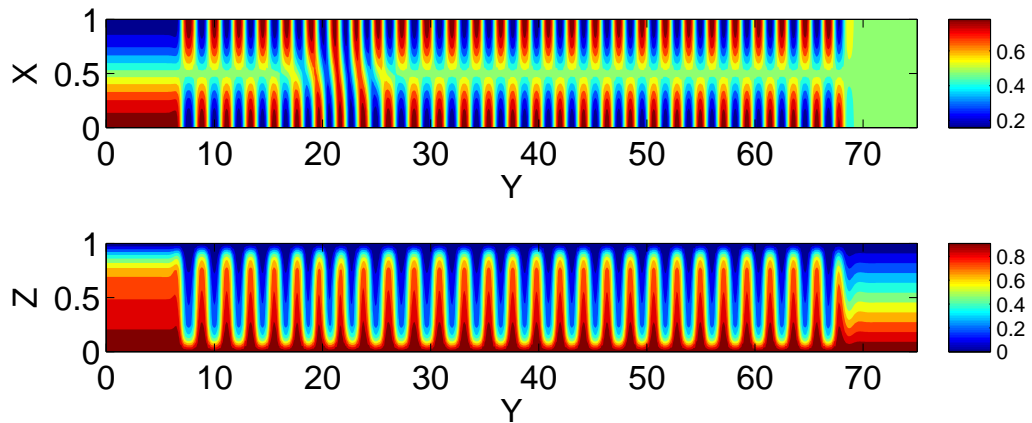


Figure 5.19: Contour plots of  $\theta$  when  $k = \pi$ ,  $Ra = 80$ ,  $p = 0.75$ ,  $q = 1.0$ , from above at  $z = 0.5$  (top) , from the side at  $x = 0$  (bottom).

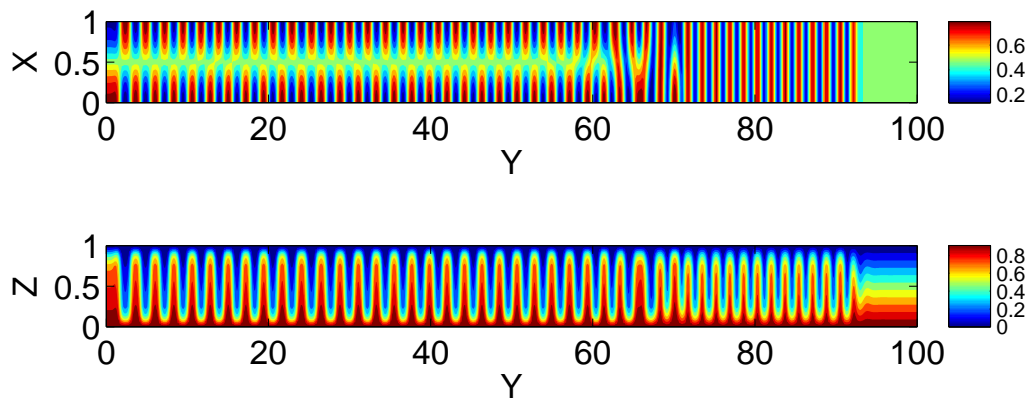


Figure 5.20: Contour plots of  $\theta$  when  $k = \pi$ ,  $Ra = 80$ ,  $p = 1.0$ ,  $q = 1.0$ , from above at  $z = 0.5$  (top), from the side at  $x = 0$  (bottom).

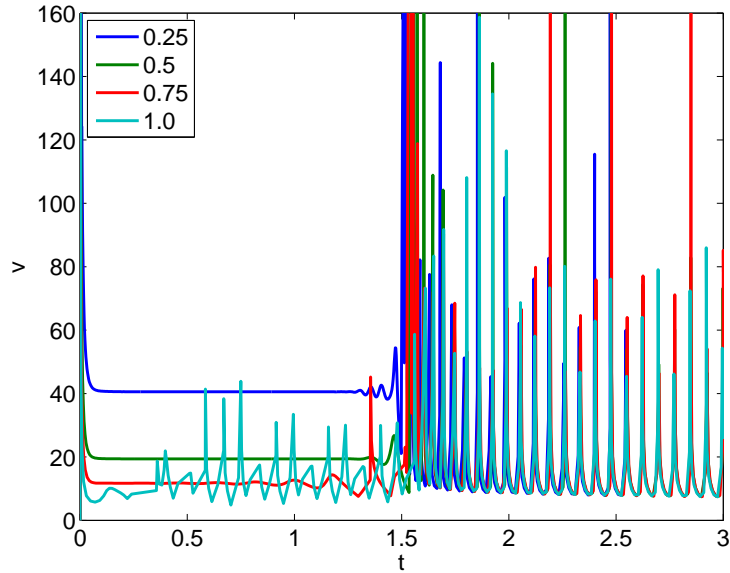


Figure 5.21: Instantaneous velocity of the front against  $t$  for  $p = 0.25, 0.5, 0.75, 1.0$ , when  $Ra = 80$ .

cillations in  $v$  are the result of the location of the front ‘jumping’ forward when a new cell gains sufficient strength for  $Q$  to exceed the threshold value. Velocity is constant while the propagating front is in the form of longitudinal rolls, and smaller values of  $p$  result in a higher front propagating velocity, however once the transition to square cells occurs the velocity appears to be the same for all values of  $p$ . The high front propagation speeds encountered at low values of  $p$  make it difficult to model the front evolution for long periods of time, as this would require very large, and therefore computationally expensive domains. However, results to date support the idea that lower values of  $p$  will eventually result in the same transitions as seen when  $p = 1$ ; longitudinal rolls, followed by square cells, followed by transverse rolls.

#### 5.6.4 Effect of Varying Fourier Wavenumber

The results shown in this section were produced using an initial condition based upon Eqn. (5.74) with  $p = q = 1.0$ . The effect of the value of Fourier wavenumber,  $k$ , chosen for the model was examined, and the results are shown in Figures 5.22 and 5.23; a plot of the front velocity against time is shown for three different values of  $k$  for  $Ra = 80$  and  $Ra = 50$  respectively. For a given value of  $Ra$  no significant differences were found in the computed values of  $v_{as}$  as  $k$  varies. The value of  $k$  chosen appears to affect the transient, small time behaviour of the propagating front, but not the large time behaviour.

The large oscillations present in both Figures 5.22 and 5.23 are a result of the presence of transverse rolls. As shown in Figure 5.24, when  $Ra = 80$  and  $k = \pi$ , the location of the front does not advance at a constant rate with respect to time for  $t \leq 4.5$ . The velocity which is calculated using central differences is therefore subject to large variations. Above  $t \approx 4.5$  the shape of the propagating front changes, with the amplitude increasing more gradually and consequently these oscillations are reduced almost to nothing.

Figure 5.20 shows temperature contours from above, and from the side, for a front propagating in the  $y$ -direction with wavenumber  $k = \pi$  when  $Ra = 80$ , with  $p = q = 1$ . Figures 5.25 and 5.26 show the same plots for a front propagating in the  $y$ -direction with wavenumber  $k = 0.1\pi$  and  $k = 1.5\pi$  respectively. At small time we see a variety of patterns propagating, including purely transverse rolls (Figure 5.25), rectangular cells, (Figure 5.20), and longitudinal rolls (Figure 5.26). However as time increases and the front spreads across the domain, a grain boundary appears and all of these patterns are replaced by transverse rolls which propagate with the same speed, and leave the same wavelength pattern in their wake, in-

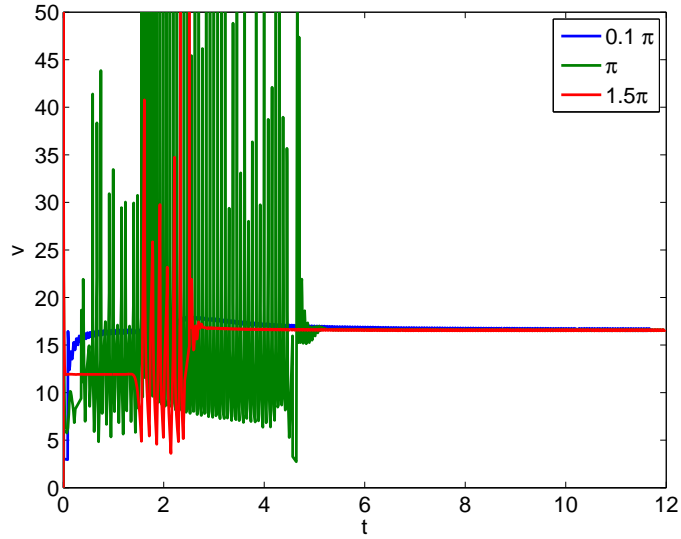


Figure 5.22: Comparison of velocity profiles for  $k = 0.1\pi$ ,  $k = \pi$ ,  $k = 1.5\pi$ .  
 $Ra = 80$ ,  $C = 0.001$  and  $p = q = 1.0$ .

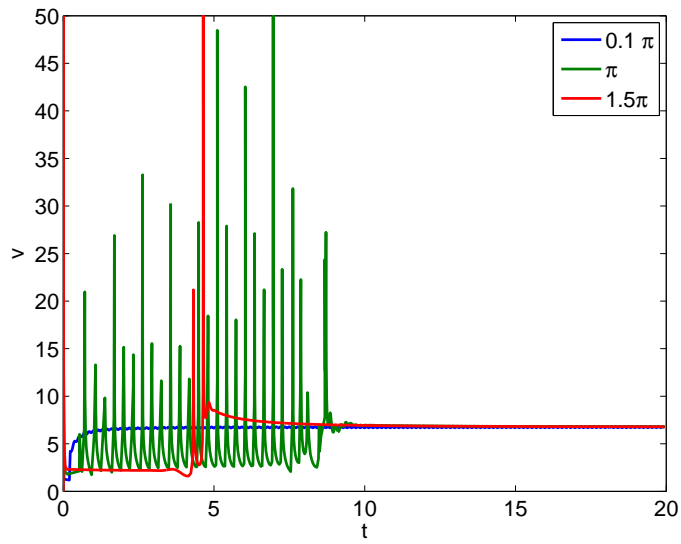


Figure 5.23: Comparison of velocity profiles for  $k = 0.1\pi$ ,  $k = \pi$ ,  $k = 1.5\pi$ .  
 $Ra = 50$ ,  $C = 0.001$  and  $p = q = 1.0$ .

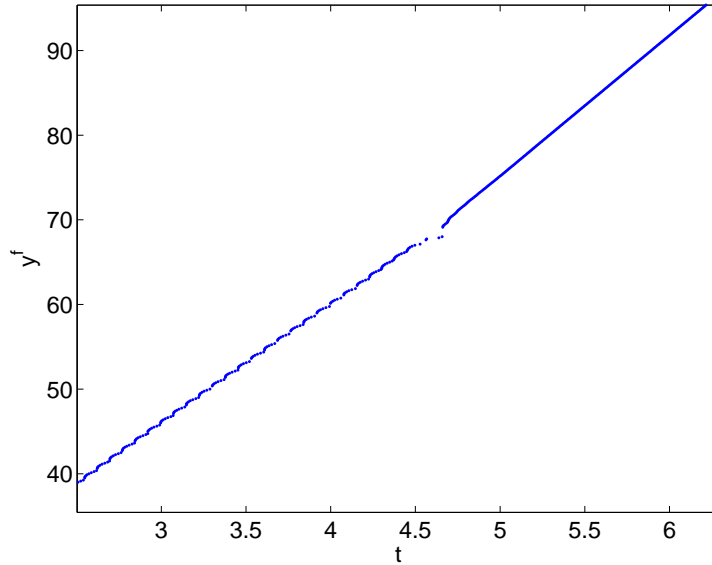


Figure 5.24: Profile of front location with respect to time when  $Ra = 80$  and  $k = \pi$ .

independently of the Fourier wavenumber. The presence of pure transverse rolls indicates that the magnitudes of all variables in modes  $N \geq 1$  have been reduced to zero. Values of  $Ra$  in the range  $40 < Ra \leq 100$  have been examined and similar behaviour is found in all cases.

In summary, it appears that while the initial conditions and value of  $k$  chosen at a given  $Ra$  may affect the initial behaviour of the propagating front, this is not the case at large times. Simulations have been run for a range of  $p$ ,  $k$ , and  $Ra$  and in all cases the propagating front takes the form of transverse rolls at large times and rolls propagate at a speed which is independent of  $k$  and  $p$  for a given value of  $Ra$ . This is at odds with the results of the weakly nonlinear analysis which predicted that longitudinal rolls would dominate. This may be a result of the numerical work being carried out at too high a value of  $Ra$  as a value of  $C = 0.001$  has

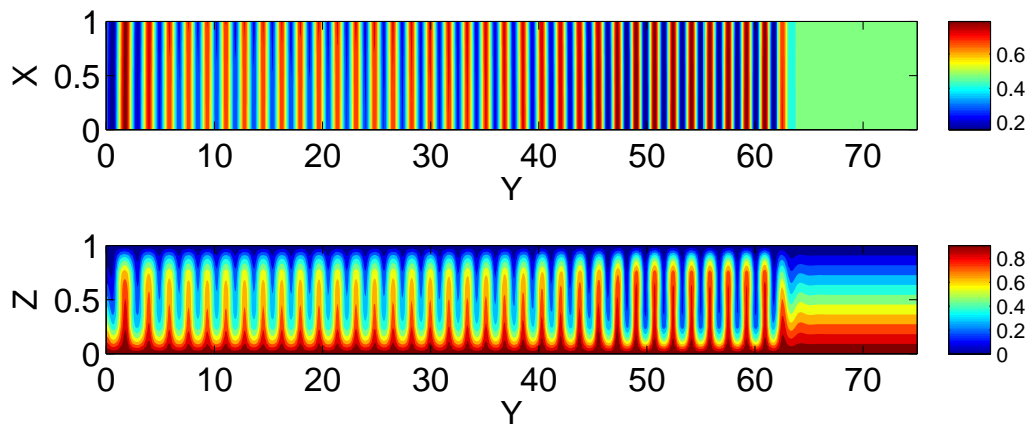


Figure 5.25: Contour plot of  $\theta$  when  $k = 0.1\pi$  from above at  $z = 0.5$  (top) and side on at  $x = 0$ (bottom),  $Ra = 80$ .

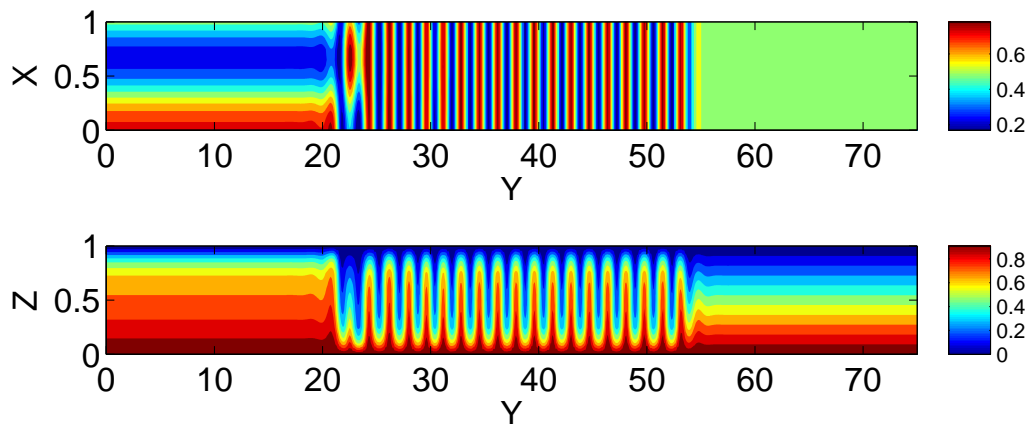


Figure 5.26: Contour plot of  $\theta$  when  $k = 1.5\pi$  from above at  $z = 0.5$  (top) and side on at  $x = 0$ (bottom),  $Ra = 80$ .

been used then for the weakly nonlinear theory to apply  $Ra - 4\pi^2 \varepsilon^2 10^{-6}$  would be required. A careful numerical study for  $Ra$  close to  $4\pi^2$  would be needed to resolve this, this could be facilitated by increasing the value of  $C$  to allow the weakly nonlinear regime to be compared to numerical simulations carried out at slightly higher values of  $Ra$ .

As would be expected the value of  $v_{as}$  calculated for the transverse rolls using the three-dimensional model is almost identical to  $v_{as}$  for transverse rolls calculated using the two-dimensional model.

## 5.7 Conclusions

An exploratory study has been made of the velocity of a propagating front and pattern selection behind such a front for the Darcy-Bénard problem in both two and three dimensions, in both the weakly nonlinear and nonlinear regimes.

In the case of the two-dimensional propagating front the evolution of the speed of the front towards its asymptotic value at large time in both the weakly nonlinear and strongly nonlinear regimes is found to be well described the unifying theory. In the weakly nonlinear regime the amplitude equation for the front takes the form of the Stuart-Landau equation, which also describes front propagation in the Rayleigh-Bénard problem. The asymptotic velocity and wavenumber of the front are found to be independent of the initial conditions. As would be expected, both  $v_{as}$  and  $k_{as}$  increase with  $Ra$ .

The weakly nonlinear analysis of the propagation of a front composed of longitudinal rolls predicts that this pattern should be preferred to transverse rolls when the flow is allowed to be three-dimensional. However this is not confirmed by

the nonlinear finite difference model, which shows transverse rolls dominating at large time. Both longitudinal rolls and rectangular cells have been seen, but the appearance of these flow patterns is dependent upon the initial conditions, and both are eventually replaced by transverse rolls.

## **5.8 Further Work**

The work has sought to apply front propagation theory within the context of the Darcy-Bénard problem for the first time. The results generated show that the situation as regards pattern selection at small time in the fully nonlinear, three-dimensional regime is relatively complex, with the degree of supercriticality, wavenumber and initial conditions all playing a role in determining the initial and asymptotic behaviours of the propagating front. The present study shows that a complete understanding of front propagation will require substantially more computational work.

## Chapter 6

# The Onset of Prandtl-Darcy Convection in a Horizontal Porous Layer subject to a Horizontal Pressure Gradient

In this chapter we consider the onset of convection within an infinite horizontal porous layer heated from below in the presence of a horizontal pressure gradient when the Prandtl-Darcy number is finite. The pressure gradient drives a fluid flow along the layer. The finite Prandtl-Darcy number means there is a delay in the response of the flow field to changes in the temperature or pressure fields.

A linear perturbation analysis is undertaken and an analytical relationship between  $Ra$  and  $k$  is derived. The minimum value of  $Ra$  and the associated wavenumber are obtained numerically using a Newton-Raphson scheme for a range of values of the nondimensional acceleration coefficient,  $\gamma$ , and background velocity,  $Q$ .

The effect of these parameters on the onset of convection is examined. Asymptotic analyses are performed for small and large  $Q$ , and for small  $\gamma$  and their results are compared with the corresponding values which were obtained numerically. We examine the range of validity of these asymptotic solutions which provides additional insight into the behaviour of  $Ra_c$  and  $k_c$  in these regimes.

## 6.1 Background

The Prandtl-Darcy number appears in the denominator of the coefficient multiplying the acceleration term in Darcy's law following nondimensionalisation as given by Eqn. (6.6). As a coefficient to the acceleration term the Prandtl-Darcy number determines how quickly the flow field responds to changes in the temperature or pressure fields. In the majority of papers the Prandtl-Darcy number has been taken to be infinite resulting in the neglect of the time derivative terms in Darcy's law, and a flow which responds immediately to changes in the temperature or pressure fields. However, as interest in porous media has increased, it has been noted that this assumption is not always valid for modern applications; see, for example, binary alloys where the Prandtl number may have values of  $Pr \approx 100$  (Vadasz and Olek (1999)). Work such as that described in Vadasz and Olek (1999) and Vadasz and Olek (2000) has shown that the inclusion of these terms can affect the route to chaos of convective flows in a porous layer.

Prats (1966) considered the effect of horizontal fluid flow on convection in the classical Darcy-Bénard problem and demonstrated that the criterion for neutral stability is unchanged by the presence of the pressure gradient from those derived by Horton and Rogers (1945) and Lapwood (1948). The underlying flow gener-

ated by the pressure gradient causes the convection cells to move along the layer with the velocity of the background flow; this results in temperature and pressure oscillations at any given fixed point in space. It is also clear that even the nonlinear dynamics of convection are unaffected by the background flow because the effect of this flow is removed completely from the governing equations and boundary conditions when using a coordinate system which moves with the flow.

Further studies have been conducted to examine the effect of a horizontal pressure gradient when combined with extensions to Darcy's law such as inertia, local thermal nonequilibrium (LTNE) and thermalsolutal convection. Rees (1997) examined the effect of inertia combined with horizontal pressure gradient and found that, providing both effects are present, the critical Rayleigh number,  $Ra_c$  is raised above  $4\pi^2$  and increases with both increasing inertia and pressure gradient. When the flow is restricted to two dimensions the critical wavenumber  $k_c$  also increases with inertia and pressure gradient, up to a maximum of  $2^{1/4}\pi$ . Postelnicu (2010) examines the case of LTNE in the presence of a horizontal pressure gradient and finds that the convection cells travel at a speed which is less than that of the underlying flow, whilst the relationship between  $Ra_c$ ,  $k_c$  and the pressure gradient is largely determined by the parameters determining heat exchange between the two phases. In the case of thermosolutal convection with a positive separation ratio Lyubimov et al (2008) finds the convection cells again travel at speeds less than the underlying flow, although the difference in speed is reduced when the underlying flow is faster.



Figure 6.1: Fully Saturated Porous Layer with Throughflow.

## 6.2 Governing Equations

We investigate the onset of convection in a fully saturated porous layer, as shown in Figure 6.1. When  $T_0 > T_1$  the layer is unstably stratified and convective motion may occur. We assume that the medium is homogeneous, isotropic, that Darcy's law is valid, that the Oberbeck-Boussinesq approximation is applicable and that the phases are in local thermal equilibrium. The governing equations for flow in a fully saturated porous layer are given by Nield and Bejan (2006) as follows;

$$\nabla \cdot \mathbf{U} = 0, \quad (6.1)$$

$$c_a \rho_\infty \frac{\partial \mathbf{U}}{\partial \hat{t}} = -\nabla \hat{P} - \frac{\mu}{K} \mathbf{U} + \rho_\infty \mathbf{g} \beta (\hat{T} - T_\infty), \quad (6.2)$$

$$\sigma \frac{\partial \hat{T}}{\partial \hat{t}} + \mathbf{U} \cdot \nabla \hat{T} = \kappa \nabla^2 \hat{T}. \quad (6.3)$$

In the case of unidirectional flow  $c_a$  is a scalar constant depending on the geometry of the porous medium which reflects how pore size may impact on the decay of transients. Darcy's law corresponds to when  $c_a = 0$ , and physically this means that

the flow adjusts instantaneously to changes in the pressure gradient. When  $c_a \neq 0$ , the flow takes time to adjust and the rate of adjustment increases as  $c_a \rightarrow 0$ . The value of  $c_a$  is determined primarily by the characteristics of the largest diameter pore tube (Nield and Bejan (2006)).

The following scalings are introduced to nondimensionalise the governing equations;

$$(X, Y, Z) = H(x, y, z), \quad \mathbf{U} = \frac{\kappa}{H} \mathbf{u},$$

$$\hat{P} = \frac{\kappa \mu}{K} P, \quad \hat{t} = \frac{\sigma H^2}{\kappa} t, \quad \hat{T} = \theta \Delta T + T_0. \quad (6.4)$$

Substitution of the scaling identities given in (6.4) into Eqs. (6.1 – 6.3) gives

$$\nabla \cdot \mathbf{u} = 0, \quad (6.5)$$

$$\gamma \frac{\partial \mathbf{u}}{\partial t} = -\nabla P - \mathbf{u} + \text{Ra} \theta \mathbf{g} \quad (6.6)$$

$$\frac{\partial \theta}{\partial t} + \mathbf{u} \cdot \nabla \theta = \nabla^2 \theta, \quad (6.7)$$

subject to the boundary conditions  $\theta = 1$  at  $z = 0$  and  $\theta = 0$  at  $z = 1$ . The two nondimensional parameters are defined as

$$\text{Ra} = \frac{\rho_\infty g \beta K H \Delta T}{\mu \kappa}, \quad \gamma = \frac{c_a K}{\sigma \text{Pr}_m H^2}, \quad (6.8)$$

where

$$\text{Pr}_m = \frac{\mu}{\rho_\infty \kappa}, \quad (6.9)$$

and where  $\gamma$  is the reciprocal of the Prandtl-Darcy number.

It is through  $\gamma$  that the Prandtl-Darcy number affects the flow, and normally this is taken to be sufficiently small that the time derivative may be neglected. Vadasz and Olek (2000) point out that  $\text{Pr}_m$  may take values in the range  $10^{-3}$  for liquid

metals to  $10^3$  for oils, which, when multiplied by the other terms in  $\gamma$  gives rise to values of this parameter in the range  $10^{-23}$  to  $10^2$ . The time derivative also needs to be retained in cases where wave effects are of interest in order to prevent the reduction of the order of the system in the time domain (Vadasz and Olek (2000)), and in cases involving high frequency g-jitter (vibration), as discussed by Bardan and Mojtabi (2000).

The problem is reduced to two dimensions, and the streamfunction is defined as

$$u = -\frac{\partial \psi}{\partial z}, \quad v = \frac{\partial \psi}{\partial x}, \quad (6.10)$$

which reduces the governing equations to the form;

$$\left[1 + \gamma \frac{\partial}{\partial t}\right] \left[\frac{\partial^2 \psi}{\partial x^2} + \frac{\partial^2 \psi}{\partial z^2}\right] = \text{Ra} \frac{\partial \theta}{\partial x}, \quad (6.11)$$

$$\frac{\partial \theta}{\partial t} - \frac{\partial \psi}{\partial z} \frac{\partial \theta}{\partial x} + \frac{\partial \psi}{\partial x} \frac{\partial \theta}{\partial z} = \frac{\partial^2 \theta}{\partial x^2} + \frac{\partial^2 \theta}{\partial z^2}. \quad (6.12)$$

### 6.3 Linear Perturbation Analysis

The basic steady state solution to Eqs. (6.11 – 6.12) is

$$\theta = 1 - z, \quad \psi = -Q(z - \frac{1}{2}), \quad (6.13)$$

where  $Q$  is the background Darcy velocity. The linear perturbation analysis proceeds by setting

$$\theta = 1 - z + \theta', \quad \psi = -Q(z - \frac{1}{2}) + \psi', \quad (6.14)$$

in Eqs. (6.11 – 6.12), to obtain,

$$\left[1 + \gamma \frac{\partial}{\partial t}\right] \left[\frac{\partial^2 \psi'}{\partial x^2} + \frac{\partial^2 \psi'}{\partial z^2}\right] = \text{Ra} \frac{\partial \theta'}{\partial x}, \quad (6.15)$$

$$\frac{\partial \theta'}{\partial t} + Q \frac{\partial \theta'}{\partial x} - \frac{\partial \psi'}{\partial x} = \frac{\partial^2 \theta'}{\partial x^2} + \frac{\partial^2 \theta'}{\partial z^2}, \quad (6.16)$$

where both  $\theta'$  and  $\psi'$  are taken to be asymptotically small. At onset, we expect convection to take the form of travelling waves, and therefore we introduce the substitutions,

$$\psi' = \text{Re} \left[ f(z) e^{ik(x-ct)} \right], \quad \theta' = \text{Re} \left[ -ig(z) e^{ik(x-ct)} \right], \quad (6.17)$$

where  $c$  is the phase velocity of the cells, into Eqs. (6.15 – 6.16). This yields,

$$[f'' - k^2 f][1 - i\gamma kc] = \text{Ra} kg, \quad (6.18)$$

$$g'' - k^2 g = kf - ig(c - Q). \quad (6.19)$$

We note that the setting of  $\gamma = 0$ ,  $Q = 0$  and  $c = 0$  leads to the recovery of the classical Darcy-Bénard perturbation equations as derived by Horton and Rogers (1945) and Lapwood (1948). Continuing with our analysis we let

$$f = A \sin(\pi z), \quad g = B \sin(\pi z), \quad (6.20)$$

and substitute these into Eqs. (6.18 – 6.19). We take both  $\text{Ra}$  and  $c$  to be purely real. The imaginary parts give

$$c = \frac{Q}{1 + (\pi^2 + k^2)\gamma}, \quad (6.21)$$

while the substitution of this into the real component gives

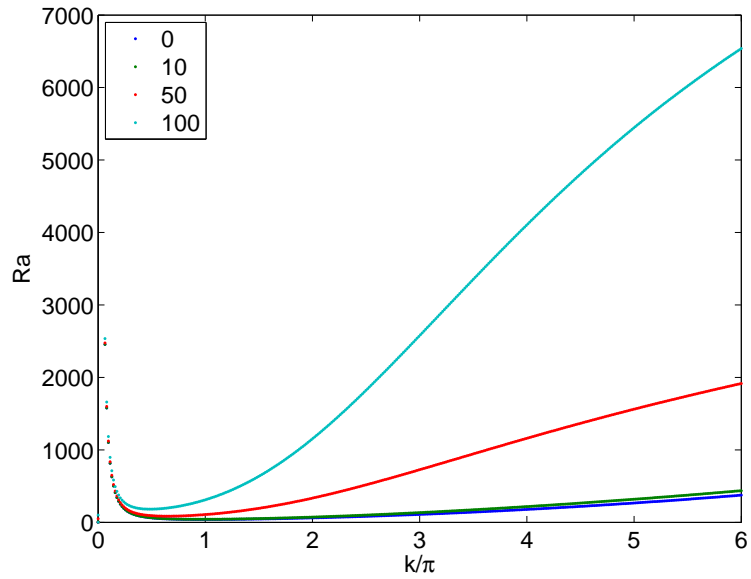
$$\text{Ra} = \frac{(\pi^2 + k^2)^2}{k^2} + \frac{\gamma^2 Q^2 (\pi^2 + k^2)^2}{(1 + \gamma(\pi^2 + k^2))^2}. \quad (6.22)$$

We note that when  $\gamma = 0$  Eqn. (6.21) gives  $c = Q$ , and we recover the case investigated by Prats (1966), where the convection patterns move with the underlying flow. Increasing the value of  $\gamma$  from zero results in a reduction of the speed of the convection pattern from  $Q$ ; that is, the convection pattern is moving slower than the underlying flow. This is in agreement with the results found by Postelnicu (2010) and Lyubimov et al (2008). Eqn. (6.22) yields neutral curves of the classical type for Bénard-like layers where one minimum exists and where  $Ra \rightarrow \infty$  as  $k \rightarrow 0$  and  $k \rightarrow \infty$ .

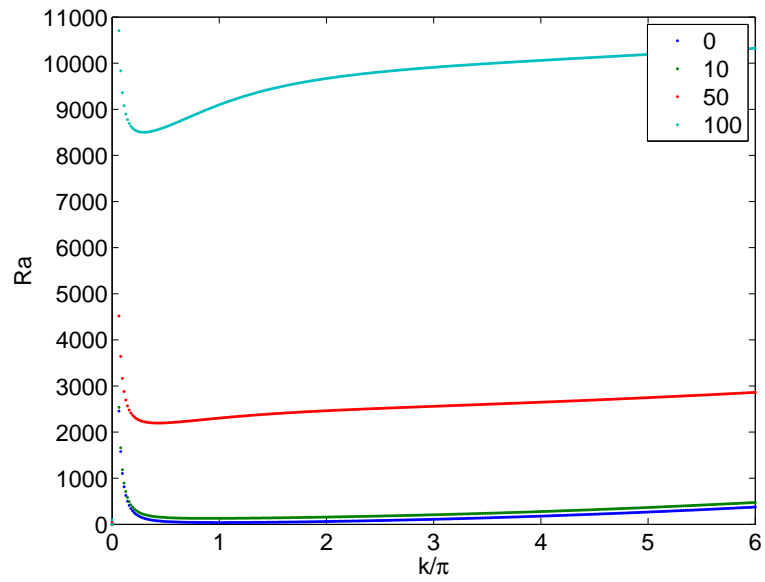
Samples of some neutral curves for fixed values of  $Q$  and  $\gamma$  are given in Figures 6.2 and 6.3. When  $Q = 0$  in Figure 6.2,  $Ra_c = 4\pi^2$  and we recover the classical Darcy-Bénard problem, as in the absence of an underlying flow the instability is stationary and therefore  $\gamma$  is irrelevant. As  $Q$  increases, so does  $Ra_c$ , whilst the range of wavenumbers over which growth occurs for a given value of  $Ra_c$  is reduced.

In Figure 6.3a we see the neutral curves forming a band with the curves clustering together at either extreme for values of  $\gamma$  which are large or small, whilst  $Ra_c$  is very sensitive to changes in  $\gamma$  when  $\gamma$  is moderate in size. The width of this band increases with  $Q$ . In all cases shown in Figures 6.2 and 6.3,  $Ra_c$  is increased as either  $\gamma$  or  $Q$  increases from zero.

The minimum value of the neutral curve corresponds to the most unstable case. While one may differentiate Eqn. (6.22) easily with respect to  $k$ , in order to determine the value of  $k$  that minimises  $Ra_c$ , the resulting expression cannot be solved analytically and therefore we resort to numerical methods.

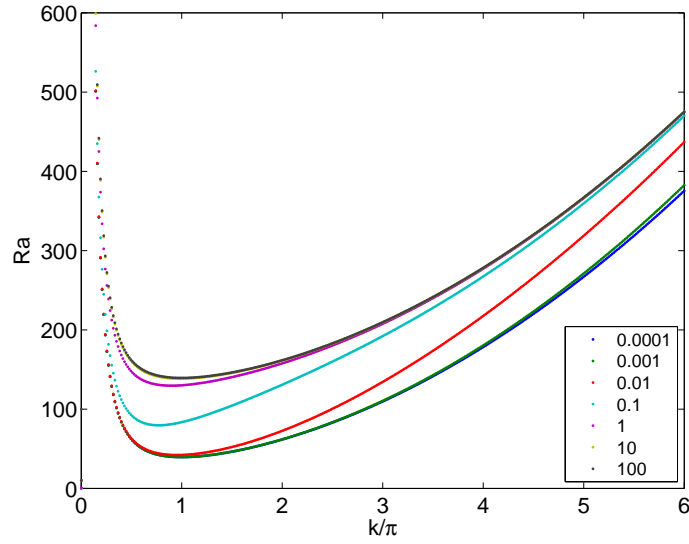


(a)

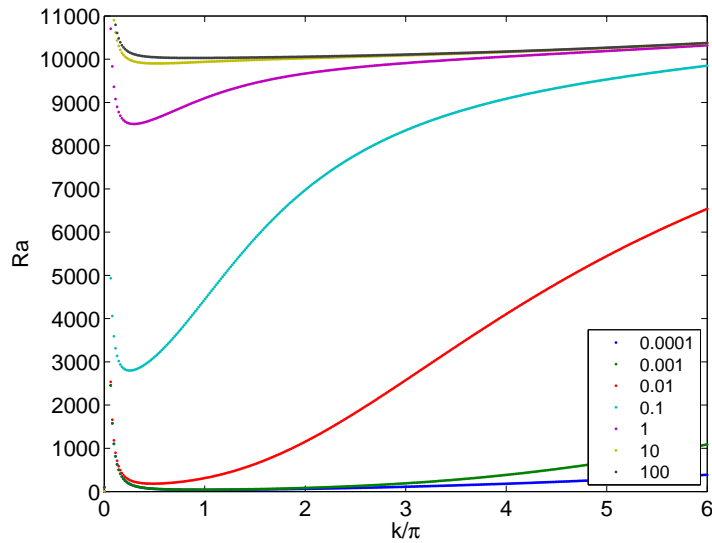


(b)

Figure 6.2: Neutral curves for (a)  $\gamma = 0.01$  and (b)  $\gamma = 1.0$ ,  $Q = 0, 10, 50$  and  $100$ .



(a)



(b)

Figure 6.3: Neutral curves for (a)  $Q = 10$ , (b)  $Q = 100$  and  $\gamma = 0.0001, 0.001, 0.01, 0.1, 1.0, 10.0$  and  $100.0$ .

## 6.4 Numerical Method

Eqn. (6.22) is minimised over  $k$  using a 2D Newton-Raphson (NR) method. At a minimum in the neutral curve the following equations are satisfied:

$$f(\text{Ra}, k) = \text{Ra} - \frac{(\pi^2 + k^2)^2}{k^2} - \frac{\gamma^2 Q^2 (\pi^2 + k^2)^2}{(1 + \gamma(\pi^2 + k^2))^2} = 0, \quad (6.23)$$

$$g(\text{Ra}, k) = \frac{\partial f}{\partial k} = 0, \quad (6.24)$$

where  $\partial \text{Ra} / \partial k = 0$  is assumed. The appropriate NR iteration scheme is

$$\begin{pmatrix} \text{Ra}_{n+1} \\ k_{n+1} \end{pmatrix} = \begin{pmatrix} \text{Ra}_n \\ k_n \end{pmatrix} - \begin{pmatrix} \frac{\partial f}{\partial \text{Ra}} & \frac{\partial f}{\partial k} \\ \frac{\partial^2 f}{\partial k \partial \text{Ra}} & \frac{\partial^2 f}{\partial k^2} \end{pmatrix}^{-1} \begin{pmatrix} f \\ \frac{\partial f}{\partial k} \end{pmatrix}_n, \quad (6.25)$$

where the subscript  $n$  denotes the iteration number. The components of the matrix are simple to evaluate analytically in the following two cases:

$$\frac{\partial f}{\partial \text{Ra}} = 1 \quad \text{and} \quad \frac{\partial^2 f}{\partial k \partial \text{Ra}} = 0. \quad (6.26)$$

The remaining components of the scheme are evaluated numerically using second order accurate central differences because this is less intensive computationally than when the exact derivatives are used. The solution is judged to have been obtained when the maximum correction term becomes less than  $1 \times 10^{-8}$ .

## 6.5 Numerical Results

The numerical scheme outlined in the previous section allows the calculation of the minimum critical values of  $\text{Ra}_c$  and the corresponding  $k_c$  across a range of values  $Q$  and  $\gamma$ . These are shown using a ‘neutral surface’ in Figure 6.4. Figure

6.4 indicates that the values of  $Ra_c$  and  $k_c$  are more sensitive to variations in  $\gamma$  than those in  $Q$ . Figure 6.4a shows that  $Ra_c$  rises with increasing  $Q$  and  $\gamma$  whilst Figure 6.4b shows that  $k_c \leq \pi$  for all values of  $Q$  and  $\gamma$  tested.

The most significant feature of Figure 6.4b is a rapid change in values of  $k_c$  as  $\gamma$  increases from zero. When  $\gamma = 0$  we recover the case investigated by Prats (1966); both  $Ra_c$  and  $k_c$  are independent of  $Q$  and remain at those values which were determined by Horton and Rogers (1945) and Lapwood (1948). However, small increases of  $\gamma$  above zero result in sharp reduction in  $k_c$ , and this is more pronounced at higher values of  $Q$ ; this behaviour is examined in Sect. 6.8. In Figure 6.4a,  $Ra_c$  increases rapidly with  $\gamma$ , and again this is amplified at higher values of  $Q$ . Figure 6.5 clarifies these results by showing the variation of  $Ra_c$  and  $k_c$  with  $\gamma$  for different values of  $Q$ .

Physically, these results imply that with increasing Prandtl-Darcy number and  $Q$  the flow becomes more stable, and the wavelength of the most dangerous disturbance increases.

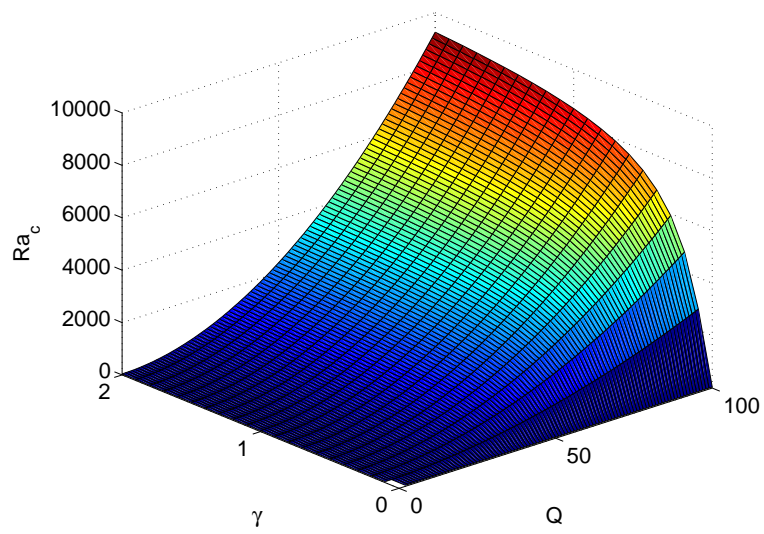
## 6.6 Asymptotic analysis for $Q \ll 1$

We investigate the regime where the underlying flow is extremely weak but where  $\gamma$  takes  $O(1)$  values. Upon setting  $\varepsilon = Q^2$ , we expand  $k$  and  $Ra$  in orders of  $\varepsilon$ :

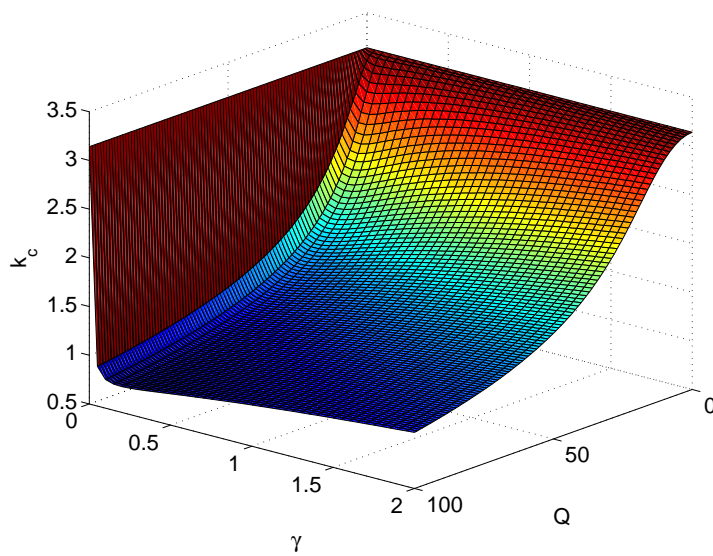
$$\begin{aligned} k &= \pi(1 + \varepsilon k_1 + \varepsilon^2 k_2 + O(\varepsilon^3) + \dots), \\ Ra &= 4\pi^2 + \varepsilon Ra_1 + \varepsilon^2 Ra_2 + O(\varepsilon^3) + \dots, \end{aligned} \quad (6.27)$$

and substitute these into Eqn. (6.22). Equating terms of order  $\varepsilon$  we obtain

$$Ra_1 = \frac{4\pi^2 \gamma^2}{(1 + 2\pi^2 \gamma)^2}. \quad (6.28)$$

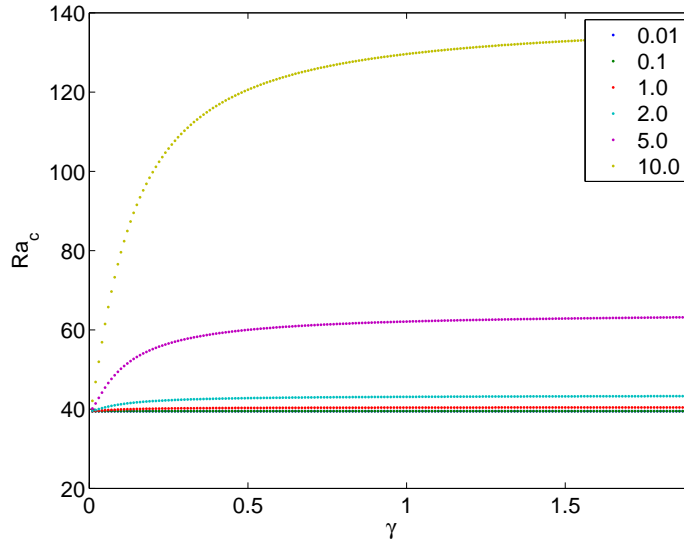


(a)

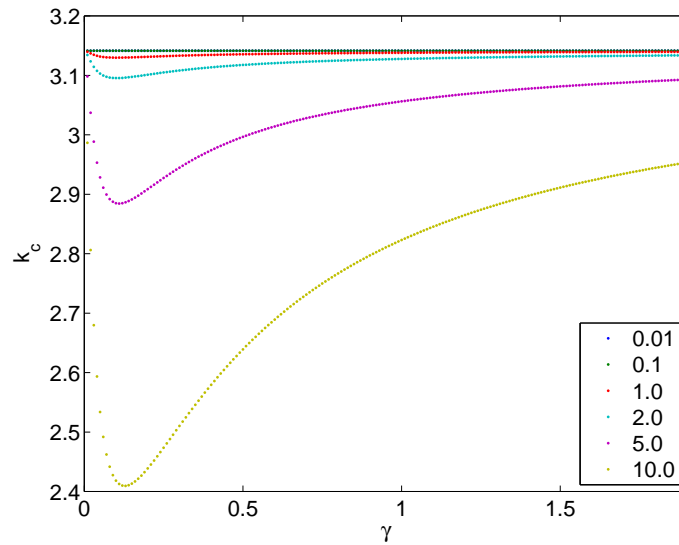


(b)

Figure 6.4: Surfaces showing (a)  $Ra_c$  and (b)  $k_c$  for the  $Q - \gamma$  parameter space.



(a)



(b)

Figure 6.5: Variation of (a)  $Ra_c$  and (b)  $k_c$  with  $\gamma$ , for  $Q = 0.01, 0.1, 1.0, 2.0, 5.0,$  and  $10.0$ .

At order  $\varepsilon^2$  we find

$$\text{Ra}_2 = 4\pi^2 k_1^2 + \frac{8\pi^4 \gamma^2 k_1}{(1 + 2\pi^2 \gamma)^3}, \quad (6.29)$$

which is a function of  $k_1$ . The value of  $\text{Ra}_2$  is minimised when its gradient with respect to  $k_1$  is zero giving;

$$k_1 = -\frac{\pi^2 \gamma^2}{(1 + 2\pi^2 \gamma)^3}. \quad (6.30)$$

Substitution of Eqs. (6.28 – 6.30) into Eqn. (6.27) gives:

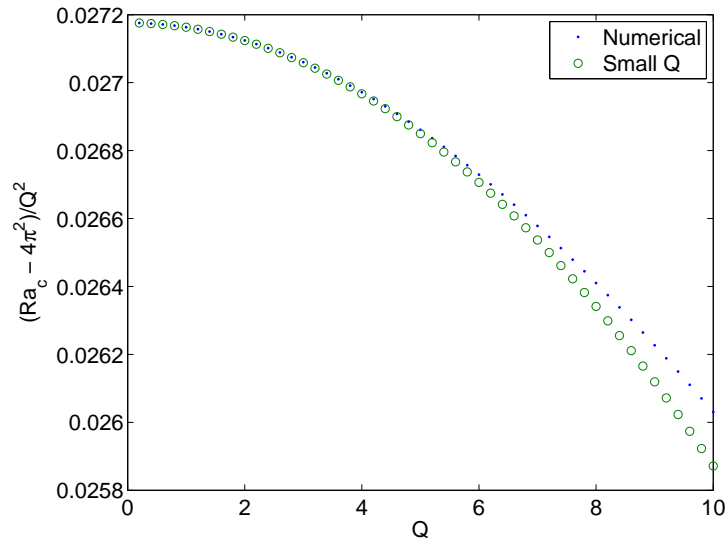
$$\text{Ra}_c = 4\pi^2 + \frac{4\pi^2 \gamma^2}{(1 + 2\pi^2 \gamma)^2} Q^2 - \frac{4\pi^6 \gamma^4}{(1 + 2\pi^2 \gamma)^6} Q^4 + O(Q^6), \quad (6.31)$$

$$k_c = \pi \left( 1 - \frac{\pi^2 \gamma^2}{(1 + 2\pi^2 \gamma)^3} Q^2 \right) + O(Q^4). \quad (6.32)$$

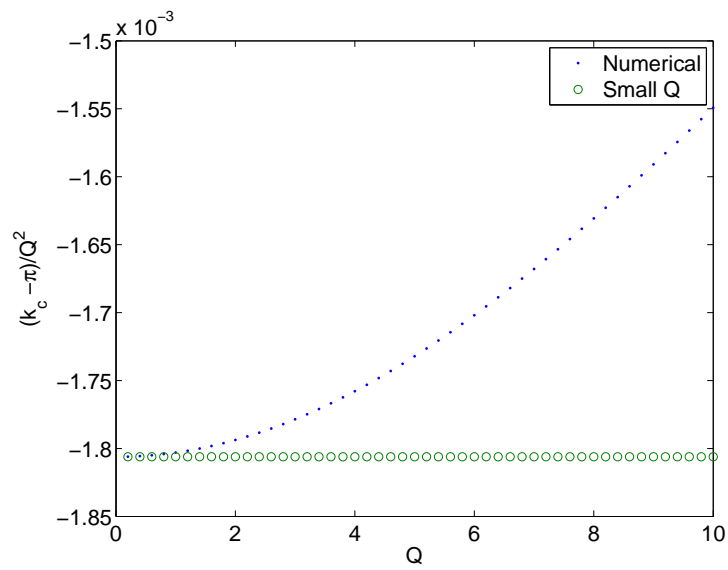
This confirms that, while the critical Rayleigh number increases by an  $O(Q^2)$  amount, the reduction in the value of  $k_c$  is of the same order of magnitude.

Sample results obtained from this analysis for  $\gamma = 0.01$  and  $\gamma = 1$  are shown in Figures 6.6 and 6.7 respectively, along with the results produced by the NR method. In order to allow better comparison between the numerical and asymptotic results, we plot the values of  $(\text{Ra}_c - 4\pi^2) / Q^2$  and  $(k_c - \pi) / Q^2$  against  $Q$  in Figures 6.6 and 6.7. Agreement between the numerical and asymptotic values of  $\text{Ra}_c$  for values of  $Q$  is extremely good. Whilst the value of  $k_c$  diverges rapidly from that predicted numerically it shows that the next term in the series is of  $O(Q^4)$ .

Table 6.1 compares, to 8 decimal places, the values of  $\text{Ra}_c$  and  $k_c$  produced by the NR scheme with those given by the asymptotic analysis for a range of  $\gamma$  and  $Q$ . It shows an excellent agreement between both methods for all values of  $\gamma$  when  $Q \leq 1$ . Agreement for  $\text{Ra}_c$  remains reasonable to  $Q = 10$ , but has deteriorated for  $k_c$ , as would be expected given the smaller order of accuracy of the asymptotic approximation to  $k_c$ .

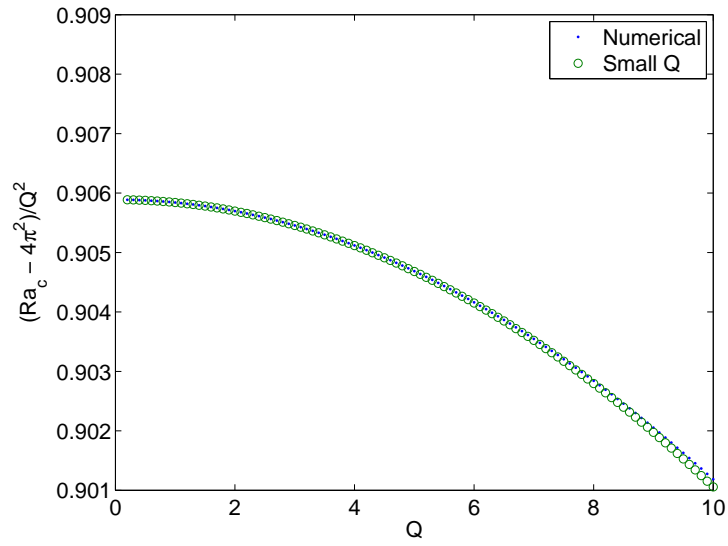


(a)

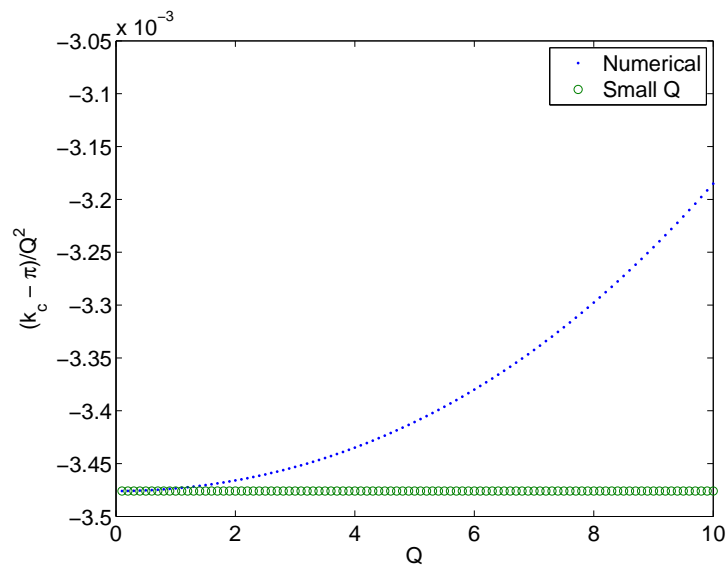


(b)

Figure 6.6: (a)  $Ra_c$  and (b)  $k_c$  for  $Q \ll 1$ , with  $\gamma = 0.01$ .



(a)



(b)

Figure 6.7: (a)  $Ra_c$  and (b)  $k_c$  for  $Q \ll 1$ , with  $\gamma = 1$ .

$Q$	$\gamma$	$Ra_c$			$k_c$		
		Exact	$Q \ll 1$	$\frac{Ra_{Q \ll 1}}{Ra_{\text{exact}}} - 1$	Exact	$Q \ll 1$	$\frac{k_{Q \ll 1}}{k_{\text{exact}}} - 1$
0.01	0.01	39.47842032	39.47842032	0.00	3.14159247	3.14159247	0.00
0.01	0.1	39.47846166	39.47846166	0.00	3.14159147	3.14159147	0.00
0.01	1.0	39.47850819	39.47850819	0.00	3.14159231	3.14159230	$-3.18 \times 10^{-9}$
1.0	0.01	39.50558065	39.50558063	$-5.06 \times 10^{-10}$	3.13978967	3.13978656	$-9.91 \times 10^{-7}$
1.0	0.1	39.91841936	39.91841726	$-5.26 \times 10^{-8}$	3.12987062	3.12980408	$-2.13 \times 10^{-5}$
1.0	1.0	40.38425855	40.38425854	$-2.48 \times 10^{-10}$	3.13811919	3.13811670	$-7.93 \times 10^{-7}$
10.0	0.01	42.08145918	42.06554590	$-3.78 \times 10^{-4}$	2.98667333	2.96098320	$-8.60 \times 10^{-3}$
10.0	0.1	79.59584290	77.97514910	-0.02	2.41831020	1.96273495	-0.19
10.0	1.0	129.59698851	129.58405612	$-9.98 \times 10^{-5}$	2.82307389	2.79399802	-0.01

Table 6.1: Comparison of  $Ra_c$ ,  $k_c$  for the exact, and  $Q \ll 1$  analyses and the relative error.

## 6.7 Asymptotic Analysis for $\gamma \ll 1$

We turn our attention to the stability of the system for small values of the inverse Prandtl-Darcy number. In this case we let  $\gamma = \varepsilon$  and expand  $k$  and  $Ra$  as in (6.27).

Substituting into Eqn. (6.22) gives  $Ra_1 = 0$  at  $O(\varepsilon)$ . At  $O(\varepsilon^2)$  we obtain  $k_1 = 0$  and  $Ra_2 = 4\pi^4 Q^2$ . Equating terms at  $O(\varepsilon^3)$  gives  $Ra_3 = -16\pi^6 Q^2$ . Finally the  $O(\varepsilon^4)$  terms give

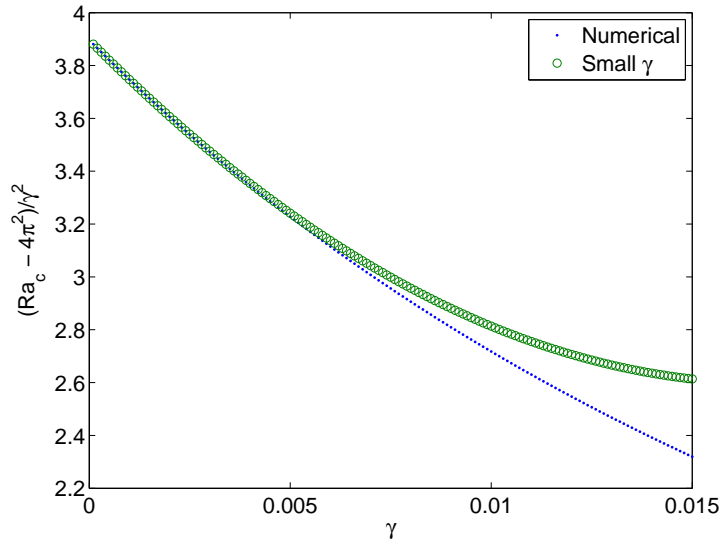
$$Ra_4 = 4\pi^2 k_2^2 + 4\pi^4 Q^2 (2k_2 + 12\pi^4), \quad (6.33)$$

which is minimised when  $k_2 = -\pi^2 Q^2$ . Consequently the critical values of  $Ra$  and  $k$  are calculated as;

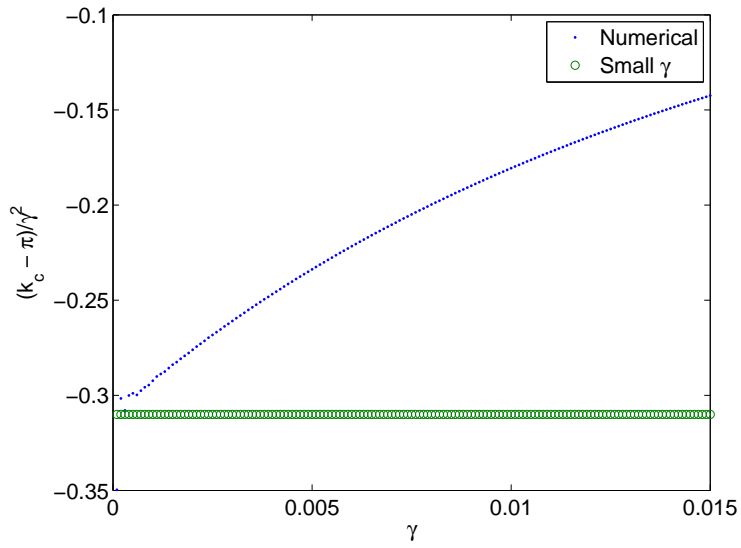
$$Ra_c = 4\pi^2 \left[ 1 + \pi^2 Q^2 \gamma^2 - 4\pi^4 Q^2 \gamma^3 + (12\pi^6 Q^2 - \pi^4 Q^4) \gamma^4 + O(\gamma^5) \right], \quad (6.34)$$

$$k_c = \pi(1 - \pi^2 Q^2 \gamma^2 + O(\gamma^3)). \quad (6.35)$$

Figure 6.8 shows a comparison of those values of (a)  $Ra_c$  and (b)  $k_c$  produced by the 2D Newton-Raphson scheme and the small- $\gamma$  asymptotic analysis. We see that the range of applicability of the small- $\gamma$  analysis is smaller than that of the small  $Q$ , however this is not altogether surprising given the increased sensitivity to  $\gamma$  versus  $Q$  as shown in Figure 6.4. Applicability for the asymptotic approximation of  $k_c$  is limited, as would be expected given that it is only approximated to  $O(\gamma^3)$ .

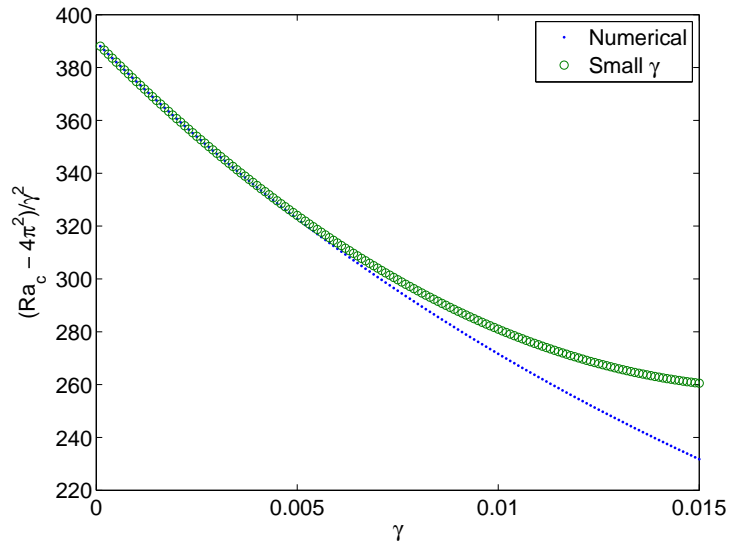


(a)

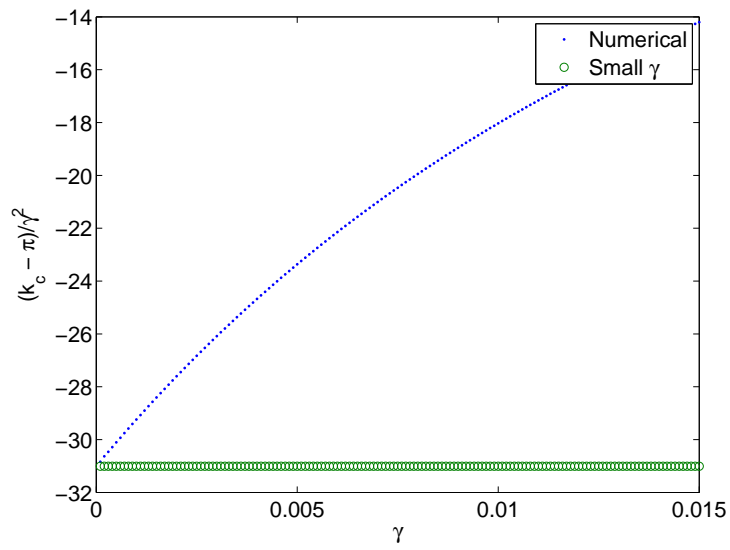


(b)

Figure 6.8: (a)  $Ra$  and (b)  $k$  for  $\gamma \ll 1$ , with  $Q = 0.1$ .

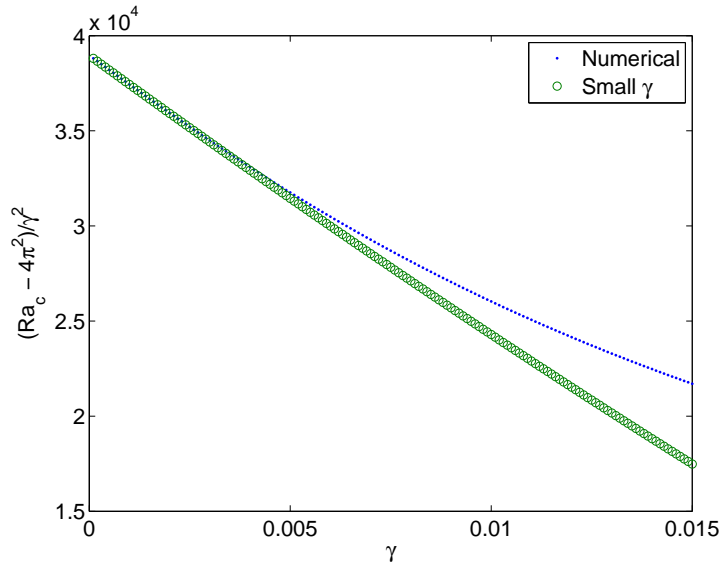


(a)

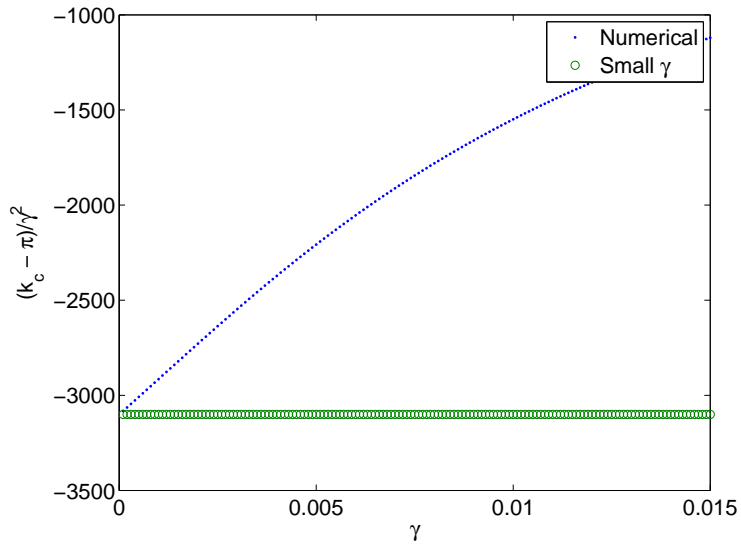


(b)

Figure 6.9: (a)  $Ra$  and (b)  $k$  for  $\gamma \ll 1$ , with  $Q = 1.0$ .



(a)



(b)

Figure 6.10: (a)  $Ra$  and (b)  $k$  for  $\gamma \ll 1$ , with  $Q = 10.0$ .

$Q$	$\gamma$	$Ra_c$			$k_c$		
		Exact	$\gamma \ll 1$	$\frac{Ra_{\gamma \ll 1}}{Ra_{\text{exact}}} - 1$	Exact	$\gamma \ll 1$	$\frac{k_{\gamma \ll 1}}{k_{\text{exact}}} - 1$
0.01	0.001	39.47841764	39.47841764	0.0	3.14159265	3.14159265	0.0
0.01	0.01	39.47842032	39.47842042	0.0	3.14159247	3.14159234	$-4.14 \times 10^{-8}$
0.01	0.1	39.47846166	39.48182351	$8.52 \times 10^{-5}$	3.14159147	3.14156165	$-9.49 \times 10^{-6}$
0.1	0.001	39.47842135	39.47842135	0.0	3.14159236	3.14159234	$-6.37 \times 10^{-9}$
0.1	0.01	39.47868936	39.47869896	$2.43 \times 10^{-7}$	3.14157459	3.14156165	$-4.12 \times 10^{-6}$
0.1	0.1	39.48282310	39.81897000	$8.51 \times 10^{-3}$	3.14147477	3.13849203	$-9.49 \times 10^{-4}$
1.0	0.001	39.47879230	39.47879231	$2.5 \times 10^{-10}$	3.14156341	3.14156165	$-5.60 \times 10^{-7}$
1.0	0.01	39.50558065	39.50651505	$2.37 \times 10^{-5}$	3.13978967	3.13849203	$-4.13 \times 10^{-4}$
1.0	0.1	39.91841936	73.15294735	0.83	3.12987061	2.83152989	-0.095

Table 6.2: Comparison of  $Ra_c$ ,  $k_c$  for the exact and  $\gamma \ll 1$  analyses and the relative error.

Table 6.2 shows detailed results for both the numerical and small  $\gamma$ , values of  $k_c$  and  $Ra_c$  along with the relative error. Agreement is excellent for all  $Q$  when  $\gamma = 0.001$  but has deteriorated significantly in the case of  $Q = 1, \gamma = 0.1$ .

## 6.8 Asymptotic Analysis for $Q \rightarrow \infty$

We investigate the situation when  $Q \rightarrow \infty$ , that is the speed of throughflow becomes large. Examination of the detailed numerical results shown in Figures 6.5b and 6.5a suggests that the expanded form of  $k$  and  $Ra$  should be:

$$k = \frac{1}{\sqrt{Q}} \left( k_1 + \frac{k_2}{Q} + O(Q^{-2}) \right), \quad (6.36)$$

$$Ra = Q^2 Ra_1 + Q Ra_2 + O(1). \quad (6.37)$$

Substituting these series into Eqn. (6.22) gives

$$Ra_1 = \frac{\gamma^2 \pi^4}{(1 + \gamma \pi^2)^2} \quad (6.38)$$

at  $O(Q^2)$  but no information is gained about  $k_1$ . At  $O(Q)$  we find that

$$Ra_2 = \frac{\pi^4}{k_1^2} + \frac{2\pi^2 \gamma^2 k_1^2}{(1 + \gamma \pi^2)^3}. \quad (6.39)$$

It is clear that  $Ra_2$  has a unique minimum value when

$$k_1 = \left( \frac{\pi^2 (1 + \gamma \pi^2)^3}{2\gamma^2} \right)^{\frac{1}{4}}. \quad (6.40)$$

Hence

$$Ra_2 = \frac{2\sqrt{2}\pi^3 \gamma}{(1 + \gamma \pi^2)^{3/2}}, \quad (6.41)$$

and therefore we find that,

$$\text{Ra}_c = \frac{\gamma^2 \pi^4}{(1 + \gamma \pi^2)^2} Q^2 + \frac{2\sqrt{2}\pi^3 \gamma}{(1 + \gamma \pi^2)^{3/2}} Q + O(1), \quad (6.42)$$

$$k_c = \left( \frac{\pi^2(1 + \gamma \pi^2)^3}{2\gamma^2} \right)^{1/4} \frac{1}{\sqrt{Q}} + O(Q^{-3/2}). \quad (6.43)$$

The next order in powers of  $Q$  will allow us to evaluate  $\text{Ra}_3$ , but this value is independent of  $k_2$ . The next term in the series for  $k$  will be obtained by minimising  $\text{Ra}_4$  with respect to  $k_2$ .

Table 6.3 compares the numerical and asymptotic results for  $\text{Ra}_c$  and  $k_c$  along with the relative error between the two sets of data. Agreement is outstanding at  $Q = 7000$ , and we would only expect this to improve as  $Q$  increases, although the limitations of the numerical method prevent us from investigating this further. The large- $Q$  relationship is shown to still provide a reasonable order of magnitude estimation as low as  $Q = 2000$ .

$Q$	$\gamma$	Ra			$k$		
		Exact	$Q \rightarrow \infty$	$\frac{\text{Ra}_{Q \rightarrow \infty}}{\text{Ra}_{\text{exact}}} - 1$	Exact	$Q \rightarrow \infty$	$\frac{k_{Q \rightarrow \infty}}{k_{\text{exact}}} - 1$
2000	0.01	33824	33800	$-7.10 \times 10^{-4}$	0.3568	0.3577	$2.52 \times 10^{-3}$
5000	0.01	205567	205544	$-1.12 \times 10^{-4}$	0.2260	0.2262	$8.85 \times 10^{-4}$
7000	0.01	400757	400734	$-5.74 \times 10^{-5}$	0.1910	0.1912	$1.05 \times 10^{-3}$
2000	1.0	3302764	3302752	$-3.63 \times 10^{-6}$	0.1999	0.1995	$-2.00 \times 10^{-3}$
5000	1.0	20623862	20623851	$-5.33 \times 10^{-7}$	0.1263	0.1262	$-7.92 \times 10^{-4}$
7000	1.0	40415907	40415896	$-2.72 \times 10^{-7}$	0.1067	0.1066	$-9.37 \times 10^{-4}$

Table 6.3: Comparison of  $\text{Ra}_c$ ,  $k_c$  for exact and  $Q \rightarrow \infty$  analyses and the relative error.

## 6.9 Conclusions

A linear perturbation analysis has been carried out for a fully saturated porous layer, heated from below, with a finite Prandtl-Darcy number in the presence of a horizontal pressure gradient. The speed of the convection pattern is found to be lower than that of the underlying flow whenever  $\gamma \neq 0$  and  $Q \neq 0$ . An expression relating  $Ra$  and  $k$  is obtained, and a 2D Newton-Raphson scheme used to minimise this expression for  $Ra_c$  and  $k_c$  over a range of  $\gamma$  and  $Q$ . These results indicate that the flow becomes more stable with increasing  $Q$ , and the wavelength of the most dangerous disturbance also increases with  $Q$ .

Asymptotic expansions for small  $Q$ , small  $\gamma$  and large  $Q$  have been undertaken. These show that, in the small  $Q$  regime, the increase in  $Ra_c$  from  $4\pi^2$  is proportional to  $Q^2$  at leading order, although the rate of increase is also a function of  $\gamma$  and varies between 0 and  $1/\pi^2$ . The same analysis shows that  $k_c$  reduces by an  $O(Q^2)$  amount. When  $\gamma$  is small,  $Ra_c$  grows in proportion to  $\gamma^2$  and  $k_c$  reduces by an  $O(Q^2)$  amount although both are also a function of  $Q^2$ . As  $Q \rightarrow \infty$ ,  $Ra_c$  increases in proportion with  $Q^2$  at leading order, and the rate of increase is a function of  $\gamma$ . The critical wavenumber,  $k_c$ , varies with  $Q^{-1/2}$ . The results of the asymptotic analyses have been compared with those produced by the Newton-Raphson scheme.

## **Chapter 7**

# **Final Conclusions and Further Work**

Three topics in the field of thermoconvective instabilities in porous media have been investigated. These are (i) vortex instability in the inclined thermal boundary layer, (ii) front propagation in the Darcy-Bénard problem and (iii) the onset of Prandtl-Darcy convection in a horizontal porous layer subject to a horizontal pressure gradient. The key results from each of these topics, along with suggestions for future work where appropriate, are detailed individually in the relevant chapter. The aim of the present chapter is to provide a brief overview of the thesis as a whole, as well as identifying areas where these topics could be combined to provide further insight into thermoconvective instability in porous media.

## 7.1 Overview

The investigation into the inclined thermal boundary layer sought to determine, without recourse to some of the approximations that have brought into question the work of other authors, the nature of the instability generated by vortex disturbances at arbitrary angles of inclination of the layer. The fully nonlinear, elliptic, governing equations were solved numerically, and extensive validation of this code was undertaken. Our key finding was that at moderate angles of inclination, and within the finite domains studied, the boundary layer was convectively, rather than absolutely, unstable to vortex type disturbances. However, when disturbances were forced (by means of boundary conditions along the whole of the heated surface, or located at the leading edge) critical distances were found to be in excellent agreement with the results of parabolic simulations.

To the author's knowledge no study of front propagation, neither experimental nor numerical, has previously been carried out for the Darcy-Bénard problem. It was found that the unifying theory described the behaviour of a two-dimensional propagating front composed of transverse rolls well, but that the situation was considerably more complicated in three-dimensions with combinations of transverse and longitudinal rolls appearing depending on initial conditions and disturbance wavenumber. This is certainly an area where further work could be undertaken.

The study of the onset of Prandtl-Darcy convection in a horizontal porous layer subject to a horizontal pressure gradient assesses the impact of combining two extensions to the classical Darcy-Bénard problem; a finite Prandtl-Darcy number and an underlying fluid flow. A linear perturbation analysis leads to the development of an analytical relationship between  $Ra$  and  $k$ , and results from a numerical minimisation of this relationship were compared to asymptotic analyses for small

and large  $Q$  and small  $\gamma$ . Results indicate that the flow becomes more stable as the underlying flow increases, and that the wavelength of the most dangerous disturbance also increases with the strength of the underlying flow.

## 7.2 Further Work

The inclined boundary layer work found the boundary layer to be convectively unstable to vortex disturbances in the range  $35^\circ \leq \alpha \leq 60^\circ$ ,  $k \leq 0.01$  and  $50 \leq \xi_{\max} \leq 100$ . In the event that computational resources allow, increasing the size of the domain and the range of parameters tested would provide additional results to support or refute the conclusions of this work. Ultimately experimental data with which to compare the results of this numerical study would be required before a definitive statement on the stability of the inclined boundary layer flow can be made. Initial work on subharmonic forcing has produced interesting results and should be expanded to constitute a more complete study. Further extensions to the code for example the modelling of flow behaviour such as chemical reactions and double diffusion would allow the investigation of Carbon Capture and Storage (CCS) as well as other topics of interest.

The work on front propagation in the Darcy-Bénard problem has produced interesting results but substantial work will be required beyond that contained in this preliminary study which has shown that situation in three dimensions is complex with the degree of supercriticality, wavenumber and initial conditions all playing a role in determining the initial and asymptotic behaviours of the propagating front. This work also provides information on the speed at which a disturbance can travel through the porous layer through the mechanism of conduction

and convection alone. In the case of the inclined thermal boundary layer the unforced vortex disturbance does not produce an absolute instability because the disturbance cannot propagate back upstream fast enough to overcome or negate the underlying flow. It would be of interest to apply the results of the front propagation work to the boundary layer problem to ascertain whether velocities of sufficient magnitude to overcome that underlying flow can ever be achieved.

# References

- Arakawa A (1966) Computational design for long-term numerical integration of the equations of fluid motion: Two-dimensional incompressible flow. Part 1. *J Comput Phys* 1:119–143.
- Aziz K, Hellums JD (1967) Numerical solution of the three-dimensional equations of motion for laminar natural convection. *Phys Fluids* 10:314–324.
- Bardan G, Mojtabi A (2000) On the Horton-Rogers-Lapwood convective instability with vertical vibration: Onset of convection. *Phys Fluids* 12(11):2723–2731.
- Bassom AP, Rees DAS (1995) The linear vortex instability of flow induced by a horizontal heated surface in a porous medium. *Q J Mech Appl Math* 48:1–19.
- Bhattacharya A, Calmidi VV, Mahajan RL (2002) Thermophysical properties of high porosity metal foams. *Int J Heat Mass Transfer* 45:1017–1031.
- Bonafede M, Boschi E (1992) A porous-flow model of flank eruptions on mount etna. *J Volcanol Geoth Res* 49(3-4):349–363.
- Briggs WL, Van Emden H, McCormick SF (2000) *A Multigrid Tutorial*. SIAM.

- Calmidi VV, Mahajan RL (2000) Forced convection in high porosity metal foams. *Trans ASME J Heat Transfer* 122:557–565.
- Chang ID, Cheng P (1983) Matched asymptotic expansions for free convection about an impermeable horizontal surface in a porous medium. *Int J Heat Mass Transfer* 26:163–174.
- Chang WJ, Jang JY (1989a) Inertia effects on vortex instability of a horizontal natural-convection flow in a saturated porous-medium. *Int J Heat Mass Transfer* 32:541–550.
- Chang WJ, Jang JY (1989b) Non-Darcian effects on vortex instability of a horizontal natural-convection flow in a porous-medium. *Int J Heat Mass Transfer* 32:529–539.
- Cheng P, Cheng ID (1976) Buoyancy induced flows in a saturated porous medium adjacent to impermeable horizontal surfaces. *Int J Heat Mass Transfer* 19:1267–1272.
- Cheng P, Hsu CT (1984) Higher order approximations for Darcian free convection about a semi-infinite vertical flat plate. *Trans ASME J Heat Transfer* 106:143–151.
- Cheng P, Minkowycz WJ (1977) Free convection about a vertical flat plate embedded in a porous medium with application to heat transfer from a dike. *J Geophys Res* 82:2040–2044.
- Cossu C, Loiseleux T (1998) On the convective and absolute nature of instabilities in finite difference numerical simulations of open flows. *J Comput Phys* 144:98–108.

- Cross M, Greenside H (2009) *Pattern Formation and Dynamics in Nonequilibrium Systems*. Cambridge.
- Czechowski L, Kossacki K (2009) Thermal convection in the porous methane-soaked regolith of Titan: Investigation of stability. *ICARUS* 202(2):599–606.
- Ebert U, van Saarloos W (1998) Universal algebraic relaxation of fronts propagating into an unstable state and implications for moving boundary approximations. *Phys Rev Lett* 80(8):1650–1653.
- Fineberg J, Steinberg V (1987) Vortex-front propagation in Rayleigh-Bénard convection. *Phys Rev Lett* 58(13):1332–1335.
- Getling AV (1992) Convection-front propagation and wavenumber selection. *Physica D* 55:121–134.
- Henson VE (2003) Multigrid methods for nonlinear problems: An overview. In: *Proc. Soc. Photo-Optical Inst. Eng. (SPIE)*, vol 5016, pp 36–48.
- Hirasaki GJ, Hellums JD (1968) A general formulation of the boundary conditions on the vector potential in three-dimensional hydrodynamics. *Q Appl Math* 16:331–342.
- Holst PH, Aziz K (1972) Transient three-dimensional natural convection in confined porous media. *Int J Heat Mass Transfer* 15:73–90.
- Horton CW, Rogers FT (1945) Convection currents in a porous medium. *J Appl Phys* 16:367–370.
- Hsu CT, Cheng P (1979) Vortex instability in buoyancy-induced flow over inclined heated surfaces in porous media. *Trans ASME J Heat Transfer* 101:660–665.

- Hsu CT, Cheng P (1980a) The onset of longitudinal vortices in mixed convective flow over an inclined surface in a porous medium. *Trans ASME J Heat Transf* 102:544–549.
- Hsu CT, Cheng P (1980b) Vortex instability of mixed convection flow in a semi-infinite porous medium bounded by a horizontal surface. *Int J Heat Mass Transfer* 23:789–798.
- Hsu CT, Cheng P, Homsy GM (1978) Instability of free convection flow over a horizontal impermeable surface in a porous medium. *Int J Heat Mass Transfer* 21:1221–1228.
- Iyer PA, Kelly RE (1974) The stability of the laminar free convection flow induced by a heated inclined plate. *Int J Heat Mass Transfer* 17:517–525.
- Jang J, Chang WJ (1988a) The flow and vortex instability of horizontal natural-convection in a porous-medium resulting from combined heat and mass buoyancy effects. *Int J Heat Mass Transfer* 31:769–777.
- Jang JY, Chang WJ (1987) Vortex instability of inclined buoyant layer in porous media saturated with cold water. *Int Comm Heat Mass Transfer* 14:405–416.
- Jang JY, Chang WJ (1988b) The flow and vortex instability of horizontal natural-convection in a porous-medium resulting from combined heat and mass buoyancy effects. *Int J Heat Mass Transf* 31:769–777.
- Jang JY, Chang WJ (1988c) Vortex instability of buoyancy-induced inclined boundary-layer flow in a saturated porous medium. *Int J Heat Mass Transfer* 31:759–767.

- Jang JY, Chen JL (1993a) Thermal dispersion and inertia effects on vortex instability of a horizontal mixed convection flow in a saturated porous-medium. *Int J Heat Mass Transfer* 36:383–389.
- Jang JY, Chen JL (1993b) Variable porosity effect on vortex instability of a horizontal mixed convection flow in a saturated porous-medium. *Int J Heat Mass Transfer* 36:1573–1582.
- Jang JY, Chen JL (1994) Variable porosity and thermal dispersion effects on vortex instability of a horizontal natural-convection flow in a saturated porous-medium. *Wärme-Stoffübertrag* 29:153–160.
- Jang JY, Leu JS (1993) Variable viscosity effects on the vortex instability of free-convection boundary-layer flow over a horizontal surface in a porous-medium. *Int J Heat Mass Transfer* 36:1287–1294.
- Jang JY, Lie KN, Chen JL (1995) The influence of surface mass flux on vortex instability of a horizontal mixed convection flow in a saturated porous medium. *Int J Heat Mass Transfer* 38:3305–3311.
- Kloker M, Konzelmann U (1993) Outflow boundary conditions for spatial Navier-Stokes simulations of transition boundary layers. *AIAA Journal* 31(4):620–628.
- Kockelkoren J, Storm C, van Saarloos W (2003) Evidence for slow velocity relaxation in front propagation in Rayleigh-Bénard convection. *Physica D* 174:168–175.
- Lage JL (1998) The fundamental theory of flow through permeable media from Darcy to turbulence. In: Ingham DB, Pop I (eds) *Transport Phenomena in Porous Media*, Pergamon.

- Lapwood ER (1948) Convection of a fluid in a porous medium. Proc Camb Phil Soc 4:508–521.
- de Lemos M (2006) Turbulence in Porous Media. Elsevier Science Ltd, Oxford.
- Lewis S, Bassom AP, Rees DAS (1995) The stability of vertical thermal boundary-layer flow in a porous medium. Eur J Mech, B/Fluids 14:395–407.
- Lie KN, Jang JY (1993) Boundary and inertia effects on vortex instability of a horizontal mixed convection flow in a porous-medium. Num Heat Transf Part A - Applications 23:361–378.
- Ljung A, Lundström TS, Marjavaara BD, Tano K (2011) Convective drying of an individual iron ore pellet – analysis with CFD. Int J Heat Mass Transfer 54:3882–3890.
- Lloyd JR, Sparrow EM (1970) On the instability of natural convection flow on inclined plates. J Fluid Mech 42:465–470.
- Lucke M, Mihelcic M, Kowalski B (1987) Propagating convection fronts. Phys Rev A 35(9):4001–4003.
- Lyubimov DV, Lyubimova TP, Mojtabi A, Sadilov ES (2008) Thermosolutal convection in a horizontal porous layer heated from below in the presence of a horizontal through flow. PhysFluids 20.
- McKibbin R (2009) Groundwater pollutant transport: transforming layered models to dynamical systems. Analele Stiintifice Ale Universitatii Ovidius Constanta Seria Matematica 17(3):183–196.

- Molle P, Lienard A, Grasmick A, Iwema A (2006) Effect of reeds and feeding operations on hydraulic behaviour of vertical flow constructed wetlands under hydraulic overloads. *Water Res* 40(3):606–612.
- Montange R, Amengual A, Hernández-García E, San Miguel M (1994) Multiple front propagation into unstable states. *Phys Rev E* 50(1):377–385.
- Nield DA, Bejan A (2006) *Convection in Porous Media*, 3rd edn. Springer, New York.
- Paul MC, Rees DAS, Wilson M (2005) The influence of higher order effects on the linear wave instability of vertical free convective boundary layer flow. *Int J Heat Mass Transfer* 48:809–817.
- Paul MC, Rees DAS, Wilson M (2008) Receptivity of free convective flow from a heated vertical surface. I. Linear waves. *Int J Thermal Sciences* 47:1382–1392.
- Phillips NA (1959) *The Atmosphere and the Sea in Motion*. Rockefeller Institute Press and the Oxford Univ. Press, New York.
- Postelnicu A (2010) The effect of a horizontal pressure gradient on the onset of a Darcy-Bénard convection in thermal non-equilibrium conditions. *Int J Heat Mass Transfer* 53:68–75.
- Prats M (1966) The effect of horizontal fluid flow on thermally induced convection currents in porous mediums. *J Geophys Res* 71(20):4835–4838.
- Rees DAS (1993) A numerical investigation of the nonlinear wave stability of vertical thermal boundary layer flow in a porous medium. *ZAMP* 44:306–313.

- Rees DAS (1997) The effect of inertia on the onset of mixed convection in a porous layer heated from below. *Int Comm Heat Mass Transfer* 24(2):277–283.
- Rees DAS (1998) Thermal boundary-layer instabilities in porous media: A critical review. In: Ingham DB, Pop I (eds) *Transport Phenomena in Porous Media*, Pergamon, pp 233–259.
- Rees DAS (2000) The stability of Darcy-Bénard convection. In: *Handbook of Porous Media*, 1st edn, Marcel Dekker, pp 521–558.
- Rees DAS (2001a) Stability analysis of Darcy-Bénard convection. Summer School on Porous Media, Neptun, Romania.
- Rees DAS (2001b) Vortex instability from a near-vertical heated surface in a porous medium I. Linear instability. *Proc R Soc Lond A* 457:1721–1734.
- Rees DAS (2002a) Recent advances in the instability of free convective boundary layers. In: Ingham DB, Pop I (eds) *Transport Phenomena in Porous Media*, 2nd edn, Pergamon, pp 54–81.
- Rees DAS (2002b) Vortex instability from a near-vertical heated surface in a porous medium II. Nonlinear evolution. *Proc R Soc Lond A* 458:1575–1592.
- Rees DAS (2003) Nonlinear vortex development in free convective boundary layers in porous media. In: *NATO ASI Proceedings*, Neptun, Romania, pp 449–458.
- Rees DAS (2010) Microscopic modelling of the two-temperature model for conduction in heterogeneous media. *J Porous Media* 13:125–143.

Rees DAS (2011) *Personal Communication*.

Rees DAS, Bassom AP (1991) Some exact solutions for free convective flows over heated semi-infinite surfaces in porous media. *Int J Heat Mass Transfer* 34:1564–1567.

Rees DAS, Bassom AP (1993) The nonlinear non-parallel wave instability of boundary-layer flow induced by a horizontal heated surface in porous media. *J Fluid Mech* 253:267–295.

Rees DAS, Pop I (2005) Local thermal nonequilibrium in porous medium convection. In: Ingham DB, Pop I (eds) *Transport Phenomena in Porous Media*, 3rd edn, Pergamon, pp 147–173.

Rees DAS, Pop I (2010) Discussion on the paper: Vortex instability of mixed convection boundary layer flow adjacent to a nonisothermal horizontal surface in a porous medium with variable permeability. *J Porous Media* 13:945–949.

van Saarloos W (2003) Front propagation into unstable states. *Physics Reports* 386:29–222.

Sigmund EE (2011) Perspectives on porous media MR in clinical MRI. In: Fantazzini P, Bortolotti V, Karger J (eds) *10th International Bologna Conference on Magnetic Resonance in Porous Media*, Leipzig, Germany, API Conference Proceedings, vol 1330, pp 13–16.

Smith FT, Bodonyi RJ (1982) Amplitude-dependent neutral modes in the Hagen-Poiseuille flow through a circular pipe. *Proc Roy Soc A-Math Phy* 384(1787):463–489.

- Sparrow EM, Hussar RB (1969) Longitudinal vortices in natural convection flow on inclined plates. *J Fluid Mech* 37:251–255.
- Storesletten L, Rees DAS (1998) The influence of higher-order effects on the linear instability of thermal boundary layer flow in porous media. *Int J Heat Mass Transfer* 41:1833–1843.
- Straus JM (1974) Large amplitude convection in porous media. *J Fluid Mech* 64:51–63.
- Tritton DJ (1988) *Physical Fluid Dynamics*, 2nd edn. Oxford Science Publications, Oxford University Press.
- Tumin A (2003) The spatial stability of natural convection flow on inclined plates. *J Fluid Eng-T ASME* 125:428–437.
- Vadasz P, Olek S (1999) Weak turbulence and chaos for low Prandtl number gravity driven convection in porous media. *Transport in Porous Media* 37:69–91.
- Vadasz P, Olek S (2000) Route to chaos for moderate Prandtl number convection in a porous layer heated from below. *Transport in Porous Media* 41:211–239.
- Whitaker S (1986) A theoretical derivation of Darcy's law. *Transport Porous Med* 1:3–25.
- Zhao JZ, Chen TS (2002) Inertia effect on non-parallel thermal instability of natural convection flow over horizontal and inclined plates in porous media. *Int J Heat Mass Transfer* 45:2265–2276.

# Appendix A

## Multigrid Schemes

This appendix details two Multigrid (MG) schemes; the MultiGrid Correction Scheme (MGCS) and the Full Approximation Scheme (FAS). Both schemes serve to increase the speed of solution when a smoother such as GS is used. As mentioned in Sect. 3.1.8 the principle behind these schemes is based on three key concepts;

- Pointwise solvers, such as Gauss-Seidel, have a smoothing effect which means they are effective at eliminating high-frequency / highly oscillatory components of the error, but struggle to remove the smoother elements; leading to the solution stalling.
- Moving a function (i.e. the error) from a coarse grid to a fine grid makes it appear more oscillatory (see Figure A.1)
- A good initial guess leads to much quicker convergence of a pointwise solver.

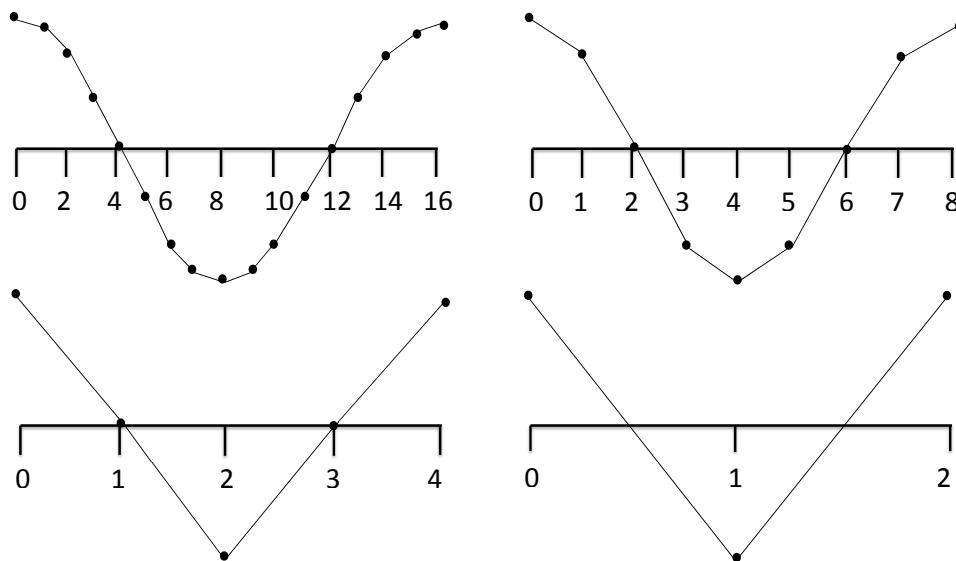


Figure A.1: Transferring a function to a coarser grid leads to a more oscillatory appearance.

## A.1 MultiGrid Correction Scheme

If the equations to be solved are linear then putting these ideas together logically leads to the MGCS as outlined by Briggs et al (2000), to wit:

- Begin by solving the system of equations  $\mathbf{A}^h \mathbf{u}^h = \mathbf{f}^h$  for the dependent variable  $\mathbf{u}$  on a fine grid  $\Omega^h$ , with an appropriate initial guess  $\mathbf{v}$ .
- Calculate the residual using the relationship  $\mathbf{r} = \mathbf{f} - \mathbf{A}\mathbf{u}$ .
- Transfer the residual to a coarser grid  $\Omega^{2h}$ . Thus making it appear more oscillatory, and amenable to relaxation.
- Relax on the residual equation  $\mathbf{A}^{2h} \mathbf{e}^{2h} = \mathbf{r}^{2h}$  to get an approximation to the error ( $\mathbf{e}$ ).
- Correct the approximation to  $\mathbf{u}$ ,  $\mathbf{v}$  on  $\Omega^h$  using the error:  $\mathbf{v}^h \leftarrow \mathbf{v}^h + \mathbf{e}^{2h}$ . Thus giving a good initial guess for the problem on the fine grid.
- Relax on the original equation  $\mathbf{A}^h \mathbf{u}^h = \mathbf{f}^h$  again using the improved initial guess  $\mathbf{v}$ .

The smooth nature of the error following solution on the coarse grid makes interpolating the error back on to the fine grid effective. The grid is usually coarsened by a factor of 2 at each level. The initial guess used ( $\mathbf{v}$ ) is zero in the first instance for all grids. The above process can be nested to allow the error to be calculated on coarser and coarser grids, before being used as a correction to the approximation on the level above. It is this down and then up approach which gives rise to the name ‘V-cycle’.

The above notation can be further refined for computational use when we realise that  $\mathbf{r}^{2h}$  can be renamed  $\mathbf{f}^{2h}$ , as it is just a right hand vector. Similarly  $\mathbf{e}^{2h}$  may be referred to as  $\mathbf{u}^{2h}$ , which is just a solution vector. Below is the full scheme, for

$n > 1$  grids, with grid length  $h, 2h, 4h, \dots, 2^{n-1}h$ . The parameter  $I_h^{2h}$  represents the interpolation from  $\Omega^h$  to  $\Omega^{2h}$ .

- Relax on  $\mathbf{A}^h \mathbf{u}^h = \mathbf{f}^h$ , with initial guess  $\mathbf{v}^h$
- Calculate  $\mathbf{f}^{2h} = I_h^{2h} \mathbf{r}^h$ .
  - Relax on  $\mathbf{A}^{2h} \mathbf{u}^{2h} = \mathbf{f}^{2h}$ , with initial guess  $\mathbf{v}^{2h} = 0$
  - Calculate  $\mathbf{f}^{4h} = I_{2h}^{4h} \mathbf{r}^{2h}$ .
    - Relax on  $\mathbf{A}^{4h} \mathbf{u}^{4h} = \mathbf{f}^{4h}$ , with initial guess  $\mathbf{v}^{4h} = 0$
    - Calculate  $\mathbf{f}^{8h} = I_{4h}^{8h} \mathbf{r}^{4h}$ .
- ⋮
- Solve  $\mathbf{A}^{2^{n-1}h} \mathbf{u}^{2^{n-1}h} = \mathbf{f}^{2^{n-1}h}$
- ⋮
- Correct  $\mathbf{v}^{4h} \leftarrow \mathbf{v}^{4h} + I_{8h}^{4h} \mathbf{v}^{8h}$
- Relax on  $\mathbf{A}^{4h} \mathbf{u}^{4h} = \mathbf{f}^{4h}$ , with initial guess  $\mathbf{v}^{4h}$
- Correct  $\mathbf{v}^{2h} \leftarrow \mathbf{v}^{2h} + I_{4h}^{2h} \mathbf{v}^{4h}$
- Relax on  $\mathbf{A}^{2h} \mathbf{u}^{2h} = \mathbf{f}^{2h}$ , with initial guess  $\mathbf{v}^{2h}$
- Correct  $\mathbf{v}^h \leftarrow \mathbf{v}^h + I_{2h}^h \mathbf{v}^{2h}$
- Relax on  $\mathbf{A}^h \mathbf{u}^h = \mathbf{f}^h$ , with initial guess  $\mathbf{v}^h$

## A.2 Multigrid Full Approximation Scheme

The method outlined in this section is that described by Henson (2003). FAS is used when a nonlinear problem is encountered, and is necessary because the residual equation underlying the MGCS is no longer valid. For the MGCS we

begin with a problem in the form  $A(\mathbf{u}) = \mathbf{f}$  and denote  $\mathbf{v}$  as an approximation to the exact solution  $\mathbf{u}$ . The error  $\mathbf{e}$  is then defined as  $\mathbf{e} = \mathbf{u} - \mathbf{v}$ . Letting the residual  $\mathbf{r} = \mathbf{f} - A(\mathbf{v})$  gives the residual equation  $A\mathbf{e} = \mathbf{r}$  if  $A$  is linear. However this is no longer the case if  $A$  is nonlinear because  $A(\mathbf{u}) - A(\mathbf{v}) \neq A(\mathbf{u} - \mathbf{v})$ . Consequently it becomes necessary to alter the approach and to solve the full approximation, rather than just the error on the coarse grid.

As above let  $\mathbf{v}^h$  be a fine-grid approximation to

$$A^h(\mathbf{u}^h) = \mathbf{f}^h. \quad (\text{A.1})$$

The coarse grid version of the residual equation is

$$A^{2h}(\mathbf{v}^{2h} + \mathbf{e}^{2h}) - A^{2h}(\mathbf{v}^{2h}) = \mathbf{r}^{2h}. \quad (\text{A.2})$$

The coarse grid residual is the restriction of the fine-grid residual giving;

$$\mathbf{r}^{2h} = I_h^{2h} \mathbf{r}^h = I_h^{2h} (\mathbf{f}^h - A^h(\mathbf{v}^h)). \quad (\text{A.3})$$

The fine-grid approximation is also restricted using the same operator;

$$\mathbf{v}^{2h} = I_h^{2h} \mathbf{v}^h. \quad (\text{A.4})$$

Substituting Eqs. (A.3) and (A.4) into Eqn. (A.2) gives

$$A^{2h}(I_h^{2h} \mathbf{v}^h + \mathbf{e}^{2h}) = A^{2h}(I_h^{2h} \mathbf{v}^h) + I_h^{2h} (\mathbf{f}^h - A^h(\mathbf{v}^h)). \quad (\text{A.5})$$

The right hand side of Eqn. (A.5) is known. The coarse grid error is

$$\mathbf{e}^{2h} = \mathbf{u}^{2h} - I_h^{2h} \mathbf{v}^h, \quad (\text{A.6})$$

and this can then be interpolated up to the fine grid and used as a correction

$$\mathbf{v}^h \leftarrow \mathbf{v} + I_{2h}^h \mathbf{e}^{2h}. \quad (\text{A.7})$$

This gives the FAS algorithm as:

- Restrict the fine-grid approximation and its residual:  $\mathbf{r}^{2h} = I_h^{2h}(\mathbf{f}^h - A^h(\mathbf{v}^h))$   
and  $\mathbf{v}^{2h} = I_h^{2h}\mathbf{v}^h$ .
- Solve the coarse-grid problem  $A^{2h}(\mathbf{u}^{2h}) = A^{2h}(\mathbf{v}^{2h}) + \mathbf{r}^{2h}$ .
- Compute the coarse-grid approximation to the error:  $\mathbf{e}^{2h} = \mathbf{u}^{2h} - \mathbf{v}^{2h}$ .
- Interpolate the coarse-grid error approximation onto the fine grid and correct the current fine grid approximation:  $\mathbf{v}^h \leftarrow \mathbf{v}^h + I_{2h}^h \mathbf{e}^{2h}$ .

As for the MGCS a V-cycle scheme was used.

# Appendix B

## Weakly Nonlinear Analysis

The method used to derive the amplitude equations here is based upon that outlined in Rees (2001a), Eqn. (B.21) is also given in Rees (2000). We are considering the slightly supercritical regime where convection is weak and the amplitude of the roll disturbance is only of  $O(\varepsilon)$  where  $\varepsilon$  is asymptotically small. We concentrate on the region where convection first occurs (i.e. close to  $\text{Ra}_c$  and  $k_c$ ) and consider the wavenumber in terms of wave-vector space; it may vary in  $x$  and  $y$  but its magnitude will remain equal to  $\pi$ . The Rayleigh number will be an  $O(\varepsilon^2)$  amount above its critical value  $\text{Ra}_c = 4\pi^2$ . The problem is three dimensional and therefore we use the pressure/temperature formulation as given by Eqs. (5.10 – 5.14), subject to the boundary conditions

$$z = 0 : \theta = 1, p_z = \text{Ra} \quad z = 1 : \theta = 0, p_z = 0. \quad (\text{B.1})$$

The conduction solution is:

$$\theta = 1 - z, \quad p = \text{Ra}\left(z - \frac{1}{2}z^2\right) + \text{constant}. \quad (\text{B.2})$$

Perturbing about this solution using

$$\theta = 1 - z + \Theta, \quad p = \text{Ra}(z - \frac{1}{2}z^2) + \text{constant} + P, \quad (\text{B.3})$$

gives

$$\nabla^2 P = \text{Ra}\Theta_z, \quad (\text{B.4})$$

$$\Theta_t + \text{Ra}\Theta\Theta_z - \nabla P \nabla \Theta = \nabla^2 \Theta + \text{Ra}\Theta - P_z, \quad (\text{B.5})$$

subject to the boundary conditions

$$z = 0 : \Theta = 0, P_z = 0, \quad z = 1 : \Theta = 0, P_z = 0. \quad (\text{B.6})$$

We introduce the expansion

$$\begin{pmatrix} P \\ \Theta \end{pmatrix} = \varepsilon \begin{pmatrix} P_1 \\ \Theta_1 \end{pmatrix} + \varepsilon^2 \begin{pmatrix} P_2 \\ \Theta_2 \end{pmatrix} + \varepsilon^3 \begin{pmatrix} P_3 \\ \Theta_3 \end{pmatrix} + \dots, \quad (\text{B.7})$$

where  $\varepsilon \ll 1$ , and

$$\text{Ra} = \text{Ra}_0 + \varepsilon^2 \text{Ra}_2 + \dots \quad \text{where} \quad \text{Ra}_0 = \text{Ra}_c = 4\pi^2. \quad (\text{B.8})$$

The exponential growth of linearised disturbances is proportional to the difference of Ra from Ra<sub>c</sub>, so time is rescaled as

$$\tau = \frac{\varepsilon^2 t}{2}. \quad (\text{B.9})$$

As the wavenumber in  $x$  varies, it gives rise to quantities such as  $\cos(\pi + \varepsilon K)x$  in wavevector space consequently the method of multiple scales is used. The  $O(1)$  scale takes account of the main convection pattern, whilst a “slow” length scale is introduced which describes the behaviour when  $x$  or  $y$  is large i.e. over many wavelengths. The “slow”  $x$ -scale,  $X$  is defined as:

$$X = \varepsilon x. \quad (\text{B.10})$$

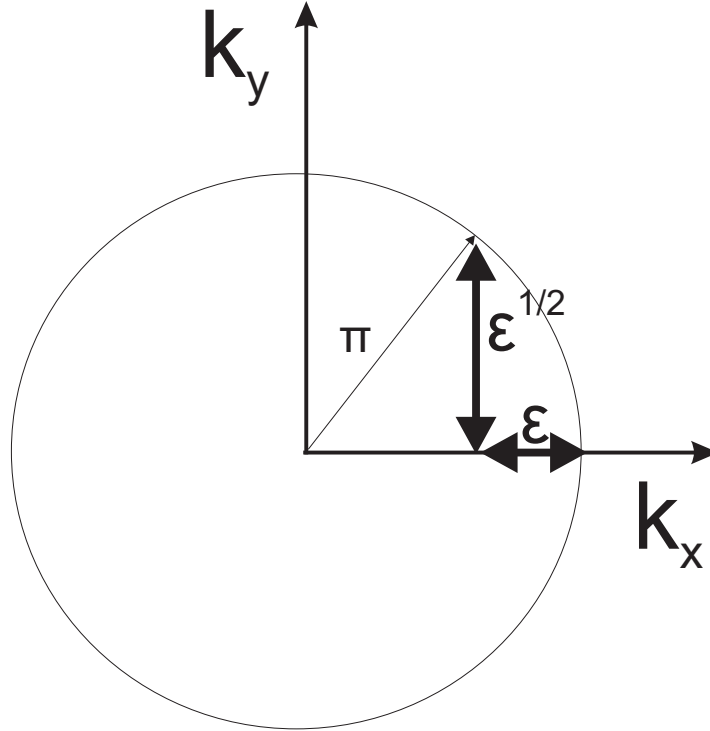


Figure B.1: Wavespace diagram showing relationship between  $x$  and  $y$  length-scales

This leads to the replacements;

$$\frac{\partial}{\partial x} \rightarrow \frac{\partial}{\partial x} + \epsilon \frac{\partial}{\partial X}, \quad (\text{B.11})$$

$$\frac{\partial^2}{\partial x^2} \rightarrow \frac{\partial^2}{\partial x^2} + 2\epsilon \frac{\partial^2}{\partial x \partial X} + \epsilon^2 \frac{\partial^2}{\partial X^2}. \quad (\text{B.12})$$

Figure B.1 depicts the relationship between the length scales  $x$  and  $y$ ; a reduction of an  $O(\epsilon)$  amount in  $x$  results in a change in  $y$  of  $O(\epsilon^{1/2})$  to retain the original

length of the wavevector, consequently we introduce a slow spatial variable for  $Y$ :

$$Y = \varepsilon^{1/2}y. \quad (\text{B.13})$$

Behaviour is not dependent on  $y$  except on the long length scale  $Y$  therefore;

$$\frac{\partial}{\partial y} = \varepsilon^{1/2} \frac{\partial}{\partial Y}, \text{ and } \frac{\partial^2}{\partial y^2} = \varepsilon \frac{\partial^2}{\partial Y^2}. \quad (\text{B.14})$$

The perturbation equations become;

$$\nabla^2 P - \text{Ra}_0 \Theta_z = \varepsilon^2 \text{Ra}_2 \Theta_z - \varepsilon (2P_{XX} + P_{YY}) - \varepsilon^2 P_{XX}, \quad (\text{B.15})$$

$$\begin{aligned} \nabla^2 \Theta &= P_z - (\text{Ra}_0 + \varepsilon^2 \text{Ra}_2) \Theta - \varepsilon (2\Theta_{XX} + \Theta_{YY}) - \varepsilon^2 \Theta_{XX} \\ &\quad - \nabla p \nabla \Theta - \varepsilon (P_x \Theta_X + P_X \Theta_x + P_Y \Theta_Y) - \varepsilon^2 P_X \Theta_X. \end{aligned} \quad (\text{B.16})$$

The analysis proceeds by equating components at increasing orders of  $\varepsilon$ . At  $O(\varepsilon)$  the solution is

$$P_1 = -\frac{1}{\pi} [Ae^{i\pi x} + \bar{A}e^{-i\pi x}] \cos \pi z, \quad (\text{B.17})$$

$$\Theta_1 = \frac{1}{2\pi^2} [Ae^{i\pi x} + \bar{A}e^{-i\pi x}] \sin \pi z. \quad (\text{B.18})$$

In these equations  $A$  is a function of  $\tau, X$  and  $Y$ . This process is repeated at  $O(\varepsilon^2)$ , giving the following results in the case of transverse(2D) rolls:

$$P_2 = 0, \quad (\text{B.19})$$

$$\Theta_2 = -\frac{1}{4\pi^3} A^2 \sin 2\pi z. \quad (\text{B.20})$$

At  $O(\varepsilon^3)$  a solution is shown to exist only if a solvability condition is fulfilled.

Application of this solvability condition gives the equation

$$A_\tau = \text{Ra}_2 A + 4 \left[ A_{XX} - \frac{i}{\pi} A_{XY} - \frac{1}{4\pi^2} A_{YYY} \right] - A^2 \bar{A} \quad (\text{B.21})$$

For transverse (2D) rolls,  $A$  is constant in  $Y$ , and we are only interested in real values of  $A$  as imaginary components will not have an effect of the speed of propagation of the front. Therefore Eqn. (B.21) becomes;

$$A_\tau = \text{Ra}_2 A + 4A_{XX} - A^3. \quad (\text{B.22})$$

For the longitudinal rolls  $A$  is constant in  $X$  but varies with  $Y$ , and  $A$  is again real. Therefore Eqn. (B.21) becomes;

$$A_\tau = \text{Ra}_2 A - \frac{1}{\pi^2} A_{YYY} - A^3. \quad (\text{B.23})$$

## Appendix C

# Analytical Calculation of Speed of Propagation

The travelling wave solution  $F = f(x - c\tau) = f(\eta)$  is substituted into Eqn. (5.28) giving

$$-cF' = F + F'' - F^3, \quad (\text{C.1})$$

where dashes denote differentiation with respect to  $\eta$ . We rearrange giving

$$F'' + cF' + F - F^3 = 0. \quad (\text{C.2})$$

Letting  $\tau = 0$  and

$$F = \frac{1}{2}(1 - \tanh \beta \xi) \quad (\text{C.3})$$

and equating coefficients gives

$$\beta = \pm \sqrt{\frac{1}{8}} \quad \text{and} \quad c = \pm \frac{3}{\sqrt{2}}. \quad (\text{C.4})$$

The front may propagate with equal speed in either the positive or negative  $\xi$  direction.

## **Appendix D**

### **Variation of Nusselt Number with $k$ in the 2D Darcy-Bénard Problem**

Figure D.1 was taken from Rees (2011) and created for the purposes described in Sect. 5.4.4.

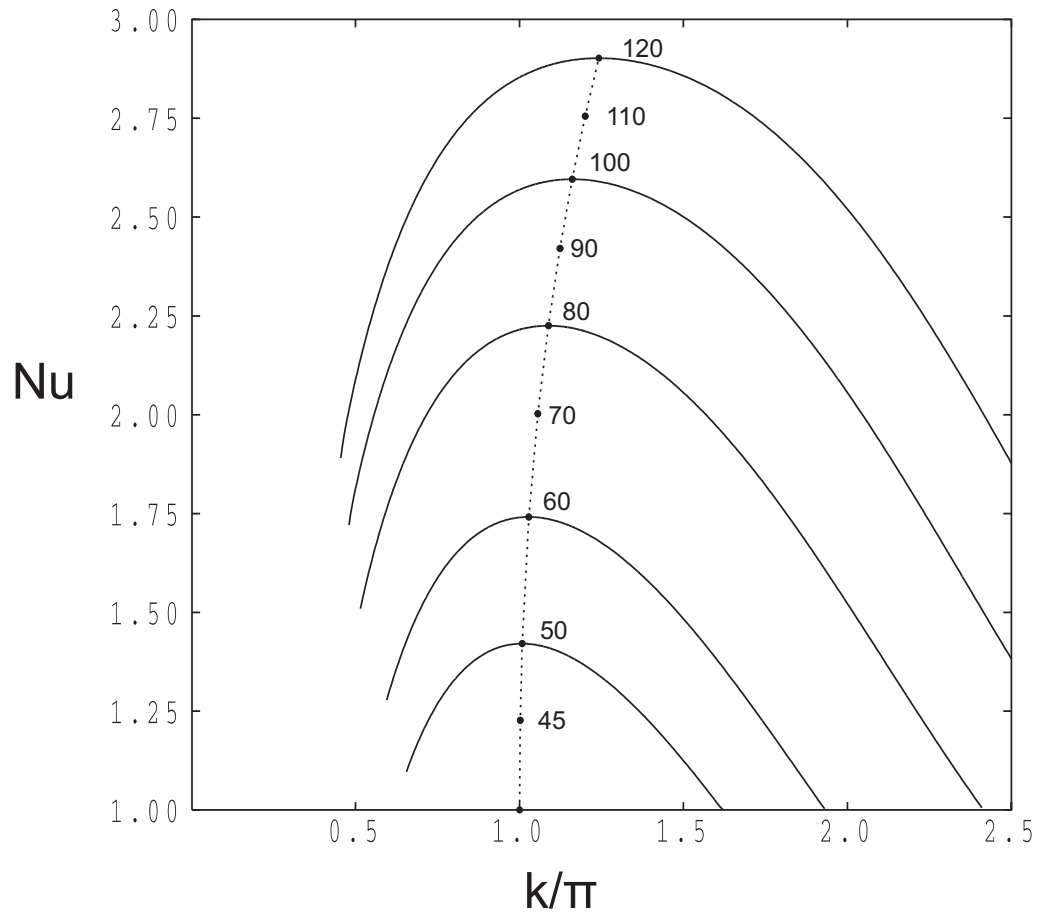


Figure D.1: Variation of the Nusselt number with wavenumber for different values of Ra in the 2D Darcy-Bénard problem (Rees (2011)).